AN INVESTIGATION OF AEROGELS, FOAMS, AND FOILS FOR MULTI-WIRE PROPORTIONAL COUNTER NEUTRON DETECTORS

by

KYLE ALAN NELSON

B.S., Nebraska Wesleyan University, 2008

AN ABSTRACT OF A DISSERTATION

submitted in partial fulfillment of the
requirements for the degree

DOCTOR OF PHILOSOPHY

Department of Mechanical and Nuclear Engineering
College of Engineering

KANSAS STATE UNIVERSITY
Manhattan, Kansas

2013

ABSTRACT

The ^{3}He gas shortage for neutron detection has caused an increase in research efforts to develop viable alternative technologies. ^{3}He neutron detectors cover areas ranging from 10–1000 cm^2 in cylindrical form factors and are ideal for many nuclear applications due to their high intrinsic thermal neutron detection efficiency (> 80%) and gamma-ray discrimination (GRR $\leq 1 \times 10^{-6}$) capabilities. Neutron monitoring systems for nuclear security applications include Radiation Portal Monitors (RPM's), backpack, briefcase, and hand-held sensors. A viable replacement technology is presented here and compares three neutron detectors, each with different neutron absorber materials, to current ^{3}He standards. These materials include Li and/or B silica aerogels, LiF impregnated foams, and metallic Li foils. Additionally, other neutron absorbing materials were investigated in this work and include LiF coated Mylar, B foils, BN coated carbon foam, and BN coated plastic honeycomb. From theoretical calculations, the Li foil material showed the greatest promise as a viable ^{3}He alternative, thus a majority of the research efforts were focused on this material.

The new neutron detector was a multi-wire proportional counter (MWPC) constructed using alternating banks of anode wires and 95% enriched ^{6}Li foils sheets spaced 1.63 cm apart. In total, six anode banks and five layers of foil were used, thus an anode wire bank was positioned on each side of a suspended foils. Reaction products from the $^{6}Li(n,\alpha)^{3}H$ reaction were able to escape both side of a foil sheet simultaneously and be measured in the surrounding gas volume concurrently. This new concept of measuring both reaction products from a single neutron absorption in a solid-form absorber material increased the intrinsic thermal neutron detection efficiency and gamma-ray discrimination compared to coated gas-filled detectors. Three different sizes of Li foil MWPC neutron detectors were constructed ranging from 25–1250 cm^2 and included detectors for RPM's, backpacks, and hand-held systems. The measured intrinsic thermal neutron detection efficiency of these devices was approximately 54%, but it is possible to exceed 80% efficiency with additional foils. The gamma-ray discrimination abilities of the detector exceeded ^{3}He tubes by almost three orders of magnitude (GRR = 7.6×10^{-9}).

AN INVESTIGATION OF AEROGEL, FOAMS, AND FOILS FOR MULTI-WIRE PROPORTIONAL COUNTER NEUTRON DETECTORS

by

KYLE ALAN NELSON

B.S., Nebraska Wesleyan University, 2008

A DISSERTATION

submitted in partial fulfillment of the
requirements for the degree

DOCTOR OF PHILOSOPHY

Department of Mechanical and Nuclear Engineering
College of Engineering

KANSAS STATE UNIVERSITY
Manhattan, Kansas

2013

Approved by:

Major Professor
Douglas S. McGregor

COPYRIGHT

ABSTRACT

The ^{3}He gas shortage for neutron detection has caused an increase in research efforts to develop viable alternative technologies. ^{3}He neutron detectors cover areas ranging from 10–1000 cm^2 in cylindrical form factors and are ideal for many nuclear applications due to their high intrinsic thermal neutron detection efficiency (> 80%) and gamma-ray discrimination (GRR $\leq 1 \times 10^{-6}$) capabilities. Neutron monitoring systems for nuclear security applications include Radiation Portal Monitors (RPM's), backpack, briefcase, and hand-held sensors. A viable replacement technology is presented here and compares three neutron detectors, each with different neutron absorber materials, to current ^{3}He standards. These materials include Li and/or B silica aerogels, LiF impregnated foams, and metallic Li foils. Additionally, other neutron absorbing materials were investigated in this work and include LiF coated Mylar, B foils, BN coated carbon foam, and BN coated plastic honeycomb. From theoretical calculations, the Li foil material showed the greatest promise as a viable ^{3}He alternative, thus a majority of the research efforts were focused on this material.

The new neutron detector was a multi-wire proportional counter (MWPC) constructed using alternating banks of anode wires and 95% enriched ^{6}Li foils sheets spaced 1.63 cm apart. In total, six anode banks and five layers of foil were used, thus an anode wire bank was positioned on each side of a suspended foils. Reaction products from the $^{6}Li(n,\alpha)^{3}H$ reaction were able to escape both side of a foil sheet simultaneously and be measured in the surrounding gas volume concurrently. This new concept of measuring both reaction products from a single neutron absorption in a solid-form absorber material increased the intrinsic thermal neutron detection efficiency and gamma-ray discrimination compared to coated gas-filled detectors. Three different sizes of Li foil MWPC neutron detectors were constructed ranging from 25–1250 cm^2 and included detectors for RPM's, backpacks, and hand-held systems. The measured intrinsic thermal neutron detection efficiency of these devices was approximately 54%, but it is possible to exceed 80% efficiency with additional foils. The gamma-ray discrimination abilities of the detector exceeded ^{3}He tubes by almost three orders of magnitude (GRR = 7.6×10^{-9}).

TABLE OF CONTENTS

LIST OF FIGURES ix
LIST OF TABLES xxii
ACKNOWLEDGEMENTS xxiii
DEDICATION xxiv
LIST OF ACRONYMS xxv
CHAPTER 1 1
1.1 Motivation for Research 1
1.2 Novel Contributions to Gas-filled Neutron Detectors 6
1.3 Organization of Thesis 7
CHAPTER 2 9
2.1 Neutron Properties 9
2.2 Neutron Scattering and Absorption for Detection 10
2.3 Neutron Absorption & Reaction Product Measurement 18
2.4 Commercially available neutron detectors 22
2.4.1 Gas-Filled Neutron Detectors 23
2.4.2 Scintillation Neutron Detectors 29
2.4.3 Coated Semiconductor Neutron Detectors 30
CHAPTER 3 32
3.1 General Overview 32
3.2 Lithium Foil 34
3.3 Impregnated Foam 42
3.4 Aerogels 45
CHAPTER 4 49
4.1 Axial Fins 50
4.2 Boron Nitride Coated Cheesecloth 53
4.3 Honeycomb plastic 54
4.4 BN coated carbon foam 57
4.5 LiF Coated Mylar Foil 59

4.6 Boron Foils 68
CHAPTER 5 73
5.1 Proof-of-principle test chambers 73
5.2 Aerogel Synthesis and Fabrication 77
5.3 Foam Synthesis and Fabrication 79
5.4 Obtaining Li Foil 81
5.5 Aerogel Test Chamber 82
5.6 Foam Test Chamber 83
5.7 Li Foil MWPC Construction 86
5.7.1 Anode wire distance determination 86
5.7.2 Li Foil Support Frame Optimization 90
5.7.3 Li Foil Detector Assembly 95
5.8 Form Fit Aerogel and Li Foil Construction 100
CHAPTER 6 111
6.1 Neutron Detector Sensitivity Evaluation Methods 111
6.2 First Evaluations 123
6.3 Aerogel Neutron Sensitivity Results and Discussion 130
6.2 Li Foil MWPC Neutron Response: Large Area, Mid-Sized, and Form Fit 132
6.2.1 Li Foil Corrugated Detector 140
6.2.2 Li Proportional Counter (LPC) Detector: Monster Truck Rally 143
6.2.3 Form-Fit Detectors 157
CHAPTER 7 167
7.1 Achievements and Comparisons 167
7.2 Novel Contributions 169
7.3 Future Work 169
7.4 Final Remarks 171
REFERENCES 172
Appendix A A.1
Appendix B B.1
Appendix B.1 – Pulse-Height Spectra: 55 μm ^{6}Li Foil B.10
Appendix B.2 – Pulse-Height Spectra: 35 μm ^{6}Li Foil B.11

Appendix C C.1
Appendix C.1 – MCNP6 pulse-height spectra C.1
Appendix C.2 – MCNP6 corrugated spectra and angular response C.3
Appendix C.3 – HDPE Moderator Optimization C.6
Appendix C.4 – LPC Modeling C.9
Appendix D D.1
Appendix E E.1
Appendix E.1 – Electric Field Derivation from Gauss's law E.1
Appendix E.2 – FWHM derivation from Gaussian function E.3

LIST OF FIGURES

Figure 2.1: A diagram of the neutron decay scheme through an intermediate heavy boson into a proton, electron, and antineutrino. 10

Figure 2.2: Microscopic absorption cross section of ^{3}He, ^{6}Li, ^{10}B, and ^{235}U as a function of neutron energy [43]. 11

Figure 2.3: Schematic of a uni-directional thermal neutron beam incident on a neutron absorber slab of thickness t. The transmitted neutron current is calculated with Eq. (8) [60]. 19

Figure 2.4: An illustration of a ^{10}B coated diode. The coating thickness is greater than the longest range reaction product and, thus, the chance exists that neither reaction product is measured, as shown in Case I. If neutron absorptions occur sufficiently close to the diode surface, only one reaction product can be measured per neutron absorption because reaction products are emitted in opposite directions (180°) due to conservation of momentum. 21

Figure 2.5: A 5.0 cm diameter x 13 cm long ^{3}He neutron detector filled to 4.0 atm is shown in the center. The four pulse-height spectra shown were collected using a 1.0 mm diameter thermal neutron beam at different distances from the base (left side of X-ray) of the detector. Only a 1.5 cm width exists where the ideal pulse-height spectrum is attainable and centered at 6.0 cm from the base. The pulse-height spectra deviate from the ideal case dramatically as the incident neutron beam moved away from the center of the anode wire. 25

Figure 2.6: Total counts were recorded as a function of position longitudinally along the same ^{3}He tube shown in Figure 2.5. The diameter of the neutron beam was approximately 1.0 mm and total counts were recorded in 0.5 cm increments from the base to the top of the detector. The active counting region is approximately 6.5 cm long (50% of the overall length), but the entire 13.0 cm of the detector will absorb neutrons. 26

Figure 2.7: A pulse-height spectrum collected with a $^{10}BF_3$ neutron detector. All features are labeled in the plot and the wall effect occurs from either the alpha particle or Li ion colliding with the wall and depositing only a fraction of its total energy. 27

Figure 2.8: An illustration of the pulse-height spectrum from a ^{10}B coated proportional counter where the wall effect is obvious. The steps coincide with the alpha particle and Li ion energies. The blue cross-hatched region is the number of interactions from neutrons that

must be eliminated from the data set in order to remove false counts from gamma-rays and electronic noise. 28
Figure 2.9: A cross-sectional side image collected with a scanning electron microscope showing 490 µm deep trenches backfilled with nano-sized ^{6}LiF powder (left). A cross-sectional schematic of a MSND detector which also depicts the neutron capture and reaction products entering the Si regions of the diode (right). As a result of the trench width, it is possible to measure both reaction products simultaneously. 31
Figure 3.1: An illustration of a multi-layered multi-wire proportional counter. The neutron absorber layers are designed to be thinner than the summed range of the reaction products. The reaction products may escape the absorber slab simultaneously and be measured in the gas volume concurrently. 34
Figure 3.2: A plot of the intrinsic thermal neutron detection efficiency of the ^{6}Li foil MWPC as a function of the foil thickness for various numbers of ^{6}Li foils. Depending on the number of foils used in the device, a specific foil thickness will optimize the overall detection efficiency. 35
Figure 3.3: The simulated pulse-height spectra for different thicknesses of Li foil. As the thickness increases, more of the reaction product energy is absorbed in the foil before escaping and, consequently, smaller signals are produced. 36
Figure 3.4: Four possible occurrences for reaction product energy deposition in the gas volume. In Case 1 (a), both reaction products enter the gas volume, while in Case 2 (b), only the triton enters the gas. In Case 3 (c), only the alpha particle escapes the foil. Lastly, Case 4 (d), neither reaction product produces any ionization in the gas. 38
Figure 3.5: Pulse-height spectral contributions from the three cases in which reaction product energy is deposited in the gas volume. The three cases are summed into one pulse-height spectrum in the lower right. 39
Figure 3.6: The probability that each case occurs per neutron absorbed as a function of the Li foil thickness. The ability of the detector to measure the triton escaping either side of the foil dominates the detection efficiency when the foil thickness is greater than 23 µm. 40
Figure 3.7: The theoretical pulse-height spectra of the Li foil MWPC obtained using MCNP6 for different P-10 pressures. The main feature of the spectra shifts to higher energies with

increasing pressure, a result of more energy deposited per unit length from the reaction products. 41
Figure 3.8: Cross-sectional illustration of ^{6}LiF impregnated foam. The red circles represent locations of the neutron absorption point in ^{6}LiF. Because of the random porosity of the foam, some reaction products may have streaming paths to escape the foam absorber, making predictions of reaction product ranges difficult. 44
Figure 3.9: The intrinsic thermal neutron detection efficiency of 20 wt% ^{6}LiF impregnated foam obtained using the simulated reaction product ranges. 45
Figure 3.10: A 1.0 cm thick sheet of aerogel is the only item separating crayons and the flame of a blow torch [68]. 46
Figure 3.11: A TEM image of graphene aerogel with a 1.0 µm scale in the lower right corner of the image [68]. 47
Figure 3.12: The fractional neutron absorption of elemental B aerogel with two different aerogel densities. 48
Figure 4.1: Neutron response pulse-height spectra from 50 µm (left) and 0.05 µm (right) thick LiF coated Al plates positioned orthogonal to the center anode wire. The thinner coating has less self-absorption and, consequently, the energy peaks are easily identified. 52
Figure 4.2: Neutron response pulse-height spectra obtained using 16 µm thick sticky tape coated with LiF. The LiF coating was not controlled and presumed to be too thick to allow reaction products to escape simultaneously from both sides of the fin. 52
Figure 4.3: Thermal neutron pulse-height spectra obtained using BN coated cheese cloth wrapped in a square spiral frame around a single anode wire. 54
Figure 4.4: Plastic tubes are cut into 0.25" or 0.5" lengths and glued together to form a sheet of corrugated plastic similar to a honeycomb. BN aerosol was sprayed on the honeycomb to create a high surface area coated neutron detector. 56
Figure 4.5: SEM image of BN aerosol sprayed onto a silicon wafer. The above coating was a single manual swipe of the aerosol canister and a thinner coating location compared to the rest of the coating. Particles or coating thicknesses were as large as 25 µm. 56
Figure 4.6: The thermal neutron response pulse-height spectra from the BN-coated plastic honeycomb finned neutron detector. 57

Figure 4.7: From left to right is carbon, alumina, and copper foam with pore sizes ranging from 1–10 mm [67]. 58
Figure 4.8: The thermal neutron response pulse-height spectra from BN-coated carbon foam. There are no distinctive features, but sensitivity to neutrons was observed. 59
Figure 4.9: A cross-sectional schematic of the LiF coated Mylar showing two different thicknesses of LiF coating. The reaction products are able to escape both sides of the absorber sheet simultaneously and be measured in separate gas compartments concurrently. 60
Figure 4.10: The theoretical intrinsic thermal-neutron detection efficiency of ^{6}LiF foils for various layers of absorber sheets as a function of foil thickness. 62
Figure 4.11: The simulated thermal-neutron response pulse-height spectra of 0.1, 4.5, 9.9, and 14.0 µm thick LiF coatings on 2-µm aluminized Mylar obtained using MCNP6. 64
Figure 4.12: The experimental and simulated (MCNP6) thermal-neutron response pulse-height spectra of 4.5 µm thick LiF coated aluminized Mylar. 65
Figure 4.13: The experimental and simulated (MCNP6) thermal-neutron response pulse-height spectra of 9.9 µm thick LiF coated aluminized Mylar. 65
Figure 4.14: The experimental and simulated (MCNP6) thermal-neutron response pulse-height spectra of 14.0 µm thick LiF coated aluminized Mylar. 66
Figure 4.15: The aluminized Mylar sheet coated with 9.9 µm of LiF which shows the flaking of the LiF occurring in the top right quadrant of the pane. 67
Figure 4.16: The intrinsic thermal neutron detection efficiency of the B foil MWPC as a function of B foil thickness for multiple layers of foil in the detector. The number of layers used in the device determines the foil thickness that maximizes the neutron detection efficiency. ... 70
Figure 4.17: Natural B foil on a stainless steel circular support structure. The diameter of the B foil is approximately 1.0 cm. (One square = 0.25" x 0.25") 70
Figure 4.18: The three 1.0 µm thick B foils positioned in a MWPC containing a single anode wire on each side of the 4.5 cm spaced B foils. 71
Figure 4.19: The thermal neutron response pulse-height spectra obtained from a three layer natural B foil detector. Two main features in the spectra are located at channel numbers 220 & 275, a result of the 94% and 6% branches of the neutron reaction. 71

Figure 5.1: Box A, a 17 cm x 17 cm x 17 cm Al chamber designed to test single sheets of neutron absorber materials. The test chamber included two anode wires, one on each side of the absorber sheet. 74
Figure 5.2: Box B was fabricated from Al and is 17 cm x 17 cm x 50 cm, and designed to hold 10 layers of neutron absorber sheets positioned 4.5 cm apart. 75
Figure 5.3: Foam (left) and Li/Mg Alloy (right) in frames used in Box A & B. The foam was clamped in place by bolting two frames together, and the foil was connected to the frame using Cu tape. 76
Figure 5.4: Aerogel samples containing B and Li. The aerogel material becomes more stable with increasing Li content. The Li content increases in the three samples from left to right. 77
Figure 5.5: Fractional thermal neutron absorption of lithium borosilicate aerogel samples provided by Aerogel Technologies. The minimum and maximum macroscopic thermal neutron absorption cross-sections were used to generate the plot and show the range of theoretical neutron absorption as a function of material thickness...... 78
Figure 5.6: A SEM image of open-celled polyurethane foam impregnated with 10% natural LiF. Cell sizes range from 1.0–5.0 mm, and struts have an average thickness of 50 µm. 79
Figure 5.7: A SEM image of open-celled polyurethane foam impregnated with 27.5% natural LiF. The LiF began to cluster at these impregnation levels creating regions of 1.0 diameter LiF volumes. This diameter is too thick for reaction products born in the center to escape the cluster or foam. 80
Figure 5.8: SEM images of LiF after titration (left) and post evaporation of the powder (right). 81
Figure 5.9: The aerogel test chamber with the sample holder positioned in the middle of the box. Anode wires were positioned on each side of the sample in order to measure reaction products escaping both sides of the aerogel samples. 82
Figure 5.10: Box B with 10% LiF impregnated foam inserts placed in the detector. The lid is removed to show the inside of the chamber, and the anode wires are connected in a serpentine manner on the outside of the device. 83
Figure 5.11: Cross-sectional schematic of the cylindrical foam insert in the coaxial detector with the collimated alpha particle source. Two pulse-height spectra were collected, one with and

one without saran wrap, to determine whether electrons are able to penetrate the foam pores and reach the anode wire. 84
Figure 5.12: The pulse-height spectra obtained for the coaxial cylindrical foam insert detector with a collimated alpha particle source positioned parallel to the anode wire and foam. The plastic wrap positioned around the foam blocked penetrating electrons, demonstrating that electrons generated between the cathode and foam insert do pass through the foam to reach the anode wire. 85
Figure 5.13: Pictures of the anode wire construction in the anode wire optimization detector. . 87
Figure 5.14: A schematic illustration of the anode wire optimization chamber with the collimated alpha particle source positioned above the anode wires. The neodymium magnet allowed the source to be moved over the anode wires and collect a profile of the count rates. 88
Figure 5.15: Pulse-height spectra collected from the anode wire optimization chamber using a multi-energetic ^{226}Ra alpha particle source. The anode wire spacing tested was 2.0 and 3.0 cm, and showed degradation in peak location, but not counting rates. 88
Figure 5.16: The neutron response pulse-height spectra obtained from the anode wire optimization chamber with anode wire spacing of 2.0 and 3.0 cm. The spectra are compared to the simulated pulse-height spectrum obtained from MCNP6. 89
Figure 5.17: The Li foil support frame of the anode wire optimization chamber. Frames were 1/8" thick and had 1/16" thick cross bars that were lined up when two frames were bolted together. 90
Figure 5.18: Pictures of several Li foil support frame concepts. Foil support frame permutations include: a) spring tension wire mesh, b) metal wire mesh stretched over support frame studs, c) metal wire mesh tied to the frame, d) metal strips running the length of the frame as one single sheet, e) metal wire mesh stretched over bolts around the frame, f)and wires soldered around the frame running the length of the frame. 92
Figure 5.19: The final design of Al Li foil support frames. Horizontal support bars are 0.5 cm thick and separated 4.5 cm apart, and vertical crossbars are 0.1 cm thick and positioned approximately 8.0 cm apart. The dot slightly above center is a pop rivet holding two frames together tightly in the center of the large-area foil support frames. 93
Figure 5.20: The smaller (550 cm^2) mid-sized Li foil support frame. 94
Figure 5.21: The large-area (1250 cm^2) Li foil support frame. 94

Figure 5.22: Anode wire bank for the mid-sized Li Foil MWPC. 95
Figure 5.23: A picture of the Li Foil MWPC in the first stages of assembly showing the Al sheet connected to the bosses in the lid. Also shown are two anode banks and two Li foil sheets indexed together using the four all-thread rods. 96
Figure 5.24: The large-area Li foil MWPC with Li foil frames and anode wire banks stacked together. The metal sheet with the handle shown in the picture covering approximately half of the foil length is a protection plate to prevent any dropped tools or materials from breaking anode wires or puncturing the Li foil. 97
Figure 5.25: The large-area Li foil MWPC with front, back, and side panels attached. 98
Figure 5.26: Four completed large-area Li foil MWPC's. The six SHV feedthroughs and gas-fill lines are visible on top of the detectors. The carpenter square is included as a metric for detector size. 98
Figure 5.27: A picture, mid-construction, of the corrugated Li foil MWPC. 100
Figure 5.28: Six form-fit designs in the top view perspective. The red represents the neutron absorber material and the black dots and grey circles are the anode and cathode, respectively. 102
Figure 5.29: Lithium Borosilicate aerogel attached to a strip of Cu tape. The sample is held with a pair of tweezers to show the Cu tape was stuck to the aerogel. 103
Figure 5.30: The aerogel cruciform design completed and positioned next to the test chamber. The aerogel insert was 5 cm in diameter and 13 cm long. 103
Figure 5.31: The 'Dual' configuration, shown in the top of the picture, is loaded with Li foil and wrapped with a perimeter coating of ^{6}Li foil. In the lower portion of the picture are ^{6}Li loaded frames for the 'Quad' design. 105
Figure 5.32: The Dual design connected to SHV feedthrough and positioned next to the test chamber. The test chamber was backfilled with P-10 gas and the detector was tested in the vertical position. 105
Figure 5.33: The 5-layer mini stack bolted together with the loaded ^{6}Li foil frames. The black plastic insert at the bottom is used as a spacer to prevent the dead end of the anodes from touching the metal casing, thereby, electrically shorting or breaking the anodes. 107

Figure 5.34: The 5-layer mini top spacer (left) has one side angled to push the stack against the side of the square device to ensure that the stack was properly grounded. The stack and spacers are inserted into the square Al housing (right). 107
Figure 5.35: The perimeter coating of the Li foil position inside the tube with the thin plastic perforated sheet to prevent the foil insert from becoming grounded...... 109
Figure 5.36: The Wagon Wheel design using eight longitudinal fins pointing inward towards the anode wire...... 109
Figure 6.1: A schematic top-view illustration of the detector setup and diffracted neutron beam. Only thermal neutrons are diffracted at the diffraction crystal and higher energy neutrons and gamma-rays transmit through the crystal. The diffracted beam contains a Cd shutter and the detector positions are shown when performing intrinsic thermal neutron detection efficiency measurements. 114
Figure 6.2: The Watt distribution (blue) of ^{235}U is the fission neutron energy distribution, but when the neutrons emerge from the beam port they are thermalized about a Maxwell-Boltzmann distribution (red). The inset shows a comparison of the two Maxwell-Boltzmann distributions discussed. 115
Figure 6.3: Depiction of Bragg diffraction off of crystal planes with spacing d and particle angle θ_B. 115
Figure 6.4: An illustration of the two ^{3}He tube RPM test setup. 120
Figure 6.5: The neutron response pulse-height spectra of single layers of 30, 50, 75, and 120 µm thick Li foils obtained using Box A. 124
Figure 6.6: Neutron response pulse-height spectra obtained using 10 layers of 30, 50, and 75 µm thick natural Li foil in Box B...... 125
Figure 6.7: A plot of the intrinsic thermal neutron detection efficiency of the natural Li foil MWPC as a function of the foil thickness for various numbers of natural Li foil layers. The three red dots represent the experimentally calculated neutron detection efficiencies of the 30, 50, and 75 µm thick 10 layer devices...... 126
Figure 6.8: The neutron response pulse-height spectrum of a single layer of open-celled polyurethane foam impregnated with 10% natural LiF. An additional measurement was made with a Cd shutter to block all incident neutrons, thus, proving the pulse-height spectrum is truly a neutron response. 128

Figure 6.9: The neutron response pulse-height spectrum of a single layer of open-celled polyurethane foam impregnated with 10% natural B_2O_3. An additional measurement was made with a Cd shutter to block all incident neutrons, thus, proving the pulse-height spectrum is truly a neutron response. 128
Figure 6.10: The neutron response pulse-height spectra of 5 & 10 layers of 4.5% ^{6}LiF impregnated open-celled polyurethane foam. 129
Figure 6.11: The thermal neutron response pulse-height spectra obtained from borosilicate and silica aerogel. This is the first known record of aerogel used as a neutron detector. 131
Figure 6.12: The thermal neutron response pulse-height spectrum obtained from a 6.0 mm thick borosilicate aerogel sample. 131
Figure 6.13: The pulse height curve (left) and counting curve (right) of the Li foil MWPC neutron detectors when positioned in front of the ^{252}Cf neutron source. 132
Figure 6.14: The thermal neutron response pulse-height spectra of the mid-sized Li foil MWPC obtained at P-10 gas pressures of 1.0, 1.5, 2.0, and 2.8 atm are shown in the lighter dashed lines. The simulated thermal neutron response pulse-height spectra obtained using MCNP6 are represented by solid lines. 134
Figure 6.15: The thermal neutron response pulse-height spectra obtained with mid-sized Li foil MPWC at different P-10 gas pressures of 1.1, 1.5, 2.0, and 2.8 atm. The pulse-height spectra are not energy calibrated and larger pulses occur at lower gas pressures. 135
Figure 6.16: The neutron and gamma-ray response pulse-height spectra obtained with the mid-sized Li Foil MWPC from two different neutron and gamma ray sources. The detector was pressurized with P-10 gas to pressures of 1.1, 1.5, 2.0, and 2.8 atm. 136
Figure 6.17: The GRR and GARRn of Build 2 (mid-sized Li foil MWPC) as a function of LLD energy. These values are within compliance of the PNNL RPM standard. 138
Figure 6.18: The GRR of Build 2 (mid-sized Li foil MWPC) as a function of the LLD energy. The values become negative because more counts were present in the background measurement. 138
Figure 6.19: The absolute neutron detection efficiency and GARRn plotted as function of LLD energy for the large-area Li foil MWPC. 139
Figure 6.20: The GRR plotted as a function of LLD energy for the large-area Li foil MWPC. The values become negative after 500 keV. 139

Figure 6.21: The neutron response pulse-height spectra collected from the corrugated pattern Li foil MWPC at P-10 gas pressures of 1.0 and 1.5 atm. 142
Figure 6.22: The pulse-height spectra obtained from the planar pattern backpack neutron detector. The detector gamma-ray sensitivity was tested at exposure rates of 10, 100, and 400 mR hr^{-1} using a ^{137}Cs source. 142
Figure 6.23: The absolute neutron detection efficiency of the small planar Li foil MWPC and the corrugated design as a function of the incident neutron angle. The phantom was positioned between the detector and the source at 0° (i.e. User facing away from the source). 143
Figure 6.24: The LPC detector delivered to ORNL for neutron and gamma-ray sensitivity testing. 144
Figure 6.25: The HDPE moderator optimization was completed using MCNP6 by varying the ratio of the front (t_f) and back (t_b) moderator for different constant middle (t_{middle}) moderator thicknesses. 145
Figure 6.26: Stationary test results from ORNL. A ^{252}Cf neutron source was positioned at various distances from the front face of the detector and absolute neutron detection efficiency is plotted as function of source distance. The plot on the right is the same data set multiplied by R^2, which in an idealized environment would shape the data into a horizontal line. 147
Figure 6.27: The stationary neutron response test setup at KSU. The ^{252}Cf is suspended in the center of the purple borated HDPE and centered in front of the LPC detector. 147
Figure 6.28: The ORNL bare ^{252}Cf static results (red) compared to the same test completed at KSU (blue). KSU results are less accurate due to neutrons scattering off of the cinderblock walls of the Ward basement hallway. The plot on the right is the same data set multiplied by R^2, which in an idealized environment would shape the data into a horizontal line. 148
Figure 6.29: The transient response of the detector for four of the ten repeated measurements. The closest distance from the source to the detector face was 2.0 meters. 150
Figure 6.30: The transient response of the detector for four of the ten repeated measurements. The closest distance from the source to the detector face was 4.0 meters. 150
Figure 6.31: An illustration of the FOV experiment set up for the LPC tests. The ^{252}Cf neutron source (blue dot) was positioned at different lateral distances over a range of 10.0 meters. The closest distance at 0.0 m varied between 25.5, 125.5, and 225.5 cm. 151

Figure 6.32: The LPC detector response to the FOV experiments. The background was approximately 7.5 cps, thus, the count rate was approximately eight times greater than the background count rate with the source 5.0 meters away. 152
Figure 6.33: A polar plot of the LPC detector angular response. The source was positioned 2.0 meters from the center of the detector and rotated around the detector in 30° increments. 154
Figure 6.34: A Cartesian plot of the LPC detector angular response. The source was positioned 2.0 meters from the center of the detector and rotated around the detector in 30° increments. There was a 15% variance between minimum and maximum count rates. 154
Figure 6.35: The LPC neutron response (purple) compared to exposure rates from a ^{137}Cs gamma ray source of 10, 50, 100, and 1000 mR hr^{-1} 156
Figure 6.36: The two investigated form-fit configurations shown with and without the HDPE moderator. The cylindrical design (left two) was used for the aerogel cruciform, Dual, and Quad designs, while the square design (right two) was used for the 5-layer mini. 158
Figure 6.37: The HDPE used in ^{3}He neutron detector comparison tests was 6.0" in diameter and 9.0" in height. Top-view schematics of the HDPE with cutouts shaded in grey are shown. 158
Figure 6.38: The neutron and gamma-ray response pulse-height spectra of the aerogel cruciform form-fit detector. The gamma-ray exposure rates investigated were 10 and 50 mR hr^{-1} using a ^{137}Cs source. 160
Figure 6.39: The neutron and gamma-ray response pulse-height spectra of the Dual form-fit detector. The gamma-ray exposure rates investigated were 10 and 50 mR hr^{-1} using a ^{137}Cs source. 160
Figure 6.40: The neutron and gamma-ray response pulse-height spectra of the Quad form-fit detector. The gamma-ray exposure rates investigated were 10 and 50 mR hr^{-1} using a ^{137}Cs source. 161
Figure 6.41: The neutron and gamma-ray response pulse-height spectra of the 5-layer mini form-fit detector. The gamma-ray exposure rates investigated were 10 and 50 mR hr^{-1} using a ^{137}Cs source. 161

Figure 6.42: The neutron and gamma-ray response pulse-height spectra of the 3He neutron detector. The gamma-ray exposure rates investigated were 10 and 50 mR hr^{-1} using a ^{137}Cs source. 163
Figure 6.43: The neutron response pulse-height spectrum of the longitudinal finned detector with floating Li foil fins and grounded perimeter Li foil coating, referred to as Wagon Wheel – A. 164
Figure 6.44: The neutron response pulse-height spectrum of the longitudinal finned detector with the Li foil fins and perimeter Li foil coating grounded, referred to as Wagon Wheel – B. 165
Figure 7.1: A picture of the large-area, mid-sized, and form-fit detectors side-by-side. HDPE moderators for form-fit devices are also included and open to expose the detector inside. This picture shows a relative scale in various sizes of detectors. 168
Figure B.1: The pulse-height spectrum contribution from the three cases where reaction product energy is deposited in the gas volume. The total of the three cases is summed into one pulse-height spectrum in the lower right. The plots are from 55 µm thick ^{6}Li foil. 10
Figure B.2: The pulse-height spectrum contribution from the three cases where reaction products deposited energy in the gas volume. The total of the three cases is summed into one pulse-height spectrum in the lower right. The plots are for 35 µm thick ^{6}Li foil. 11
Figure C.1: The HDPE moderator optimization for a single detector was completed using MCNP6 by varying the ratio of front t_f to total t_{tot} moderator for 5, 7, 15, and 20 cm of total moderator. 7
Figure C.2: The HDPE moderator optimization for three detectors all back-to-back was completed using MCNP6 by varying the ratio of the front (t_f) to back (t_b) moderators while the two middle layer thicknesses (t_{middle}) of HPDE remained constant for various middle thicknesses. 8
Figure C.3: A top cross-sectional schematic of the large area device used in the LPC for the MTR at ORNL. The device contains 5 parallel layers of 75 µm thick ^{6}Li foil spaced 1.6 cm apart. The schematic is proportional to scale except for the Li foil thickness. 12
Figure C.4: A side cross-sectional schematic of the large area detector used in the LPC for the MTR at ORNL. 13
Figure C.5: A top view schematic of the LPC detector containing the two large area detectors. 14

Figure D.1: The three fractional solid angle formulas plotted together as a function of the source to detector distance. (Gossman and DNDO overlap.) 3
Figure D.2: The percent difference between the fractional solid angle presented by Gossman et alli and the circular equivalent for a rectangular aperture. 3

LIST OF TABLES

Table 1: Reaction product ranges from ^{10}B and ^{6}Li neutron reactions in foam and aerogel. Porosity and non-uniform density cause inaccurate predictions [65]. 43

Table 2: Various lithium borosilicate aerogel samples estimated elemental composition, density, and macroscopic thermal neutron absorption cross-section. 78

Table 3: The reported measurements of RPM ^{3}He alternative neutron detector systems completed by PNNL. 122

Table 4: The exposure rate, source distance, and count rates from the front, back, and total of the LPC detector collected using the EDL custom electronics and the KSU ^{137}Cs gamma ray source. 156

Table 5: The total count rates of the six detectors tested against the ^{3}He neutron detector. Count rates were normalized to total absorption length, 13 cm, and total counting length, 6.5 cm, of the ^{3}He counter. 163

ACKNOWLEDGEMENTS

The research described herein was performed at the Kansas State University (KSU) Semiconductor Materials and Radiological Technologies (S.M.A.R.T.) Laboratory in Manhattan, KS. The execution of the research would not have been possible without the assistance of the KSU TRIGA Mark II nuclear reactor, along with the Electronics Design Laboratory (EDL). This research was supported in part by the Defense Threat Reduction Agency (DTRA), under contract HDTRA1-12-c-0002.

The development of the detectors would not have been possible without the help of Saint-Gobain Crystals and their extensive knowledge of anode wire assemblies and insight into the overall design process and feasability. Thus, a special thanks is in order to Dr. Michael R. Mayhugh, Michael R. Kusner, John M. Frank, and Charles Cooper for their efforts.

The author would like to show the utmost gratitude to Prof. Douglas S. McGregor, you took in a last second student and gave me valuable knowledge that will guide me for the rest of my life. The author would also like to thank the S.M.A.R.T. Laboratory Research Assistant Professor, Dr. Philip B. Ugorowski , and the current and former graduate students, in no particular order, for their support both in and out of the laboratory: Dr. Walter J. McNeil, Dr. Steven L. Bellinger, Dr. Alireza Kargar, Dr. Elsa Ariesanti, Troy Unruh, Adam Brooks, Benjamin W. Montag, Brian Cooper, Nate Edwards, Ryan Fronk, Simon Bolding, and Michael Reichenberger. The author would also like to thank the undergraduates who contributed to the research: Todd A. Riedel, Jim Neihart, Aaron J. Schmidt, Dominic Francia, Clayton Wayant, and Niklas J. Hinson. Additionally, much appreciation is given to Dr. Jeffrey Geuther the TRIGA Mark II reactor manager and Russell Taylor a member of the EDL group. Further, this work would not have been completed without the hard work and talents of Eric Wagner and the KSU machineshop team.

Lastly, the author would like to extend his gratitude to his loving family and friends who have shown support through thick and thin of this endeavor. Without them, this would have never been possible.

DEDICATION

I dedicate this work to my wonderful family

and to those who overcame that which they were once told was unachievable.

LIST OF ACRONYMS

MWPC	Multi-Wire Proportional Counter
PMT	Photomultiplier Tube
PSD	Pulse Shape Discrimination
BCS	Boron Coated Straw
SMART	Semiconductor Materials And Radiological Technologies
LLD	Lower Level Discriminator
MCA	Multi-Channel Analyzer
CLYC	Cs_2LiYCl_6:Ce
RPM	Radiation Portal Monitor
MSND	Microstructured Neutron Detectors
RDT	Radiation Detection Technologies, Inc
TEM	Transmission Electron Microscopy
Bo-PET	Biaxially oriented polyethylene terephthalate
KSU	Kansas State University
TRIGA	Training, Research, Isotopes, General Atomics
SHV	Super High Voltage
SEM	Scanning Electron Microscopy
MCNP6	Monte Carlo N-Particle Transport Code – Version 6
HDPE	High-Density Polyethylene
PNNL	Pacific Northwest National Laboratory
SGC	Saint Gobain Crystals
GRR	Gamma-ray Rejection Ratio
GARRn	Gamma Absolute Rejection Ratio in the presents of neutrons
eV	electron Volt
NEMA	National Electrical Manufacturers Association
LPC	Lithium Proportional Counter
ORNL	Oak Ridge National Laboratory
MCS	Multi-Channel Scaler
FOV	Field of View

EDL	Electronics Design Laboratory
TTL	Transistor-Transistor Logic
NORM	Naturally Occurring Radioactive Materials
DNDO	Domestic Nuclear Detection Office
NNSS	National Nuclear Security Site
DTRA	Defense Threat Reduction Agency

CHAPTER 1

INTRODUCTION

"Do not go where the path may lead, go instead where there is no path and leave a trail."

-Ralph Waldo Emerson

Discussed in this chapter is the motivation for neutron sensitive aerogel, impregnated foam, and ^{6}Li foil multi-wire proportional counter (MWPC) neutron detector development. First, a small introduction about the history and discovery of the neutron is included followed by a brief overview of neutron detector history and current commercially available neutron detectors. Their advantages and disadvantages are presented along with how the aerogel, foam, and foil MWPC's resolve those issues. Lastly, three main materials were investigated and many 'proof-of-principle' experiments were conducted in this research project, thus the last section of this chapter discusses the organization of the dissertation.

1.1 Motivation for Research

First proposed by Ernest Rutherford in 1920 and experimentally proven in 1932 by James Chadwick, the neutron was the last of the subatomic radii to be discovered [1, 2]. The X-ray, alpha particle, beta particle, and gamma-ray were discovered and characterized around the turn of the 20th century between 1895 and 1914 [3-5]. During the 1940's and 1950's, the neutron was heavily studied and materials with specific absorption, scattering, and fission properties were discovered, ushering in the development of atomic weapons and nuclear power. With the wide interest in neutrons, neutron monitoring systems were developed in parallel with other neutron

oriented technologies. The first electronic radiation detectors were simple gas-filled devices developed by Rutherford and Geiger, which were later redesigned by Müller as the Geiger-Müller counters in common use today [6]. Chadwick used a gas-filled ionization chamber to measure protons generated by the neutron bombardment of paraffin to prove the existence of the neutron. Thus, the neutron recoil effect was the first method used to detect neutrons and determine neutron energies. The neutrons in Chadwick's experiment were detected in a gas filled chamber by measuring the recoil kinetic energy of protons created from caused by incident neutron scatter reactions [7]. Developed in the 1940's, the first neutron detectors based on a 'converter' material were $^{10}BF_3$ gas-filled proportional counters (1939), 'boron foil' sensors (*e.g. B coated devices*), and fission chambers [7-11]. Shortly after, ^{3}He gas-filled devices were in production by the early 1950's [12-15]. Solid-state neutron detectors using a coating of ^{10}B were developed in the late 1950's, a less understood technology at the time [16].

Today, there are many real-time neutron detector monitoring systems, including gas-filled detectors (*e.g.* ^{3}He *and* $^{10}BF_3$), neutron sensitive scintillator materials (typically coupled to a photomultiplier tube (PMT)), and coated semiconductor detectors [17, 18]. There are also many other types of neutron detectors available today, but the prior list represents the most commonly used devices. The common commercial neutron detectors all have neutron sensitive materials which allow for neutron reactions such as transmutation, fission, or recoil to produce ionizing radiation that is measured in a sensor volume. Examples of the most frequently used neutron sensitive isotopes that undergo transmutation include ^{3}He, ^{6}Li, ^{10}B, and ^{157}Gd [17, 18]. Fission materials in detectors typically include ^{233}U, ^{235}U, and ^{239}Pu. The neutron absorption probability of the aforementioned isotopes, or neutron absorption cross-section, is strongly dependent upon the incident neutron energy. Neutrons are typically born at higher energies, > 1.0 MeV, referred to as fast neutrons. In order for these isotopes to be effective neutron absorbers, the incident neutron energy must be reduced to lower energies, optimally thermal energy, 0.0253 eV. The absorption cross-sections of some isotopes can increase more than three orders of magnitude when the incident neutron energy decreases from 1.0 MeV to 0.0253 eV. Both fission isotopes and transmutation isotopes have reaction products that are emitted at relatively high energies (> 500 keV). These reaction products have relatively short ranges in most detection mediums (< 5.0 cm). Recoil neutron detectors are typically less efficient due to the smaller electronic signals created in the detectors. Signals generated with energies less than 10 keV are typically difficult

to measure due to interference with background radiation and electronic noise in the measurement systems. Consequently, using a recoil mechanism to measure thermal neutrons is impractical. The recoil detectors often rely on a transfer of kinetic energy to nuclei through scattering in gases such as H_2 or He [17, 19]. In an ideal recoil detector, assuming no upscattering, a complete transfer of energy from a thermal neutron would only result in a 0.025 eV hydrogen nucleus, which is not enough energy to cause sufficient ionization to create a measurable signal. Thus, neutron measurement systems using recoil mechanisms are typically limited to fast neutron detection and have relatively low overall detection efficiency.

Most neutron monitoring stations are stationary, and thus do not have ruggedness requirements, but recently there has been increased interest in vehicle mounted, backpack, and handheld neutron detectors. For the stationary monitoring systems, ^{3}He gas-filled proportional counters have been the most common devices used and are considered the standard by which all other neutron detectors are compared. However, there is presently a shortage of ^{3}He gas, a rare isotope with an extremely low natural abundance, approximately 0.000137% (1.37 ppm) [20]. The ^{3}He gas used for detectors was extracted as a byproduct of the nuclear weapons program, specifically, from tritium decaying into ^{3}He [21]. However, since the time when the United States ceased the fabrication of nuclear weapons, the supply of ^{3}He has dwindled to such small amounts that government agencies are now regulating its distribution. As of 2010, the demand for ^{3}He gas was ~65K liters/year, while the decay of the tritium supply produces ~8 kiloliters/year [22]. The price for a single liter of ^{3}He in 2010 was $2,100, but recent projections are contradictory with some reports predicting prices decreasing and others reporting increasing costs [23]. As a result, there has been an aggressive investigation for an alternative to the ^{3}He neutron sensors. The standard created by ^{3}He neutron detectors for replacement technologies includes detectors with high intrinsic thermal neutron detection efficiency (> 80%), high gamma-ray discrimination (GRR $\leq 10^{-6}$), and economical in price. Additionally, for the non-static neutron monitoring systems, a minimal ruggedness is required that matches or exceeds the durability of ^{3}He proportional counters. Specifications for ^{3}He alternative detectors are discussed in greater detail in the following Chapters.

Commercially available neutron detectors mentioned previously have various advantages and disadvantages. A number of candidate ^{3}He replacement detectors can be eliminated immediately because of low detection efficiency, including $^{10}BF_3$ counters, ^{10}B-lined proportional counters,

coated planar semiconductors, and recoil detectors. Further, the $^{10}BF_3$ gas is toxic and thus creates safety concerns [18]. Other detectors can be eliminated because of their inability to sufficiently discriminate gamma-rays, an important feature that removes false-positive neutron events. These materials are typically scintillators. Scintillators are most commonly composed of high Z-number elements and have a higher density than gas-filled detectors, making them more likely to absorb gamma-rays readily. However, pulse-shape discrimination (PSD) may allow these detectors have acceptable gamma-ray discrimination properties while still maintaining high neutron detection efficiency. For a better description of PSD, the reader is directed to the literature [17, 18]. The price of these scintillator devices is also expensive, mostly because of the associated PMT and PSD software. Additionally, PMT's are easily broken and are sensitive to magnetic fields. Further, many neutron sensitive scintillators are limited in size to 1–2 cm thick and 2–5 cm in diameter [17, 18]. In order to cover sufficient area for portal or handheld monitors, several scintillators must be arrayed together, causing the cost to rise dramatically.

There are presently three commercially available neutron detector systems for ^{3}He neutron detector replacement. The first uses ^{6}LiF and ZnS(Ag) powders mixed together and formed into thin sheets, which are placed between scintillating fibers [24]. Another permutation is constructed by coating optical fibers with the ^{6}LiFZnS(Ag) blend, or reversely, surrounding ^{6}LiFZnS(Ag) with optical fibers [25]. The fibers lead to a PMT, which again has the disadvantages of using PMT's in monitoring systems. However, a large sensitive area, comparable to ^{3}He tubes, can be covered by the scintillating fibers and coupled to a single PMT. Further, these devices suffer from acceptable, but still poor gamma-ray discrimination [26]. The second alternative is provided by Proportional Technologies and uses bundles of ^{10}B lined tubes to create high efficiency detectors, referred to as Boron Coated Straws (BCS) [27]. The BCS's are 4.0 mm in diameter in the largest configuration, but currently other forms of cathode materials are being investigated that are beveled, referred to as Star BCS's. Some simulations reported in literature use up to 800 BCS's in a single detector in order to maximize neutron detection efficiency [28]. These devices meet both of the neutron detection efficiency and gamma-ray discrimination requirements, but the feasibility or widespread use of these devices is still unknown, and prices are not easily available. Ruggedness of these devices is also currently under investigation, and post processing electronics are presently used to remove noise generated from vibrations and shock. A third alternative was also recently developed by the Semiconductor

Materials And Radiological Technologies (SMART) laboratory using perforated surfaces of Si diodes to create high-efficiency neutron detectors. A conformal diffusion of dopants in the trenched Si devices creates a diode and the trenches are backfilled with ^{6}LiF. This creates a high-efficiency neutron detector with acceptable gamma-ray discrimination. Recently, perforated neutron detectors have been developed and reached an efficiency of 38%, with theoretical simulations showing efficiencies as high as 70%, making them a viable replacement of ^{3}He based technology [29-32]. However, these detectors lack the easy ability to cover large areas and creating neutron monitoring systems covering greater than 1000 cm^2 would be costly and difficult. Yet, the MSND technology creates an advantage for small volume applications because gas-filled devices cannot be constructed as compact as the MSND diodes and still maintain relatively high neutron detection efficiency. Further, the compactness of solid-state measurement systems allows for these detectors to be packed in such a way that their ruggedness is much better than any other currently available neutron monitoring system. Additionally, the form factor of the diodes allows them to be applied to new types of neutron monitoring systems never created before and applied systems where ^{3}He tubes would be inappropriate.

The first use of a gas-filled detector was invented and characterized by Hans Geiger in 1909 followed by Walther Müller continuing the work with Geiger in 1928, resulting in the well-known Geiger-Müller counter [7, 17, 18]. Over 100 years later, gas-filled detectors are still being developed and optimized for a variety of applications. MWPC's were first developed in 1968 and have had large impacts on the radiation detection and physics community since then [33-35]. The first MWPC's were used for imaging radiation paths and trajectories, but at the Kansas State University (KSU) Semiconductor Materials And Radiological Technologies Laboratory (SMART Lab) a MWPC neutron detector has been developed by suspending neutron sensitive materials between planes of anode wires. These materials are typically thin sheets that allow reaction products to escape both sides per neutron absorption. This property greatly increases the neutron detection efficiency and gamma-ray rejection capabilities compared to devices that only measure one reaction product per neutron absorption. The consequences of suspending the material are discussed in greater detail in the following chapters. These suspended sheets have the general characteristic that they are either high-porosity and low-density or ultra-thin materials. The most promising neutron absorbers include Li and/or B doped aerogels, impregnated foams (high-porosity low-density materials), and pure Li foils (ultra-thin materials).

The Li foil MWPC is a detector that meets all of the requirements for ^{3}He replacement neutron detectors. The price of the detectors is not discussed here, but should be lower in cost than ^{3}He detectors and other alternatives of the same scale. The ruggedness of the detectors has not been investigated to date, but is expected to be equivalent to that of current ^{3}He neutron detectors. The aerogel and impregnated foam detectors still have a significant amount of research to be completed in order to be considered a ^{3}He alternative, but early experiments and theory show promise that these materials can reach those goals.

1.2 Novel Contributions to Gas-filled Neutron Detectors

A summary of the novel contributions to the gas-filled neutron detector science and technology is listed below.

- Assembled and tested LiF coated longitudinal fins in a coaxial detector.
- Constructed and collected pulse-height spectra with LiF coated cheesecloth neutron absorber sheets.
- Developed and tested a BN coated plastic honeycomb neutron detector that created a plethora of BN coated plastic tubes pointing at a central anode wire.
- Coated carbon foam with BN and collected neutron sensitivity data.
- Assembled, tested, and simulated LiF coated Mylar sheets that were suspended in a MWPC that allowed more than one reaction product to escape per neutron absorption.
- Calculated the intrinsic thermal neutron detection efficiency of ^{6}LiF foils as a function of foil thickness for multi-layered devices.
- Tested the neutron sensitivity of 1.0 μm thick B foils, simulated the pulse-height spectra, and calculated the theoretical efficiency of multi-layered ^{10}B foil devices.
- Assembled and tested open-celled polyurethane foam impregnated with two separate materials, LiF and B, configured into coaxial and planar detector geometries.
- Predicted the theoretical intrinsic thermal neutron detection efficiency of 20% LiF impregnated open-celled polyurethane foam.

- Showed that porous materials like aerogel and foam allow reaction products to have streaming paths, which causes the reaction product path lengths to cover a range of distances over several orders of magnitude.
- Collected neutron response pulse-height spectra and performed neutron attenuation calculations using borosilicate and lithium borosilicate aerogel materials.
- Suspended ^{6}Li foil in a MWPC that was thinner than the summed ranges of the triton and alpha particle reaction products, thus, allowing for more than one reaction product to be measured per neutron absorption.
- Simulated neutron response pulse-height spectra of various ^{6}Li foil detector configurations.
- Generated intrinsic thermal neutron detection efficiency plots of Li and ^{6}Li foil.
- Built a backpack neutron detector that had better neutron sensitivity than two currently available ^{3}He backpack neutron detectors.
- Built form-fit cylindrical and parallelepiped detectors in six different configurations.
- Simulated a RPM using 5-layerd Li foil MWPC neutron detectors that achieved 4.0 cps ng^{-1}, which was better than the 2.5 cps ng^{-1} requirement.
- Developed a new approach to designing MWPC neutron detectors by suspending thin neutron absorber materials between anode wires that allowed for the possibility of measuring more than one reaction product per neutron absorption, which typically increased the neutron detection efficiency and generated larger pulses than signals observed with typical coated devices.

1.3 Organization of Thesis

The aerogel, foam, and foil gas-filled neutron detectors are each the first of its kind and two U.S. patents have been filed, one already allowed and one pending, on the technology [36, 37]. As in any research endeavor, when starting from scratch there were many preliminary experiments that often lead to improved models. In the immediate following chapter, the properties and characteristics of the neutron are discussed to give insight to basic neutron detector operation and theory. Thus, commercially available neutron detectors are discussed in

detail thereafter. Chapter 3 includes a description of the theoretical operation and properties of the aerogel, foam, and foil MWPC. However, before delving into the assembly, experimentation, and results of the MWPC neutron detectors, Chapter 4 includes a discussion about the preliminary experiments completed that led to the aerogel, foam, and foil MWPC design. Following Chapter 4, the experimental arrangement of each aerogel, foam, and foil detector is contained in a single chapter, also in the same order as described. Chapter 5 briefly discusses the construction details of the various detectors assembled for the aerogel, foam, and foil neutron detectors. The results and discussion follow in Chapter 6 with the sections in the same order as presented in Chapter 5 with the aerogel. Lastly, in Chapter 7 some conclusions are made about the detectors and how they fit the ^{3}He replacement neutron detector requirements. Additionally, future work and direction of the project is discussed. Included at the end of this thesis is an appendix of the computer simulations used to develop and optimize portions of the MWPC neutron detectors.

CHAPTER 2

NEUTRON INTERACTIONS FOR DETECTORS

"Science is a way of thinking more than it is a body of knowledge."

-Carl Sagan

In the following chapter neutron properties, characteristics, and those interactions pertaining to neutron detection are presented. Subsequently, a brief review of common neutron detectors, including their advantages and disadvantages, are briefly discussed.

2.1 Neutron Properties

Neutrons are subatomic hadron particles composed of two down quarks with charge -1/3q and an up quark with charge +2/3q, thereby having a total charge of zero (neutral). Thus, the neutron is not a fundamental particle as originally thought and is classified as a baryon [38, 39]. The neutron has a mass slightly higher than that of a proton and will actually decay into a proton, electron, and antineutrino, as depicted Figure 2.1. The average mean lifetime of a free neutron is approximately 881.5 ± 1.5 sec (14 min, 42 sec) [40], thereby, having a half-life conducive to relatively straight-forward detection. Most neutrons are usually born with energies ranging from a few meV to tens of MeV. The neutron emission energy depends of the neutron source and is typically not monoenergetic. Instead, neutrons are commonly emitted over a range of energies, commonly referred to as a Watt distribution. Neutron sources generate the free neutrons through nuclear reactions through either: nuclear fusion, nuclear fission (*i.e.* nuclear reactor), photo-neutrons, (n, 2n) reaction, or high-energy interactions (*i.e.* accelerators and spallation sources).

An extensive neutron source list and associated properties and mechanisms can be found in [18, 41, 42].

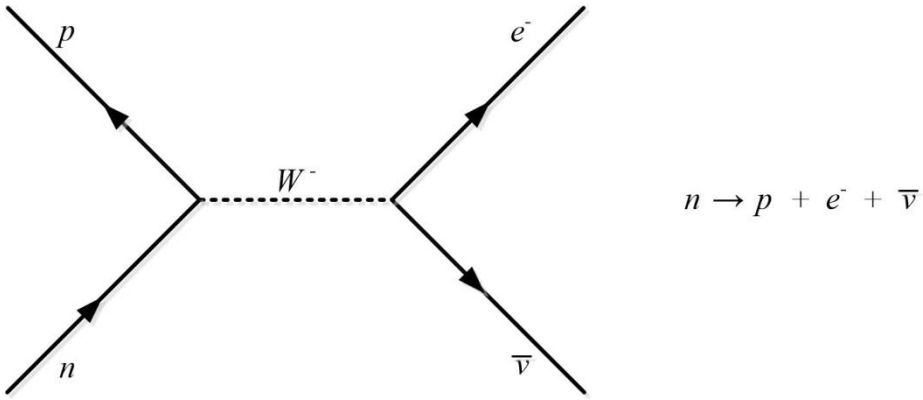

Figure 2.1: A diagram of the neutron decay scheme through an intermediate heavy boson into a proton, electron, and antineutrino.

2.2 Neutron Scattering and Absorption for Detection

The neutron charge neutrality makes direct detection difficult, hence, indirect ionizing methods are employed. Typically, neutrons are detected through capture and scatter reactions that result in the release of ionizing reaction products. The degree to which the neutron interacts with a material depends on the type of interaction of interest (scattering or absorbing), the target isotope, density of the interacting medium, and energy of the neutron. Although all materials interact with neutrons to some degree, either though scattering or absorption, some isotopes have interaction probabilities that are considered negligible (transparent) to neutrons. Hydrogen has the highest scattering cross section, σ_s, of the elements and is closest in size and mass of a neutron of all the elements. In general, the lower the atomic number, *Z*, of a material, the higher the scattering probability. Low energy neutrons, < 1 eV, typically undergo elastic scattering where their direction changes, but the energy may change only slightly. However, high energy neutrons, > 1 MeV, referred to as fast neutrons, undergo inelastic scattering where both the direction and neutron energy change. In inelastic scattering, a portion of the kinetic energy from

the neutron is transferred to the target nucleus, thus the scattered neutron loses energy and velocity.

Neutron absorption is isotope specific and heavily dependent on neutron energy. Common isotopes for neutron detection include ^{3}He, ^{6}Li, ^{10}B, ^{113}Cd, and ^{157}Gd, each having different neutron absorption cross sections, reaction products, and Q-values [17, 18]. In general, most isotopes have increasing absorption cross-sections with decreasing incident neutron energy. Typically the 'thermal' neutron absorption cross section σ_{th} is reported for isotopes because the neutrons are at thermal equilibrium with the ambient surroundings. 'Thermal' refers to the room temperature contribution to neutron energy, or Boltzmann's constant multiplied by the room temperature, resulting in 0.025 eV [42]. The microscopic absorption cross-sections of ^{3}He, ^{10}B, ^{6}Li, and ^{235}U are shown in Figure 2.2 in which the neutron absorption cross section increases with decreasing neutron energy. Microscopic neutron absorption cross sections (and scattering cross sections) are presented in units of barns (b) where 1 b = 10^{-24} cm^{2}. Absorption cross sections and probabilities of transmission and absorption are discussed in further detail in the following section.

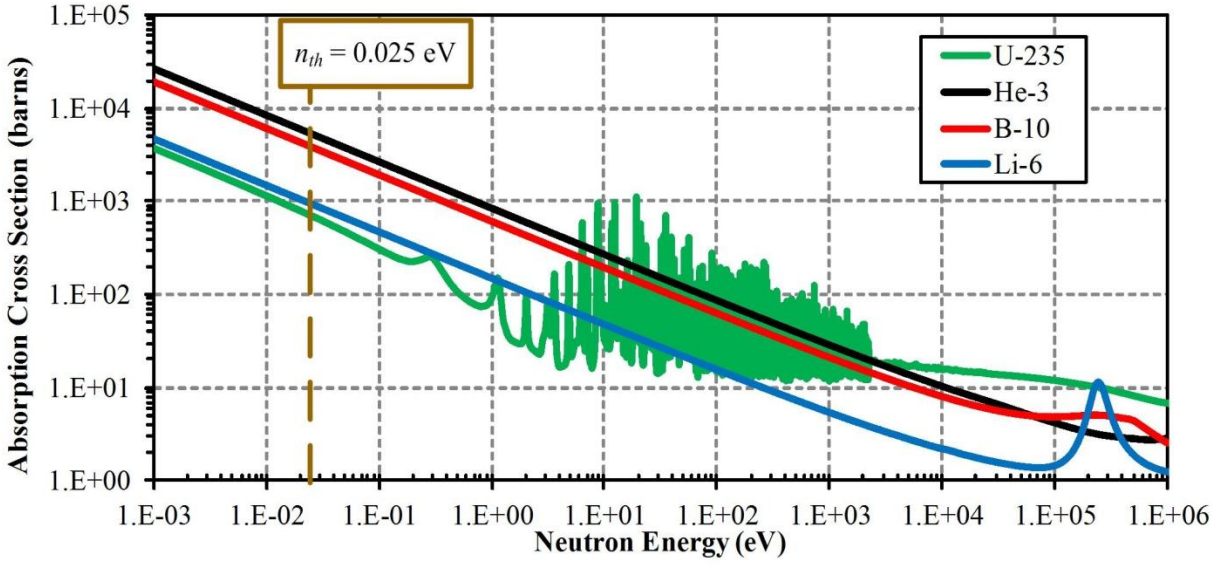

Figure 2.2: Microscopic absorption cross section of ^{3}He, ^{6}Li, ^{10}B, and ^{235}U as a function of neutron energy [43].

The microscopic neutron absorption cross-sections of ^{3}He, ^{6}Li, and ^{10}B are all proportional to the inverse of the neutron velocity. This region of inverse proportionality is considered the '1/*v*' neutron absorber region. ^{235}U is not considered a 1/*v* neutron absorber due to the resonances that are shown in Figure 2.2. The radiative neutron capture of isotopes can be accurately modeled by the Breit-Wigner formula originally developed for (n,γ) reactions [44]

$$\sigma_{\gamma}(E_c) = \pi\lambda_1^2 g\sqrt{\frac{E_1}{E_c}}\,\frac{\Gamma_n\Gamma_{\gamma}}{(E_c - E_1)^2 + \Gamma^2/4}, \tag{2.1}$$

where

E_1 = energy of lowest energy resonance

E_c = center-of-mass (COM) between neutron and target nuclei

λ_1 = reduced wavelength for a particle at energy E_1

Γ_n = neutron line width

Γ_{γ} = radiation line width

Γ = total decay width,

and,

$$g = \frac{(2J+1)}{(2s_1+1)(2s_2+1)} \tag{2.2}$$

where J is the spin resonance and s_1 and s_2 are the spins of the two particles forming the resonance [45]. In other words, g is a statistical factor of the spins of the target and resulting nuclei. Since $E_1, \lambda_1, \Gamma_n, \Gamma\gamma$, and Γ are all constants Eq. (2.1) can be rewritten as

$$\sigma_{\gamma}(E_c) = Cg\sqrt{\frac{E_1}{E_c}} \tag{2.3}$$

where,

$$C = \pi\lambda_1^2 \frac{\Gamma_n\Gamma_\gamma}{(E_c - E_1)^2 + \Gamma^2/4}, \text{ and } E_c \neq \text{constant.} \tag{2.4}$$

If $E_c << E_1$, then Eq. 2.5 becomes

$$C = \pi\lambda_1^2 \frac{\Gamma_n\Gamma_\gamma}{E_1^{\,2} + \Gamma^2/4} = K_1, \tag{2.5}$$

and applying $v = \sqrt{2E/m}$, Eq. 2.4 is now

$$\sigma_\gamma(E_c) \approx K_1\sqrt{\frac{E_1}{E_c}} = \frac{K_2}{v_c}, \tag{2.6}$$

where K_1 and K_2 are proportionality constants [44].

As mentioned, Eq. 2.2 was developed for (n,γ) reactions, but the following is more accurate for cross sections in which the neutron capture results in the release of a charged particle. For X(a,b)Y reactions, the cross section can be expressed as [44, 46]

$$\sigma_{(a,b)} = \sqrt{\frac{E_b}{E_a}}H(E_a) \approx \frac{K_3}{v_a}, \tag{2.7}$$

where the kinetic energies of the particles are E_a and E_b in the center-of-mass system, $H(E_a)$ is a correction factor for non-1/v absorbers for moderately large $E_a < E_b$, and K_3 is a proportionality constant. When low energy neutrons are absorbed they do not contribute significantly to the Q-value of the reaction. At times the Q-value of a reaction can be greater than 2.0 MeV, thus absorbing a 1 eV neutron would have minimal contribution to the total Q-value of the reaction. In these cases when low energy neutrons are absorbed $H(E_a) \approx 1$.

The 1/v absorbers have the advantage of having a constant reaction rate independent of neutron energy as long as the neutron energy is in the 1/v region. This trend of neutron count rate remaining constant is explained below, but developed by McGregor and Shultis [44]. In the

laboratory system neutrons approach target nuclei with velocity vector $\bar{v}$ while the target nuclei have velocity vector $\bar{V}$, which can be expressed as

$$\bar{v}_r = \bar{v} - \bar{V} . \tag{2.8}$$

Using the target nuclei as a reference point, incident neutrons have a differential beam intensity of

$$dI = n(\bar{v}) v_r d\bar{v} , \tag{2.9}$$

where $n(\bar{v})$ is the neutron density distribution and v_r is the magnitude of the relative velocity vector

$$v_r = |\bar{v}_r| . \tag{2.10}$$

The density rate of the neutrons interacting with the nuclei can be represented by

$$dF = n(\bar{v}) N(\bar{V}) \sigma(v_r) v_r d\bar{v} d\bar{V} \text{ (cm}^{-3} \text{ s}^{-1}) \tag{2.11}$$

where $N(\bar{V})$ is the target nuclei velocity density distribution and $\sigma(v_r)$ is the neutron interaction cross section at relative speed v_r. Solving for F,

$$F = \iint n(\bar{v}) N(\bar{V}) \sigma(v_r) v_r d\bar{v} d\bar{V} . \tag{2.12}$$

If the absorber material has a $1/v$ characteristic, then according to Eqs. 2.7 and 2.8, any arbitrary cross-section $\sigma(v_{ro})$ for relative speed v_{ro} is related to the cross section at v_r by

$$\sigma(v_r) = \frac{\sigma(v_{ro}) v_{ro}}{v_r} . \tag{2.13}$$

Substituting Eq. 2.14 into Eq. 2.13 and solving for *F*

$$F = \iint n(\bar{v}) N(\bar{V}) \frac{\sigma(v_{ro}) v_{ro}}{v_r} v_r d\bar{v} d\bar{V}$$

$$F = \sigma(v_{ro}) v_{ro} \iint n(\bar{v}) N(\bar{V}) d\bar{v} d\bar{V}$$

$$F = \sigma(v_{ro}) v_{ro} n \int N(\bar{V}) d\bar{V}$$

$$F = \sigma(v_{ro}) v_{ro} n N . \tag{2.14}$$

N is the density of the absorbing nuclei, which allows the macroscopic absorption cross-section Σ to be substituted into Eq. 2.15, thus, knowing that $\Sigma = N\sigma$, *F* now becomes

$$F = \Sigma_a(E_o) v_o n , \tag{2.15}$$

where $\Sigma_a(E_o)$ is the macroscopic neutron reaction cross section at corresponding speed v_o and n is the total neutron density. Eq. 2.16 can be interpreted to mean the reaction rate of neutrons absorptions with 1/*v* absorber materials is independent of the neutron or absorber nuclei velocity distribution. However, if the absorber material does not have the 1/*v* behavior, then a Westcott correction factor $g_a(t)$ can be applied that is thermally dependent. If the Westcott correction factor is applied, then Eq. 2.16 becomes

$$F = g_a(T) \Sigma_a(E_o) v_o n , \tag{2.16}$$

where T is the neutron temperature in the Maxwell-Boltzmann distribution. (The Westcott correction factor for ^{235}U is 0.9956 ± 0.0016 [47].)

^{3}He gas-filled neutron detectors have been a staple in the neutron detection industry for several decades, mainly because of the relatively high microscopic thermal neutron absorption cross section, 5330 b. The reaction Q-value is 0.763 MeV

$$^{3}He + n \rightarrow ^{3}H(0.191MeV) + p(0.573MeV). \quad (2.17)$$

For thermal neutron absorptions, the reaction products are emitted in opposite directions. Thus, common proportional counters filled with ^{3}He gas collect all ionization species resulting from the reaction product energy deposition. Unlike recoil gas-filled neutron detectors, the incident neutron energy is not critical to the overall detection. The Q-value (0.763 MeV) is usually high enough above electronic noise that the kinetic energy transfer from the incident neutron is relatively negligible.

$$n + ^{6}Li \rightarrow ^{3}H(2.73MeV) + \alpha(2.05MeV) \quad (2.18)$$

The Q-value of the ^{6}Li interaction is 4.78 MeV and has a microscopic thermal neutron absorption cross-section of 940 b and a natural abundance of 7.4% [17, 18, 48]. The neutron absorption cross-section decreases rapidly with increasing neutron energy and demonstrates an inversely proportional response to increasing neutron velocity ($1/v$) (Figure 2.2). The relatively high Q-value of the reaction produces large electronic signals above the electronic white noise for most neutron detectors. The capability to measure both reaction products allows for large pulses compared to other neutron absorbing isotopes, thereby allowing for straightforward noise discrimination. Pure ^{6}Li can be obtained from The Y-12 Corporation with 95% ^{6}Li enrichment. The Li material can be pressed into various thicknesses of foils by Rockwood Lithium. Pure Li metal will react with ambient atmosphere, or catch fire if submerged in water or placed in a flame. The reactivity of Li metal is similar to other alkali metals, but it is the least reactive of the alkali metals. Many detectors use a stable compound in neutron detectors, such as ^{6}LiF, in order to avoid decomposition of the Li. Additionally, the atomic density of ^{6}Li atoms in ^{6}LiF, 0.61 g cm^{-3} is higher than pure ^{6}Li, 0.463 g cm^{-3}.

The neutron absorption interaction of ^{10}B, approximately 20% natural abundance with a microscopic thermal neutron cross section of 3840 barns, is

$$n + {}^{10}B \rightarrow \alpha(1.47MeV) + {}^{7}Li(0.840MeV) + \gamma(0.480MeV) \qquad 94\%, \qquad (2.19)$$

$$n + {}^{10}B \rightarrow \alpha(1.78MeV) + {}^{7}Li(1.02MeV) \qquad 6\%. \qquad (2.20)$$

Each branch results in a reaction Q-value of 2.792 MeV [17, 18, 48]. Boron can be used in many different compound forms for a variety of neutron detectors.

The ^{113}Cd(n,γ)^{114}Cd reaction has a Q-value of 1.21 MeV generated by two prompt gamma-ray emissions. Although ^{113}Cd has a lower Q-value than the other isotopes discussed, ^{113}Cd has a higher microscopic thermal neutron cross section at approximately 20,000 b and a natural abundance of 12.26% [49, 50]. Thus, natural Cd has a microscopic thermal neutron cross section of 2,450 b. When a thermal neutron is absorbed by ^{113}Cd, several gamma-rays are emitted, but only two prompt gamma-rays are most commonly used in detector applications. The general reaction can be represented by [51]

$$n + {}^{113}Cd \rightarrow \gamma_1(558.6keV) + \gamma_2(651.3keV) + \gamma's. \qquad (2.21)$$

Cd foils can be used as neutron shutters to test detectors with and without neutrons. Consequently, Cd foils generate gamma rays that can be also used for investigating gamma ray sensitivity of neutron detectors. However, it is desirable to design neutron detectors that are "gamma-ray blind". Because neutron detectors based on the ^{113}Cd(n,γ)^{114}Cd reaction must measure and identify the characteristic prompt gamma rays, these detectors are also sensitive to background gamma-rays and other gamma-ray sources. Consequently, these neutron detectors have an added element of difficulty for realization.

The remaining common neutron absorbing material used in neutron detectors is ^{157}Gd (or natural Gd). This material has a thermal neutron absorption cross section of 259,000 b, the highest of any stable isotope. However, ^{155}Gd, another common isotope of Gd, has a lower thermal neutron absorption cross-section of 61,100 b. The natural abundances of ^{155}Gd and ^{157}Gd

are 15.7% and 14.8%, respectively. The reactions of both isotopes, $^{157}Gd(n,\gamma)^{158}Gd$ and $^{155}Gd(n,\gamma)^{156}Gd$, result in the emission of conversion electron reaction products. The conversion electrons range in energy from 29 keV to 1.78 MeV and are emitted in varying branching ratios. Approximately 60% of the thermal neutron absorptions result in a conversion electron emission. Of the 60% emitted, approximately 88.5% are less than 100 keV [52-57]. The low energies of the conversion electrons make them difficult to distinguish above electronic white noise of typical neutron detectors. A low-noise electronic system would be required, but the energy continuum from the reaction products would make determining energy threshold to eliminate electronic noise and background radiation interactions difficult. Furthermore, gamma-ray interaction in neutron detectors may deposit an equivalent amount of energy as some of the lower energy conversion electrons. Thus, when combining the branching ratios and necessary discrimination levels, neutron detectors constructed with Gd isotopes are limited in neutron detection efficiency.

2.3 Neutron Absorption & Reaction Product Measurement

Tables of microscopic thermal neutron absorption and scattering cross-sections (σ) are listed in units of barns and can be found readily throughout the literature [42, 58]. These values are converted to macroscopic cross-sections, which can be used to understand the probability or percentage a material may absorb or scatter certain neutron energies. The macroscopic cross-section, Σ (cm^{-1}), is calculated from the microscopic cross-section,

$$\Sigma = \frac{\rho N_o}{A}\sigma \quad , \tag{2.2}$$

where ρ is the density (g cm^{-3}), N_o is Avogadro's number, 6.02 x 10^{23}, and A is the molecular weight [59]. The macroscopic thermal neutron absorption cross section for ^{6}LiF and ^{6}Li are 57.51 cm^{-1} and 43.56 cm^{-1}, respectively, resulting from differences in density as described in the previous chapter. The densities of ^{6}LiF and ^{6}Li are 2.54 g cm^{-3} and 0.463 g cm^{-3}, respectively. In pure ^{6}LiF the total ranges of the triton and alpha particle are 34.9 μm and 6.28 μm, respectively.

Note, measurement systems require a minimum energy deposition, thus the 'effective ranges' are less than the total ranges and account for threshold energy. The total ranges of the triton and alpha particle in pure ^{6}Li are 133 µm and 23.2 µm, respectively.

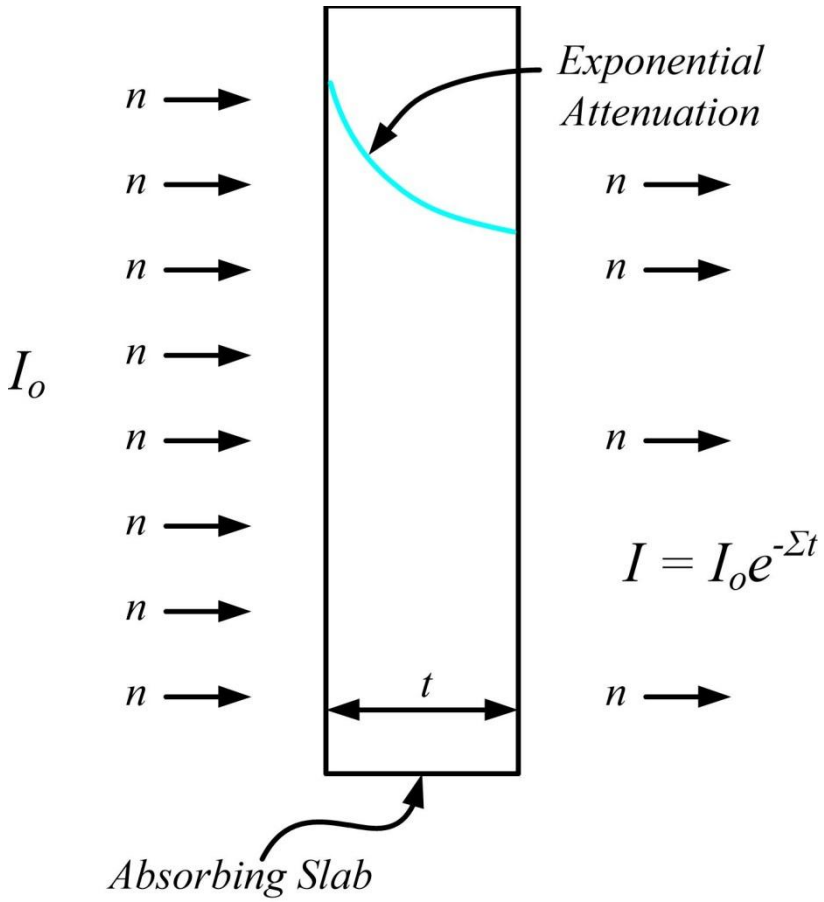

Figure 2.3: Schematic of a uni-directional thermal neutron beam incident on a neutron absorber slab of thickness t. The transmitted neutron current is calculated with Eq. (8) [60].

Consider a uni-directional beam of thermal neutrons normally incident onto a neutron absorbing slab with intensity I_o as shown in Figure 2.3. The neutrons are absorbed exponentially as they travel through the slab, as shown by Eq. (2.23).

$$I(t) = I_o e^{-\Sigma_a t}, \tag{2.23}$$

where Σ_a is the macroscopic thermal neutron absorption cross section and t is the absorber thickness. The neutron fraction absorbed, I_F, by the neutron absorber is,

$$I_F = 1 - \frac{I(t)}{I_o} = 1 - e^{-\Sigma_a t} \quad (2.24)$$

.

Thus, from above, an indicator of relative detection efficiency is the Σt product where increasing Σt product value generally is accompanied by increasing detection efficiency. Because ^{6}LiF has a higher macroscopic thermal neutron absorption cross-section than pure ^{6}Li, a higher fraction of neutrons will be absorbed in a slab of ^{6}LiF than ^{6}Li for the same given thickness. In order to make a high efficiency neutron detector, the detector must first have high thermal neutron absorption efficiency. However, the second factor, the reaction product escape probability, is equally as crucial and also dependent on the absorber thickness. For example, a 1.0 μm thick slab of ^{6}Li foil will have a high reaction product escape probability, but the percentage of neutrons absorbed in 1.0 μm of foil is too low for a high efficiency detector. Conversely, for a thick slab 1.0 cm thick, the reaction product escape probability will be limited by the reaction location and particle trajectory, although neutron absorption may approach 100%. Hence, an optimum absorber thickness can be determined.

Many available gas-filled neutron detectors consist of a grounded outer casing, serving as the cathode, and a centrally positioned small diameter (≤100 μm) high voltage (500V–2500V) wire, serving as the anode. The smaller anode electrode surrounded by an outer grounded electrode is the same basic design that has been used for over 100 years. Today the anode wire is typically 20–50 μm thick gold coated tungsten wire, which optimizes ruggedness and electrical properties. In gas-filled neutron detectors, such as ^{3}He and $^{10}BF_3$, the neutron sensitive gas fills the region between the anode and cathode. Reaction products emitted from these gases create electron-ion pairs along their path length through Coulombic interactions. Electrons are swept to the anode wire while the ions drift towards the cathode. If the electric field surpasses a critical field around the anode wire, the electrons may gain enough kinetic energy to cause Townsend avalanching, thereby creating a cascade of electron-ion pairs. Greater detailed descriptions of gas-filled detector operation and optimization can be found in the literature [17, 18]. When the reaction products in gas-filled neutron detectors are emitted in opposite directions, both reaction products

can deposit all of their energy in the gas volume. However, a percentage of neutron absorptions that occur near the cathode wall may result in one of the reaction products colliding with the cathode wall before depositing all of its energy in the gas volume. This creates a continuum of energy observed in the pulse-height spectrum referred to as the 'wall effect' [17, 18]. There is minimal 'wall effect' in most gas-filled neutron detectors, while this same effect can be reduced by increasing the tube diameter. Characteristically, in gas-filled detectors, both reaction products can be measured simultaneously, which is physically impossible with common coated detectors, such as ^{10}B coated pin diodes or a ^{10}B coated gas-filled detectors.

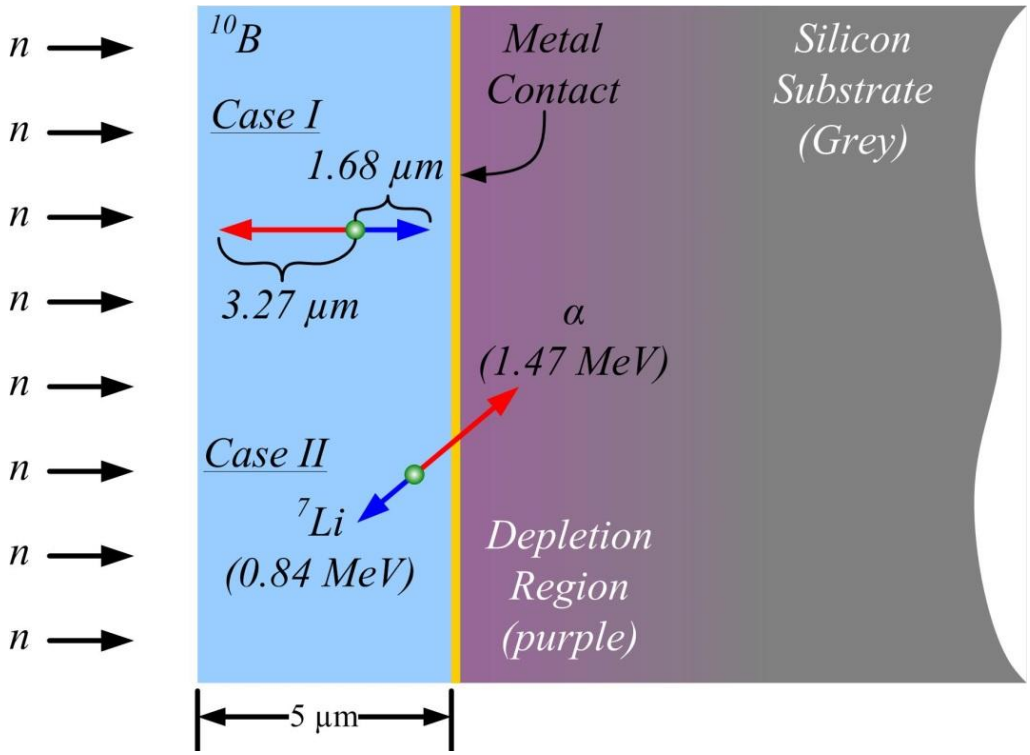

Figure 2.4: An illustration of a ^{10}B coated diode. The coating thickness is greater than the longest range reaction product and, thus, the chance exists that neither reaction product is measured, as shown in Case I. If neutron absorptions occur sufficiently close to the diode surface, only one reaction product can be measured per neutron absorption because reaction products are emitted in opposite directions (180°) due to conservation of momentum.

Shown in Figure 2.4 is an illustration of a ^{10}B coated pn junction diode with a 5.0 μm thick layer of ^{10}B on the diode, a layer thicker than the longest range reaction product (alpha particle at 3.27 μm for the 94% branch). Because the coating thickness is greater than the alpha particle range, there is a possibility exists that neither reaction product enters the diode, as shown in *Case I* (Figure 2.4). In *Case II*, the neutron absorption occurs near the diode region. Because the reaction products are emitted in opposite directions from thermal neutron absorption, only one reaction product can enter the diode. The other reaction product will deposit its energy in the coating layer and will not be measured by the diode. Depending on the neutron absorption location, only a fraction of energy of one of the reaction products can be measured, creating a pronounced wall-effect that ultimately restricts the overall neutron detection efficiency and makes gamma-ray discrimination difficult.

In order to develop a high efficiency neutron detector, two factors must be met. The first is that the absorber medium must have a high neutron absorption cross section. For example, a 1.0 cm thick slab of pure ^{10}B would absorb essentially all thermal neutrons. However, the neutron detection efficiency would not be 100%, but closer to 4.0% because a majority of the reaction products would deposit their energy in the slab and not reach the detection medium. The wall effect will appear for any coated device, whether it be a gas-filled, scintillator, or semiconductor detector. Thus, the second factor to consider when developing a high efficiency neutron detector is the ability to measure as many of the reaction products as possible and as much of their resultant energy as possible. Visualizing the absorption of a large percentage of neutrons is easy, but there are many methods as to how to cleverly measure the reaction products, and many of those methods are discussed in the following sections.

2.4 Commercially available neutron detectors

Neutron detectors are fashioned as gas-filled, scintillator, semiconductor, and various other forms of radiation detectors. Commercially available neutron detectors in ^{3}He, $^{10}BF_3$, and ^{10}B-lined proportional counters, LiI, Li glass, plastic, and liquid scintillators, coated and perforated diodes, thermoluminescent dosimeters (TLD's). Some more recent neutron detectors to hit the

market are coated optical fiber scintillators and new Li based scintillators, both discussed in the following sections.

2.4.1 Gas-Filled Neutron Detectors

The ^{3}He gas-filled proportional counter has widespread use due to the high neutron detection efficiency and simple design, thereby, becoming one of the most popular neutron detectors. These detectors are capable of intrinsic thermal neutron detection efficiencies greater than 80% while coming in a variety of effective volumes and areas ranging from 5–1000 cm^{2}. The smaller detectors have high demand in the oil-well logging industry while the larger devices are used at neutron testing facilities and also for security monitoring. Further, because the absorbing medium is a gas, the detector has the ability discriminate gamma rays from neutrons with relative ease. Gamma-ray discrimination is critical in many applications because reducing the gamma-ray interactions reduces the amount of false-positive signals during measurements. Most gamma-ray interactions in gas-filled detectors occur through Compton scattering in the cathode wall and the resulting Compton electron occasionally creates an electronic pulse. When the gamma-ray flux is high enough that two or more gamma-rays are incident within the detection system integration time, the two signals will sum together to create a larger pulse. This result may be misinterpreted as a neutron measurement and cause a false count. However, an energy or pulse-height threshold, referred to as the lower level discriminator (LLD), can be set to eliminate pulses from gamma rays being counted as neutrons. Because both reaction products are measured in ^{3}He gas-filled neutron detectors, pulses are relatively large compared to pulses generated from gamma-ray interactions. Thus, an LLD can be set to eliminate gamma-ray interactions without sacrificing neutron measurements.

Shown in Figure 2.5c is a typical pulse-height spectrum of a ^{3}He gas-filled device with obvious identifiable features. In Figure 2.5, there is a wall effect continuum that appears below the full energy peak at channel 500, a result of the proton and triton colliding with the chamber wall and depositing only a fraction of their energy. Gamma rays, however, interacting in the ^{3}He detector would create an electronic pulse in the lower channel numbers, typically less than channel 50. From the pulse-height spectrum, it becomes obvious the gamma rays do not deposit

much energy in the detector and, therefore, blend in with the electronic noise of the system. Pulses from electronic noise and gamma-ray background do not appear in the pulse-height spectra because they fall below the lower level discriminator.

The ^{3}He neutron detector, however, does not have a uniform count rate or pulse-height spectrum over the entire length of the device. Shown in Figure 2.5 and Figure 2.6 is an X-ray image of the ^{3}He neutron detector frequently used by the S.M.A.R.T. Laboratory group with dimensions 5.0 cm diameter x 13.0 cm long. The detector has a measured intrinsic thermal neutron detection efficiency of 80.5% and is pressurized to 4.0 atm. In the X-ray image there is an electrical field tube at the live end of the detector (right side of the image) which prevents the anode wire high voltage from arcing to the cathode at the end of the tube. Consequently, the field tubes create dead space at the live and dead end of the tube, as shown in Figure 2.6, where the total counts are plotted as a function of position along the length of the detector. The bottom 2.5 cm and top 4.0 cm do not have the same count rate response as the center of the device. Thus, only 50 percent of the ^{3}He tube shown in Figure 2.6 is active, but the entire length of the device will absorb neutrons. Those neutrons absorbed at the ends of the detector are not recorded. Further, the pulse-height spectra resolution becomes nearly unidentifiable where the anode wire is connected in the field tubes, as shown in the pulse-height spectra of Figure 2.5.

The nonuniformity of pulse-height spectra and insensitive zones of ^{3}He detectors have not deterred the use of the detectors in industry or research, mostly likely a result of the relatively high detection efficiency compared to alternative neutron detectors. Further, the insensitive region percentage of a tube is dependent upon the length of the tube. The insensitive region discussed above was 50 percent, but in a 30 cm long detector the dead region would only be 21.7% of the total neutron absorbing region assuming similar field tube lengths. This percentage decreases with increasing tube length. A recent serious disadvantage is the limited availability of the ^{3}He gas. Many users of neutron monitoring systems are willing to pay the increased cost of ^{3}He gas, but scarcity has thwarted such desires. The United States is said to have the largest ^{3}He supply, with the only other having an appreciable stockpile being Russia [21].

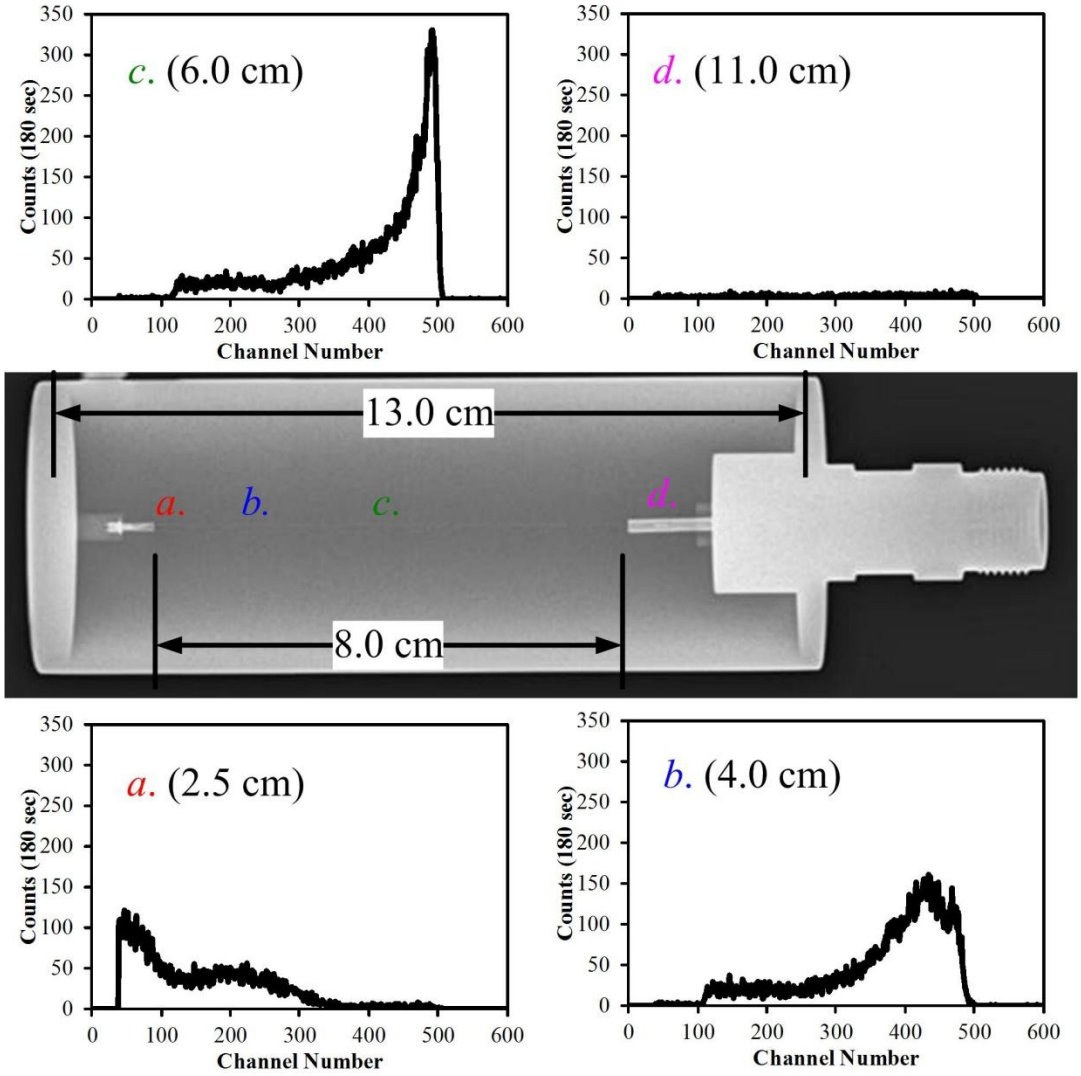

Figure 2.5: A 5.0 cm diameter x 13 cm long ^{3}He neutron detector filled to 4.0 atm is shown in the center. The four pulse-height spectra shown were collected using a 1.0 mm diameter thermal neutron beam at different distances from the base (left side of X-ray) of the detector. Only a 1.5 cm width exists where the ideal pulse-height spectrum is attainable and centered at 6.0 cm from the base. The pulse-height spectra deviate from the ideal case dramatically as the incident neutron beam moved away from the center of the anode wire.

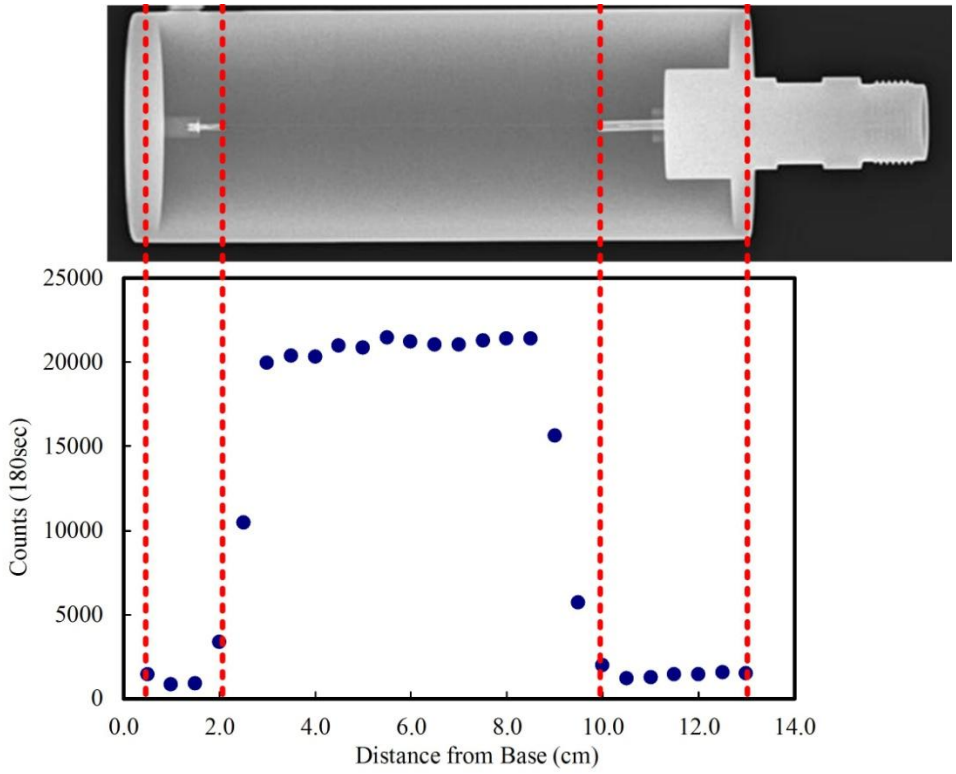

Figure 2.6: Total counts were recorded as a function of position longitudinally along the same ^{3}He tube shown in Figure 2.5. The diameter of the neutron beam was approximately 1.0 mm and total counts were recorded in 0.5 cm increments from the base to the top of the detector. The active counting region is approximately 6.5 cm long (50% of the overall length), but the entire 13.0 cm of the detector will absorb neutrons.

An alternative neutron detection gas to ^{3}He is $^{10}BF_3$, whereby the detector designs are essentially the same. Sometimes these gases are mixed with a small percentage of quench gas such as P-10 (90% Ar, 10% CH_4) or CO_2 to help improve charge carrier velocity and resolution. Argon has also been added to these devices with similar results [10]. $^{10}BF_3$, although a gas, is not considered an ideal proportional gas when compared to traditional proportional gases (such as noble or halogen gases). The addition of Ar improves charge carrier mobility and reduces the detector deadtime. These detectors also have similar gamma-ray discrimination abilities and can span similar effective areas as ^{3}He tubes. Shown below in Figure 2.7 is the pulse height spectrum from a typical $^{10}BF_3$ tube, where both the 94% and 6% reaction product branches are identifiable. The wall effect continuum begins around channel 180 and 340. With improved resolution, the different reaction product branching ratios from the wall effect would be observable. An LLD set

in the valley between the wall effect continuum and the electronic noise (approximately channel 150) would discriminate nearly all gamma-ray interactions while maintaining high thermal neutron detection efficiency. These devices typically have a maximum thermal neutron detection efficiency of 30%, and are dependent upon fill pressure and diameter [61]. $^{10}BF_3$ detectors are approximately half as efficient as some ^{3}He detectors, which is acceptable in some instances, but the most imposing drawback is the toxicity of the BF_3 gas. This poisonous gas is accompanied by stringent government regulations on fill pressure, and, consequently, the thermal-neutron detection efficiency. However, $^{10}BF_3$ detectors do have similar gamma-ray discrimination characteristics as the ^{3}He neutron detectors.

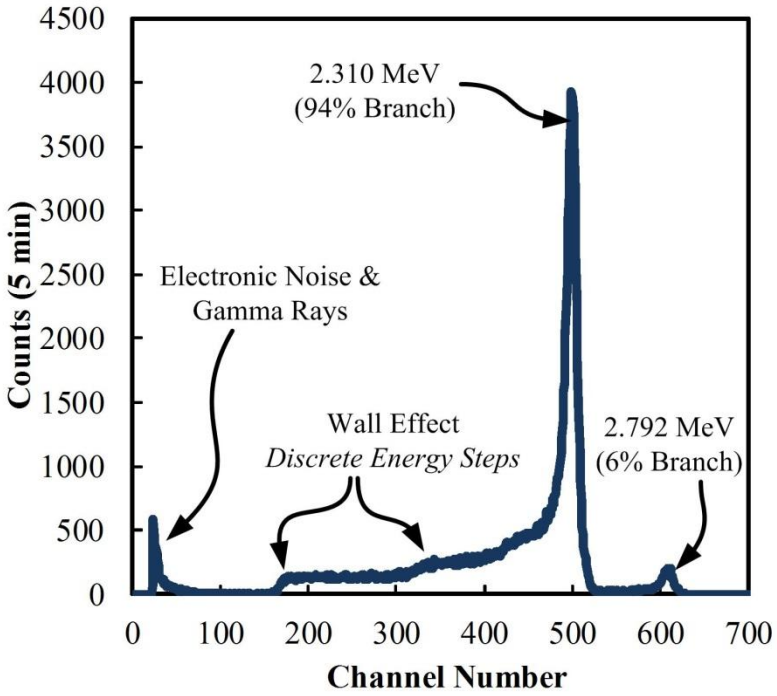

Figure 2.7: A pulse-height spectrum collected with a $^{10}BF_3$ neutron detector. All features are labeled in the plot and the wall effect occurs from either the alpha particle or Li ion colliding with the wall and depositing only a fraction of its total energy.

A lower efficiency alternative is a ^{10}B coated proportional counter. A thin layer of ^{10}B (1–3 μm) is coated on the inner wall of a cathode and the rest of the volume is filled with a proportional gas such as P-10. This configuration results in a pulse-height spectrum with a stair-step wall effect blending with both electronic noise and gamma-ray features, as shown in Figure 2.8. The intrinsic thermal-neutron detection efficiency of ^{10}B-coated proportional counters and ion chambers is significantly lower than ^{3}He tubes, maximizing around 9.0% [61]. However, the detection efficiency may be even less if the detector is in a high gamma-ray radiation field. Pulses generated from gamma-ray interactions will overlap with neutron interactions in lower energy portions of the pulse-height spectrum. Thus, in order to discriminate gamma-rays and measure only neutrons, some of the interactions from neutrons must be eliminated from an increased LLD level. Consequently, this higher LLD setting also lowers the overall thermal neutron detection efficiency.

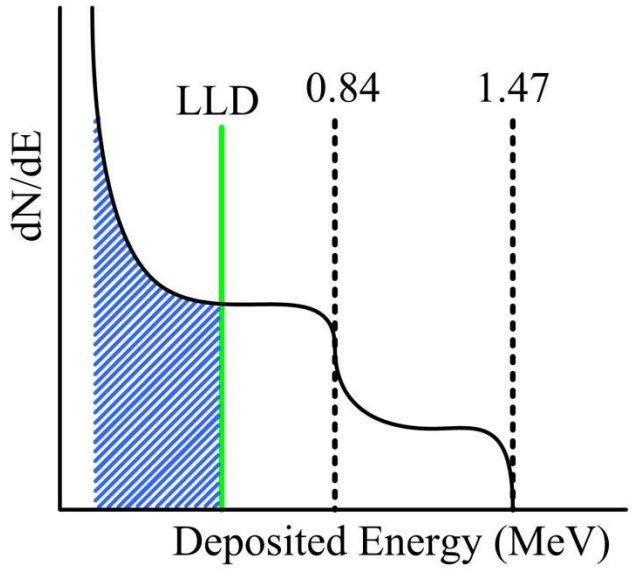

Figure 2.8: An illustration of the pulse-height spectrum from a ^{10}B coated proportional counter where the wall effect is obvious. The steps coincide with the alpha particle and Li ion energies. The blue cross-hatched region is the number of interactions from neutrons that must be eliminated from the data set in order to remove false counts from gamma-rays and electronic noise.

2.4.2 Scintillation Neutron Detectors

Scintillator neutron detectors are composed of neutron reactive materials that are coupled with a scintillation material. The neutron interaction produces energetic reaction products that deposit their energy in the scintillating material, thereby, releasing visible light. Some common scintillator neutron detectors include organic liquids, Li glass (Ce), LiI(Eu), B or Li doped plastics, and ZnS(Ag) coupled with LiF powder. Recently, Cs_2LiYCl_6:Ce (CLYC) and ^{6}LiF coated ZnS(Ag) scintillating fibers have become known as promising scintillator neutron detectors. CLYC detectors have an intrinsic thermal neutron detection efficiency of almost 100% with similar gamma-ray discrimination abilities as ^{3}He neutron detectors. However, the efficiency and gamma-ray discrimination are only achievable through pulse-shape discrimination (PSD) techniques. The tail of a pulse generated from a gamma-ray absorption decays to the baseline quicker than the tail of a pulse generated from neutron absorptions. Computer algorithms reveal that the two interactions can be separated electronically resulting in the ability to measure both types of radiation simultaneously. ZnS(Ag) scintillating screens were first used by Becquerel and Rutherford in many of the earliest radiation experiments. Hence, surrounding these scintillators with a neutron sensitive material is an obvious adaptation. A slurry of ZnS(Ag) and ^{6}LiF are mixed together and coated as a thin layer around an optical fiber. The light generated is channeled to a PMT through the fiber. Bundling many coated fibers together results in a detector with high thermal neutron detection efficiency. Initially, these detectors suffered from low gamma-ray discrimination abilities, but recently PSD was applied to the output pulses and the problem has been resolved.

Innovative American Technologies has developed several neutron monitoring systems using the ZnS(Ag) scintillating fiber technology. They offer several different sized detectors including Radiation Portal Monitors (RPM) and backpacks. These devices have good reported neutron detection efficiency and gamma-ray discrimination, but appear to have technical and cost issues due to the complexity of the assembly. Both the CLYC and ^{6}LiF coated scintillating fibers use PMT's and thus accrue the associated costs and ruggedness issues. The CLYC detector suffers mostly from limited size, typical detector crystals being 2.5 cm in diameter and 1–2 cm thick. Larger crystals have proven difficult to grow.

2.4.3 Coated Semiconductor Neutron Detectors

The first coated semiconductor neutron detectors utilized a ^{10}B layer deposited on a simple pn junction diode, similar to the illustration shown in Figure 2.4. These devices have been studied since the late 1950's for relatively fast signal speeds [16, 17]. However, these devices are limited to a maximum efficiency of approximately 4.5% [48]. Methods for stacking several of these detectors together to fabricate a multi-layered devices have been discussed in the literature, but the reported efficiencies were still considerable less than that of ^{3}He devices [48]. Additionally, the coated devices have a relatively small effective area; a 1.0 cm^2 device is considered large. However, these devices can be ganged together in an array, but achieving 10 cm^2 area is still difficult. Regardless, the limiting factor is the relatively low neutron detection efficiency.

Recently, Radiation Detector Technologies (RDT), originating in the S.M.A.R.T. Laboratory, has begun commercializing microstructured semiconductor neutron detector (MSND). MSND's are fabricated by etching deep ($\geq$ 400 μm) trenches into the surface of silicon, the silicon wafer is turned into a diode through specific oxidation and diffusion processes, and the trenches are backfilled with a neutron reactive material, typically ^{6}LiF, as shown in Figure 2.9 [29, 32, 48, 62-64]. As a result of the trenching, there is an order of magnitude increase in thermal neutron detection efficiency compared to planar coated devices. However, recently it has been shown to be difficult and time consuming to produce arrayed versions as large 1000 cm^2. The ruggedness, low power, light weight, and high efficiencies of these devices prove to be more effective than ^{3}He tubes in certain applications. Several neutron monitoring systems have been delivered to date including handheld, briefcase, and ^{3}He form fit designs, some which have performed better than 4.0 atm ^{3}He neutron detectors. Currently, the only observable disadvantage of these devices is the struggle to easily fabricate large area arrays ($\geq$1000 cm^2) of detectors. However, the size of these devices in combination of the high thermal neutron detection efficiency makes these devices candidates for neutron monitoring systems not presently applicable by other commercially available neutron detectors, such as personal dosimetry and remote sensing.

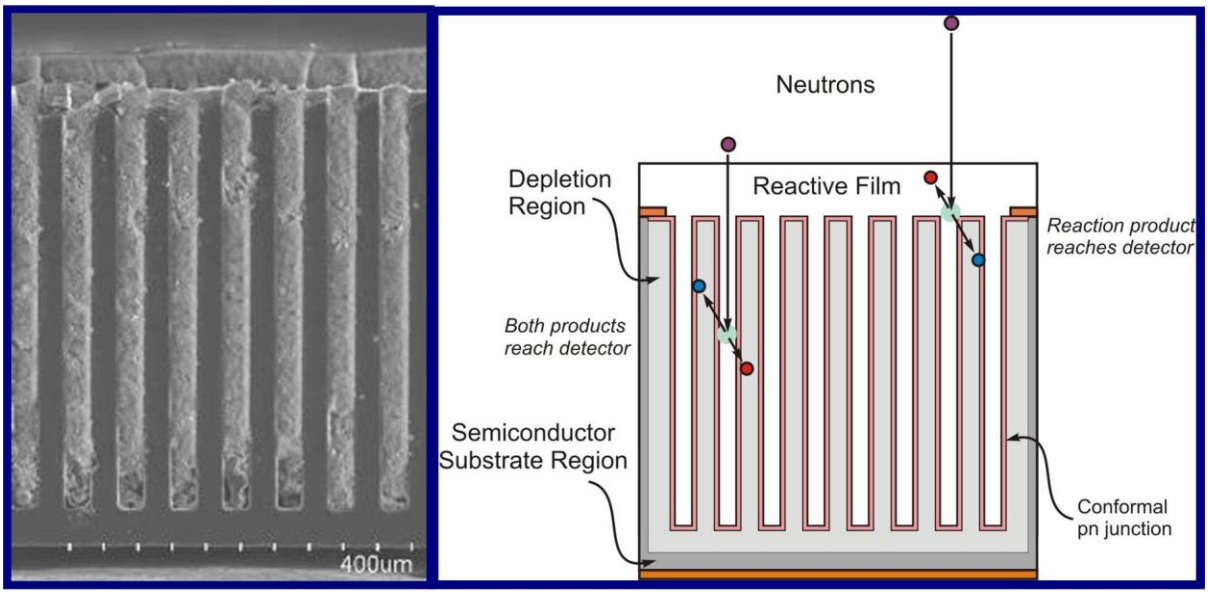

Figure 2.9: A cross-sectional side image collected with a scanning electron microscope showing 490 µm deep trenches backfilled with nano-sized ^{6}LiF powder (left). A cross-sectional schematic of a MSND detector which also depicts the neutron capture and reaction products entering the Si regions of the diode (right). As a result of the trench width, it is possible to measure both reaction products simultaneously.

CHAPTER 3

COMPARTMENTALIZED GAS-FILLED NEUTRON DETECTORS: THEORY

"The most beautiful thing we can experience is the mysterious.
It is the source of all true art and science."
-Albert Einstein

Described in chapter three is the theoretical operation of compartmentalized gas-filled multi-wire proportional counter (MWPC) neutron detectors. Materials used in construction of the devices were ^{6}Li foil, ^{6}LiF impregnated open-celled polyurethane foam, and aerogels containing either (or both) ^{6}Li and ^{10}B materials. Detailed descriptions and properties of gas-filled proportional counters and MWPC's can be found in the literature [7, 17, 18].

3.1 General Overview

The ability to measure all reaction products produced by neutron absorptions is an inherent property of ^{3}He and $^{10}BF_3$ gas-filled neutron detectors. However, in order to absorb a large percentage of incident neutrons, the devices must be overpressured to several atmospheres (up to 10 atm). Conversely, neutron detectors using common solid-form neutron absorber materials absorb a significant percentage of neutrons in a few micrometers or millimeters of material. However, if the solid-form neutron absorber material is used as a coating layer, the detector will suffer from the inability to measure more than one reaction product, thereby, reducing neutron

detection efficiency. However, if the solid-form neutron absorber material is suspended in the detector, compartments are created within the device which may allow for more than one reaction product to be measured per neutron absorption. Commercially available neutron detectors based on solid-form surfaces, typically coated detectors, measure only one reaction product per neutron absorption, while the other reaction product deposits its energy in the neutron absorbing material (or some other non-sensing medium) and is lost. The ^{10}B-lined counter is an example of a neutron detector that uses a solid-form neutron absorber material and only measures one reaction product per neutron absorption. The pulse-height spectrum from neutron detectors that only measure one reaction product have a stair-step appearance, referred to as the 'wall-effect' (discussed in Chapter 2). The consequences of the wall-effect result in lower neutron detection efficiency and poor gamma-ray discrimination [3,4]. Gamma-ray discrimination can be achieved with these devices, but a large percentage of the neutron counts must be sacrificed in order to achieve acceptable gamma-ray rejection ratios (GRR). Neutron detectors utilizing compartmentalization have the ability to measure both reaction products by suspending self-supporting neutron absorber materials that allow reaction products to escape both sides of the neutron absorber sheet simultaneously. In order to have a high probability of measuring both reaction products, the absorber sheet thickness must be less than the summed reaction products range. Consequently, this requirement decreases the neutron absorption probability of the detector. However, a high-efficiency neutron detector can be created by stacking multiple consecutive layers of thin sheets within the detector.

Illustrated in Figure 3.1 is a series of thin neutron-absorbing slabs stacked in a row with anode wires positioned between each neutron absorber sheet. If the neutron absorber slab thickness is less than the summed range of reaction products, then reaction products from a single neutron absorption can escape both sides of the absorber sheet simultaneously and be measured concurrently in the surrounding gas-filled compartments. The anode wires are coupled together, thereby, allowing signals generated in two adjacent gas-filled compartments to be summed together. Consequently, a larger signal is generated than observed from a coated neutron detector. Measuring both reaction products simultaneously improves intrinsic neutron detection efficiency and gamma-ray discrimination abilities of the MWPC neutron detector compared to coated detector configurations. Three main materials were investigated as the thin suspended neutron absorbing sheets, which include ^{6}Li foil, impregnated foam, and aerogels.

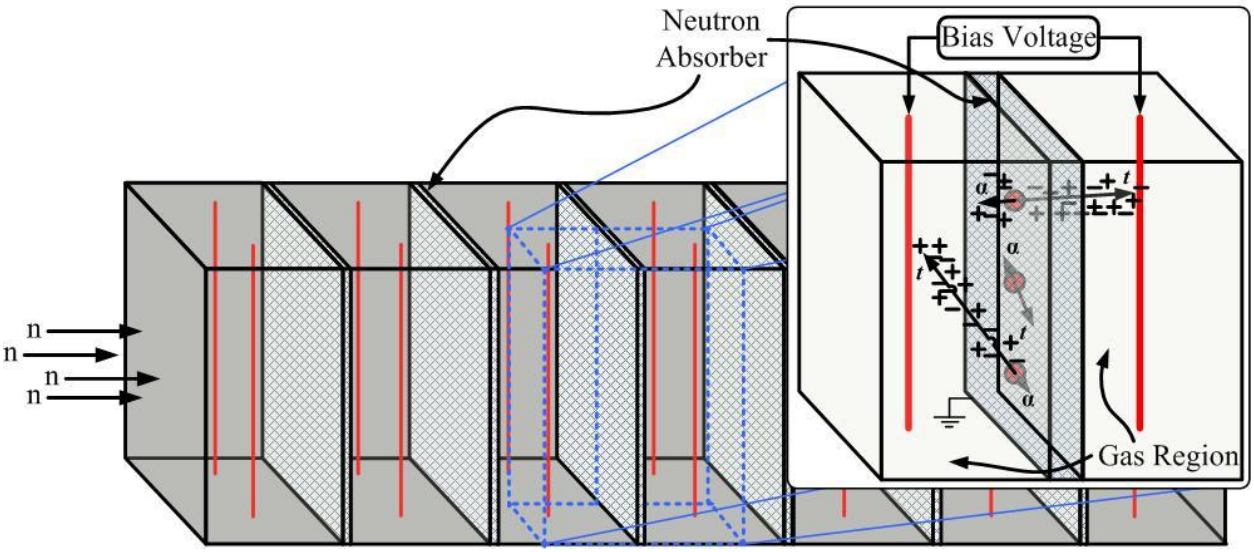

Figure 3.1: An illustration of a multi-layered multi-wire proportional counter. The neutron absorber layers are designed to be thinner than the summed range of the reaction products. The reaction products may escape the absorber slab simultaneously and be measured in the gas volume concurrently.

3.2 Lithium Foil

As a result of the Li battery industry, Li foil is now produced at thicknesses ranging from 30–120 µm, less than the summed range of the $^{6}Li(n,\alpha)^{3}H$ reaction products in pure Li metal (156 µm). The range of 2.73 MeV tritons and 2.05 MeV alpha particles in 95% enriched ^{6}Li metal is 133 µm and 23 µm, respectively [65]. Consequently, reaction products can escape both sides of a single Li foil simultaneously. The ability of the neutron detector to measure both reaction products simultaneously affects both the intrinsic thermal neutron detection efficiency and the pulse-height spectrum.

Shown in Figure 3.2 is the intrinsic thermal neutron detection efficiency plotted as a function of Li foil thickness for various numbers of Li foil layers. The neutron detection efficiency is dependent on the number of Li foils used in the detector. Additionally, the number of Li foils in a MWPC dictates the ideal Li foil thickness that maximizes the neutron detection efficiency. For example, a 5-layer Li foil MWPC has a maximum intrinsic thermal neutron detection efficiency

of 58% if 75 μm thick pure ^{6}Li foils are used in the detector, while a 10-layer device can achieve 72% detection efficiency with 55 μm thick ^{6}Li foils [66, 67]. The reaction product escape probability and neutron absorption probability are the two contributing factors that dictate the Li foil thickness that maximizes the neutron detection efficiency for a specific number of Li foil layers. A thorough explanation of this concept and the equations used to create the plot in Figure 3.2 is discussed by McGregor et alii [48].

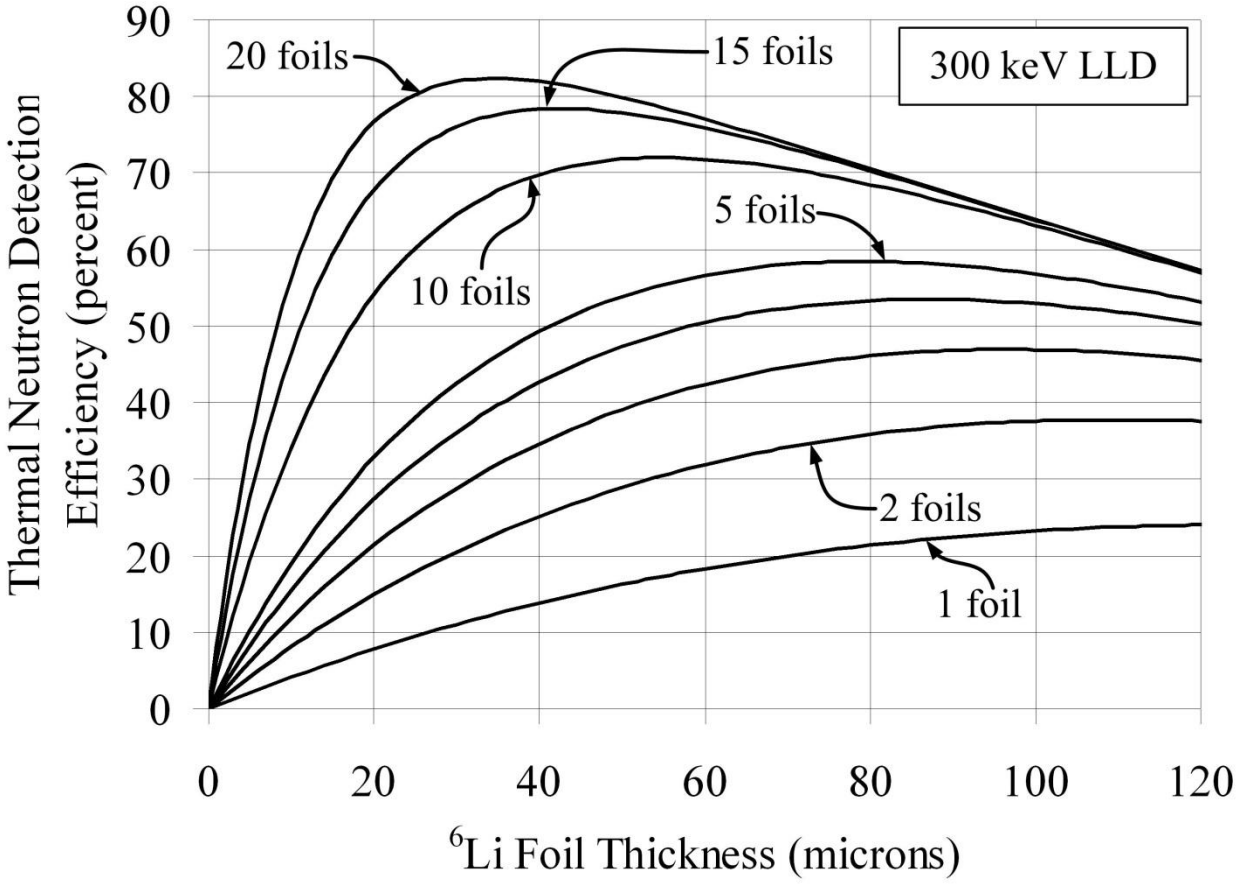

Figure 3.2: A plot of the intrinsic thermal neutron detection efficiency of the ^{6}Li foil MWPC as a function of the foil thickness for various numbers of ^{6}Li foils. Depending on the number of foils used in the device, a specific foil thickness will optimize the overall detection efficiency.

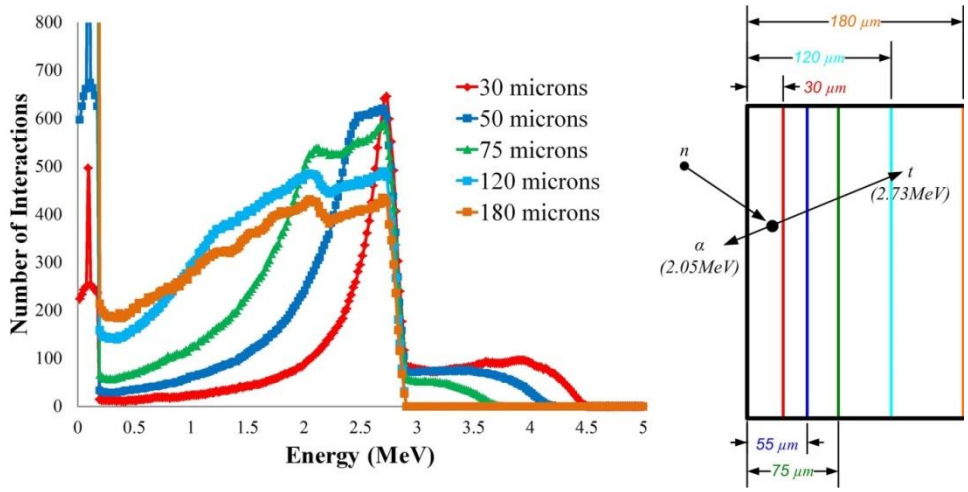

Figure 3.3: The simulated pulse-height spectra for different thicknesses of Li foil. As the thickness increases, more of the reaction product energy is absorbed in the foil before escaping and, consequently, smaller signals are produced.

The thickness of ^{6}Li foil also affects the pulse-height spectrum. Shown in Figure 3.3 are pulse-height spectra of various Li foil thicknesses obtained with Monte Carlo N-Particle Transport Code version 6 (MCNP6) simulations.[1] The thinnest Li foil simulated, 30 μm, has the largest signals compared to the other thicker Li foils because it has the smallest amount of reaction product self-absorption occurring in the Li foil. In other words, the reaction product escape probability increases with decreasing Li foil thickness. If reaction products have more energy before entering the gas volume, then more gas ionization will be created, thus, producing larger signals. In general, the magnitude of the signals generated increases as the Li foil thickness decreases. Additionally, a valley appears in the pulse-height spectra in Figure 3.3 between the low energy region (<300 keV) and the main feature of the spectra. The valley depth decreases as Li foil thickness increases because the reaction products are undergoing more self-absorption in the Li foil. Further, the percent of total neutron interactions that create signals greater than the triton energy (2.73 MeV) decreases as the Li foil thickness increases, which is also a result of the increased reaction product self-absorption in the Li foil.

[1] MCNP6 is a software program that models neutron, photon, and electron transportation and reactions with different materials. The software was developed by Los Alamos National Laboratory (LANL) and is able to track neutron reaction product paths and energies.

The Li foil MWPC neutron detector discussed in the following chapters contains five layers of 75 μm thick Li foil. Thus, to retain consistency, the theoretical treatment is presented for the same detector arrangement. Shown in Figure 3.4 are the four possible outcomes the reaction products can experience in the Li foil sheets, three of which result in a measurable signal. In *Case 1*, both reaction products escape the foil, *Case 2* only the triton escapes, *Case 3* only the alpha particle enters the gas region, and for *Case 4* neither reaction product deposits energy in the gas volume. These four cases develop the total pulse-height spectrum and each case was broken down by individual contributions using Monte-Carlo simulations (as shown in Figure 3.5, for a 75 μm thick foil). The same number of neutrons were simulated for *Case 1*, *2*, and *3*, therefore, each contribution was plotted on the same scale in Figure 3.5. From plots of the individual contributions in Figure 3.5, it can be concluded that *Case 2*, in which only tritons deposit energy, is the dominating feature of the total pulse-height spectrum. Further, the total pulse-height spectrum in Figure 3.5 has a sudden drop in the number of interactions above 2.73 MeV, the energy of the triton, as expected. The small shoulder occurring at energies higher than 2.73 MeV is a result of measuring both reaction products simultaneously. However, there are also occurrences in which both reaction products escape the Li foil, but the energy deposited is less than 2.73 MeV. Further, the smallest contribution to the total pulse-height spectrum is from *Case 3*, in which only the alpha particle escapes the Li foil. The difference in reaction product contribution between *Case 2* and *Case 3* is the result of two factors: the first factor is the short range of the alpha particle compared to the triton, and the second factor is the difference in reaction product energy. Thus, the increased neutron detection efficiency for this particular foil thickness is not necessarily the result of measuring both reaction products simultaneously, but instead the ability to measure the triton reaction product no matter what side of the Li foils it escapes.

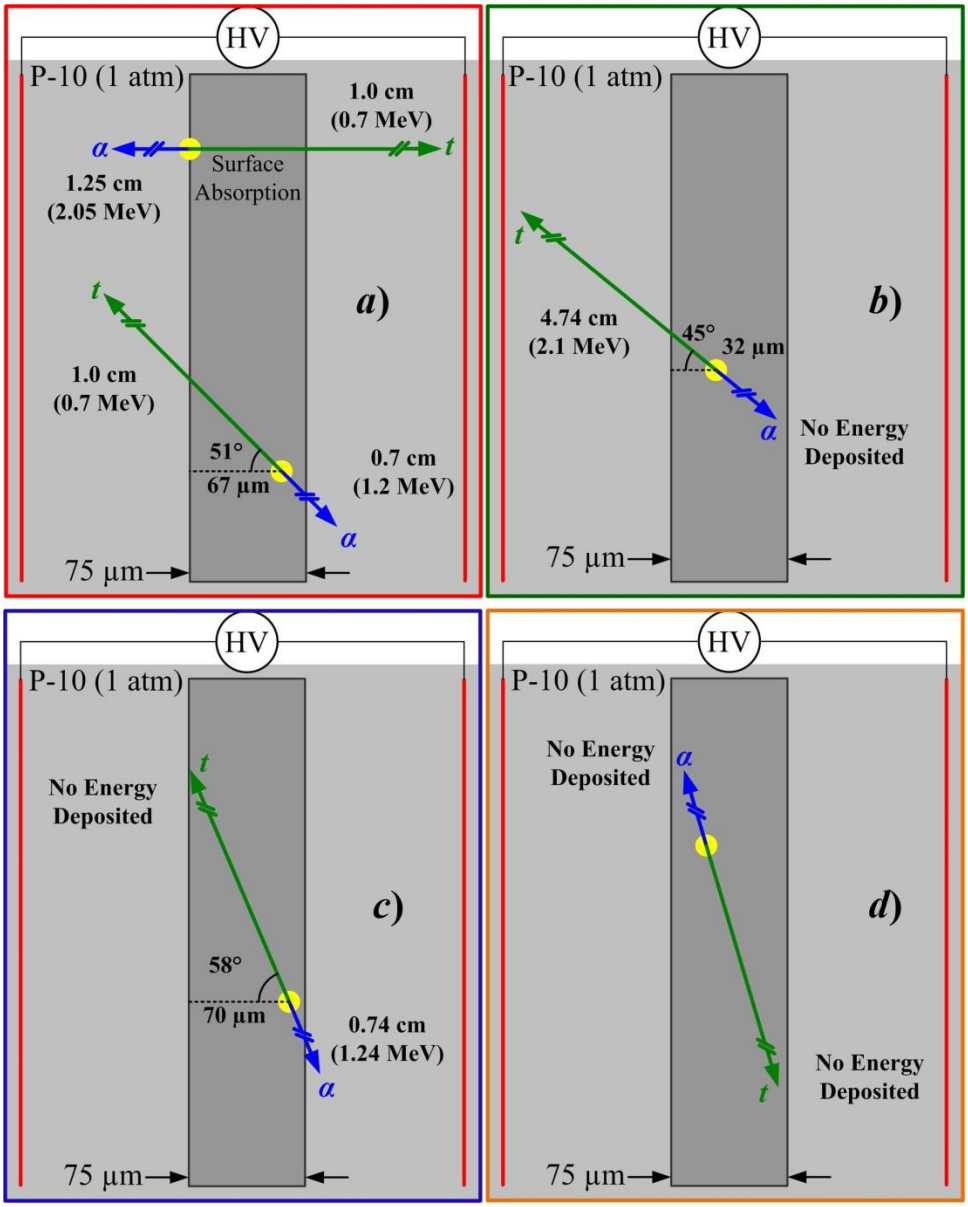

Figure 3.4: Four possible occurrences for reaction product energy deposition in the gas volume. In Case 1 (a), both reaction products enter the gas volume, while in Case 2 (b), only the triton enters the gas. In Case 3 (c), only the alpha particle escapes the foil. Lastly, Case 4 (d), neither reaction product produces any ionization in the gas.

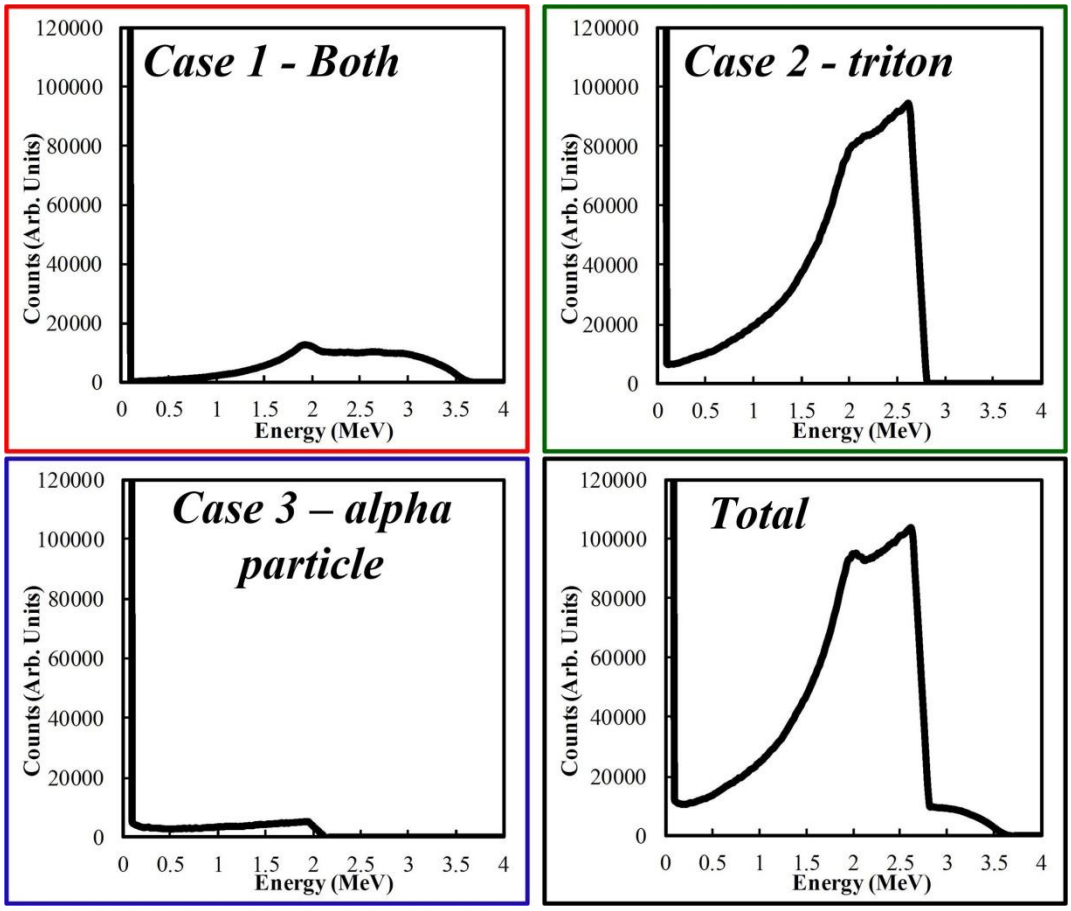

Figure 3.5: Pulse-height spectral contributions from the three cases in which reaction product energy is deposited in the gas volume. The three cases are summed into one pulse-height spectrum in the lower right.

The probability each *Case* occurs is dependent on the Li foil thickness, and these probabilities are plotted in Figure 3.6. The neutron detection efficiency can be estimated from Figure 3.6 by summing the probabilities of *Cases 1*, *2*, and *3* together for any particular thickness and subsequently multiplying by the total neutron absorption probability. In Figure 3.6, the intersection between *Case 1* and *Case 2* occurs at the thickness equivalent to the alpha particle range, and the intersection of *Case 2* and *Case 4* occurs at the Li foil thickness equivalent to the triton range. Between these two points of intersection occurring at Li foil thicknesses of 23 μm and 133 μm, measuring only the triton reaction product is the dominating factor of the pulse-height spectrum. For foils less than 23 μm thick, *Case 1* is the dominating contributor to the pulse-height spectrum and neutron detection efficiency. However, in order to maximize intrinsic

thermal neutron detection efficiency, more than 20 layers of Li foil would be required for foil thicknesses less than 23 µm. Detectors using Li foils greater than 133 µm thick rely on the ability to measure the triton on either side of the Li foil. The probability of measuring both reaction products simultaneously at 133 µm, and acquiring signals greater than 300 keV, becomes nearly impossible. Further, measuring both reaction products concurrently past foil thicknesses of 156 µm is impossible. Additionally, at Li foil thicknesses equivalent to, or greater than, 156 µm, there is a higher probability of losing both reaction products in the Li foil than measuring a signal produced by either reaction product individually.

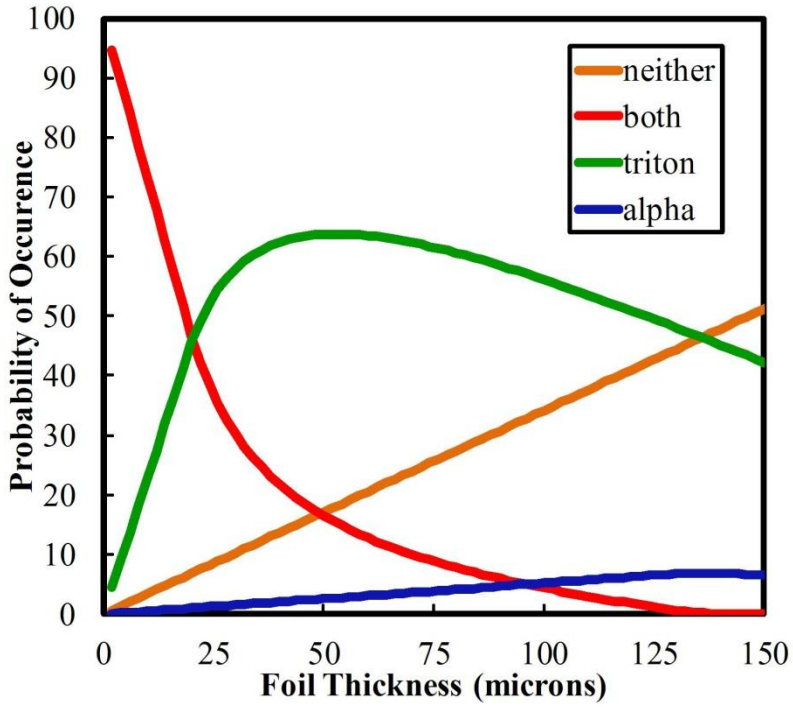

Figure 3.6: The probability that each case occurs per neutron absorbed as a function of the Li foil thickness. The ability of the detector to measure the triton escaping either side of the foil dominates the detection efficiency when the foil thickness is greater than 23 µm.

The ranges of 2.73 MeV tritons and 2.05 MeV alpha particles in 1.0 atm of P-10 gas are 7.26 cm and 1.25 cm, respectively [64]. In principle, the largest possible signal results if all the reaction product energy that escapes the foil is deposited in the gas. Designing for this maximum energy capture would require spacing the Li foils approximately 7.3 cm apart to ensure all triton energy is deposited in the P-10 gas volume. As a practical matter, pulses only need to exceed a

value that places them solidly above attendant electronic white noise or interfering signals. Particles depositing approximately 500 keV of energy meet this criterion and the detector was designed accordingly by spacing the foils only 1.63 cm apart. This foil spacing allows the triton to deposit at least 500 keV in the gas region. In theory, by setting the electronic lower level discriminator (LLD) at 500 keV or below, all high energy triton depositions will be counted.

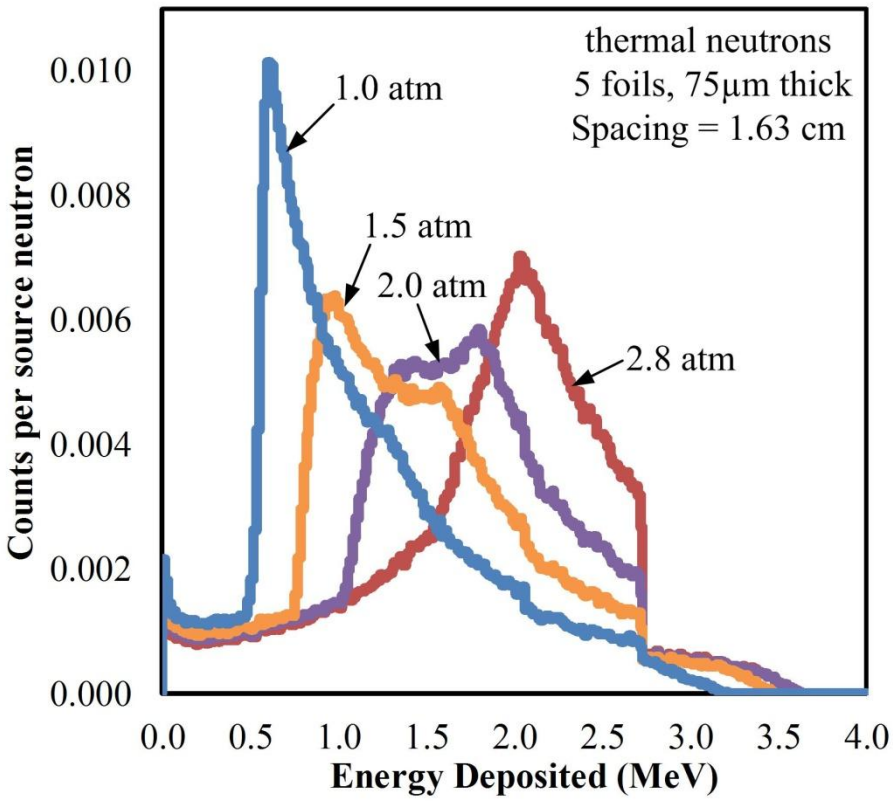

Figure 3.7: The theoretical pulse-height spectra of the Li foil MWPC obtained using MCNP6 for different P-10 pressures. The main feature of the spectra shifts to higher energies with increasing pressure, a result of more energy deposited per unit length from the reaction products.

Shown in Figure 3.7 are the theoretical neutron response pulse-height spectra obtained with MCNP6 for the detector configuration described previously. The simulated pulse-height spectra were obtained for P-10 gas pressures of 1.1, 1.5, 2.0, and 2.8 atm by changing the P-10 density. From Figure 3.7, the peak in the pulse-height spectra increases to higher energies as the P-10 gas pressure is increased. The increase in peak location is a result of the higher gas density, which

causes more energy to be deposited per unit length by the reaction products. Consequently, the magnitude of the signals is also increased because of the increased ionization. Further, the total number of reaction products escaping the Li foils does not change with pressure, but reaction product ranges and energy deposition does vary with gas pressure. For example, increasing P-10 gas pressure increases the amount of energy deposited by the triton in the gas region, resulting in larger pulses. The amount of energy deposited by the alpha particle in the gas volume does not change with increasing P-10 pressure because at 1.0 atm the alpha particle range in the gas is less than the distance between Li foils. Thus, increasing the P-10 gas pressure only shortens the alpha particle range in the gas region and not the energy deposited.

3.3 Impregnated Foam

Open-cell polyurethane foam is the most commonly manufactured type of foam and is used in many consumer products ranging from mattress pads and couches to packing containers and sound proofing materials. Envelope densities of this type of foam typically ranges from 1.0–3.0 lbs ft^{-3} (0.016–0.0481 g cm^{-3}), less than typical solid form neutron absorber materials. Polyurethane foam has been impregnated with different materials to change the properties of the foam for a variety of applications. Open-celled polyurethane foam can be impregnated with neutron absorbing compounds and these impregnated foams can be manufactured on large scales, 6’ x 4’ x 100’, and cut into strips only a few millimeters thick. These thin sheets are similar to Li Foils and can be used in place of Li foil in MWPCs.

The foam is impregnated with neutron sensitive powder, either ^{10}B compounds or ^{6}LiF, during the foam manufacturing process and the powder is incorporated into the foam structure. Shown in Figure 3.8 are two neutron absorptions with associated reaction product trajectories. Depending on trajectory angle, the porosity and pore size of the foam allows a reaction product originating in the bulk of the foam to escape the foam absorber sheet surface. A triton or alpha particle can reach the absorber sheet surface without traversing any foam struts by passing through the open cells of the foam, referred to as streaming. Conversely, a reaction product traveling the same length in a typical uniform solid material may not have sufficient energy to escape the absorber. Thus, the main advantage of the high-porosity low-density open-celled foam

is the reaction products may have longer ranges than in typical solid materials, which may result in higher neutron detection efficiencies. Reaction product streaming makes predicting the reaction product ranges difficult. Reaction products in typical homogenous solid-form neutron absorbers have specific ranges with relatively small variances about that distance. The maximum reaction product ranges in the foam are equivalent to the range in P-10 gas, which is a result of the streaming effects possible in the foam. Conversely, the minimum reaction products ranges are equivalent to the ranges in the foam strut material ($\rho \approx 1.6$ g cm^{-3}), only a few micrometers. The theoretical reaction product ranges obtained using envelope densities and assuming ideal homogeneous uniform solids are reported in Table 1.

The porosity and non-uniformity of foam not only affects reaction product ranges, but also the neutron absorption properties of foam. In a thin sheet (0.5 mm–5.0 mm), the total thickness of the foam (not including voids) varies from 0.0 mm, where there is no foam and only open pores, to the total thickness of the foam sheet in which the entire cross-section of the foam is filled with polyurethane and has no pores. When a 3.0 mm thick sheet of foam is held up to light, openings in the foam are visible and are also streaming paths for neutrons. Conversely, neutron absorption in local positions on foam slabs may be higher than predicted values because of closely packed struts. Additionally, a thermal neutron may scatter in a strut and change directions, ultimately being absorbed in the foam slab away from its point of entry into the sheet. Thus, predicting neutron absorption probabilities also becomes difficult.

Table 1: Reaction product ranges from ^{10}B and ^{6}Li neutron reactions in foam and aerogel. Porosity and non-uniform density cause inaccurate predictions [65].

	Range of the interaction products in aerogel and foam in microns					
	^{10}B(n,α)^{7}Li				^{6}Li(n,α)^{3}H	
	α 1.777 MeV	α 1.470 MeV	^{7}Li 1.015 MeV	^{7}Li 840 keV	^{3}H 2.73 MeV	α 2.050 MeV
Aerogel	378	285	118	93	4440	798
Foam	801	651	369	331	5580	946

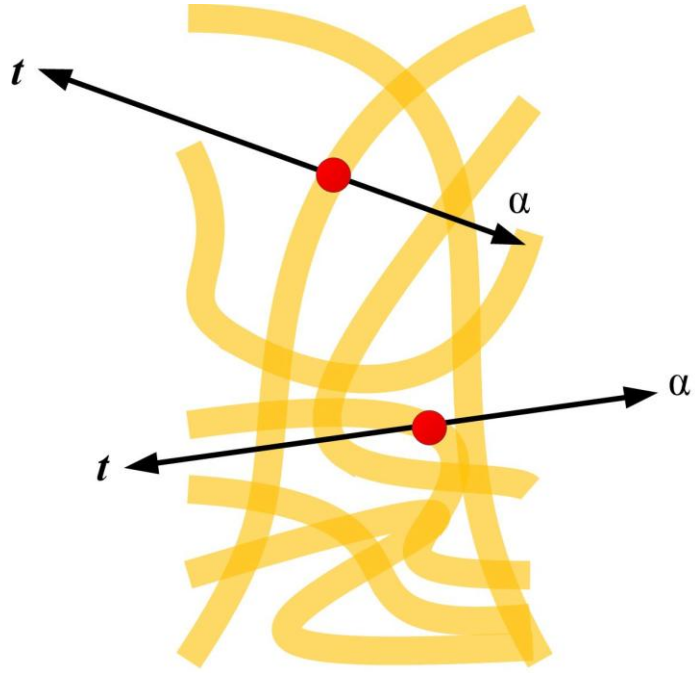

Figure 3.8: Cross-sectional illustration of ^{6}LiF impregnated foam. The red circles represent locations of the neutron absorption point in ^{6}LiF. Because of the random porosity of the foam, some reaction products may have streaming paths to escape the foam absorber, making predictions of reaction product ranges difficult.

The intrinsic thermal neutron detection efficiency of impregnated foam is also difficult to predict because of the breadth of reaction product ranges. Another factor contributing to neutron detection efficiency in the open-celled polyurethane foam is the impregnation level of the neutron absorbing materials. Ultimately, the saturation level would result in the highest neutron detection efficiency. Shown in Figure 3.9 is the intrinsic thermal neutron detection efficiency for 20 wt% impregnated ^{6}LiF open-celled polyurethane foam as a function of foam thickness for multiple layered devices. These values were calculated using the ranges in Table 1. Further research needs to be conducted in order to determine the accuracy of these ranges, or more specifically, a model should be created to validate the probability distribution of the range of lengths traveled by the reaction products.

Another factor to consider that may improve the neutron detection efficiency is the possibility of charge transport through foam or extracting charge out of a foam absorber slab. Reaction products that do not escape the foam sheets are creating ionization in the pores within

the bulk of the foam absorber. If this charge is extracted, then the current predicted thermal neutron detection efficiency is an underestimation. The predicted intrinsic thermal-neutron detection efficiency in Figure 3.9 assumes no charge generated in the foam contributes to signals.

Overall, the theoretical intrinsic thermal neutron detection efficiency is less than that of pure ^{6}Li foils for the same detector geometry, and there may be some inaccuracies in the reported data due to the reaction product ranges. The primary advantage of these devices is the low cost of foam neutron absorber sheets. Five sheets of impregnated foam, 4 x 6 ft and a few millimeters thick, would cost less than $100. However, there is little to no demand for low-cost detectors of such large sizes.

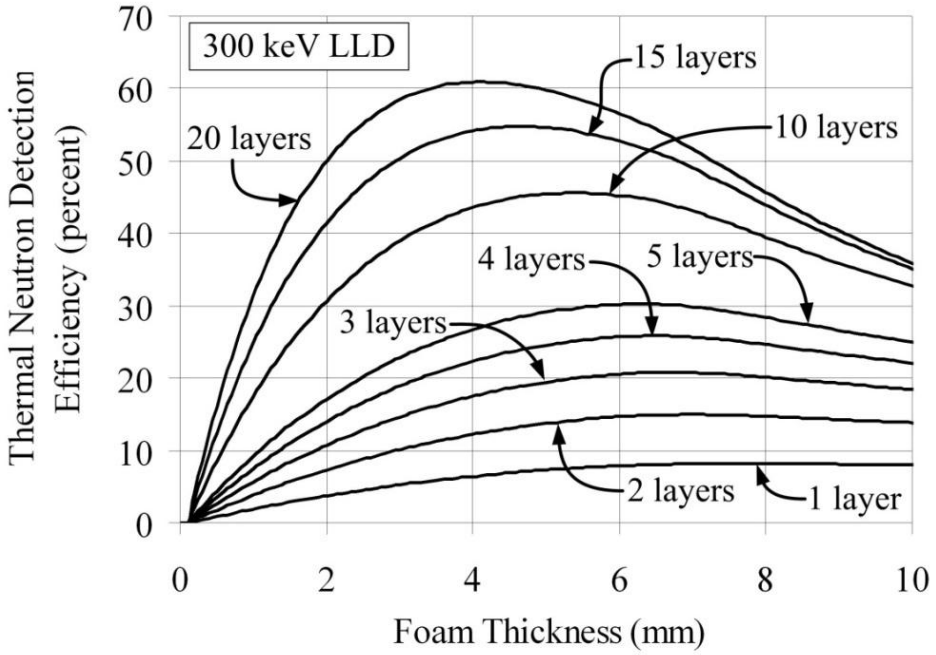

Figure 3.9: The intrinsic thermal neutron detection efficiency of 20 wt% ^{6}LiF impregnated foam obtained using the simulated reaction product ranges.

3.4 Aerogels

Aerogel is typically a silica based material composed of 99.98% air by volume and is the lightest known solid material in the world. Aerogels are typically used in superinsulating applications such as oil pipelines in cold regions or the cold and harsh environments of space.

The thermal insulating properties are demonstrated in Figure 3.10 where crayon are placed atop a 1.0 cm thick sample of silica aerogel and does not melt when heated with a blowtorch. Thermal properties have been studied in great detail and are a result of the high porosity and low density of the materials [68]. Silica aerogel density can range from 650–1.1 mg cm^{-3}, similar to those of gas densities, and pore and strut sizes are on the nanometer scale, as shown in Figure 3.11.

Aerogel samples can be formed into almost any shape, ranging from thin sheets to complex designs. Synthesis of silica aerogel is well-known, but incorporating neutron sensitive isotopes such as ^{10}B, ^{6}Li, or Gd can make fabrication complex [68]. Further, it is theoretically possible to construct aerogels completely from ^{10}B or Gd, which would result in at least a higher thermal neutron absorber material. Forming any neutron sensitive material into a thin sheet would allow a MWPC to be constructed in the same manner as the Li foil and impregnated foam detectors.

Figure 3.10: A 1.0 cm thick sheet of aerogel is the only item separating crayons and the flame of a blow torch [68].

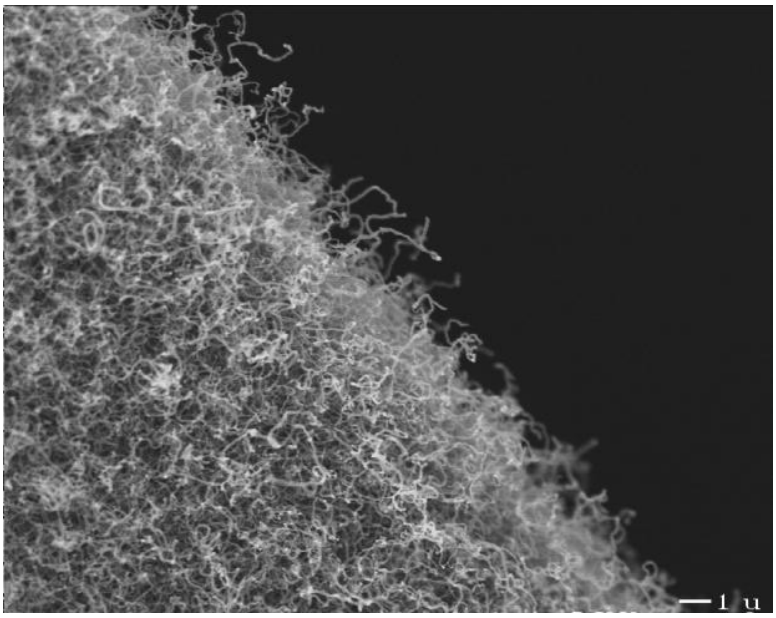

Figure 3.11: A TEM image of graphene aerogel with a 1.0 µm scale in the lower right corner of the image [68].

The low density and high porosity of the aerogel allows the material to have the same advantages and disadvantages as impregnated foam materials. Identical difficulties of determining the reaction product ranges and neutron absorption properties in the foam also apply to the aerogel materials. However, the reaction products ranges in aerogel obtained using the envelope densities are shown in Table 1. As a result of the reaction product and neutron streaming effects, it is difficult to determine intrinsic thermal neutron detection efficiency, which was therefore not calculated. Another factor affecting the intrinsic detection efficiency is the isotope included in the aerogel material. Theoretically, a pure ^{10}B sample is possible to synthesize and would have higher neutron detection efficiency than a borosilicate aerogel sample with less than 1.0% B content. Other possible neutron sensitive aerogel materials include boron carbide, pure gadolinium, silica samples with B, Li, or a combination of both. The densities of these aerogels typically range from 10–70 mg cm^{-3}. These densities can be used to estimate fractional neutron absorption probabilities, and is shown in Figure 3.12 for elemental B aerogel of two different densities. High neutron absorption should be possible with most aerogel samples containing neutron sensitive isotopes. However, the difficulty now becomes fabricating detectors with thicknesses less than the summed reaction product ranges. High neutron absorption is a good indicator that aerogel could be fabricated into a good thermal-neutron detector. However,

neutron detection efficiency is dependent on reaction product ranges and further research needs to be completed to determine reaction product ranges in aerogel. Additionally, similar to impregnated foam, it is also critical to determine if free charge carriers can pass through the aerogel samples. The high-porosity and low-density nature of aerogels may allow electrons, or a fraction of electrons, to pass through the aerogel material. This transmission is dependent upon the electric field strength and thickness of the aerogel sample, but would ultimately increase the neutron detection efficiency compared to a device that would not allow electron transmission.

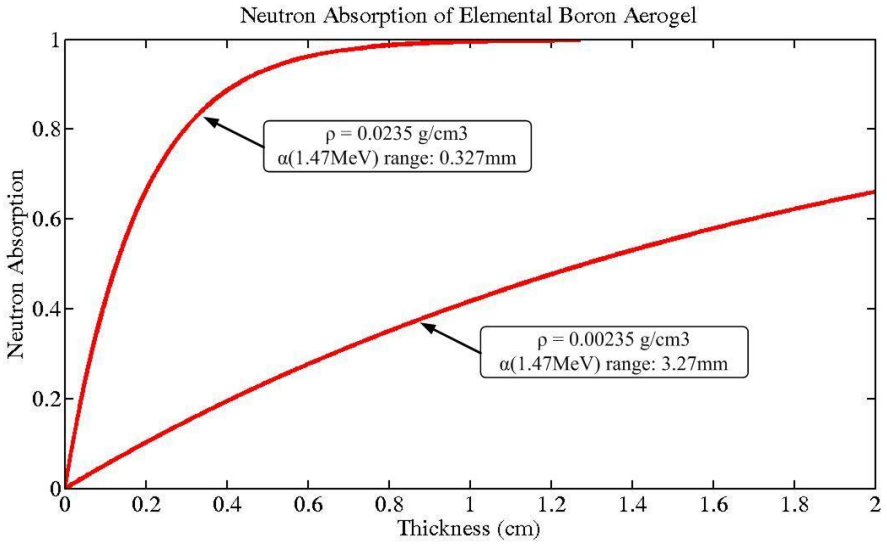

Figure 3.12: The fractional neutron absorption of elemental B aerogel with two different aerogel densities.

CHAPTER 4

Preliminary Embodiments: Theory, Experimentation, & Neutron Sensitivity

"If your experiment needs statistics, you ought to have done a better experiment."

-Ernest Rutherford

The development of aerogel, impregnated foam, and foil radiation detectors was the result of several experiments in the S.M.A.R.T. Laboratory. The ultimate goal was to create a device that could replace ^{3}He neutron detectors, which required accomplishing three main factors: high neutron detection efficiency, large area, and good gamma-ray discrimination. The research was inspired by the idea of increasing the cathode surface area so as to increase the amount of neutron sensitive coating material. In other words, the goal was to construct a proportional counter with a large surface area coated with ^{10}B or LiF, thereby, yielding higher neutron detection efficiency than ^{3}He detectors. The cathode was designed with a variety of different shaped fins pointing inward towards the anode wire. The added cathode material increased the surface area, but only one reaction product was measured per neutron absorption. However, it was realized that the neutron detection efficiency would be increased dramatically if the cathode fins were thin enough to allow more than one reaction product to escape the absorber material. After several preliminary experiments, three materials were chosen for further experimentation. The first material investigated was the ultra-low density aerogels. These aerogels should have reaction product mean free paths that are longer than found in typical solid-form neutron absorbers. The second material investigated was impregnated foam, which was an inexpensive alternative to aerogels. These foam materials can be easily fabricated for rapid experimentation. The use of impregnated foam resulted in the development of a new type of detector rather than a

backup for aerogel based neutron detectors. The last material investigated, Li foil, was a product found on a website while searching for alternative Li based compounds for foam impregnation. After completing simulations to determine reaction product ranges, it was discovered that the available Li foil thicknesses were less than the summed reaction product ranges. Thus, Li foil met the material requirements for the alternative neutron-detector research. All three of these devices emphasize measuring both reaction products simultaneously from a solid-form neutron absorber, a concept which is a first of its kind. The following chapter details the experiments that led to the decision regarding the final three material candidates for the MWPC's.

4.1 Axial Fins

In typical ^{10}B-lined proportional counters, only the inner wall of the cathode is coated with neutron absorbing material. One method to increase the neutron detection efficiency of these coated gas-filled devices is to increase the surface area of the cathode wall. Increasing the surface area was previously accomplished by using baffled, or waveform, cathode walls, a design which slightly increased the cathode surface area. Another previous method explored used alternating spacers and washers stacked longitudinally in a coaxial gas-filled device [69, 70], thereby, significantly increasing the cathode surface area as compared to sinusoidal cathode designs. However, both designs suffer from non-uniform electric fields and regions where the reaction product ranges are restricted. Consequently, smaller signals are more frequent and may be excluded if the LLD is set too high.

A ^{3}He gas-filled neutron detector that failed to hold the ^{3}He gas was obtained from Reuter-Stokes and used to develop the first Kansas State University (KSU) finned gas tube neutron detector. In order to confirm the device would function properly, two sets of two Al plates (2 cm x 5 cm) were coated with LiF, one set coated with 50 μm and the other with 0.05 μm. The plates were positioned inside of the coaxial tube resting on the cathode wall and the detector was positioned in the neutron beam at the KSU TRIGA Mark II nuclear reactor. The pulse-height spectra obtained with the LiF coated plates are shown in Figure 4.1, which confirmed the tube was functioning properly. Next, vertical Al fins with double-sided sticky tape on both sides were coated with LiF and positioned longitudinally in the detector cavity with the fins pointing

towards the anode wire. These fins increased the cathode surface area but only one reaction product was measurable per neutron absorption. However, it was desired to measure both reaction products, thus, 16 μm thick double-sided sticky tape was used as the longitudinal fin. The tape was supported at each end using plastic rods connected to an aluminum baseplate. The LiF was coated on one side of the tape, and the goal was to have the total thickness (LiF + tape) be less than the summed ^{6}Li reaction product range. The LiF coating was not controlled in this experiment due to the fragile nature of the tape fins, thus the thickness was unknown. The neutron response pulse-height spectrum obtained from the longitudinal fins is shown in Figure 4.2.

Radiation measurements with thin and thick coatings of LiF on Al substrates demonstrated expected results of these neutron absorber materials. There are two peaks in pulse-height spectra obtained with the thin LiF coating, as shown in Figure 4.1. The peak at the higher channel is a result of the triton reaction product entering the gas volume and the peak at the lower channel number is from the alpha particle. Because the reaction products are emitted in opposite directions, only one reaction product will be measured per neutron absorption. Further, peaks are observed versus a typical ‘wall-effect’ pulse-height spectrum because there is minimal reaction product self-absorption occurring in the thin LiF coating before the reaction products enter the gas region. In the thick coating, there is significant self-absorption occurring in the LiF coating, thereby, causing various amounts of energy deposited in the gas volume. Consequently, a continuum appears in the pulse-height spectrum rather than peaks. Therefore, there are no easily identifiable features in the pulse-height spectra. Also, no identifiable features were obvious in the pulse-height spectrum obtained from the longitudinally coated fins. Thus, the conclusion was made that the LiF thickness was too thick to allow reaction products to escape both sides of the fin simultaneously. Additionally, the distance between adjacent fins was narrow and did not allow for significant energy deposition from the reaction products before they collided with the cathode wall or adjacent fin. However, these coated fin experiments led to the idea of obtaining a design or material that would allow reaction products to escape both sides of an absorber material while maintaining structural rigidity.

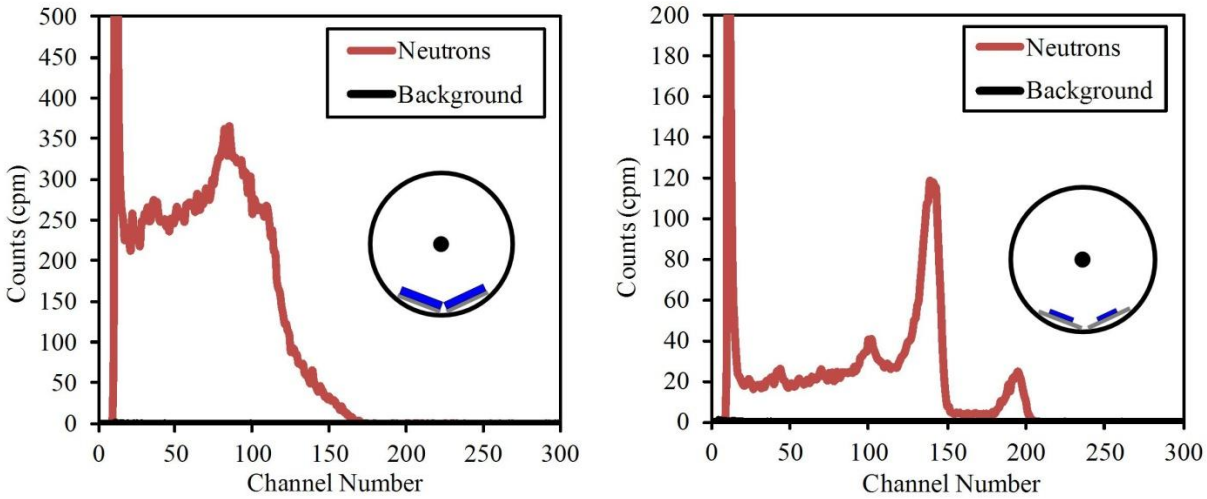

Figure 4.1: Neutron response pulse-height spectra from 50 µm (left) and 0.05 µm (right) thick LiF coated Al plates positioned orthogonal to the center anode wire. The thinner coating has less self-absorption and, consequently, the energy peaks are easily identified.

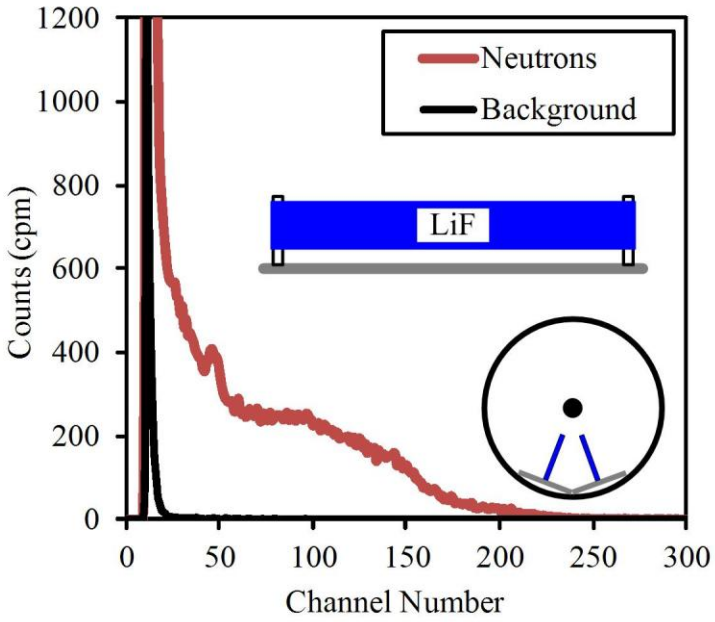

Figure 4.2: Neutron response pulse-height spectra obtained using 16 µm thick sticky tape coated with LiF. The LiF coating was not controlled and presumed to be too thick to allow reaction products to escape simultaneously from both sides of the fin.

4.2 Boron Nitride Coated Cheesecloth

After conducting the LiF coated fin experiments, the research goal was to find additional structures that could be inserted in the gas volume that would increase surface areas for neutron absorption. Cheesecloth, a loosely woven cotton based material, was the next material investigated as a neutron absorber medium because, compared to solid metal sheets, the large voids between the cotton strings of the cloth created a higher surface area to coat with neutron absorbing material. Additionally, a suspended cloth would allow reaction products ejected in both directions to be measured, rather than measuring only one reaction products emitted from only one face of the absorber coating. The voids in the cheesecloth were approximately 3 x 3 mm or smaller, but large enough to allow reaction products to escape with trajectories in the plane of the cheesecloth and still deposit at least a fraction of their energy. The cheesecloth sample was cut into a 15 x 15 cm square and placed in a rigid Al frame. The cloth was sprayed thoroughly with BN aerosol from ZYP Coatings, LLC (intended as a high temperature lubricant) and the frame was placed between two anode wires. P-10 gas was allowed to continuously flow through the detector volume enclosed by an Al case that also serves as the cathode. The box was purged with the P-10 gas for 20 minutes and placed in the diffracted thermal neutron beam at the KSU TRIGA Mark II nuclear reactor and a neutron response pulse-height spectrum was obtained. Next, a Cd foil sheet was positioned between the beam and detector to remove essentially all incident neutrons, and another pulse-height spectrum was collected. Lastly, a background pulse-height spectrum was obtained and all spectra were plotted together, as shown in Figure 4.3, and shows the device was sensitive to neutrons. However, no identifiable spectral features were present in the pulse-height spectrum and a large portion of the counts occurred in lower channels where signals from gamma rays and electronic noise reside. Overall, this detector led to the general concept of investigating high-porosity low-density materials for neutron detectors.

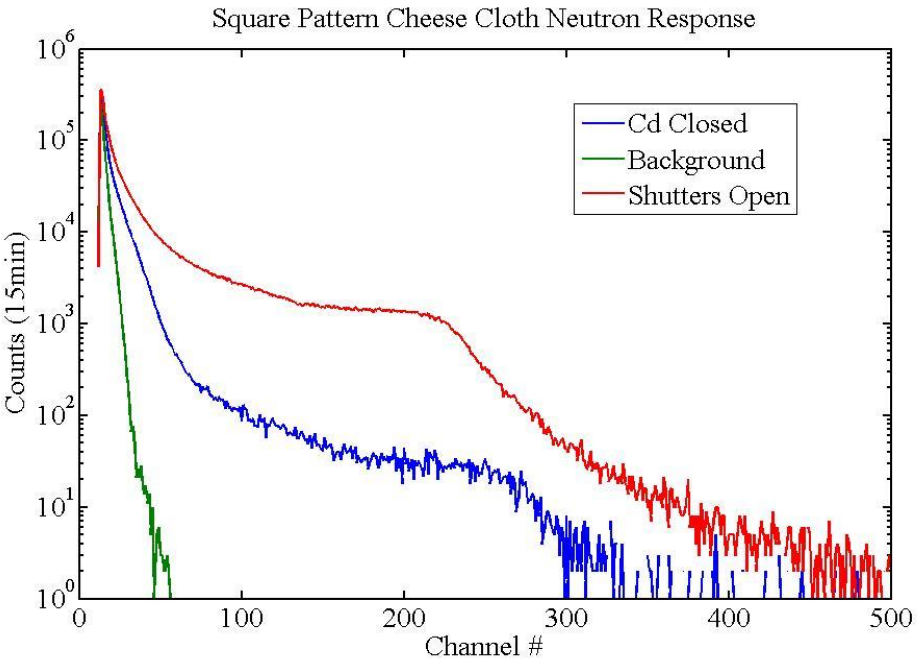

Figure 4.3: Thermal neutron pulse-height spectra obtained using BN coated cheese cloth wrapped in a square spiral frame around a single anode wire.

4.3 Honeycomb plastic

The speed and luxury boat industry uses short plastic tubes, either 0.25 inches or 0.5 inches long and 0.25 inches in diameter, glued together to form a sheet of corrugated plastic similar to a sheet of honeycomb plastic, as shown in Figure 4.4. These sheets of honeycomb plastic were cut to dimensions that when rolled into a cylinder they fit inside the perimeter of a 2.0 inch diameter Al tube. This plastic insert created a plethora of plastic tubes pointing towards the anode wire and contained the largest cathode surface area of all the finned cathode permutations investigated.

Before inserting the honeycomb into the Al tube, BN aerosol spray from ZYP coatings was used to thoroughly coat each wall. Particles emitted from the BN aerosol were examined under a scanning electron microscope (SEM) and determined to range in diameter from 1–25 μm thick. However, in order to coat the entire surface, several manual passes with the aerosol canister had to be completed. Thus, the coating thickness could be 100 μm thick in some locations. The thick

BN coating resulted in a large percentage of reaction products being self-absorbed in the coating layer. Further, only one reaction product can be measured per neutron absorption because the coating thickness is much greater than the range of the longest range reaction product, the alpha particle, which is 4.1 μm in BN (E_α = 1.47 MeV). The neutron response pulse-height spectrum of the BN-coated honeycomb is shown in Figure 4.6. Two additional measurements were completed: one measurement with a Cd foil sheet acting as a neutron shutter, and the other measurement was background measurement. From the pulse-height spectra in Figure 4.6, there is obvious neutron sensitivity, which was reduced when the Cd foil was positioned in the thermal neutron beam. However, the pulse-height spectrum did have a wall-effect feature, which is consistent with other ^{10}B-coated gas-filled detectors. Because there was low ^{10}B content in the coating material and the coating thickness was not controlled, the intrinsic thermal-neutron detection efficiency was not measured. Further, inaccuracies in thermal neutron measurements may arise because the plastic walls of the honeycomb would cause some incident neutrons to scatter either into neutron absorbing material or out of the detector. However, the increased surface area would dramatically increase the thermal neutron detection efficiency compared to typical ^{10}B-lined proportional counters. The coated surface area was seven times greater with the honeycomb compared to typical ^{10}B-lined counters. The narrow diameters of the plastic tubes comprising the plastic honeycomb restrict the reaction product ranges and energy deposition. Consequently, small pulses were measured and some may have been lower than the LLD setting. However, these diameters can be increased to allow for greater energy deposition. Further, the lengths of the tubes can be increased, which would increase the surface area of the coating material and also increase the neutron detection efficiency.

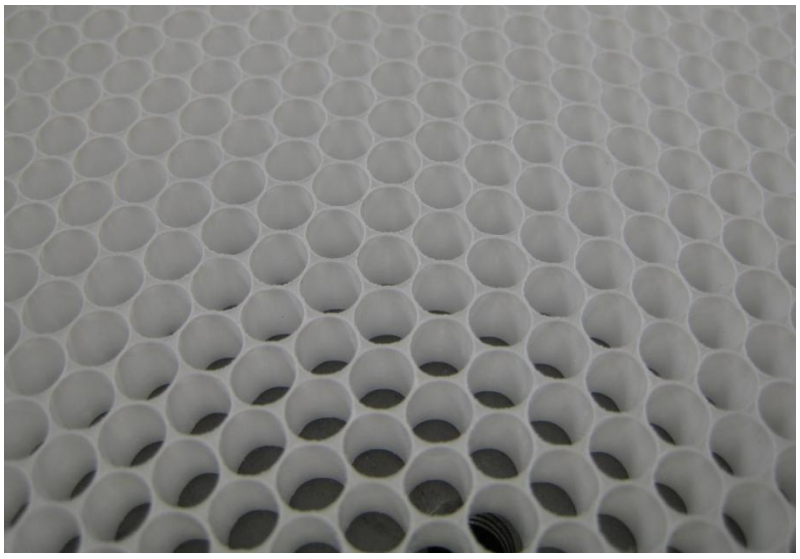

Figure 4.4: Plastic tubes are cut into 0.25″ or 0.5″ lengths and glued together to form a sheet of corrugated plastic similar to a honeycomb. BN aerosol was sprayed on the honeycomb to create a high surface area coated neutron detector.

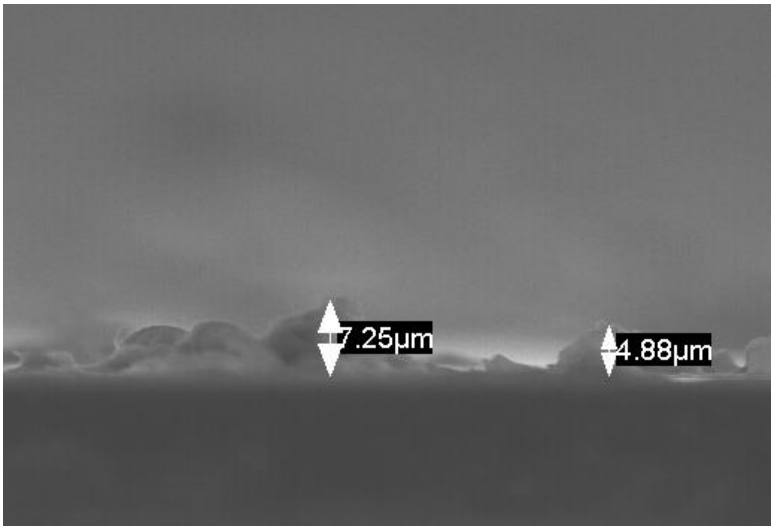

Figure 4.5: SEM image of BN aerosol sprayed onto a silicon wafer. The above coating was a single manual swipe of the aerosol canister and a thinner coating location compared to the rest of the coating. Particles or coating thicknesses were as large as 25 µm.

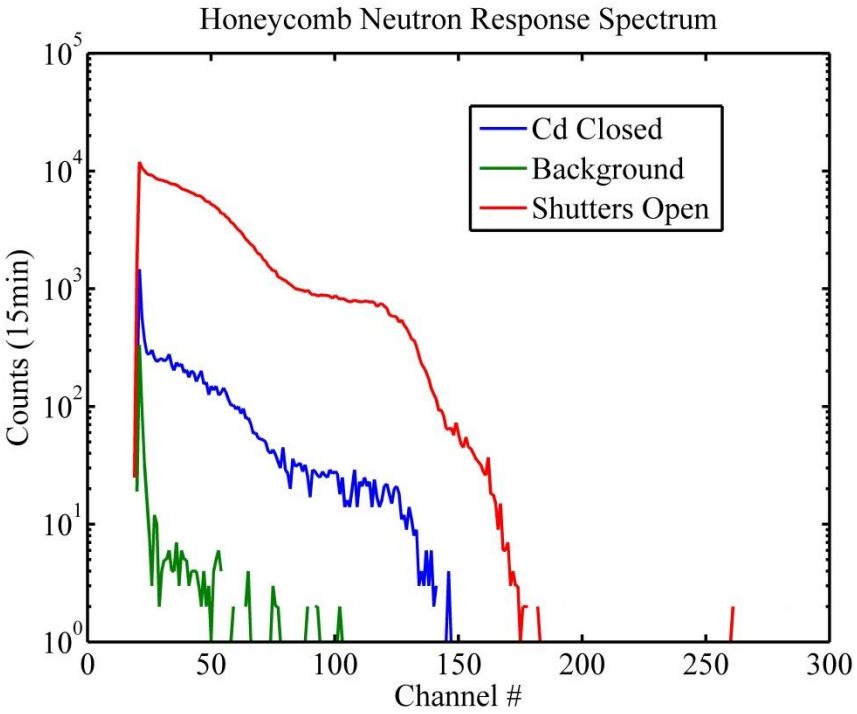

Figure 4.6: The thermal neutron response pulse-height spectra from the BN-coated plastic honeycomb finned neutron detector.

4.4 BN coated carbon foam

ERG Aerospace Corporation fabricates carbon foam and other ceramic and metal foams for various uses in industry. Carbon foams, similar to polyurethane foam, is comprised of struts approximately 1 mm in diameter and pore sizes ranging between 2-5 mm in diameter. The C foam can be coated with neutron sensitive materials and positioned into a MWPC similar to the Li foil and foam detectors. Shown in Figure 4.7 is a picture of carbon foam with no neutron absorber coating material. A cylindrical tube of C foam, approximately 1 inch diameter with a wall thickness of 0.25 inch, was coated with BN aerosol spray and inserted into a 2 inch diameter Al tube. A thin anode wire was positioned down the center of the C foam tube and the neutron response pulse-height spectrum was collected and is shown in Figure 4.8. The pulse-height spectrum shows the detector was sensitive to neutrons, but does not have any distinctive spectral features. One possible reason for the absence of identifiable spectral features was the thickness of the BN material, which could be thick enough to cause complete self-absorption of the

reaction products. Thus, the same reaction product self-absorption that occurs with typical ^{10}B coated proportional counters also occurs with the BN coated C foam, which typically results in the ‘wall-effect’ pulse-height spectrum. Additionally, no experiments were performed to determine if free electrons deep in a C foam medium can be extracted, or if electrons can pass through the C foam. Collecting as much ionization as possible from the bulk of the C foam, or from electrons passing through the foam, would increase the neutron detection efficiency. Lastly, the variation in pore sizes in conjunction with the isotropic emission of the reaction products creates a continuum of energies with no distinct average energy deposition. Thus, there is a large range of reaction product energies being deposited in the gas volume, which may be the cause of the featureless pulse-height spectrum. ERG Products fabricates boron carbide foam, which may be a better option than the method presented in this research. However, only one reaction product will be measured per neutron absorption with this technology. Additionally, other research has been completed in parallel with these experiments, which also shows similar neutron sensitivity results [71].

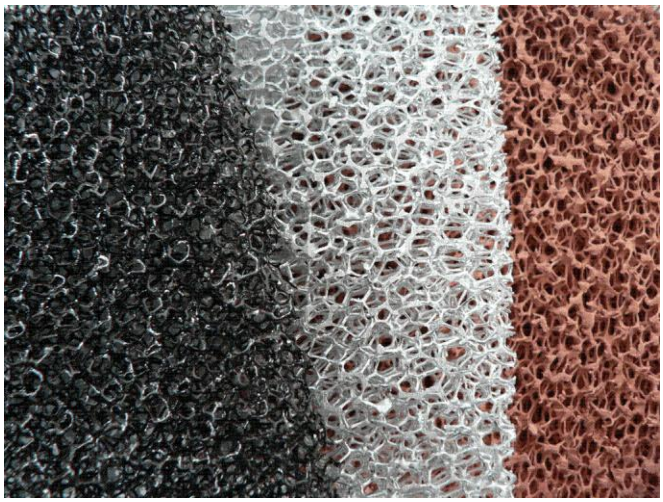

Figure 4.7: From left to right is carbon, alumina, and copper foam with pore sizes ranging from 1–10 mm [67].

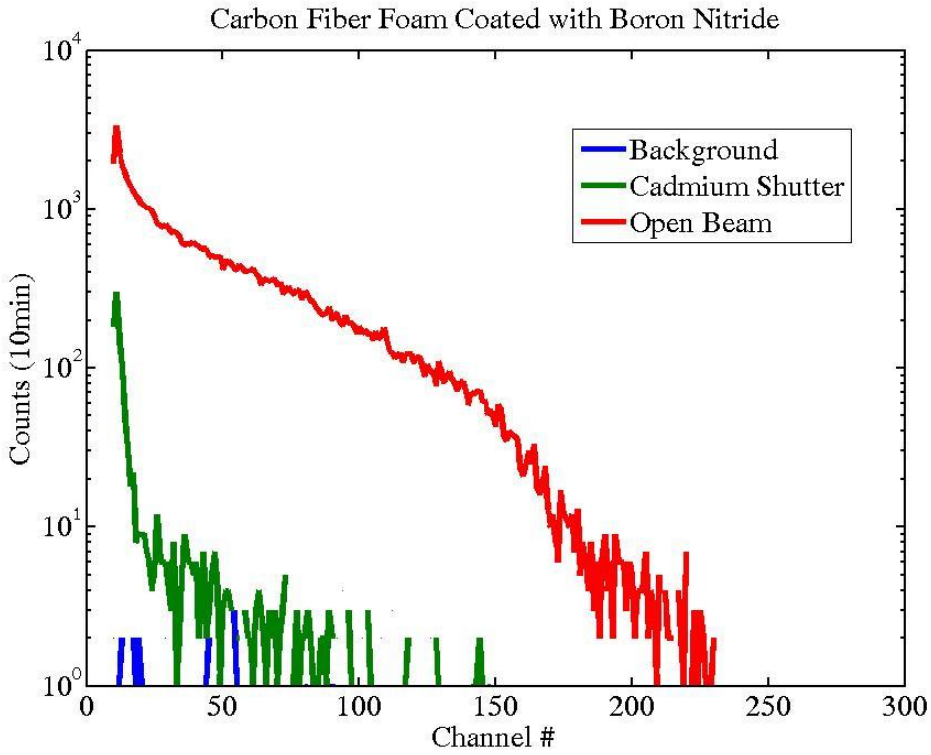

Figure 4.8: The thermal neutron response pulse-height spectra from BN-coated carbon foam. There are no distinctive features, but sensitivity to neutrons was observed.

4.5 LiF Coated Mylar Foil

Shown in Figure 4.9 is a cross-sectional schematic of LiF coated aluminized biaxially-oriented polyethylene terephthalate (BoPET), or more commonly known as aluminized Mylar. The thicknesses reported in Figure 4.9 are less than the summed range (39.65 μm) of the reaction products from the $^{6}Li(n,t)^{4}He$ reaction. (The ranges of the triton and alpha particle in pure ^{6}LiF are 33.6 μm and 6.05 μm, respectively [61].) Thus, reaction products can escape both sides of a LiF coated Mylar sheet simultaneously. However, the Mylar can absorb a portion of the reaction product energy before it reaches the proportional gas volume. The minimum energy loss of the alpha particle and triton reaction products when they traverse the Mylar before entering the gas volume is 440 keV and 70 keV, respectively [61]. The differences in energy loss are a result of the amount energy deposited per unit length of the alpha particle being greater than that of the

triton [45,62,69]. It should also be noted that the Al coating is thin (< 0.05 μm) enough to be considered negligible in the cases described here.

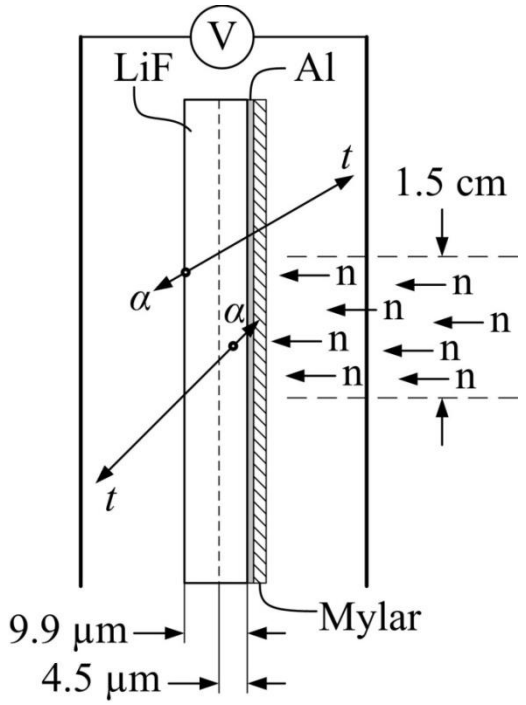

Figure 4.9: A cross-sectional schematic of the LiF coated Mylar showing two different thicknesses of LiF coating. The reaction products are able to escape both sides of the absorber sheet simultaneously and be measured in separate gas compartments concurrently.

There are three possible reaction product combination paths that can result in a measurable event. The first occurs when both reaction products escape the absorber/Mylar and are measured simultaneously in the gas region, the second is when only the triton escapes the absorber/Mylar sheet, and the last when only the alpha particle enter the gas region. In the latter two occurrences, the second reaction product is not measured and absorbed by the LiF and/or Mylar, thereby, not contributing to the signal generation. For the LiF and Mylar total thicknesses investigated here, the signal measured is most likely generated by measuring only the triton. The probability the signal is generated by the measuring both reaction products simultaneously is less than measuring only the triton reaction product, but both occurrences have a higher probability than measuring only the alpha particle reaction product. There is also a probability that neither reaction product escapes and no signal is generated, a probability that increases with absorber

thickness. After reaction products enter the gas medium, they deposit their energy and generate free electron-ion pairs through Coulombic interactions. The electrons travel to the central anode wire under the applied electric-field where the device operates as a conventional proportional counter by creating a Townsend avalanche, while the associated ions travel towards the cathode wall.

The intrinsic thermal-neutron detection efficiency was calculated for various layers of pure ^{6}LiF foils as a function of the foil thickness, as shown in Figure 4.10. The method used to obtain these values is described in greater detail elsewhere [45], and uses an energy threshold, or lower level discriminator (LLD), setting of 300 keV while accounting for the attenuation of neutrons through successive foils. The calculations were performed for ^{6}LiF foils with no substrate because these values are the absolute highest detection efficiencies possible with LiF sheets completely independent of the substrate material and thickness. Substrates as thin as 1.0 nm may be possible, but as the substrate thickness decreases, the intrinsic thermal-neutron detection efficiency will approach the values shown in Figure 4.10. Additionally, from Figure 4.10, for a specific number of LiF foil layers, there is an ideal LiF thickness that maximizes neutron detection efficiency. The ideal thickness for 15 ^{6}LiF foils ranges between 9-10 μm and has a neutron detection efficiency of 57%, while a five layer device has an efficiency of 32% with an optimized coating thickness of 14 μm. The added 2.0 μm thick Mylar will only decrease the overall neutron detection efficiency and minimally change the ideal thickness for a specific number of layers. The Mylar will increase self-absorption of the reaction products and reduce their escape probabilities because of the added thickness. Further, as the substrate material thickness increases, the ideal coating thickness and detection efficiency both decrease.

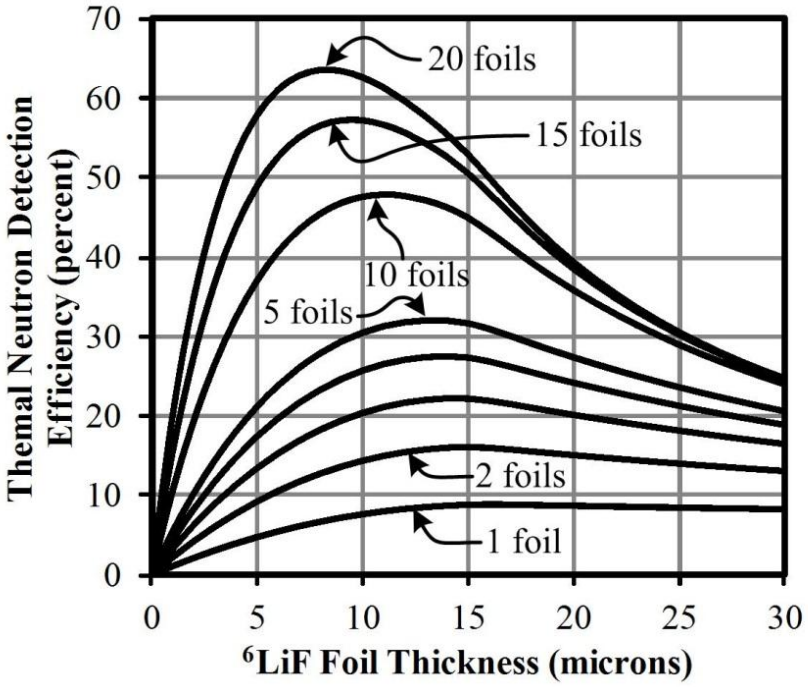

Figure 4.10: The theoretical intrinsic thermal-neutron detection efficiency of ^{6}LiF foils for various layers of absorber sheets as a function of foil thickness.

The theoretical thermal-neutron response pulse-height spectra obtained for LiF coating thicknesses of 0.1 μm, 4.5 μm, 9.9 μm, and 14.0 μm on 2 μm thick Mylar sheet were obtained using MCNP6 and are shown in Figure 4.11. In the simulation, a uniformly distributed 1.5 cm diameter collimated thermal-neutron beam was centered on a 15-cm x 15-cm ^{6}LiF coated aluminized Mylar sheet centered within an Al test chamber 15 cm x 15 cm x 15 cm and filled with P-10 proportional gas (90% Ar, 10% CH_4). Centering the beam allows the entire energy of the triton to be absorbed in the gas without the reaction product escaping the boundary of the simulation. The range of the triton in 1.0 atm of P-10 gas is 7.26 cm [61]. The beam dimensions and energy were chosen to resemble the diffracted thermal-neutron beam at the KSU TRIGA Mark II nuclear reactor. Hence, a direct comparison can be made between the experimental LiF coated Mylar pulse-height spectra and the simulated data. An additional 0.1-μm thick ^{6}LiF coating pulse-height spectrum is included in Figure 4.11 to demonstrate the simulation was functioning properly. The largest peak occurs slightly below the reaction Q-value (4.78 MeV) at 4.71 MeV, which occurs when the triton traverses the Mylar before entering the P-10 gas and the alpha particle enters directly into the gas from a surface absorption. Additionally, there are peaks

at each of the reaction product energies, which occur when only one reaction product is measured and the other is absorbed in the Mylar. Obviously, the alpha particle being absorbed to the Mylar occurs more frequently than absorption of the triton, thus the differences in peak heights in the spectrum. There is an additional feature at 4.34 MeV, 440 keV below the Q-value, which is the result of the triton immediately entering the P-10 gas region from a surface absorption and the alpha particle traversing the Mylar before entering the gas region.

The theoretical pulse-height spectra with thicker ^{6}LiF coatings, shown in Figure 4.11, reveal a sudden drop in counts at 2.73 MeV, the energy of the triton. Any pulses that occur above this value are from both reaction products escaping the absorber simultaneously. These pulses decrease in frequency with increasing LiF coating thickness. Additionally, the width of the main feature in the pulse-height spectra, positioned between 1.5 MeV and 2.73 MeV, increases with increasing LiF coating thickness. The thicker coatings cause more self-absorption of the reaction products to occur before they escape the surface of the absorber assembly. However, each coating thickness simulated has a large valley occurring between the lowest energy region, where gamma-rays and electronic noise might appear, and the main feature of the pulse-height spectra. This valley is an important feature because it allows the LLD to be set relatively high to eliminate most gamma-ray induced pulses with minimal sacrifice of neutron generated events. Thus, the intrinsic thermal-neutron detection efficiency should remain relatively constant over a wide range of LLD settings compared to a device with a prominent wall-effect in the pulse-height spectrum.

The absorber sheets were constructed by stretching aluminized Mylar, 2.0 μm thick, across 15-cm x 15-cm Al frames and taping material to the edges using Cu tape. The open area of the frames was 12.7 cm x 12.7 cm and the Mylar was stretched to a mirror smooth finish. Natural LiF was deposited on the aluminized side of the Mylar using an electron-beam evaporation system. The LiF adhered better to the aluminized side rather than the Mylar. Three frames were constructed and three rounds of the evaporation process were completed. Each round deposited between 4–5 μm of LiF. At the end of each evaporation round, one of the frames was removed. Thus, the final thicknesses of the LiF coatings were 4.5 μm, 9.9 μm, and 14.0 μm. The thicknesses were obtained from the electron-beam evaporation system film measurement feature. At each thickness, the LiF coated Mylar sheets were centered in an Al test chamber approximately 15 cm x 15 cm x 15 cm. The test chamber was purged with P-10 gas and

positioned at the KSU TRIGA Mark II nuclear reactor diffracted thermal-neutron beam. The reactor power was increased to 100 kW and a 1.5 cm beam irradiated the center of the sheet. Two 10 minute pulse-height spectra were collected: one with a Cd-shutter to block all incident thermal neutrons and another without the Cd-shutter.

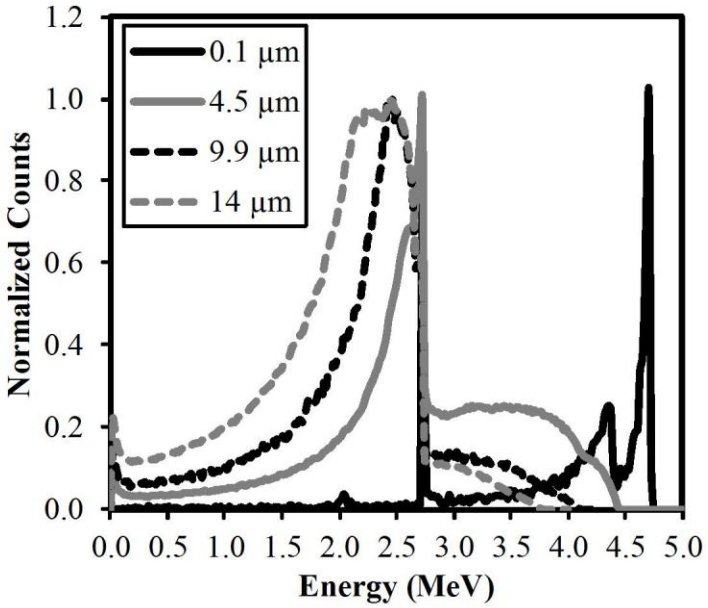

Figure 4.11: The simulated thermal-neutron response pulse-height spectra of 0.1, 4.5, 9.9, and 14.0 µm thick LiF coatings on 2-µm aluminized Mylar obtained using MCNP6.

The thermal-neutron response pulse-height spectra obtained for the 4.5, 9.9, and 14.0 µm thick LiF coated aluminized Mylar sheets are shown in Figure 4.12, Figure 4.13, and Figure 4.14, respectively. Additionally, the theoretical pulse-height spectra of the absorber sheets obtained with MCNP6 are included in these figures. Each pulse-height spectra had the expected valley as described previously, but the electronic noise is apparent in the experimentally obtained spectra, as expected. The percentage of total counts with energy greater than 2.73 MeV decreases with increasing LiF coating thickness as predicted by the simulations. Only natural LiF was investigated and thus no intrinsic thermal-neutron detection efficiency measurements or calculations were completed.

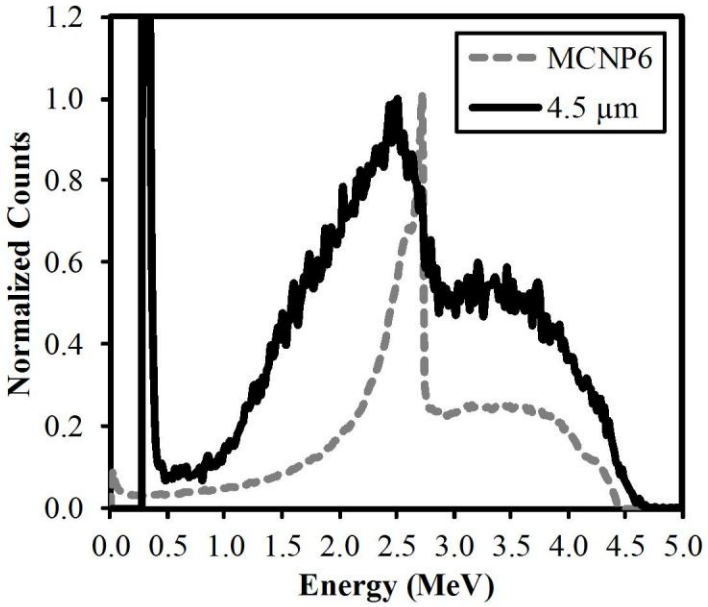

Figure 4.12: The experimental and simulated (MCNP6) thermal-neutron response pulse-height spectra of 4.5 µm thick LiF coated aluminized Mylar.

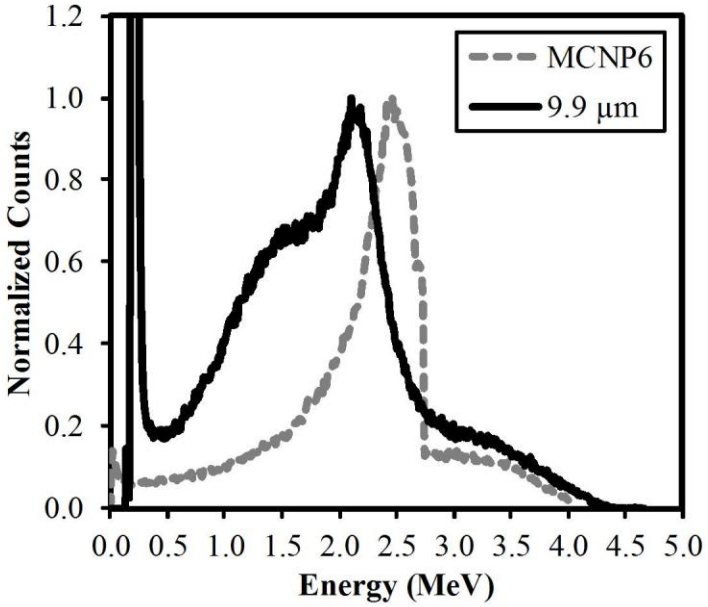

Figure 4.13: The experimental and simulated (MCNP6) thermal-neutron response pulse-height spectra of 9.9 µm thick LiF coated aluminized Mylar.

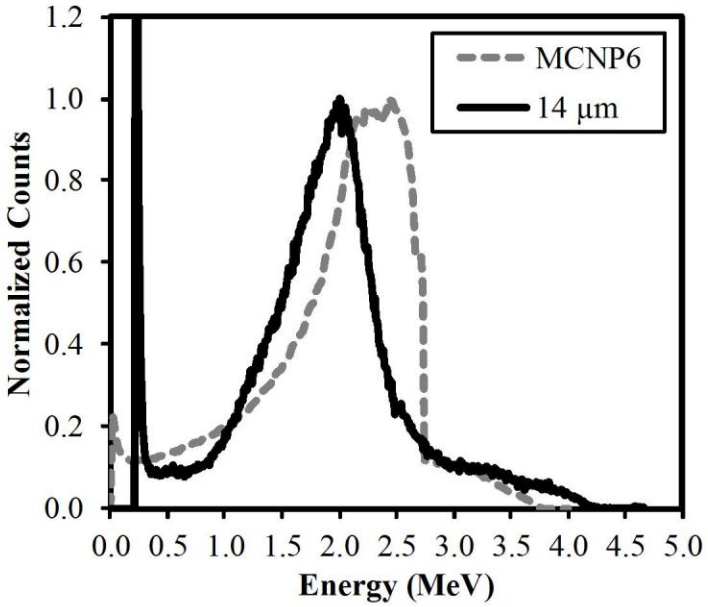

Figure 4.14: The experimental and simulated (MCNP6) thermal-neutron response pulse-height spectra of 14.0 μm thick LiF coated aluminized Mylar.

The spectral shapes of the different experimental pulse-height spectra do not exactly match the simulated spectra although the shapes are in general agreement. There are three main reasons for the discrepancies. First, and most likely, is the delamination of the LiF from the Mylar, which is discussed in greater detail in the following paragraph. Second, the MCNP6 model does not contain any code to simulate the resolution of the gas-filled detector. Thus, the sharp peaks in the simulation are not possible experimentally. Lastly, there are many neutrons scattering in the nuclear reactor bay making the collimated thermal-neutron beam not the only source of incident neutrons, although a significantly lower flux than the collimated beam. However, the pulse-height spectral shape changes in both the experiments and simulated data when using a collimated source versus an isotropic point source. Reaction products born near the cathode wall may deposit less energy in the gas volume due to the restricted ranges. These smaller pulses would shift pulse-height features to lower energies, or channel numbers, and broaden peaks as well. Consequently, sometimes a shoulder will appear on the left side of the main feature of the pulse-height spectra depending on the amount of neutron interactions originating near the cathode wall, which is prevalent in the 9.9 μm thick spectrum in Figure 4.13. The simulated

pulse-height spectra do not display this feature because a collimated source was focused on the center of the absorber slab.

The normalized counts above 2.73 MeV of the experimental spectra match the simulated spectra well for the 9.9 µm and 14.0 µm thick coatings, which was not the case for the 4.5 µm thick spectra. It is not definitively conclusive why the 4.5 µm pulse-height spectra do not agree to the same level of accuracy. Thinner coatings would result in more events above 2.73 MeV and there could be some inaccuracies and inconsistencies to the coating thickness. One possible cause for the irregularity could be parallax effects in the evaporator, but this was not investigated. Another indication of thickness variation is the delamination of sections of the LiF coating. The chances of material flaking off increased rapidly with increasing coating thickness, and were observed on all samples with coatings greater than 5.0 µm. The flaking of one of the 9.9 µm thick LiF coated Mylar is shown in Figure 4.15 in the upper right quadrant of the sheet. It was also unclear if only a fraction of the total LiF coating was detached. Further, the coated sample shown in Figure 4.15 was exposed to open air for approximately 18 months and showed no further signs of degradation.

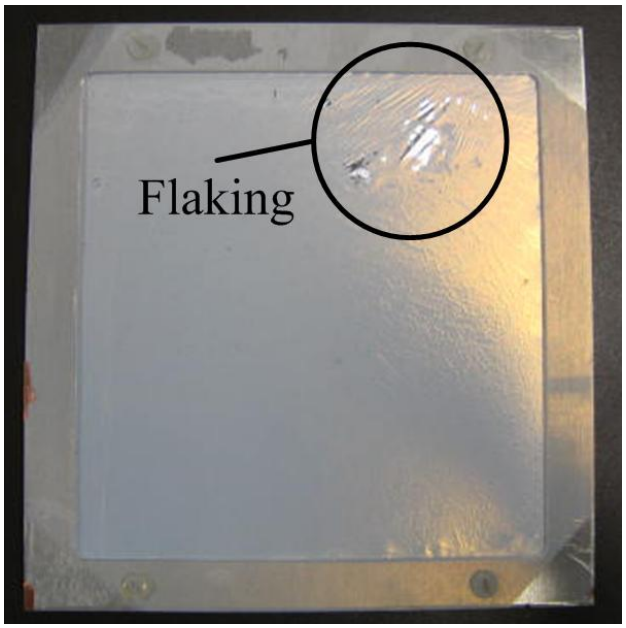

Figure 4.15: The aluminized Mylar sheet coated with 9.9 µm of LiF which shows the flaking of the LiF occurring in the top right quadrant of the pane.

The feasibility of consistently producing repeatable results with these detectors is low due to the delamination of the LiF coating at thicknesses that are less than ideal for maximizing thermal-neutron detection efficiency. LiF detachment was reduced when the Mylar material was stretched to a mirror finish, yet, any vibration to the frame also caused the LiF to delaminate. Some options to decrease the amount of flaking are to spray a coating material on top of the LiF or trap the LiF between additional Mylar. However, this coating process would only decrease the intrinsic neutron detection efficiency and possibly add more complications to the construction technique. Further, other materials could be used as a substrate including Kapton tape and Al or Cu foil, which may have better LiF adhesion.

Overall, the LiF coated Mylar MWPC can achieve intrinsic thermal neutron detection efficiencies greater than 30%, but consistently fabricating repeatable films proves difficult due to the delamination of the material. This would consequently affect the reliability and neutron detection efficiency of the devices. In future work, additional structural or adhesive materials must be used in order to reduce LiF detachment. However, the pulse-height spectra reveal a large valley, which is helpful in eliminating gamma-ray interactions without sacrificing a large percentage of neutron counts.

4.6 Boron Foils

In theory, ^{6}Li is a better isotope for neutron absorber materials in detectors than ^{10}B due to the reaction product ranges being approximately 5-15 times longer. However, ^{10}B has a higher thermal neutron absorption cross-section, which would be better in cases where measuring the reaction products were of no concern (*i.e.* shielding). Because the reaction product ranges of the $^{10}B(n,\alpha)^{7}Li$ reaction are short (< 5.0 μm) in solid materials, fabricating a suspended material with any ^{10}B material becomes difficult. For example, ^{10}B could be coated onto Mylar sheets, but the coating thickness would be less than 1.0 μm in order to optimize neutron detection efficiency for a multiple layered device. The total thickness would be comprised of nearly 1/3-2/3 of a non-reactive material. The neutron detection efficiency would be limited with this coating arrangement because of the high self-absorption of the reaction products occurring in the Mylar.

However, The Lebow Company fabricates 1.0 μm thick free standing B foils using a proprietary evaporation method.

The intrinsic thermal neutron detection efficiency of the B foils was calculated using a method described in greater detail by McGregor, et alli [45]. The calculations multiply the total neutron absorption probability by the reaction product escape probability for a specific foil thickness. The results of the theoretical calculations are shown in Figure 4.16 and show that for a specific number of B foil layers in a detector there is an ideal foil thickness that maximizes intrinsic thermal neutron detection efficiency. Requiring reaction products to deposit at least 300 keV of energy in the gas region, the path lengths of the alpha particle and Li ion reaction products in ^{10}B foil are 2.65 μm and 0.81 μm, respectively, for the 94% branch, and 3.52 μm and 1.05 μm, respectively, for the 6% branch [61]. The assumed density was 2.34 g cm^{-3} with an absorption cross-section of 3840 b, and thus the macroscopic thermal neutron absorption cross-section, Σ, is 500 cm^{-1}. From Figure 4.16, the ideal thickness of the ^{10}B foils is less than the total summed total range of the reaction products in ^{10}B, 4.97 μm (R_α = 3.28 μm, $R_{^7Li}$ = 1.69 μm) and 5.96 μm (R_α = 4.06 μm, $R_{^7Li}$ = 1.90 μm) for the 94% and 6% branches, respectively [61].[2] Consequently, both reaction products are able to escape both sides of the B foil simultaneously and be measured in the gas volume concurrently.

Three B foils, one shown in Figure 4.17, were obtained by the SMART Laboratory and positioned in a MWPC approximately 4.5 cm apart, as shown in Figure 4.18. The distance between B foils was enough space to allow the reaction products to deposit all of their energy in the gas volume. A single anode wire was positioned on both sides of each foil for a total of four anodes. The detector was purged with P-10 gas, and 800V was applied to all four anode wires. The detector was aligned in the diffracted thermal neutron beam port at the KSU TRIGA Mark II nuclear reactor for neutron sensitivity testing. Shown in Figure 4.19 is the thermal-neutron response pulse-height spectrum obtained from the B foil MWPC. Two distinct spectral features appear, the largest peak occurs from the 94% branch while the other, higher channel number (higher energy peak), is from the 6% branch. The wall-effect typically associated with ^{10}B-coated gas-filled neutron detectors is not prevalent in the pulse-height spectrum because the B foil thickness, 1.0 μm, is less than the summed reaction product range [45,61].

[2] The summed ranges do not include a minimum amount of energy deposited in the gas volume.

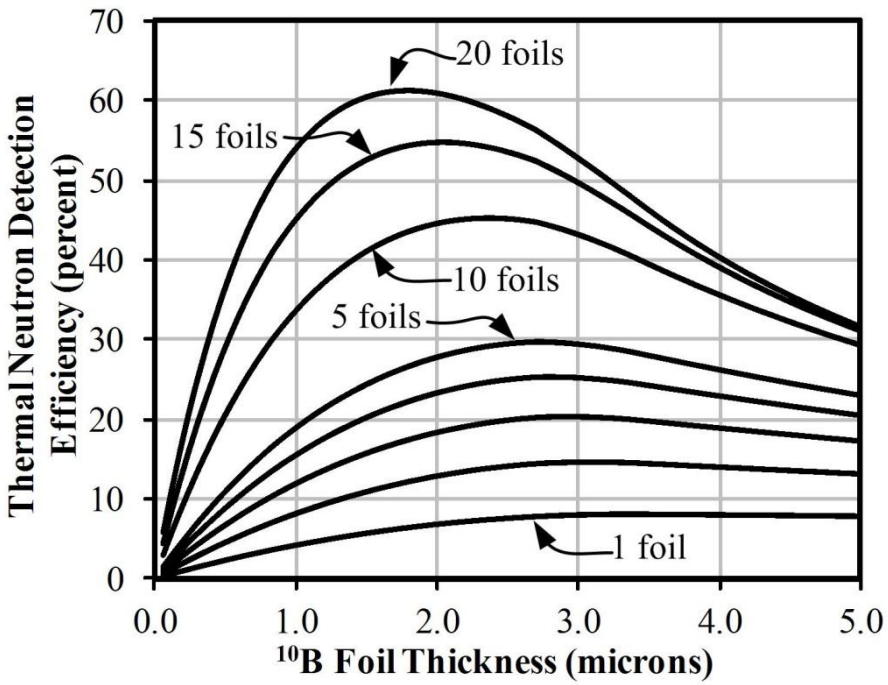

Figure 4.16: The intrinsic thermal neutron detection efficiency of the B foil MWPC as a function of B foil thickness for multiple layers of foil in the detector. The number of layers used in the device determines the foil thickness that maximizes the neutron detection efficiency.

Figure 4.17: Natural B foil on a stainless steel circular support structure. The diameter of the B foil is approximately 1.0 cm. (One square = 0.25″ x 0.25″)

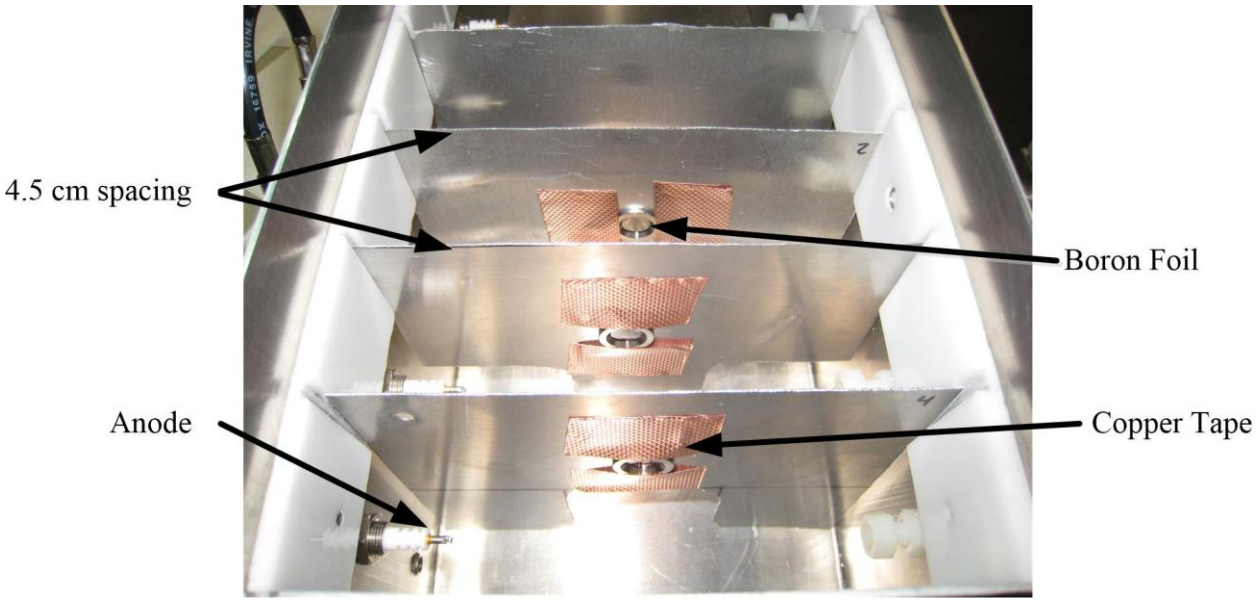

Figure 4.18: The three 1.0 μm thick B foils positioned in a MWPC containing a single anode wire on each side of the 4.5 cm spaced B foils.

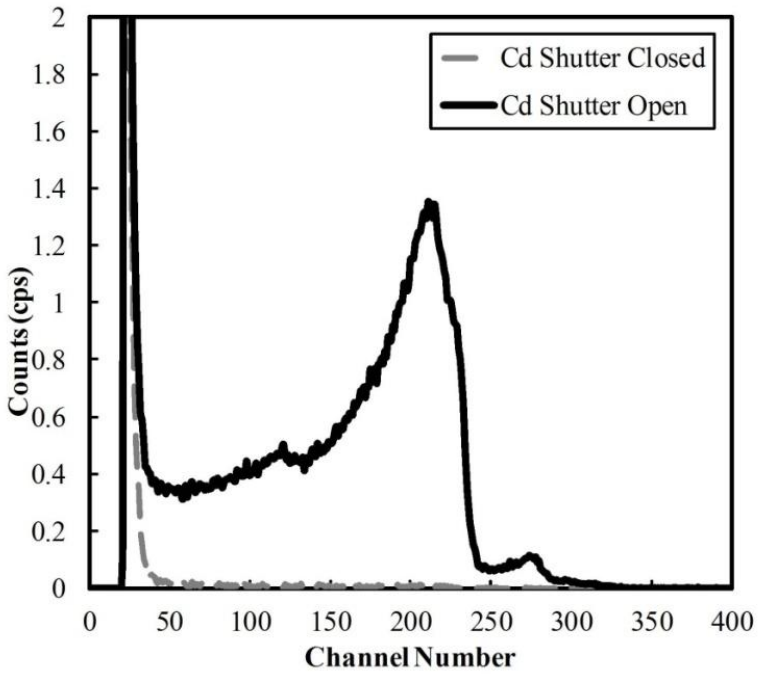

Figure 4.19: The thermal neutron response pulse-height spectra obtained from a three layer natural B foil detector. Two main features in the spectra are located at channel numbers 220 & 275, a result of the 94% and 6% branches of the neutron reaction.

The three 1.0 μm thick B foils obtained were made from natural B, and the theoretical intrinsic thermal neutron detection efficiency of the detector shown in Figure 4.18 was 2.34%, and the measured intrinsic thermal neutron detection efficiency was 2.2 ± 0.20%. The difference between the theoretical and measured intrinsic thermal neutron detection efficiency is most likely a result of the non-uniformity in B foil thickness. The Lebow Company does not report foil thickness uniformity of their delivered foils. Further, foil thicknesses is estimated around the edge of the foil samples. Additionally, as the diameter of the foils increases, the thickness at the center of the sample decreases. The 1.0 cm diameter used in the three B foils obtained by KSU is considered the maximum diameter for elemental B foil.

The B foils have a limited maximum thickness of 1.5 μm and would almost be too fragile to handle.[3] Furthermore, the B foil thickness available is less than the thickness that optimizes the intrinsic thermal neutron detection efficiency, even if a 20 layer device were assembled. Thus, the neutron detection efficiency is not optimized. However, the advantage of thinner foils is the ability to discriminate gamma-ray interactions. Gamma-ray interactions with this device would generate electronic pulses in the lower channel numbers, close to channels 25–50 in Figure 4.19. Increasing the LLD to eliminate gamma-ray pulses would only remove a small percentage of the neutron counts, opposite of what occurs with typical B coated gas-filled neutron detectors. Ultimately, these devices are not viable ^{3}He replacement detectors because of limited sizes of the foils and their fragility. Generating a detector with enough B foils to cover 100 cm^2 would become costly with no guarantee of ruggedness and have lower neutron detection efficiency than other alternative devices. Additionally, isotropically enriching the foils would add difficulty to the foil fabrication process and are not currently available.

[3] It was recommended to hold one's breath when handling the foils because they might break from the pressure of one's own breath on the face of the foil.

CHAPTER 5

MULTI-WIRE PROPORTIONAL COUNTER CONSTRUCTION AND MATERIAL FABRICATION

"A scientist in his laboratory is not a mere technician: he is also a child confronting natural phenomena that impress him as though they were fairy tales."

-Marie Curie

Described in chapter five is the assembly and design process or the MWPCs. This chapter is arranged to describe the sequential order in which the research was conducted, which includes construction of all MWPC detectors.

5.1 Proof-of-principle test chambers

The first test chamber, *Box A*, was designed to test single suspended layers of neutron absorber materials and allow reaction products escaping from both sides of the neutron absorber sheet to deposit all energy in the gas volume without colliding into the chamber wall. The dimensions of *Box A* were 17 cm x 17 cm x 17 cm, a design decision based upon the 7.25 cm range of the triton and a 1.5 cm diameter neutron beam incident on the center of the absorber slab. Thus, a triton can travel in any direction in the gas volume and deposit all of its energy. A single anode wire was centrally positioned in the two compartments on each side of the neutron absorber sheet. The anode wires were led into the box using SHV feedthroughs on the 'live' end, and for the 'dead' end the wires were positioned through holes in the top of plastic screws. A

plastic nut was used to anchor the dead end of the wire and two additional nuts sandwiched the chamber wall to control wire tension, which can be seen in Figure 5.1. The tungsten anode wires were 50 µm in diameter and soldered to the SHV feedthroughs. The anode wires were joined together externally from the chamber using a T-connector leading to a single preamplifier (Ortec 142PC) and additional pulse processing electronics. The materials tested in *Box A*, and discussed in the following chapter, include various thicknesses of Li foil, Li/Mg alloys, and ^{10}B and ^{6}Li impregnated foam.

Figure 5.1: Box A, a 17 cm x 17 cm x 17 cm Al chamber designed to test single sheets of neutron absorber materials. The test chamber included two anode wires, one on each side of the absorber sheet.

The second test chamber, *Box B*, was the same width and height as *Box A* (17 cm x 17 cm), but length was increased to allow for 10 layers of neutron absorber sheets to be added with 4.5 cm spacing between each layer and the ends of the test chamber, a total length of approximately 50.0 cm. *Box B*, shown in Figure 5.2, contains two absorber frames, one frame with Al foil across the top and bottom thirds of the frame opening, and the other contains cheesecloth taped to the Al frame. Single centrally positioned anode wires were arranged between each absorber layer and the ends of the chamber, 11 anode wires in total. (All anodes were assembled in the same manner as in *Box A*.)

Figure 5.2: Box B was fabricated from Al and is 17 cm x 17 cm x 50 cm, and designed to hold 10 layers of neutron absorber sheets positioned 4.5 cm apart.

Al frames used to support the neutron absorber materials had a 15 cm x 15 cm open region. The frames were also designed to clamp absorber sheets between two frames, or the absorber material could be taped to the Al frame with conductive Cu tape. The frames were positioned upright in *Box A* using Al tabs welded to the side of the chamber walls. In *Box B,* the frames were supported vertically with two slotted plastic sheets connected to the sides of the chamber wall, which is the white strip running inside the length of the box in Figure 5.2.

The foil used in all experiments was 5 cm wide, thus the 15 cm opening of the frames was covered using two additional 5.0 cm wide Al foil strips taped to the top and bottom thirds of the open frame. The foam, however, was cut in sheets large enough to cover the entire 15 cm x 15 cm opening. A single frame with impregnated foam and a single frame with Li/Mg alloy foil are shown in Figure 5.3. The Al strips used to fill the frame opening are also shown in Figure 5.3.

The open area of the support frame was filled with Al foil to ensure that reaction products did not enter an adjacent detector compartment. If the Al foil were not in place, the triton range is long enough in P-10 gas that it could escape the surface of one Li foil and enter an adjacent gas compartment, thereby, creating a signal larger than possible with the foil spacing.

Both *Box A* and *Box B* were used to conduct preliminary neutron measurements for proof-of-principle experiments. These simple detectors were designed to be reused many times and were restricted to minimal feasibility studies. The neutron materials tested and their results are discussed in the following chapter, including the first impregnated foam and Li foil neutron results.

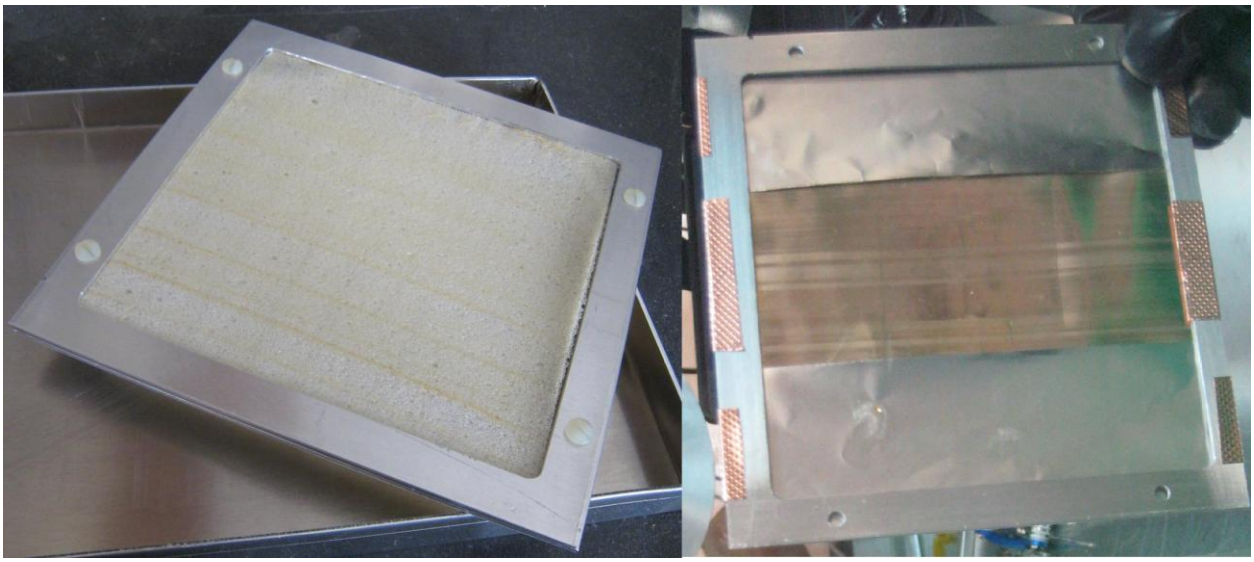

Figure 5.3: Foam (left) and Li/Mg Alloy (right) in frames used in Box A & B. The foam was clamped in place by bolting two frames together, and the foil was connected to the frame using Cu tape.

5.2 Aerogel Synthesis and Fabrication

A relationship between KSU and Aerogel Technologies, LLC was developed in 2009 in an attempt to create new types of aerogels that include neutron sensitive materials such as ^{6}Li, ^{10}B, and Gd. The formulas for synthesizing these new aerogels are based on the well-known silica aerogel formulation, but the synthesis process is proprietary and not reported here. (Basic silica aerogel fabrication is detailed on the Aerogel Technologies' website [68].) To date, disc shaped samples with natural Li and/or B were obtained with a diameter of 2.54 cm and thickness ranging from 2–7 mm. Sample content can be found in Table 2 where most samples contain more than 60% O and 25% Si, while the remaining were different ratios of B and/or Li. Three lithium borosilicate samples are shown in Figure 5.4 with Li content increasing from left to right. The Li addition causes the samples to be stronger than samples with higher B content. The lithium borosilicate aerogel samples with the highest and lowest macroscopic thermal neutron absorption cross-sections (Σ_a) reported in Table 2 were used to plot the fractional thermal neutron absorption as a function of aerogel thickness, as shown in Figure 5.5. Additionally, Σ_a values were calculated using enriched ^{6}Li and ^{10}B, thereby, demonstrating expected minimum and maximum neutron absorption of the aerogel samples provided. The fractional thermal neutron absorption is typically a good indicator of the neutron detection efficiency. Thus, depending on reaction product ranges, the potential exists for detectors incorporating these materials to have relatively high thermal neutron detection efficiency.

Figure 5.4: Aerogel samples containing B and Li. The aerogel material becomes more stable with increasing Li content. The Li content increases in the three samples from left to right.

Table 2: Various lithium borosilicate aerogel samples estimated elemental composition, density, and macroscopic thermal neutron absorption cross-section.

SAMPLE I.D.	Envelope Density (g cm^{-1})	atm% Si	atm% B	atm% Li	atm% O	Macroscopic thermal neutron absorption Cross Section (cm^{-1})	Assumed density
44-3	-	27.1%	6.1%	2.4%	64.4%	4.13	0.5
49-3	-	29.4%	0.0%	7.8%	62.7%	**1.18**	0.5
44-4	-	28.6%	0.0%	9.5%	61.9%	1.45	0.5
55-1	-	26.6%	6.0%	3.6%	63.9%	4.37	0.5
55-2	-	25.2%	5.7%	6.8%	62.3%	4.72	0.5
55-3	-	23.4%	5.3%	11.1%	60.2%	**5.33**	-
1-5	0.36	26.7%	0.0%	13.3%	60.0%	1.52	-
3-1	0.54	26.2%	6.0%	4.2%	63.6%	4.77	-
3-2	0.50	26.3%	6.0%	4.2%	63.6%	4.4	-
5-1	0.52	27.5%	6.2%	1.2%	65.0%	4.16	-
5-2	0.51	27.5%	6.2%	1.2%	65.0%	4.08	-

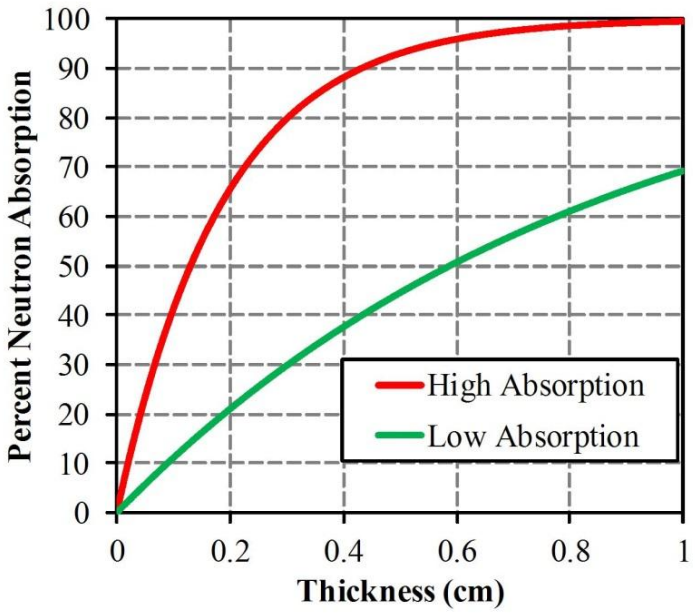

Figure 5.5: Fractional thermal neutron absorption of lithium borosilicate aerogel samples provided by Aerogel Technologies. The minimum and maximum macroscopic thermal neutron absorption cross-sections were used to generate the plot and show the range of theoretical neutron absorption as a function of material thickness.

5.3 Foam Synthesis and Fabrication

Impregnated foam samples were produced by Future Foam using their own proprietary methods. The open-celled polyurethane foam was impregnated with natural LiF and natural B_2O_3 (boron oxide). The first attempts of impregnating open-celled polyurethane foam utilized various quantities of powder in order to find the foam saturation level. The powder was mixed with polyurethane material to create a homogenous solution, and the foam was produced from the viscous material. Impregnation levels of 1.0, 5.0, 10 and 27.5% were completed with the LiF, while 5.0% and 10.0% were achieved with the B_2O_3. However, the saturation point was not achieved with the LiF at the reported percentages, but was obtained for the B_2O_3 at 10%. The higher impregnation level of foam with LiF showed promise as a neutron detector and, therefore, enriched ^{6}LiF was used to obtain a foam sample with a 5.0% impregnation level. The 5% ^{6}LiF foam was cut into 10 sheets, each approximately 2.0 mm thick, and placed in *Box B.* The test chamber was purged with P-10 gas and positioned at the diffracted neutron beam port. (Neutron sensitivity results are discussed in the following chapter.)

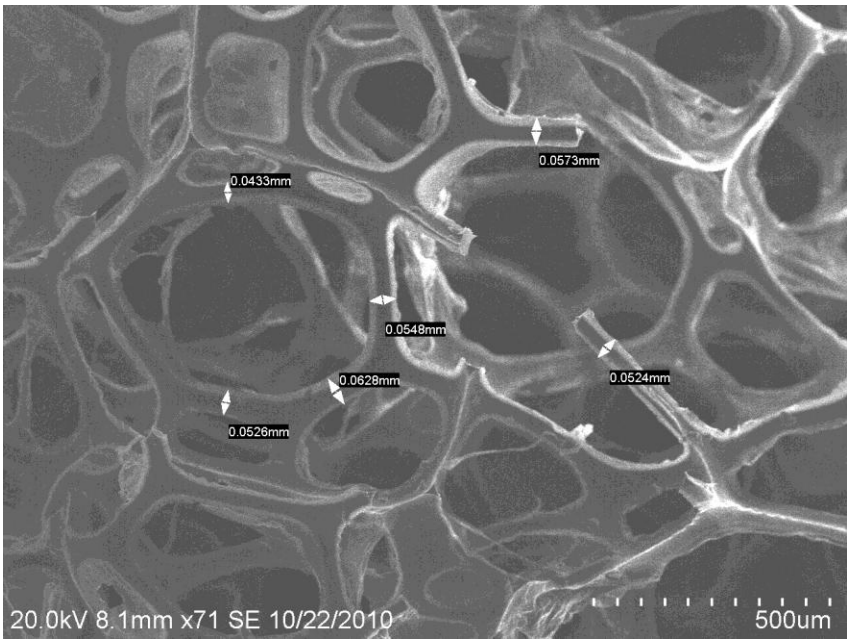

Figure 5.6: A SEM image of open-celled polyurethane foam impregnated with 10% natural LiF. Cell sizes range from 1.0–5.0 mm, and struts have an average thickness of 50 µm.

At the highest LiF impregnation level, 27.5%, the LiF began to cluster and form globules as large as 1.0 mm in diameter, as shown in Figure 5.7. The diameter of the LiF spheres is too large for reaction products to escape simultaneously. Further, the sphere diameter is two orders of magnitude larger than the summed reaction product range, thus, neither reaction product will be measured. The LiF clustering could be a result of mixing materials prior to foam extraction and lower impregnation levels will need to be used in the detectors. Another cause of the clustering could be the initial size of the LiF powder granules. Thus, 50 g of nano-^{6}LiF was synthesized and sent to Future Foam to find the saturation point of LiF in open-celled polyurethane foam. A viscosity matching technique will determine the saturation point of the foam and foam extraction will reveal if the LiF is still forming large clusters with the nano-sized LiF material. The ^{6}LiF was synthesized by dropping small pieces of ^{6}Li metal into deionized water until saturation, followed by titration of the solution using hydrofluoric acid (HF). This titration creates a sub-micron-sized material, but nanoization is completed using an evaporative method. SEM images of the post titration and post evaporation are shown in Figure 5.8.

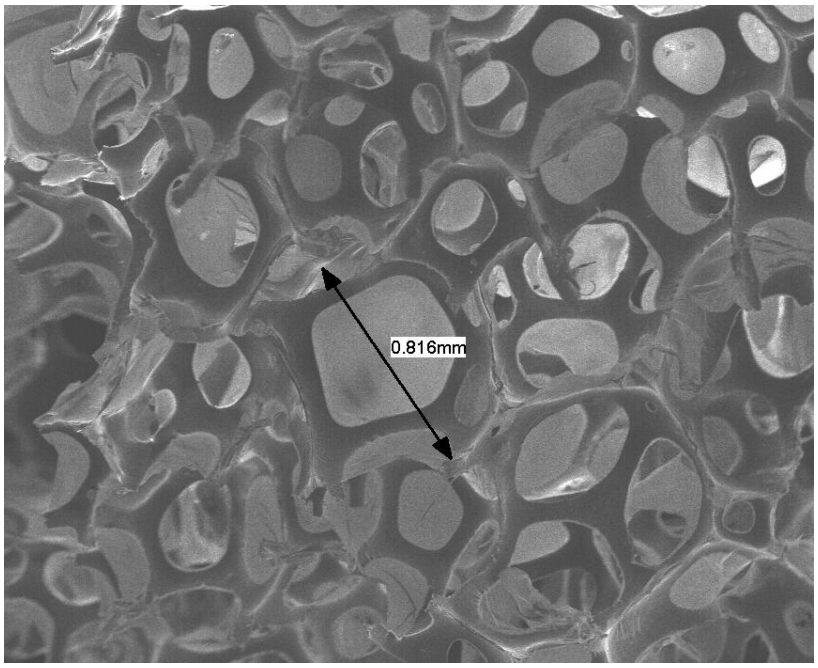

Figure 5.7: A SEM image of open-celled polyurethane foam impregnated with 27.5% natural LiF. The LiF began to cluster at these impregnation levels creating regions of 1.0 diameter LiF volumes. This diameter is too thick for reaction products born in the center to escape the cluster or foam.

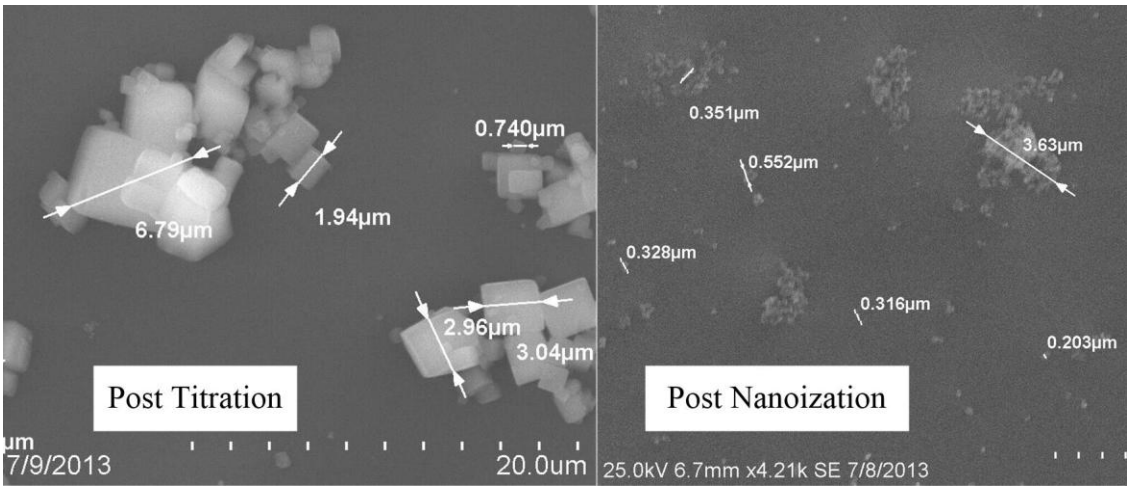

Figure 5.8: SEM images of LiF after titration (left) and post evaporation of the powder (right).

5.4 Obtaining Li Foil

The first rolls of Li foil were obtained from Honjo Metals in Japan and were natural Li foils at thicknesses of 35, 55, and 75 µm. An additional natural 120 µm thick Li foil sample was obtained from American Elements. (The 120 µm sample was lower quality and had signs of oxidation.) All Li foil strips were 5 cm wide and only 5 meters long of 35, 55, and 75 µm thick foil were obtained. (Only a length of 25 cm was obtained for the 120 µm thick Li foil.) Each thickness was cut, taped to the Al frame, and placed into *Box A*. P-10 gas flowed through the chamber continuously to prevent oxidation of the Li foils and the test chamber was positioned at the diffracted neutron beam port. The 35, 55, & 75 µm thick Li foils were cut into 10 layers each, positioned in *Box B*, and the same neutron tests completed with *Box A* were repeated. Neutron sensitivity results are presented in the following chapter.

After preliminary Li foil neutron sensitivity tests were completed, enriched ^{6}Li (95% enrichment) metal ingots were obtained from The Y-12 National Security Complex in Oak Ridge, Tennessee. These ingots were sent to Rockwood Lithium to be formed into foils at thicknesses of 55 and 75 µm, the ideal thicknesses for 5 & 10 layer devices, respectively. Additionally, each Li foil roll was 5.0 cm wide and 2.5 kg of Li foil at each thickness were

obtained. The enriched ^{6}Li foil was used in similar MWPC detectors, but is discussed in grater detail in section 5.7.

5.5 Aerogel Test Chamber

An off-the-shelf Al electronics project box was used as the aerogel test chamber. An Al piece was centered between two wires with a 3.0 cm diameter hole positioned in the middle, where disc samples were situated for neutron measurements. Anode wires measured reaction products ejected from each side of the aerogel samples; however, reaction product ranges remain to be determined. Thus, if reaction products can escape both sides of the sample simultaneously, the chamber was designed to measure reaction products escaping both sides of the aerogel sample. When performing neutron measurements, P-10 continuously flowed into the test chamber and voltage lines were connected outside the test chamber to allow pulses in the two compartments to be combined if they originated from the same neutron absorption. Neutron sensitivity tests are presented and discussed in the following chapter.

Figure 5.9: The aerogel test chamber with the sample holder positioned in the middle of the box. Anode wires were positioned on each side of the sample in order to measure reaction products escaping both sides of the aerogel samples.

5.6 Foam Test Chamber

Open-celled polyurethane foam was impregnated with 10.0% LiF and cut into 10 sheets, each approximately 2.0 mm thick, were placed into *Box B*. The lid to the test chamber was sealed using conductive Cu tape and P-10 gas was allowed to purge through the device for 20 minutes prior to neutron sensitivity testing at the diffracted thermal neutron beam port. A picture of the detector with the impregnated foam inserts is shown in Figure 5.10. Anode wires were connected externally from the device in a serpentine manner and led to a single preamplifier. The foam oriented parallel to each other is the simplest detector geometry, but the foam can be cut into other more complex shapes.

Figure 5.10: Box B with 10% LiF impregnated foam inserts placed in the detector. The lid is removed to show the inside of the chamber, and the anode wires are connected in a serpentine manner on the outside of the device.

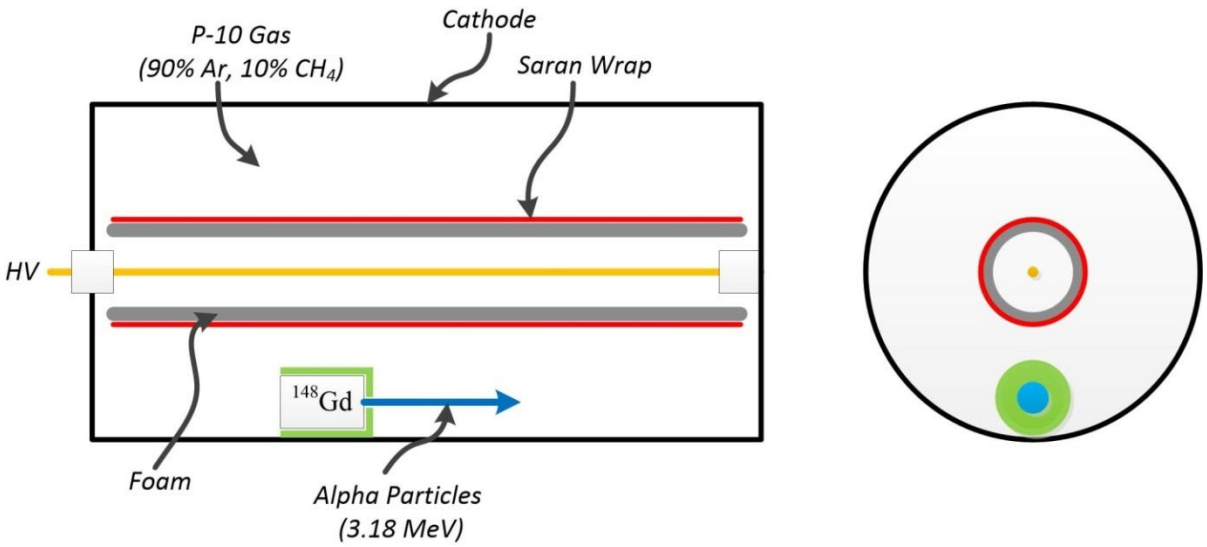

Figure 5.11: Cross-sectional schematic of the cylindrical foam insert in the coaxial detector with the collimated alpha particle source. Two pulse-height spectra were collected, one with and one without saran wrap, to determine whether electrons are able to penetrate the foam pores and reach the anode wire.

Foam can be cut using a hot wire method, which allows a variety of foam designs to be tested. (The hot wire melts foam and can cause burn marks if cut slowly.) The hot wire cutting method was used to form a cylindrical foam insert for a coaxial device. The foam tube was 2.5 cm in diameter and had a wall thickness was approximately 3.0 mm. Reaction products were able to escape both sides of the foam insert, approximately half towards the inside of the cylinder near the anode wire, and the other half between the foam and the cathode wall. The foam tube insert was used to determine if electrons could pass through the relatively large pores of the impregnated foam. The experiment completed to determine if electron transmission was possible used a collimated ^{148}Gd alpha particle source (E_α = 3.18 MeV) positioned in the tube such that alpha particles were emitted parallel to the foam and anode wire, which is depicted in Figure 5.11. The alpha particle trajectory mimicked reaction product energy deposition that occurred between the cathode wall and foam insert. A pulse-height spectrum was collected for 1.0 hour with the collimated alpha particle source and foam insert. Next, plastic wrap was wrapped around the exterior of the foam insert to block any penetrating electrons from reaching the anode wire. Again, a 1.0 hour long pulse-height spectrum measurement was collected. The two pulse-height spectra collected are plotted together in Figure 5.12. The pulse-height spectra indicate the

plastic wrap blocked any penetrating electrons. Thus, the conclusion is made that electrons pass through the foam pores and reach the anode wire. The resolution of the alpha particle peak was less than expected with a typical proportional counter, typically a peak similar to a Gaussian shape is observed. The feature in the pulse-height spectrum with the alpha particle source present has a large continuum with a constantly decreasing slope from the peak, or highest count rate, towards electronic noise in the spectrum. Therefore, it can be concluded that if the electric field is strong enough, a portion of the electrons initially generated are able to traverse the foam. The percentage transmitting through the foam is most likely dependent on the electric field strength and the thickness of the foam absorber. An additional measurement should have been completed with no foam present and the alpha particle source remaining in the detector. Thus, a metric could have been created using the alpha particle peak to predict the amount of charge loss due to the foam insert. Next, neutron sensitivity of the device was investigated and is presented in the following chapter.

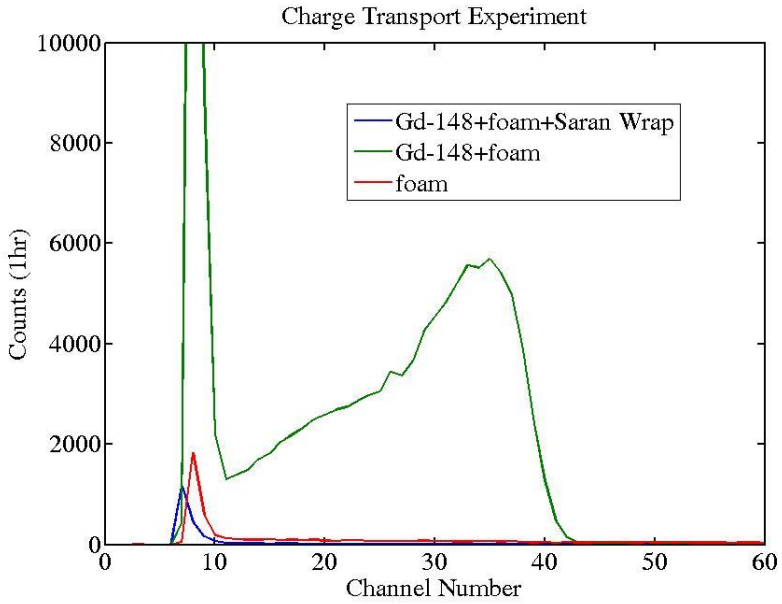

Figure 5.12: The pulse-height spectra obtained for the coaxial cylindrical foam insert detector with a collimated alpha particle source positioned parallel to the anode wire and foam. The plastic wrap positioned around the foam blocked penetrating electrons, demonstrating that electrons generated between the cathode and foam insert do pass through the foam to reach the anode wire.

5.7 Li Foil MWPC Construction

The following sub-sections describe the processes and experiments pertaining to the development of the mid-sized and large-area Li foil MWPC neutron detectors. The first section describes experiments and results to determine anode wire spacing. Furthermore, as a result of the restricted width (5 cm) of the Li foils, support frames were constructed allowing for larger Li foil sheets to be constructed. Anode wire construction was completed by Saint Gobain Crystals in Hiram, Ohio and is considered a proprietary process. Thus, anode wire construction is not discussed. Lastly, the detector assembly process of two different sized Li foil MWPC neutron detectors is discussed. The two different detector sizes were approximately 550 cm^2 and 1250 cm^2 in effective area, referred to as the mid-sized and large-area detectors, respectively.

5.7.1 Anode wire distance determination

Typically MWPCs are used for imaging and particle tracking systems [72]. Banks of anode wires are spaced 1.0 mm apart and cathode wires are typically angled or perpendicular to the anode wires. Spatial resolutions of 300 μm have been reported with these systems [72], but is not necessary for simple neutron counting applications where particle tracking and resolution are of no concern. All that is required for a neutron counting system is a set of anodes that collects all energy deposited in the gas volume is. A plurality of anode wires can be used with spacing as close as 0.5 cm, but is not necessary and only increases the assembly time and cost of the detectors. Thus, the ideal anode wire distance was determined to maximize anode wire distance while maintaining uniform charge collection. In other words, the goal was to determine the maximum distance between anode wires while showing no decrease in neutron detection efficiency.

A custom MWPC was constructed to determine the optimal anode wire distance. An Al metal box containing 30 anode wires spaced 0.5 cm apart was used as the anode wire test chamber. The anode wires were soldered to SHV bulkhead feedthroughs penetrating the Al cathode. The gold plated tungsten anode wires were 25 μm in diameter and anode wire dead ends were soldered to an eyehook and connected to an expansion spring that was anchored to a plastic

base. Plastic tubes were placed over the springs and eyehooks in order to prevent any inconsistencies in the electric field. The anode test chamber and anode wire construction are shown in Figure 5.13.

A collimated alpha particle source was suspended above the anode wires using a strong rare earth neodymium magnet, as shown in Figure 5.14. The suspended source allowed the anode wire response to be profiled by collecting count rates and pulse-height spectra at specific location across the anode wires. Anode wire profiles were completed for 0.5, 1.0, 2.0, and 3.0 cm anode wire spacing. Profiles were also completed at P-10 gas pressures of 1.0, 1.5, and 2.0 atm. However, the profiles with the collimated source were inconclusive. However, a ^{226}Ra alpha particle source, which has four easily identifiable alpha particle energies, was placed in the anode wire test chamber and not collimated. The pulse-height spectra were collected at 2.0 cm and 3.0 cm anode wire spacings and results are shown in Figure 5.15. Minimal degradation occurred between the two anode wire spacings, primarily resulting in the peak location moving to lower channel numbers. However, the total number of counts under each alpha particle peak remained the same. In conclusion, 2.5 cm anode wire spacing was chosen as the initial anode wire spacing because it split the difference between the 2.0 and 3.0 cm tests and could be spaced symmetrically over the 5.0 cm wide Li foils.

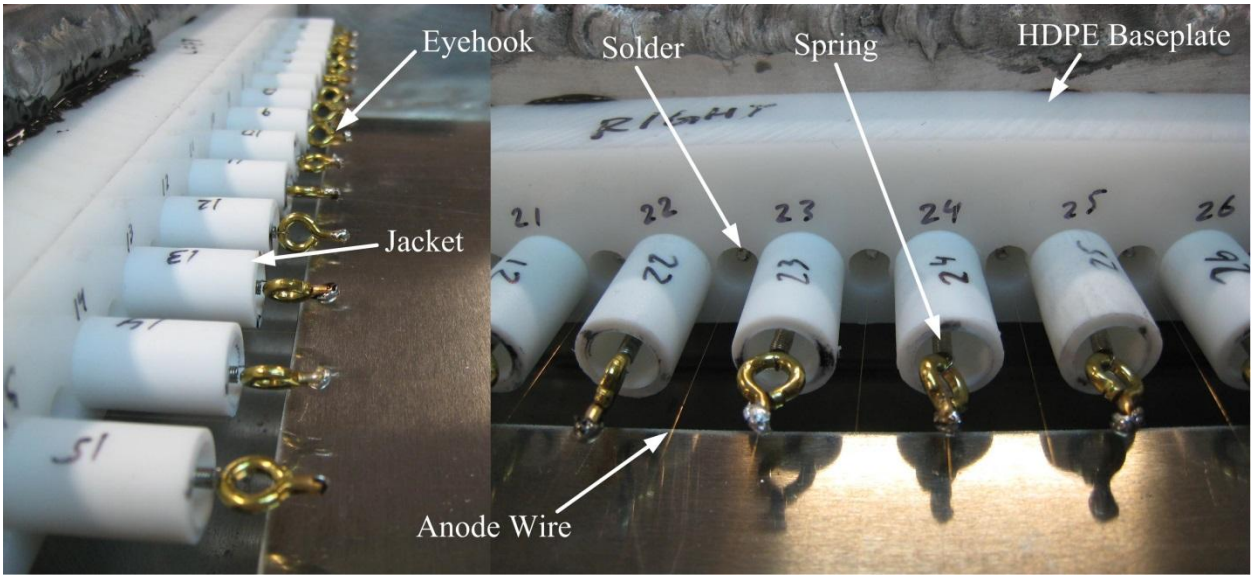

Figure 5.13: Pictures of the anode wire construction in the anode wire optimization detector.

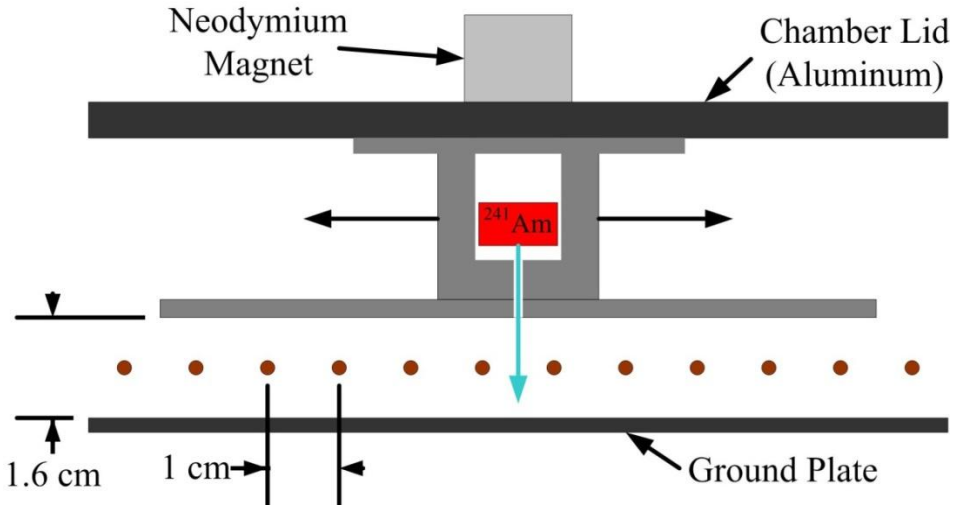

Figure 5.14: A schematic illustration of the anode wire optimization chamber with the collimated alpha particle source positioned above the anode wires. The neodymium magnet allowed the source to be moved over the anode wires and collect a profile of the count rates.

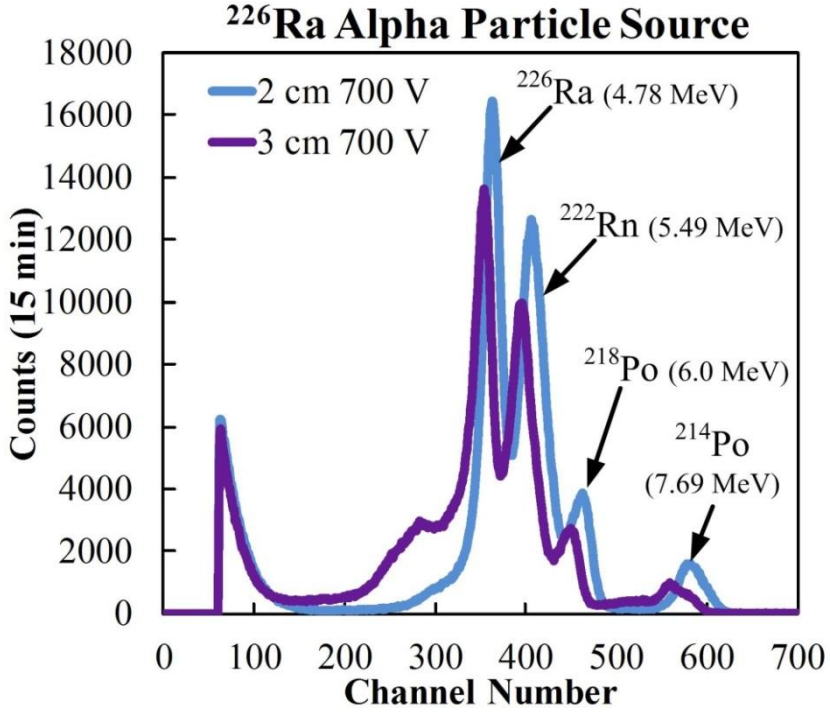

Figure 5.15: Pulse-height spectra collected from the anode wire optimization chamber using a multi-energetic ^{226}Ra alpha particle source. The anode wire spacing tested was 2.0 and 3.0 cm, and showed degradation in peak location, but not counting rates.

The ^{226}Ra alpha particle source was removed from the test chamber, and natural Li foil (75 μm thick) was positioned in the test chamber above the anode wires. The anode wire optimization device was positioned in front of a ^{252}Cf neutron source to irradiate the entire 625 cm^2 Li foil surface area. Two pulse-height spectra were collected at the 2.0 cm and 3.0 cm anode wire spacings. These pulse-height spectra are shown in Figure 5.16 along with the simulated pulse-height spectra of the same detector geometry and setup obtained using MCNP6. Determining which anode wire spacing demonstrated better performance in the neutron tests was inconclusive, but 2.5 cm spacing was still concluded as a good initial distance.

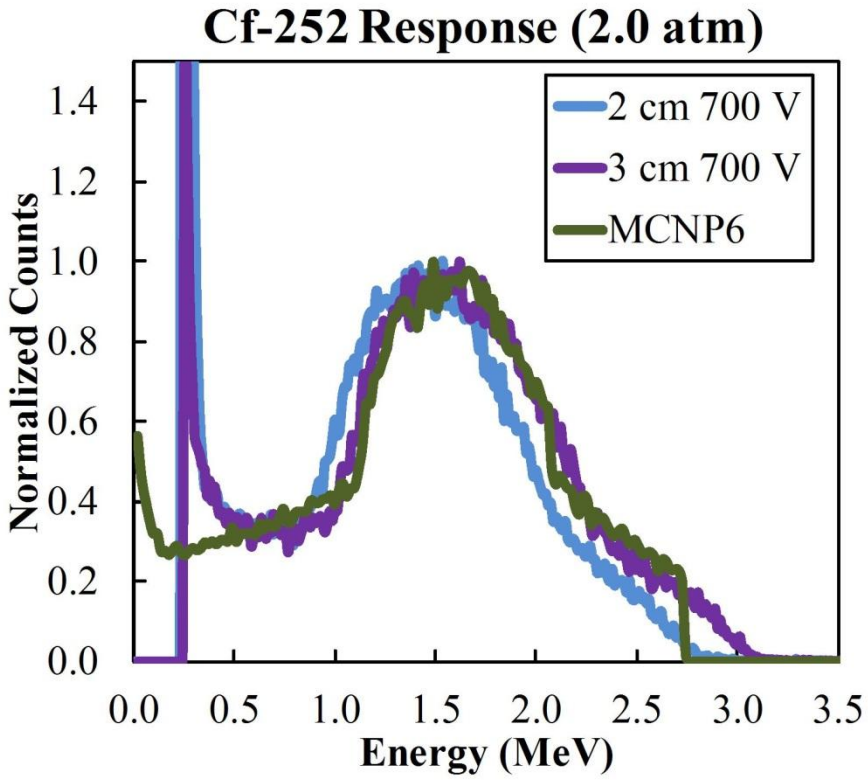

Figure 5.16: The neutron response pulse-height spectra obtained from the anode wire optimization chamber with anode wire spacing of 2.0 and 3.0 cm. The spectra are compared to the simulated pulse-height spectrum obtained from MCNP6.

5.7.2 Li Foil Support Frame Optimization

Li foil, similar to Cd and Pb foil, is malleable and tears easily at thicknesses less than 1.0 mm. Therefore, a rigid Al frame was required to support large-area Li foil sheets. The Al support framework must also be thin in profile in order not to increase the overall thickness of the detector. The first embodiment, used in the anode wire optimization chamber, was water jet cut from a single sheet of 1/8″ Al, as shown in Figure 5.17. The water jet cutting method resulted in straight smooth edges compared to plasma cut frames, which prevented the frames from tearing the Li foil. Bolting two of the support frames together and sandwiching the Li foil in the middle was structurally rigid and prevented the Li foil from sagging.

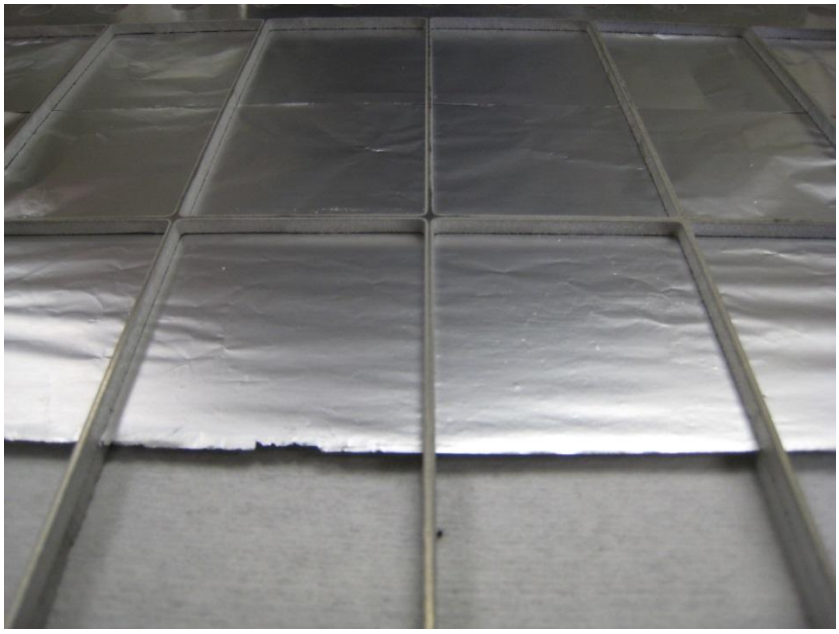

Figure 5.17: The Li foil support frame of the anode wire optimization chamber. Frames were 1/8″ thick and had 1/16″ thick cross bars that were lined up when two frames were bolted together.

The Li foil support frame used in the anode wire test chamber led to frame permutations that focused on structural rigidity to prevent the foil from sagging, or deforming, while maintaining a high open-area percentage. The first designs began with metal wire mesh because of high open-area percentages. However, problems arose when attempting to connect wire meshes to the

perimeter support frame. Some wire mesh attachment methods included twist ties, expansions springs, and protruding studs. These attachment methods are shown in Figure 5.18. These Li foil support frame prototypes were as thick as 1.0 cm and not uniform. Furthermore, the frames were difficult and time consuming to assemble and, therefore, are not good choices for large-scale manufacturing.

The Li foil support frames in Figure 5.17 and Figure 5.18d led to the final Li foil support frame design concept, which used no wire mesh. The outer edge of the support frame was part of the same original Al sheet used to comprise the inner support grid. Foil support frames were constructed from 1/16″ thick Al and grid openings were 4.5 cm wide by 8.0 cm long. Square Al bars, 0.5 cm wide, also part of the frame ran parallel to the foil length and 1/32″ thick crossbars perpendicular to the lengths of the foil positioned every 8 cm. The Li foil was sandwiched by two connected foil support frames. The edges of the 5 cm wide Li foil strips were clamped by the 0.5 wide Al bars and covered approximately 0.25 cm on each Li foil edge. This basic foil support frame design was used in all of the Li foil construction designs and is something that could be manufactured cheaply and easily on large scales.

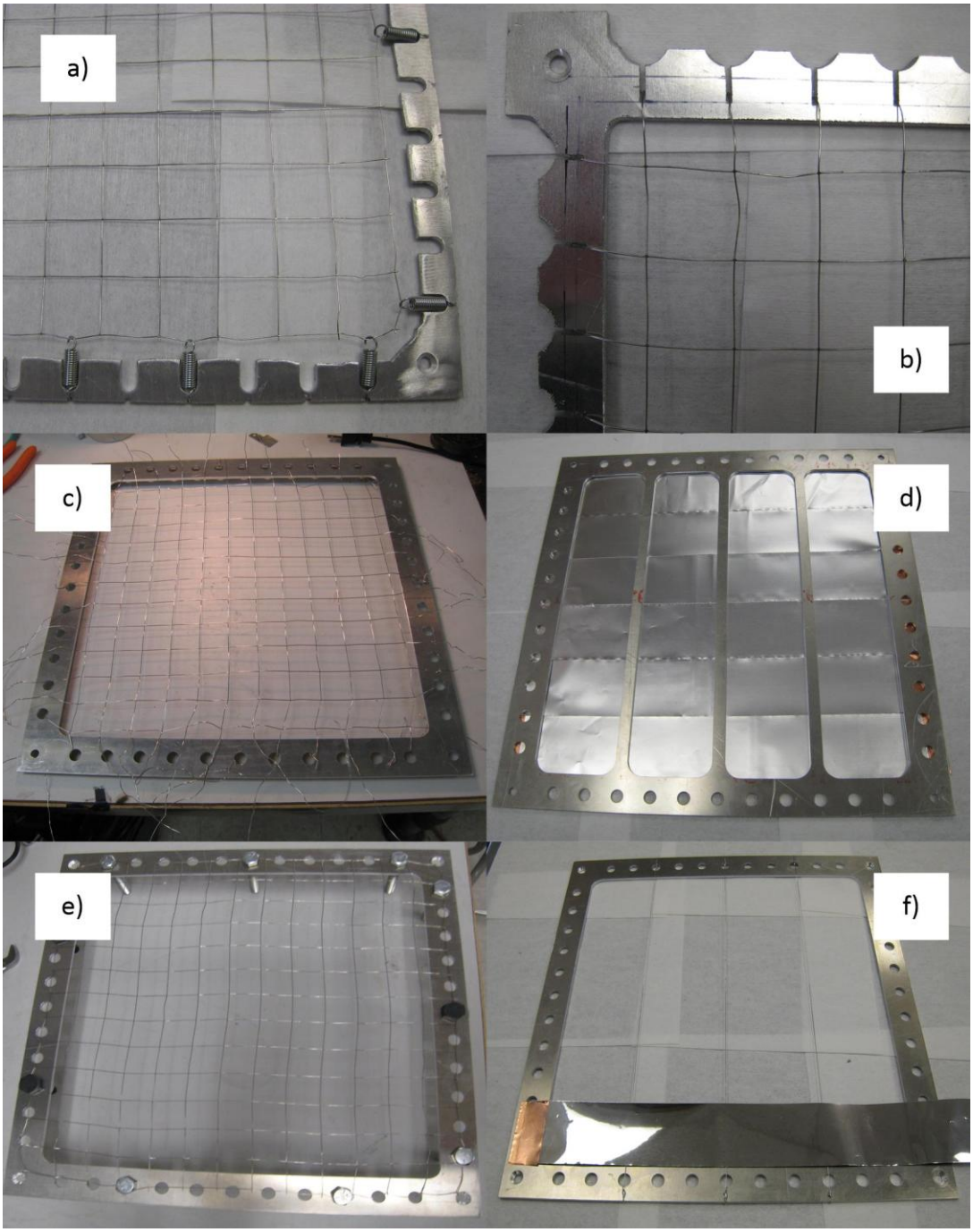

Figure 5.18: Pictures of several Li foil support frame concepts. Foil support frame permutations include: a) spring tension wire mesh, b) metal wire mesh stretched over support frame studs, c) metal wire mesh tied to the frame, d) metal strips running the length of the frame as one single sheet, e) metal wire mesh stretched over bolts around the frame, f)and wires soldered around the frame running the length of the frame.

Figure 5.19: The final design of Al Li foil support frames. Horizontal support bars are 0.5 cm thick and separated 4.5 cm apart, and vertical crossbars are 0.1 cm thick and positioned approximately 8.0 cm apart. The dot slightly above center is a pop rivet holding two frames together tightly in the center of the large-area foil support frames.

Large-area MWPCs used Li foil support frames similar to those shown in Figure 5.19. The largest foil frames, 57 cm long and 25 cm wide, began to sag in the middle when clamped together on the ends. Therefore, to prevent sag, pop-rivets were used in three of four holes located symmetrically around the center point of the support frames. A 4-40 screw was used in the remaining hole with a ceramic spacer on the other side to prevent the foils from touching the anode wire banks. The ceramic spacer was 1.5 cm long and the spacing between foils was 1.63 cm, preventing the foils from touching an anode wire bank when laid horizontally. The mid-sized (550 cm^2) and large-area (1250 cm^2) Li foil support frames used in the MWPC neutron detectors are shown in Figure 5.20 and Figure 5.21, respectively.

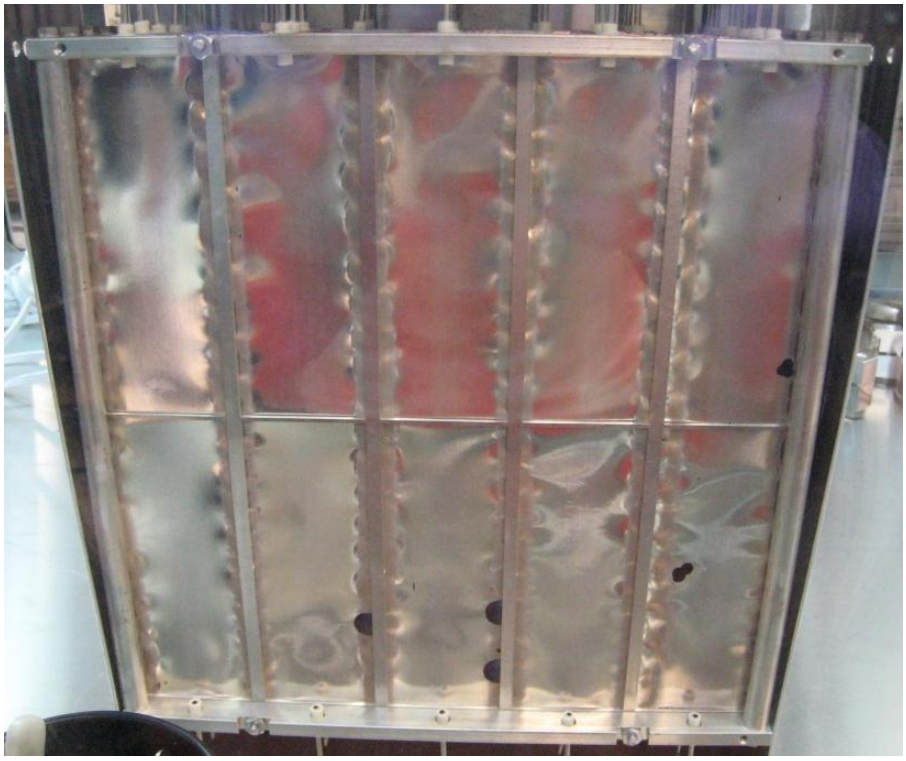

Figure 5.20: The smaller (550 cm^2) mid-sized Li foil support frame.

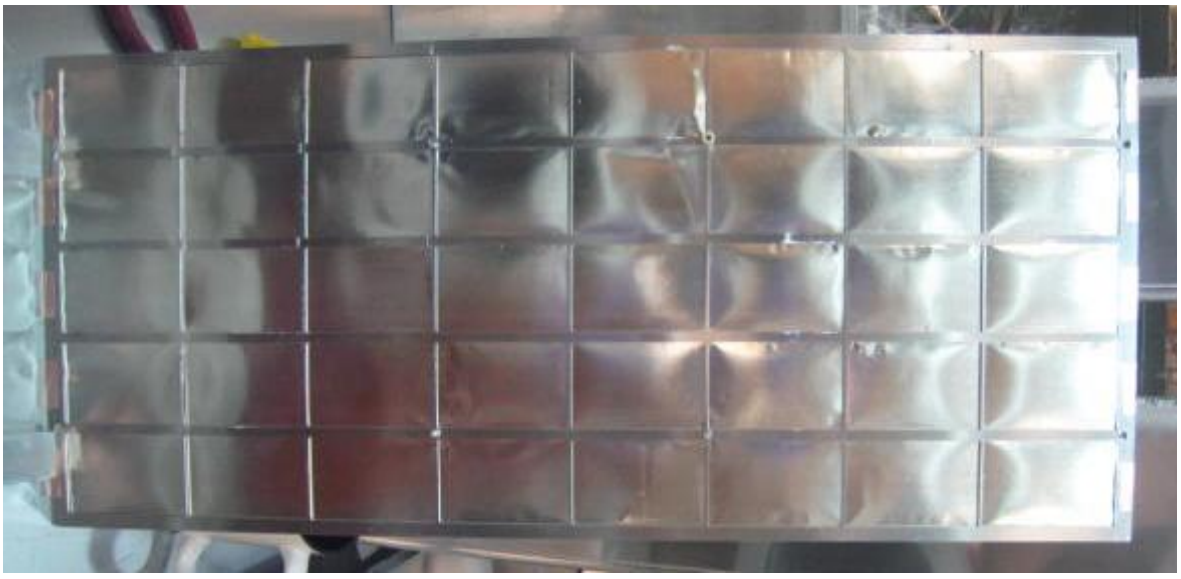

Figure 5.21: The large-area (1250 cm^2) Li foil support frame.

5.7.3 Li Foil Detector Assembly

Aluminum frames were constructed to support the anode wire used in the detectors. These anode bank frames were loaded with the anode wires by Saint-Gobain Crystals. The anode wire construction is a proprietary process and, thus, details of anode wire assembly are not discussed. Several permutations of anode wire support frames were completed, but the most recent permutation is discussed here. The anode banks were assembled the same way for both the mid-sized and large-area Li foil MWPCs using a ½″ by ¼″ thick square rod with chamfered holes positioned every 2.5 cm for the anode wires. The hole locations on the square rode were chosen such that the anode wires were positioned symmetrically over the open Li foil regions. The length between the live and dead end of the anode banks was supported and controlled by cylindrical rods that were bolted perpendicular to the ends of the square rods. A picture of an anode wire bank is shown in Figure 5.22. The assembly for the larger-area MWPC was exactly the same, except for the anode wire diameter increased from 25.0 μm to 50.0 μm, and cylindrical side rod length increased from 25.0 cm to 57.0 cm. Once the anode wire banks were returned from Saint-Gobain Crystals with the anode wires, all components were loaded into an Ar atmosphere glovebox for detector assembly.

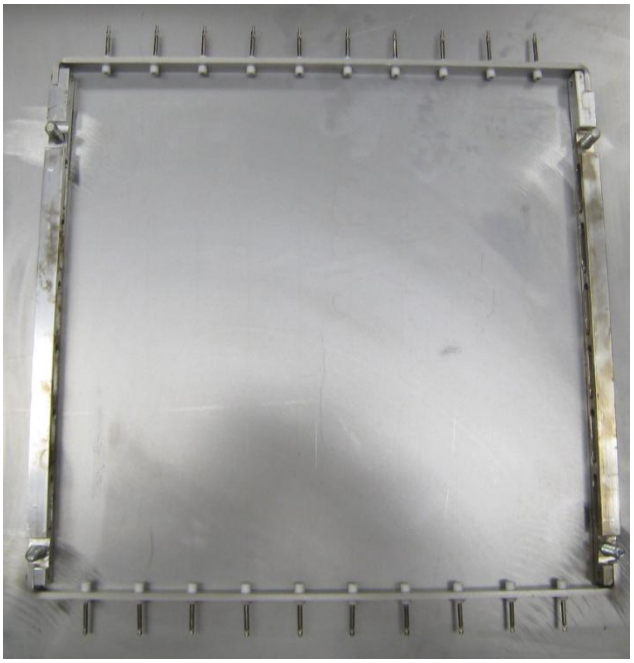

Figure 5.22: Anode wire bank for the mid-sized Li Foil MWPC.

The Li foil MWPC assembly process began by attaching a flat 1/16″ Al sheet, 30 cm x 25 cm for the mid-sized detector and 65 cm x 25 cm for the larger-area device, to the first anode bank using four 4-40 button cap screws and lock washers. The Al sheet and attached anode bank was turned over and four 4-40 all-thread bolts were fed through the top and bottom square anode bars (live and dead ends), two all-threads in each bar. Lock nuts were attached to the all-threads in cavities in the anode bars to secure the all-thread bolts in place. These all-threads are the support and guide pillars which all foil frames and anode banks were stacked on top of and attached. The lid contained four riser blocks, or bosses, and the assembly was bolted to the blocks, as shown in Figure 5.23.

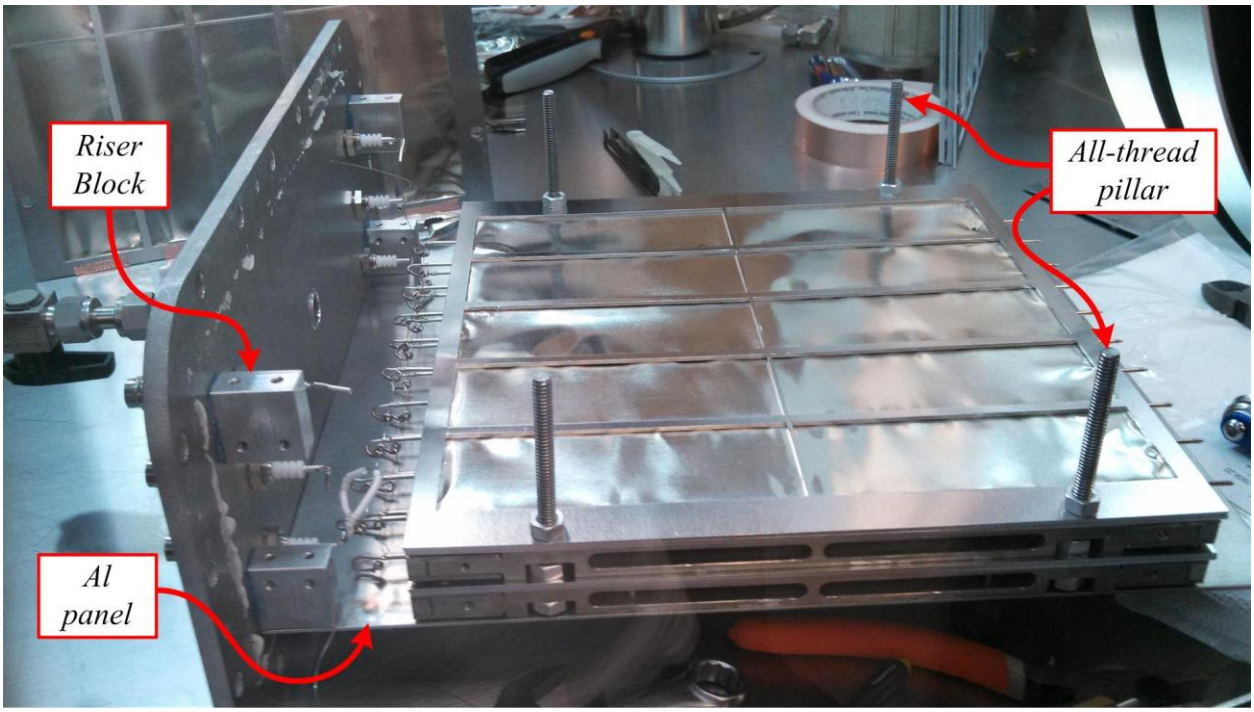

Figure 5.23: A picture of the Li Foil MWPC in the first stages of assembly showing the Al sheet connected to the bosses in the lid. Also shown are two anode banks and two Li foil sheets indexed together using the four all-thread rods.

The Li foil was unrolled in strips and cut with scissors to a length approximately 1.0 cm less than the total length of the Li foil support frame. The foil ends were connected to the Al support frame using conductive Cu tape. This foil layout process was repeated across the frame four more times and positioned on the stack using the all-thread pillars. A second foil support frame

was placed on top of the support frame containing the Li foil strips and the frames were pressed together with a hex head lock nut tightened on the all-thread pillar. The lid contained six hermetically sealed SHV feedthroughs and Cu wires were soldered to the solder-cup connectors. All anode wires in each bank were connected together and each bank of anode wires was connected to a single anode feedthrough using a butt connector crimped to the Cu wire. The wires used to connect the anode banks to the SHV feedthrough were shielded with alumina fisheye beads to prevent the high voltage from electrically shorting to the cathode. These steps were repeated alternating anode banks and Li foil support frames until there were five layers of 75 μm thick Li foils with anode wires positioned on both sides of each foil layer. A picture of this stage in the assembly process is shown in Figure 5.24, which contains all five foil layers and six anode banks.

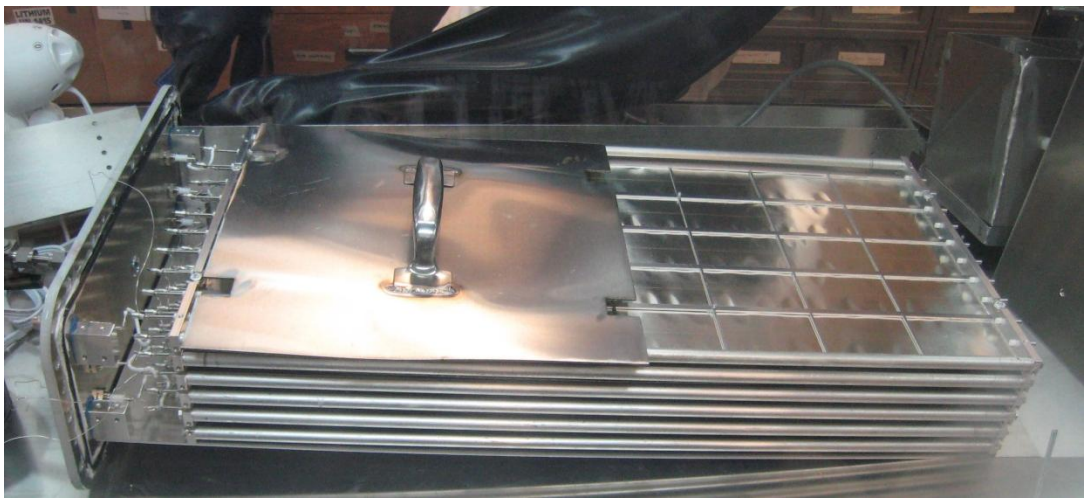

Figure 5.24: The large-area Li foil MWPC with Li foil frames and anode wire banks stacked together. The metal sheet with the handle shown in the picture covering approximately half of the foil length is a protection plate to prevent any dropped tools or materials from breaking anode wires or puncturing the Li foil.

Additional Al panels, similar to the first panel, were connected to both sides of the anode bank and Li foil sheet assembly and to the bosses in the lid. The side panels increased structural rigidity of the assembly when connected to the lid. In addition, another Al panel with the same dimensions as the first panel was attached to the on top of the assembly. (The detector with side

and front panels attached is shown in Figure 5.25.) The assembly was then slid into an Al metal box with 1/8″ thick walls and the lid was bolted to the top flange of the box. A Viton gasket and ¼-20 bolts positioned every 2.0″ ensured a relatively air-tight seal. The device was removed from the glovebox and purged with P-10 gas through a gas-fill line in the detector lid. All six feedthroughs on top of the device were connected together and a single preamplifier was used in detector testing. Four of the large-area detectors are shown in Figure 5.26.

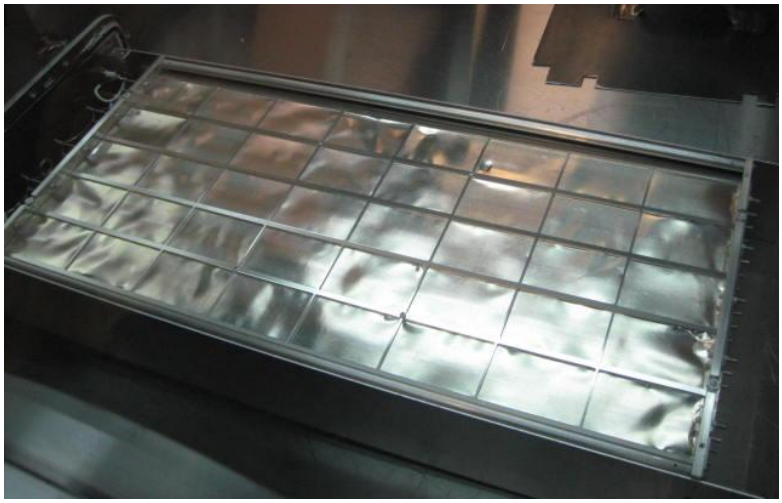

Figure 5.25: The large-area Li foil MWPC with front, back, and side panels attached.

Figure 5.26: Four completed large-area Li foil MWPC's. The six SHV feedthroughs and gas-fill lines are visible on top of the detectors. The carpenter square is included as a metric for detector size.

All Li foil MWPC's were constructed with planar sheets of Li foil, but alternative Li foil designs such as herringbone and sinusoidal patterns are possible. Although the planar patterns offer the advantage of simple construction, the detector has streaming paths if incident neutrons are parallel to the Li foils. However, neutron moderator is typically used on neutron detectors and scatters neutrons at random angles. Further, the scattered neutron is typically at lower energy after the scattering event. Thus, only neutrons scattered with new trajectories approximately parallel to the Li foils will stream through the device. However, as the distance between adjacent Li foils decreases, the range of angles which would allow neutrons to stream through the device decreases. Nevertheless, a corrugated design was constructed by creating 2.5 cm x 2.5 cm square P-10 gas filled regions defined by 75 um thick ^{6}Li foil sheets. Each square section contained a single anode wire. The corrugated design allowed reaction products to be measured on both sides of the ^{6}Li foil, same as the planar pattern. The corrugated design was constructed in a similar manner to the planar pattern, but only used three sets of anode banks, each 1.0″ thick containing 10 anode wires. Between each wire, a 1.0″ wide strip of Li foil loaded into a support frame was slid into place. Thus, a total of nine 1.0″ cross-frames of Li foil were used per anode bank. The first anode bank was attached to an Al panel and the lid in the same manner as the planar pattern detectors. The nine slots were filled with Li foil strips and a large sheet of planar pattern Li foil was stacked on all-thread pillars on top of the anode bank. The middle anode bank was set on top of the Li foil sheet and the Li foil loading process was repeated. Partial construction of the corrugated design is shown in Figure 5.27. The same chamber used for the mid-sized planar pattern detector was used for the corrugated design. Because the planar pattern and corrugated design had similar effective Li foil exposure areas, 3125 cm^2 for the planar pattern and 2937.5 cm^2 for the corrugated design, they were both tested as backpack neutron detector, which is discussed in the following chapter.

Figure 5.27: A picture, mid-construction, of the corrugated Li foil MWPC.

5.8 Form Fit Aerogel and Li Foil Construction

Some neutron monitoring systems require the replacement detector fit within the cavity previously occupied by the ^{3}He neutron detector. Thus, smaller devices than previously discussed were assembled and compared to a 13 cm x 5 cm ^{3}He neutron detector, described in Chapter 2. As stated, the effective counting length of the ^{3}He detector was 6.5 cm, while the entire 13 cm length absorbs neutrons. The first devices built were also 5.0 cm in diameter and the neutron absorbing length was 13.0 cm. These devices were filled with different configurations of lithium borosilicate aerogel and ^{6}Li foil. The second form factor assembled was a square tube 2″ x 2″ with an effective counting length of 6.5 cm and consisted of five layers of 75 μm thick ^{6}Li foil. The five designs investigated are shown in top-view perspective in Figure 5.28. An additional conical design is presented, but has not yet been tested.

The first aerogel configuration investigated in the cylindrical form factor, from a top-view perspective, was a cruciform pattern. Slabs of lithium borosilicate were supplied by Aerogel Technologies, LLC in dimensions of ~1.5 cm x 15 cm x 0.4 cm. The aerogel sample composition was 11% enriched ^{6}Li, 60% O, 24% Si, 4% ^{11}B, and 1% ^{10}B. A sample of the lithium borosilicate aerogel, shown in Figure 5.29, was attached to Cu tape approximately one week prior to assembly to ensure the aerogel would not react, or degrade, when in contact with the epoxy on the Cu tape. The slab length was cut to the correct dimension using an Alaskan ulu knife and connected to an Al frame using Cu tape. The first frame was 5 cm wide and four aerogel slabs filled the open space of the frame. Two 2.5 cm wide frames containing two aerogel slabs each were positioned perpendicular to the first frame to form the cruciform. The distance between the caps containing the live and dead ends of the anode wires were supported with either two or three all-thread bolts. The inside of the caps contained grooves approximately 0.3 cm deep for the frames to slide into place. Figure 5.30 shows the aerogel loaded insert next to the cylindrical test chamber. Once assembled, the aerogel insert was positioned in a test chamber, which could be opened and repaired, or the aerogel samples could be replaced.

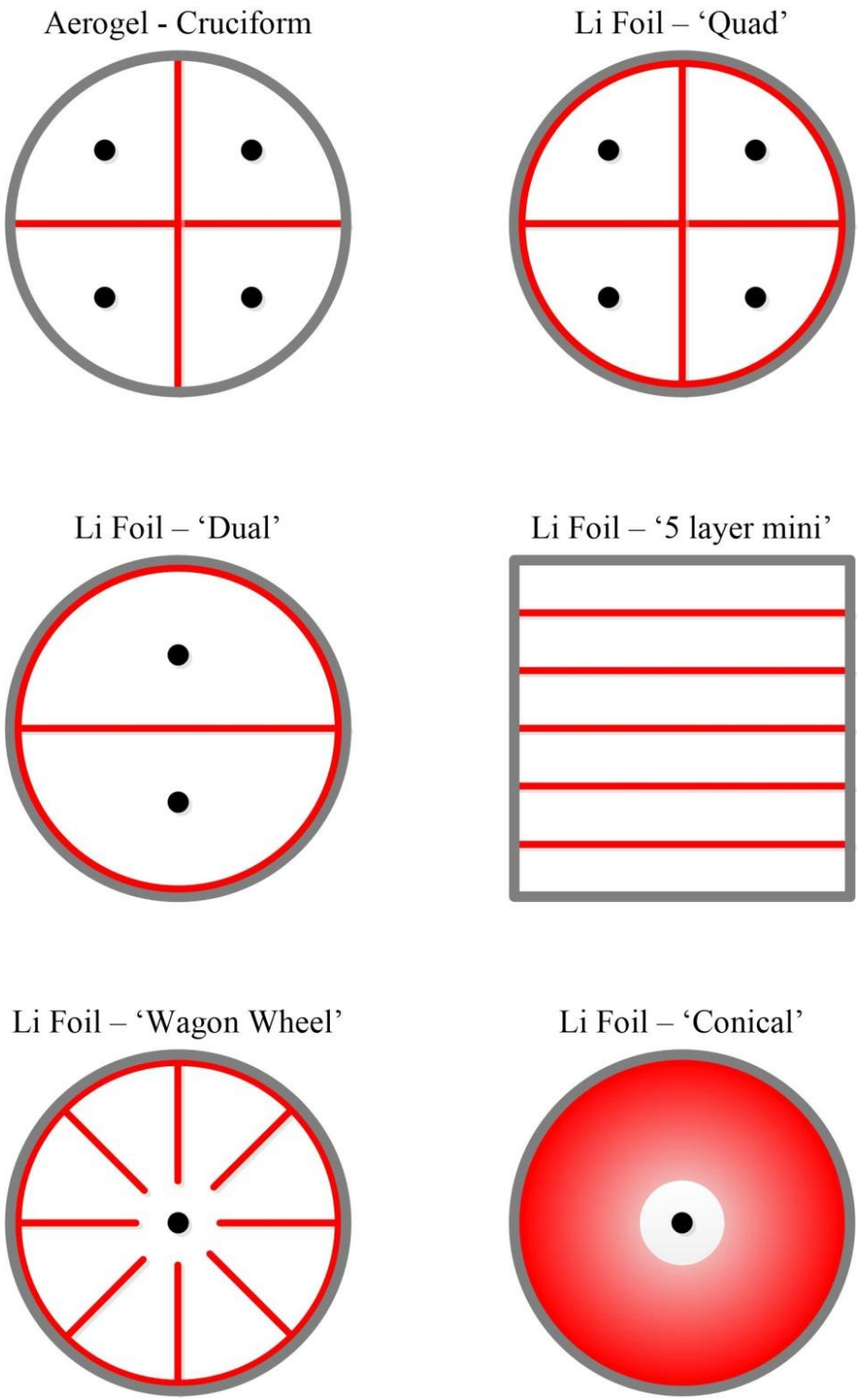

Figure 5.28: Six form-fit designs in the top view perspective. The red represents the neutron absorber material and the black dots and grey circles are the anode and cathode, respectively.

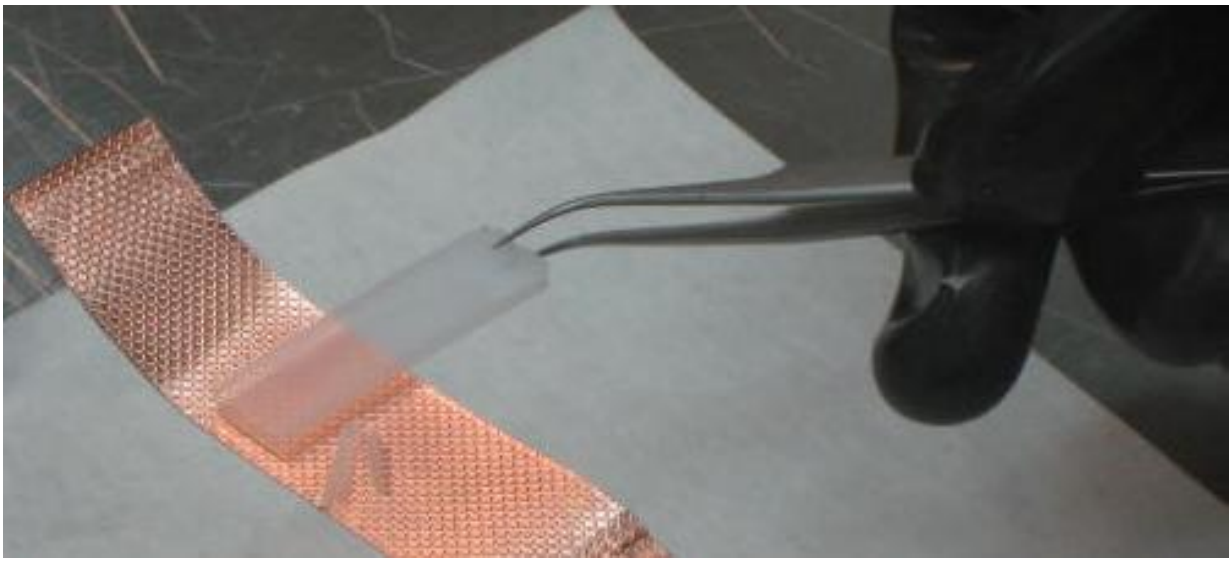

Figure 5.29: Lithium Borosilicate aerogel attached to a strip of Cu tape. The sample is held with a pair of tweezers to show the Cu tape was stuck to the aerogel.

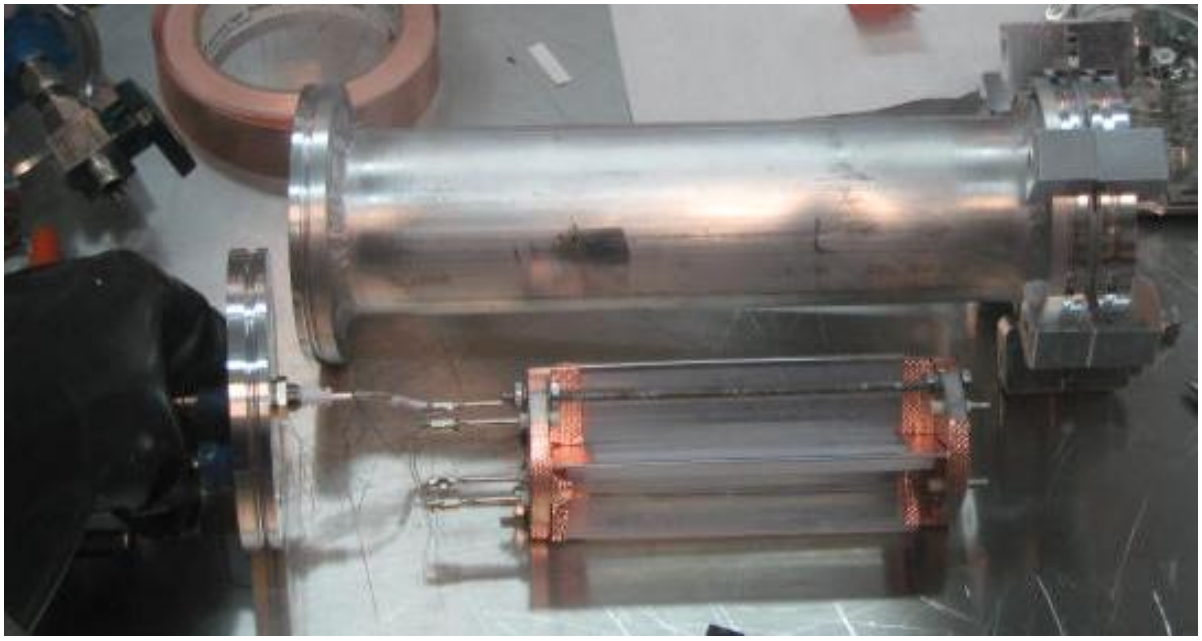

Figure 5.30: The aerogel cruciform design completed and positioned next to the test chamber. The aerogel insert was 5 cm in diameter and 13 cm long.

A HDPE cylinder 6″ diameter x 9″ tall with a 2.5″ diameter cylindrical cutout running the center of the cylinder was positioned around the detector. A 60 ng ^{252}Cf sample was positioned next to the detector and the counts were recorded for 30 seconds in 100V increments from 0–1300V. These measurements developed the counting curve, which showed the ideal bias was approximately 1100V. The neutron response pulse-height spectra and ^{3}He neutron detector comparison are included in the following chapter.

The Quad and Dual Li foil form-fit designs were similar in construction techniques. ^{6}Li foil was attached to a single Al frames using Cu tape. The frames with ^{6}Li foil were slid into place using the precut channels on the insides of the top and bottom end caps, similar to the aerogel construction. The Dual design had a single Li foil in the middle of the insert, dividing the detector into two halves. Each half had a single anode wire which were connected together to sum any pulses in the separate compartments. The Quad design had the same Li foil sheet in the middle as the Dual design, but two additional Li foil frames divided the detector into four quadrants, each having a single anode wire. Lastly, a perimeter coating of ^{6}Li foil was added to the insert using Cu tape and stretching three sheets of ^{6}Li foils around the perimeter. A portion of the perimeter coating and ^{6}Li loaded foil frames are shown in Figure 5.31. The perimeter coating did not cover the entire border of the insert and the remaining void was positioned over an all-thread bolt. The bolt prevented any reaction products from entering the gas volume, thus the choice for positioning the void over the bolt location. The coating method used was sufficient for feasibility studies, but should not be something adapted to commercialized products. The Dual and Quad designs were positioned in a test chamber similar to the aerogel insert, as shown in Figure 5.32. A counting curve was collected using a ^{252}Cf source while the detector was centered in the middle of the HDPE cylinder. Once the ideal voltage was determined, neutron measurements were collected, which are presented in the following chapter.

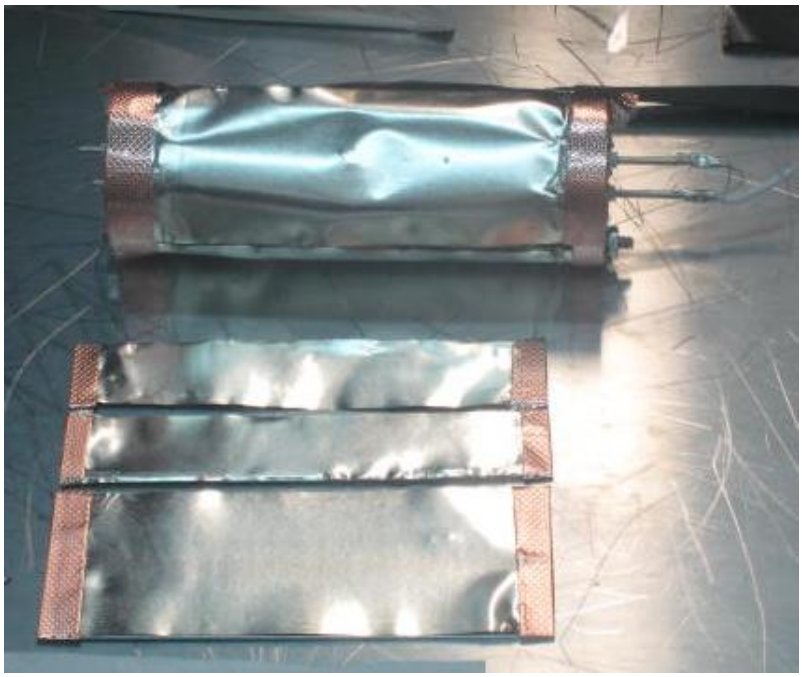

Figure 5.31: The 'Dual' configuration, shown in the top of the picture, is loaded with Li foil and wrapped with a perimeter coating of ^{6}Li foil. In the lower portion of the picture are ^{6}Li loaded frames for the 'Quad' design.

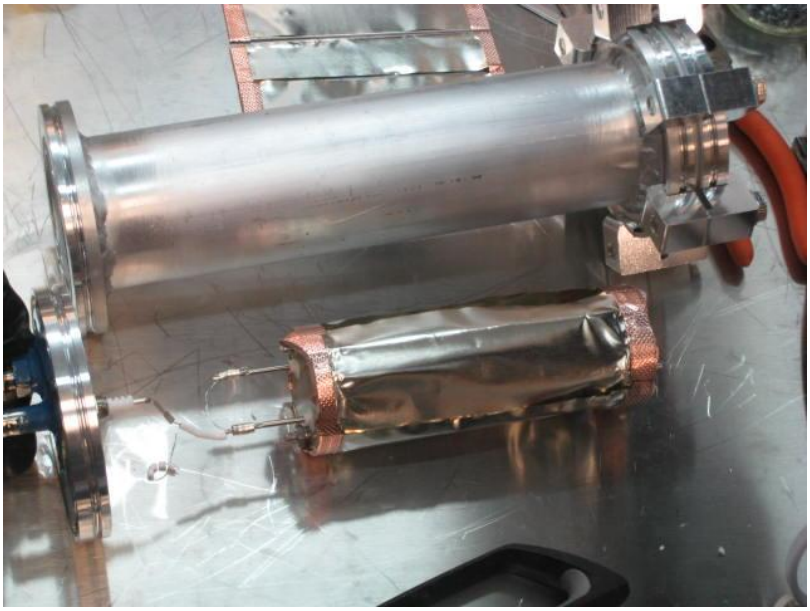

Figure 5.32: The Dual design connected to SHV feedthrough and positioned next to the test chamber. The test chamber was backfilled with P-10 gas and the detector was tested in the vertical position.

The form-fit square pattern design consisted of five parallel layers of 75 μm thick ^{6}Li foil spaced 8.0 mm apart. An illustration of this device is shown in Figure 5.28 and referred to as the '5-layered mini'. The ^{6}Li foil was sandwiched between two 1/32″ thick Al support frames. The Li foil frames were positioned between banks of anode wires and the stack of alternating anode banks and Li foil frames were held together using a single bolt at the live and dead ends of the stack. Anode wires were connected together and the stack was positioned inside the square chamber using rapid prototyped plastic inserts at each end. The live and dead end plastic inserts were used as spacers to prevent the stack ends from sliding inside the tube and either electrically shorting to ground or causing the anode connectors to break. One of the side walls on the top and bottom spacers were angled and aligned together to force the stack to be in contact with one side of the Al tube. The stack in contact with the Al square tubing ensured the stack was grounded and not separated by the top and bottom plastic inserts. The plastic inserts did cover all four sides of the tube above and below the stack where the live end crimps were located. The plastic inserts prevented the crimps from electrically shorting to ground. The Li foil and anode bank stack, before being inserted into the test chamber, is shown in Figure 5.33, and the stack with the plastic attachments is shown in Figure 5.34. A counting curve was obtained using a 6″ x 9″ HDPE moderator cylinder with a 2″ x 2″ square cutout around the detector and a ^{252}Cf neutron source. Once the ideal operating bias was determine, neutron and gamma-ray measurements were collected and are presented in the following chapter.

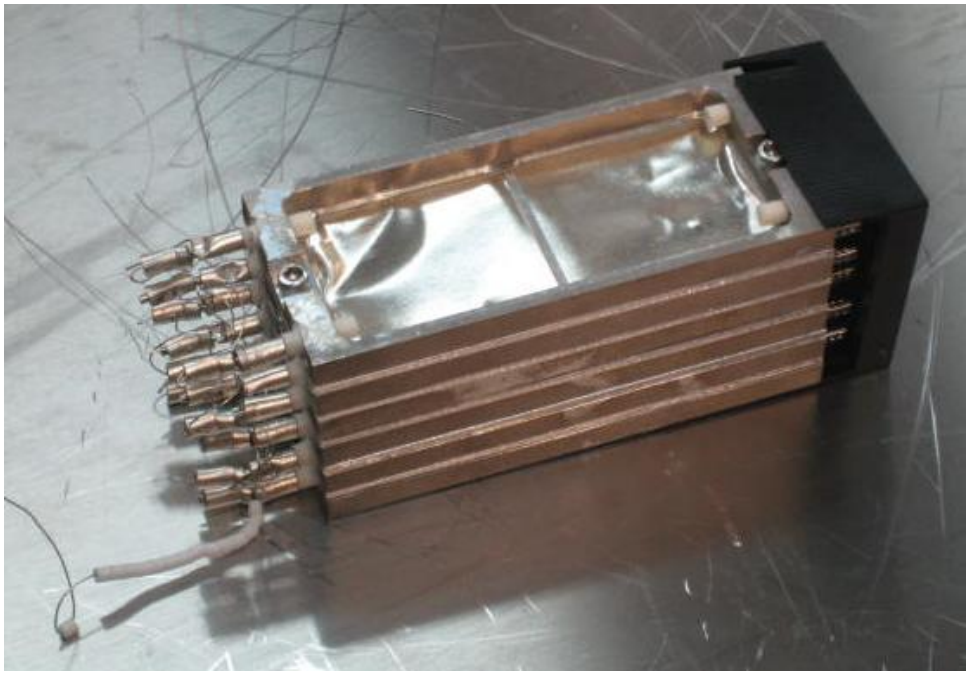

Figure 5.33: The 5-layer mini stack bolted together with the loaded ^{6}Li foil frames. The black plastic insert at the bottom is used as a spacer to prevent the dead end of the anodes from touching the metal casing, thereby, electrically shorting or breaking the anodes.

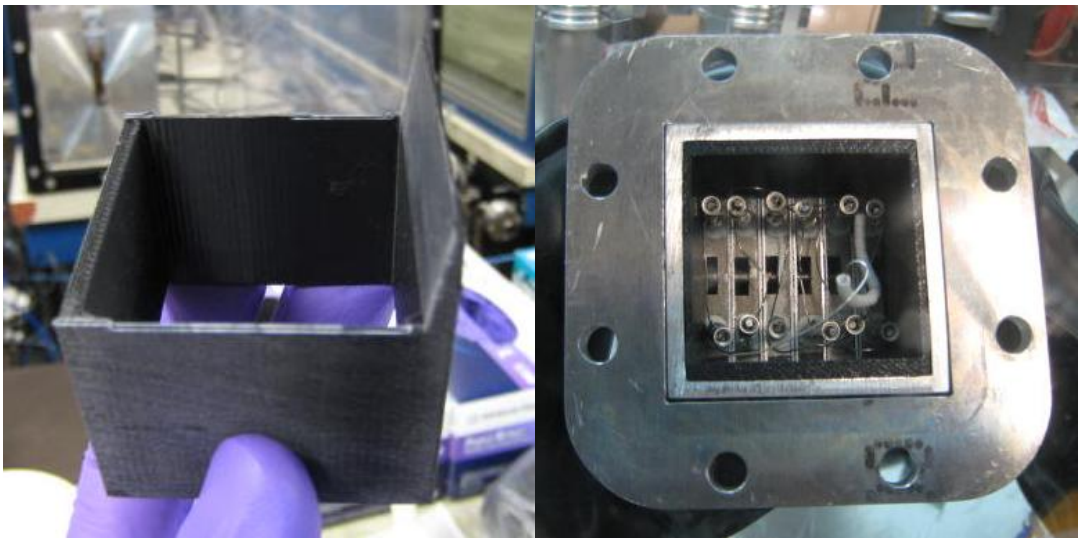

Figure 5.34: The 5-layer mini top spacer (left) has one side angled to push the stack against the side of the square device to ensure that the stack was properly grounded. The stack and spacers are inserted into the square Al housing (right).

Two additional permutations of longitudinal cylindrical form-fit detectors were assembled last. Both detectors consisted of eight Li foil longitudinal fins that were pointing towards the central anode wire. The radius of the detector was 2.5 cm and the width of the fins was 1.5 cm. An additional perimeter coating of ^{6}Li foil was included on both designs, and referred to as Wagon Wheels. The difference between the two designs was the electric field within the detectors. In Wagon Wheel A, the longitudinal fins remained electrically neutral, or floating, while the perimeter coating of Li foil was grounded. The grounded perimeter coating and finned insert were separated by a thin sheet of HDPE wire mesh. This detector configuration allowed the electric field to extend between the fins to the perimeter Li foil coating. The perimeter coating with the HDPE sheet is shown in Figure 5.35. In Wagon Wheel B, the thin HDPE layer was removed, which grounded both the longitudinal fins and the perimeter coating. These two designs were fabricated because it was unclear how the electric field would affect the charge collection between the longitudinal fins. If the electric field strength is too weak to extract charge from between the Li foil fins, then the charge collection efficiency would be low as well as the neutron detection efficiency. Furthermore, the distances between the longitudinal fins restricted the reaction product ranges more than the planar pattern devices, resulting in a higher percentage of smaller pulses compared to the signals from a planar pattern device. Thus, it is critical that no signals are lost due to insufficient electric field strength.

The longitudinal fins were constructed in the same manner as in the Dual and Quad designs. However, the Al frames had one of the longer sides of the square Al frame removed to form a square ‘C’ shape. When the frames remained as complete squares, the side of the frames closest to the anode caused the channel between two adjacent fins to be too narrow for sufficient charge extraction. The frames were still structurally rigid when the side was removed and fins were slid into placing using top and bottom cap groves. A perimeter coating was added to the devices in different manners as previously described. The detector without the Li foil perimeter coating is shown in Figure 5.36. Once the detectors were assembled and inserted into the test chambers, a counting curve was collected using the same cylindrical moderator and ^{252}Cf neutron source. Neutron and gamma-ray sensitivity measurements are presented in the following chapter.

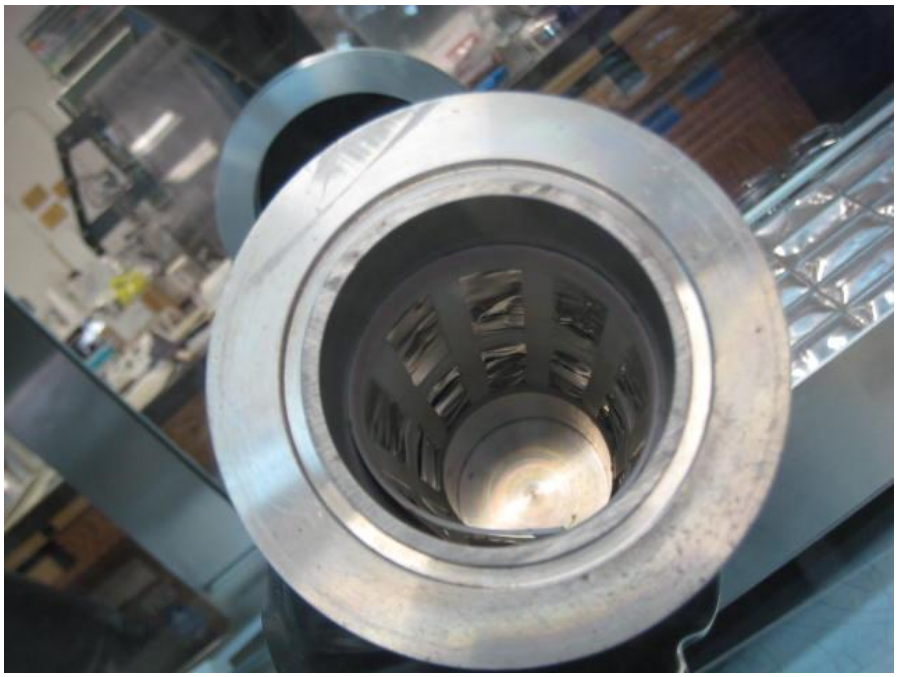

Figure 5.35: The perimeter coating of the Li foil position inside the tube with the thin plastic perforated sheet to prevent the foil insert from becoming grounded.

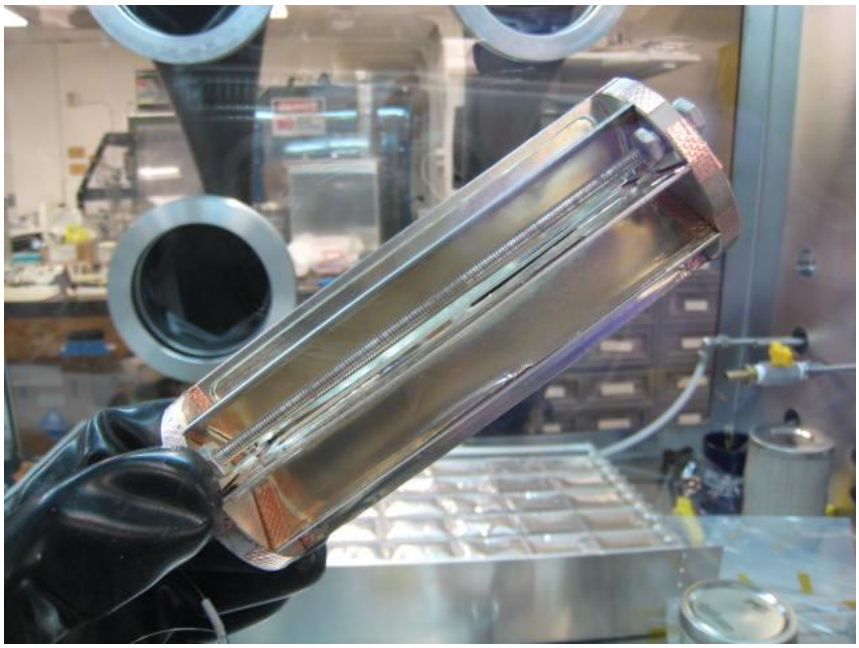

Figure 5.36: The Wagon Wheel design using eight longitudinal fins pointing inward towards the anode wire.

The remaining ‘conical’ design is the only design that does not have a neutron streaming path without the perimeter coating included. The conical design consists of angled Li foil washers stacked on top of one another with a space between them to allow for reaction product energy deposition. The distance between the foils would need to be optimized and might also affect the Li foil thickness that maximizes the thermal neutron detection efficiency. This design has not been constructed yet, and requires a different assembly method than the other form fit designs. Typically, the parts were designed and constructed at KSU and then mailed to SGC to be loaded with anode wires. The devices were mailed back to KSU and loaded with Li foil. The conical design, however, requires that the parts be constructed and loaded with Li foil at KSU initially. Then, the anode wire inserted down the middle of the detector. The anode wire loading would require an Ar glovebox and be more difficult due to the reduced finger dexterity caused by the gloves.

CHAPTER 6

NEUTRON SENSITIVITY TESTING OF AEROGEL, IMPREGNATED FOAM, AND LI FOIL MWPC'S

"It doesn't matter how beautiful your theory is, it doesn't matter how smart you are. If it doesn't agree with experiment, it's wrong"

-Richard P. Feynman

Described in chapter six are neutron and gamma-ray sensitivity results of aerogel, impregnated foam, and Li foil MWPCs. Results are presented in the same order as the detectors described in the previous chapter. However, the chapter begins by describing neutron detector evaluation methods. Following the evaluation methods, the earliest proof-of-principle test chambers using impregnated foam and Li foil are discussed first. Next, the results of the ^{10}B and ^{6}Li containing aerogels are presented, followed by mid-sized and large-area Li foil MWPC neutron and gamma-ray sensitivity results. Lastly, form-fit neutron detectors are discussed in detail and compared to a ^{3}He neutron detector.

6.1 Neutron Detector Sensitivity Evaluation Methods

Neutron detectors are typically evaluated, and compared, by their intrinsic thermal neutron detection efficiency, ε_{int}, defined qualitatively as [17]:

$$\varepsilon_{int} = \frac{number\ of\ radiation\ induced\ pulses\ per\ unit\ time}{number\ of\ radiation\ quanta\ incident\ upon\ the\ detector\ per\ unit\ time}, \qquad (6.1)$$

and quantitatively represented as

$$\varepsilon_{\text{int}} = \frac{r}{\Omega_f (BR) S}, \tag{6.2}$$

where r is the net count rate recorded from the detector, S is the source activity, and BR is the branching ratio of the emitted radiation. Ω_f is the factional solid angle calculated by:

$$\Omega f = 0.5(1 - \cos\theta), \tag{6.3}$$

where,

$$\cos\theta = \frac{d}{\sqrt{d^2 + R^2}}, \tag{6.4}$$

and d is defined as the distance from the source to the detector and R is the radius of the detector face [17].[4]

Another method for evaluating the intrinsic thermal neutron detection efficiency can be completed using experimentation. At the KSU TRIGA Mark II nuclear reactor, a diffracted neutron beam is essentially a pure collimated thermal neutron source, which is illustrated in Figure 6.1. Neutrons generated in the fuel of the reactor have a prompt fission spectrum from ^{235}U can be represented by the Watt distribution, as shown in Figure 6.2 [46, 73],

$$\chi(E) = ae^{-E/b} \sinh\sqrt{cE}\ , \tag{6.5}$$

where a = 0.5535, b = 1.0347, c = 1.6214, and E is the neutron energy [46, 73]. The neutrons are moderated in the water and graphite reflector of the reactor and a portion of the neutrons pass

[4] These equations are for point sources and detector with a circular effective area. More equations for other source and detector types and dimensions can be found in the literature [17].

through the radial beamport. The neutrons passing through the beamport are now incident on the pyrolytic graphite diffraction crystal. The thermal neutron energy spectrum from neutron leakage through the radial beamport can be represented by the Maxwell-Boltzmann distribution [73]

$$M(E) = \frac{2\pi}{(\pi kT)^{3/2}} \sqrt{E} \exp\left(-\frac{E}{kT}\right), \tag{6.6}$$

where E is the neutron energy, k is Boltzmann's constant (k = 8.617 x 10^{-5} eV K^{-1}) and T is the thermal equilibrium temperature. The flux distribution of the thermalized neutrons can be approximated by multiplying Eq. 6.6 by the neutron velocity v and the neutron number density n_o in the medium [73]

$$\phi_M(E) = v n_o M(E) = \frac{2\pi m_o}{(\pi kT)^{3/2}} \left(\frac{2}{m}\right)^{1/2} E \exp\left(-\frac{E}{kT}\right) \tag{6.7}$$

Both forms of Maxwell-Boltzmann distribution for the thermal neutrons are shown in Figure 6.2, which reveal the most probable energy E_p and velocity v_p are

$$E_p = \frac{1}{2} kT, \tag{6.8}$$

and

$$v_p = \sqrt{\frac{2kT}{m_n}}, \tag{6.9}$$

which for thermal equilibrium at T = 20°C, E_p = 0.0126 eV and v_p = 2200 m/s [73].

Once the thermal neutrons enter the diffraction crystal, Bragg scattering occurs. Bragg diffraction of the thermal neutrons in the crystal relies on the lattice spacing between the crystal planes to couple with the incident thermal neutron wavelength (λ = 1.8 Å). The relationship between the diffracted neutron wavelength λ and the crystal plane spacing d of the pyrolytic

graphite and elastic scattering angle θ_B (shown in Figure 6.3) is represented mathematically as [74, 75]

$$n\lambda = 2d \sin \theta_B , \tag{6.10}$$

where n is an integer. The pyrolytic graphite has a unique periodic hexagonal lattice, which produces a quasi-single crystal in which the ordering of the crystal is in only two dimensions. This crystal behaves as almost a pure monochromator, but there is some slight contamination of the odd harmonic states (n = 3 and 5), but they are essentially considered negligible because the higher harmonic energies are almost outside of the Maxwell-Boltzmann distribution and, thus, their probabilities are low. More information and discussion about the diffracted thermal neutron beam can be found in [74, 75]. However, the detectors neutron sensitivity is measured with an almost pure thermal neutron beam.

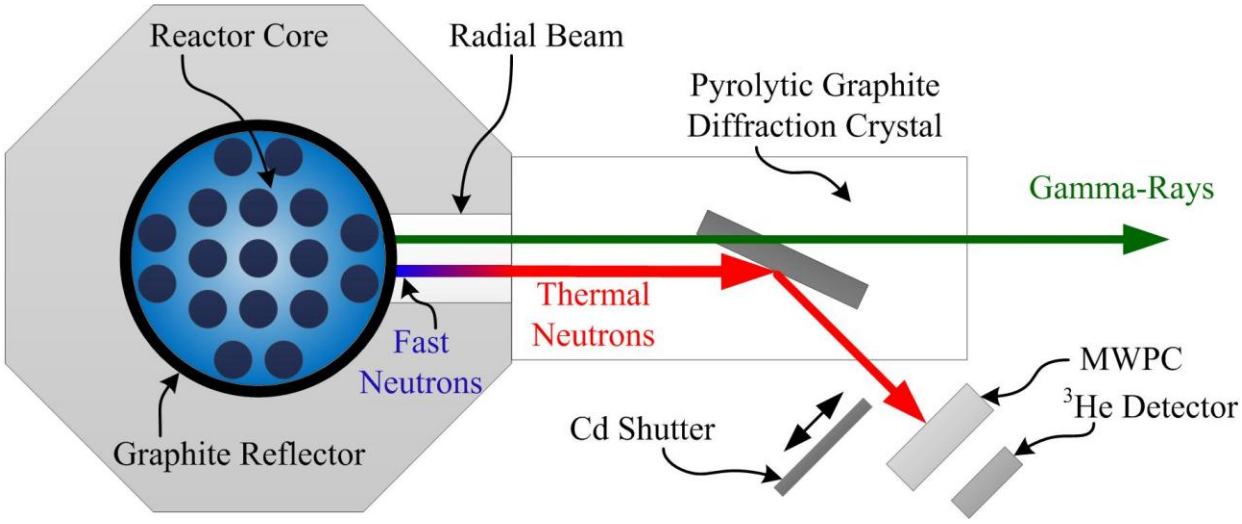

Figure 6.1: A schematic top-view illustration of the detector setup and diffracted neutron beam. Only thermal neutrons are diffracted at the diffraction crystal and higher energy neutrons and gamma-rays transmit through the crystal. The diffracted beam contains a Cd shutter and the detector positions are shown when performing intrinsic thermal neutron detection efficiency measurements.

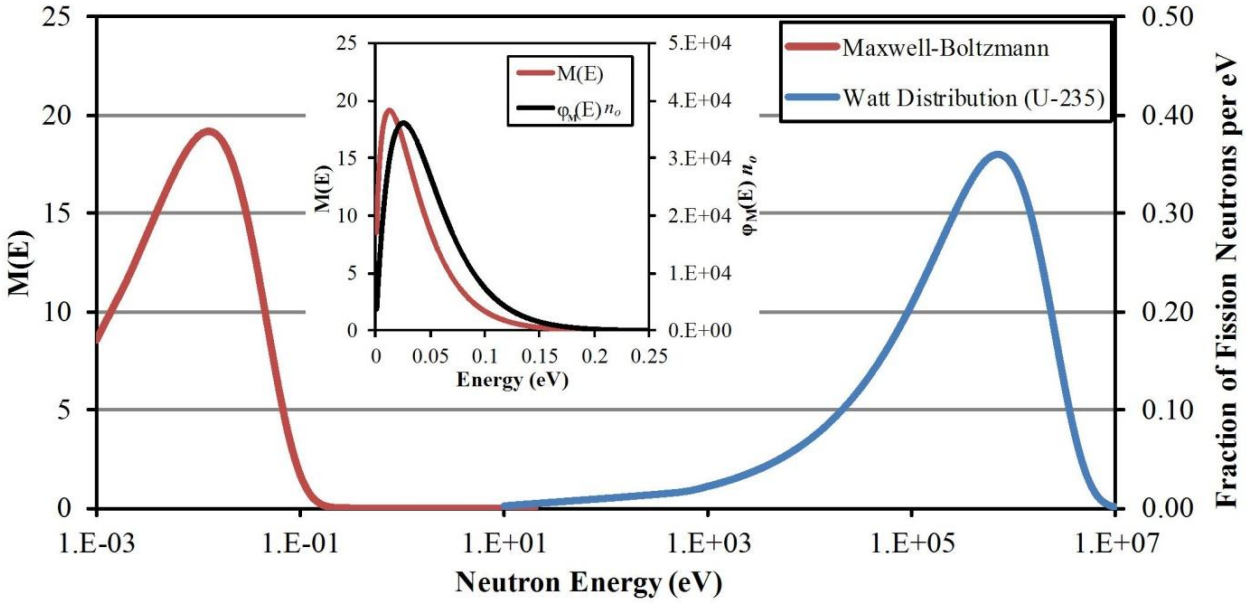

Figure 6.2: The Watt distribution (blue) of ^{235}U is the fission neutron energy distribution, but when the neutrons emerge from the beam port they are thermalized about a Maxwell-Boltzmann distribution (red). The inset shows a comparison of the two Maxwell-Boltzmann distributions discussed.

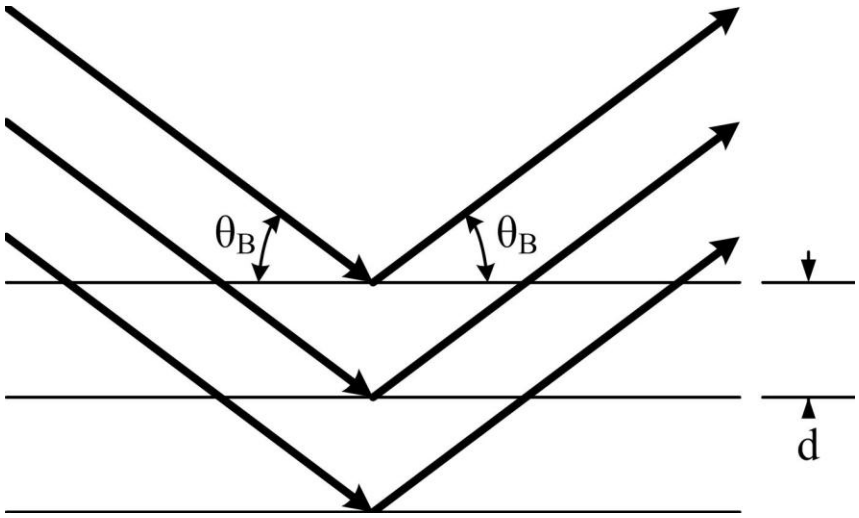

Figure 6.3: Depiction of Bragg diffraction off of crystal planes with spacing d and particle angle θ_B.

The intrinsic thermal neutron detection efficiency can be obtained by completing three measurements with the diffracted neutron beam. The first measurement, *a*, was obtained by placing the MWPC in the collimated neutron beam port. The second measurement, *b*, was collected from a calibrated ^{3}He neutron detector (ε_{int} = 80.5%), positioned directly behind the MWPC detector in the neutron beam with the MWPC detector remaining in position. The final measurement, *c*, was collected from the ^{3}He neutron detector in the same position, but the MWPC detector was removed. The detector setup in relation to the diffracted neutron beam is shown in Figure 6.1.

$$\left(1-\frac{b}{c}\right) = \text{neutron attenuation,} \tag{6.11}$$

$$\left(\frac{a}{c-b}\right) = \text{neutron fraction,} \tag{6.12}$$

$$\left(1-\frac{b}{c}\right)\left(\frac{a}{c-b}\right)\varepsilon_{^{3}He} = \varepsilon_{\text{int}}. \tag{6.13}$$

A simpler method of calculating detector efficiency using measurements *c* and *a* is possible

$$\left(\frac{a}{c}\right)\varepsilon_{^{3}He} = \varepsilon_{\text{int}}, \tag{6.14}$$

but does not provide any information regarding percent of neutrons absorbed (neutron attenuation, Eq. 6.11) or the percent of neutrons absorbed that are also counted (neutron fraction, Eq. 6.12) [62]. However, knowledge of the neutron attenuation can be vital information in confirming and understanding new neutron detector technology.

Although the best way to measure the thermal neutron detection efficiency of a detector is by using a diffracted thermal neutron beamport, the intrinsic neutron detection efficiency of a device can be measured as long as the incident neutron energies fall in the 1/*v* region of the neutron absorber used in the detector. As shown in Chapter 2, the Breit-Wigner formula defines the 1/*v*

region of neutron absorbers and shows that this region only begins below the lowest resonance energy [44]. In this region, even though the neutron absorption cross section is lower at higher energies, the count rate will not change because the velocity of the neutrons is higher. Thus, even if a continuum of neutron energies is present, as long as the neutron energies fall within the $1/v$ absorption cross section region the neutron count rate will not change.

The method described above to obtain the intrinsic thermal neutron detection efficiency requires a calibrated detector with a known thermal neutron detection efficiency. However, methods do exist that do not require a calibrated detector or a calibrated neutron beam. The following method used to determine neutron detection efficiency of a detector without a calibrated source was developed by McGregor and Shultis [44]. This method utilizes the fact that count rates do not change in a detector if the neutron absorber medium in the device follows the $1/v$ behavior. Two detectors can be placed in the path of the thermally diffracted neutron beam; one used a reference detector and the other as the 'test' detector. The thermal neutrons pass through the test detector first and a count rate in the reference detector can be recorded. The count rate R_{out} recorded by the reference detector can be represented as [44]

$$R_{out} = R_{in} e^{-\Sigma_w t_w} e^{-\Sigma_g t_g} e^{-\Sigma_w t_w} = R_{in} e^{-2\Sigma_w t_w} e^{-\Sigma_g t_g} \tag{6.15}$$

where R_{in} is the count rate recorded by the reference detector when the test detector is not in position, Σ_w is the macroscopic cross section of the outer material, or shell, of the test detector, which may be stainless-steel in many cases, Σ_g is the macroscopic cross section of the neutron absorber material inside the test detector, t_w is the thickness of the outer casing of the test detector, most likely less than 1.0 mm, and t_g is the inner dimension of the test detector that absorbs neutrons. If the test detector is filled with a neutron sensitive gas, then t_g would be the inner diameter of the tube. The neutron transmission factor T_d of the test detector is [44]

$$T_d = e^{-2\Sigma_w t_w} e^{-\Sigma_g t_g} = \frac{R_{out}}{R_{in}}, \tag{6.16}$$

where the macroscopic absorption cross section of the outer material of the test detector is multiplied by two because the neutron beam passes through the casing twice, once when entering

the detector and again when exiting the device. Eq. 6.16 also accounts for the neutron absorption purely from the material inside the test detector. The neutron absorption cause by the outer casing of the test detector can be determined by placing a test detector in the same position as before, but removing the neutron absorber material from inside the detector. The neutron transmission of the outer wall T_{2w} can be represented by [44]

$$T_{2w} = e^{-2\Sigma_w t_w} = \frac{R_w}{R_{in}}, \tag{6.17}$$

where R_w is the count rate recorded by the reference detector with the empty test detector positioned in the neutron beam. The neutron transmission factor by the material inside the test chamber T_g can be obtained by substituting Eq. 6.17 into Eq. 6.16 to show [44]

$$T_g = \frac{R_w}{R_{in}} e^{-\Sigma_g t_g} = \frac{R_{out}}{R_{in}}$$

$$T_g = e^{-\Sigma_g t_g} = \frac{R_{out}}{R_{in}} \frac{R_{in}}{R_w}$$

$$T_g = \frac{R_{out}}{R_w} = e^{-\Sigma_g t_g}. \tag{6.18}$$

However, this does not reveal the true neutron detection efficiency because the neutron beam passed through one layer of the outer material of the test detector. Thus, the neutron transmission fraction through one outer wall of the test chamber is [44]

$$T_{1w} = \sqrt{T_{2w}} = \sqrt{e^{-2\Sigma_w t_w}} = e^{-\Sigma_w t_w} = \sqrt{\frac{R_w}{R_{in}}}. \tag{6.19}$$

If the test detector and reference detector both contain neutron absorber materials that demonstrate the 1/*v* behavior, then the intrinsic neutron detection efficiency ε_g of the test detector can be calculated by [44]

$$\varepsilon_g = e^{-\Sigma_w t_w}(1-e^{-\Sigma_g t_g}), \tag{6.20}$$

and substituting Eqs. 6.18 and 6.19 into Eq. 6.20 yields

$$\varepsilon_g = \sqrt{\frac{R_w}{R_{in}}}\left(1-\frac{R_{out}}{R_w}\right). \tag{6.22}$$

However, if the test detector does not follow a 1/*v* behavior, then a slight correction factor can be applied to solve the intrinsic neutron detection efficiency [44]

$$\varepsilon_g = \frac{\sigma_{ao}}{\sigma_{to}} e^{-\Sigma_w t_w}(1-e^{-\Sigma_g t_g}), \tag{6.23}$$

where σ_{ao} is the absorption cross section that results in events that contribute to the counts recorded by the test detector and σ_{to} is the total interaction cross section of the target nuclei.

The diffracted thermal-neutron beam is available at KSU, but is not a common characterization tool for many institutions or research facilities. The increasing amount of research focused on alternative ^{3}He neutron detectors requires a new universal evaluation method that does not require a nuclear reactor. Thus, a team of scientists determined the new testing procedure for evaluating neutron detectors that did not require a nuclear reactor, but the tests only evaluate radiation portal monitors (RPMs). However, the thermal neutron beam port is the best method for determining the intrinsic thermal neutron detection efficiency of a detector. Most RPMs use two 5 cm diameter x 180 cm long ^{3}He neutron detectors in a 12.7 x 30.5 x 200 cm volume also partially filled with HDPE moderator. The two tube RPM neutron and gamma-ray sensitivity results were chosen as the minimum requirements for alternative neutron detector technology.

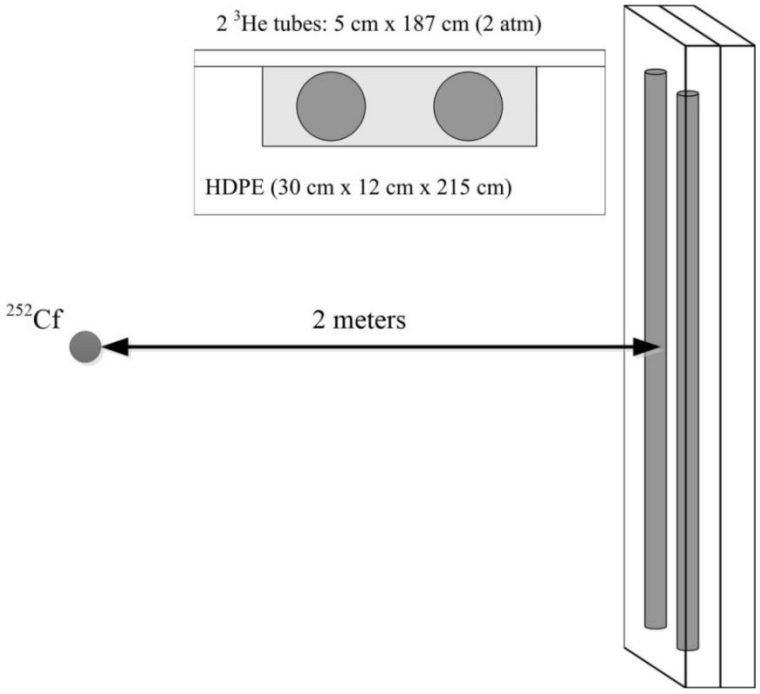

Figure 6.4: An illustration of the two ^{3}He tube RPM test setup.

The new RPM tests created by Pacific Northwest National Laboratory (PNNL) require a ^{252}Cf neutron source positioned 2.0 m from the front detector face, as shown in Figure 6.4. This test investigates the neutron sensitivity of the detectors by recording the net counts per second (cps) from the detector with the ^{252}Cf source. However, because ^{252}Cf neutron sources do not all have the same activity, the net cps are normalized by the source mass, in nanograms (ng). Thus, the numerical value used for detector comparison is in units of cps ng^{-1}, referred to as the absolute neutron detection efficiency, ε_{abs}, and represented as [24]:

$$\varepsilon_{abs} = \frac{Total\ Neutron\ Counts - Total\ Background\ Counts}{nanograms^{252}Cf \times Time}. \tag{6.24}$$

Additionally, the ^{252}Cf source may be moderated or bare during the ε_{abs} measurements. If moderated, the thickness is limited to 5.0 mm of Pb followed by 25.0 mm of HDPE. The source must also be centered on the front face of the detector. The second measurement tests gamma-ray sensitivity of the detector, which is a critical evaluation of RPM replacement detectors. If a detector is sensitive to gamma rays, then gamma-ray events may cause false-positive alarms,

thereby mistaking a gamma ray source for a neutron source. If every Naturally Occurring Radioactive Material (NORM) were to set off alarms, stopping commerce transportation for further investigation of false-positive alarms would add many time delays with significant added cost. A detector's ability to discriminate gamma rays is evaluated using the Gamma-ray Rejection Ratio (GRR). GRR is the net number of counts recorded by the detector divided by the number of gamma rays striking the active area of the detector. Typically, a ^{60}Co gamma ray source is positioned at a distance that the exposure rate to the front face of the detector is 10 mR hr^{-1}. The GRR is found quantitatively by [24]

$$GRR = \frac{Total\ Gamma\ Counts - Total\ Background Counts}{S \times BR \times \Omega_f \times Time}, \tag{6.25}$$

where S is the source strength in Bq, BR is the branching ratio (for ^{60}Co, BR = 2). The fractional solid angle, Ω_f, is slightly different than presented earlier because the detector now has a square shaped effective area,

$$\Omega_f = \frac{1}{\pi} \arctan\left[\frac{W \times L}{4 \times D \times \sqrt{\frac{W^2}{4} + \frac{L^2}{4} + D^2}} \right], \tag{6.26}$$

where W is detector width, L is detector length, and D is the distance from the source to the detector [24]. (Note, GRR is obtained without the neutron source present.) The last nuclear test involves both radiation sources present and is referred to as the Gamma Absolute Rejection Ratio in the presence of neutrons (GARRn). The GARRn is the absolute neutron detection efficiency in the presence of both neutrons and gamma rays, $\varepsilon_{abs+\gamma}$, divided by the absolute neutron detection efficiency without the gamma ray source present, or ε_{abs}. The GARRn can be represented by [24]:

$$GARRn = \frac{\varepsilon_{abs+\gamma}}{\varepsilon_{abs}}, \tag{6.27}$$

where,

$$\varepsilon_{abs+\gamma} = \frac{TotalCounts(n+\gamma) - TotalBackgroundCounts}{nanograms^{252}Cf \times Time}. \tag{6.28}$$

RPMs must pass several other non-nuclear tests, including sensitivities to temperature, moisture and dust, humidity, impact, magnetic fields, RF susceptibility, electrostatic discharge, and vibration [24]. However, these non-nuclear tests have not been performed with the MWPC and are, thus, not presented. These tests, however, will be completed by Saint Gobain Crystals when the MWPC detectors are ready for those tests. The requirements set by the two ^{3}He tube RPM are shown in Table 3 along with results of other commercially available RPM systems. However, Table 3 does not include the cost of each detector, which may be a significant contributing factor in determining a viable RPM replacement.

Table 3: The reported measurements of RPM ^{3}He alternative neutron detector systems completed by PNNL.

Test	Requirement	Wavelength Shifting Fibers[5]	Boron Coated Straws	^{10}B lined counters: 3 tubes	^{3}He: 2 tubes	BF_3: 3 tubes
ε_{abs} (cps/ng)	2.5	2.65	4.0	3.2	3.0	3.7
GRR @ 10 mR/hr	$1x10^{-6}$	$1x10^{-7}$	$1x10^{-9}$	$6x10^{-9}$	$1x10^{-7}$	$6x10^{-9}$
GARRn @ 10 mr/hr	0.90 – 1.10	1.08	1.00	1.01	1.00	-

[5] Recent reports show detectors from IAT with ^{6}LiFZnS(Ag) coated fibers were able to achieve 4.2 cps ng^{-1}.

6.2 First Evaluations

The first measurements performed with the 'proof-of-principle' detectors used natural Li foil of thickness less than the summed range of the reaction products. *Box A* was used to obtain neutron response pulse-height spectra of 30, 50, 75, and 120 μm thick Li foil, and the results are shown in Figure 6.5. Approximately 10.0 m of Li foil was obtained of 30, 50, and 75 μm thicknesses, thus, 10 layers of each foil thickness were positioned in *Box B*, and neutron response pulse-height spectra were collected. Pulse-height spectra obtained with *Box B* for the three Li foil thicknesses investigated are shown in Figure 6.6. The intrinsic thermal neutron detection efficiency was measured for the three 10 layer detectors tested at the KSU diffracted beam port using the method described in the previous section with a ^{3}He proportional counter. The intrinsic thermal neutron detection efficiency of 30, 50, and 75 μm thick 10 layer devices was 8.1, 11.1, and 15.7%, respectively, and the theoretical efficiency values are 8.4, 12.6, and 16.3%, respectively. These neutron detection efficiencies are plotted with the theoretical values in Figure 6.7.

From the pulse-height spectra in Figure 6.5, it can be concluded that the amount of energy deposited by the reaction products was significantly higher than most commercially available neutron detectors. The high energy deposition assists with setting a relatively high LLD to eliminate gamma-ray signals. The gamma-ray sensitivity tests were obtained using the 75 μm thick 10 layer Li foil MWPC with a 70 mCi ^{137}Cs gamma ray source (E_{γ} = 661.7 keV) positioned 6.0″ from the front of *Box B*. The pulse-height spectra obtained with the 60Co source gamma-ray exposure is shown in Figure 6.6. As seen in Figure 6.6, the gamma rays created small pulses in the device, lower than a typical LLD setting of the MWPC. The materials used to assemble the detector were Li and Al, both relatively low Z-materials, thus, low gamma-ray sensitivity was expected. The valley created between the electronic noise and the main features of the pulse-height spectra allows the LLD to be set high enough to remove essentially all gamma-ray interactions with minimal loss in total neutron counts or neutron detection efficiency. Additionally, a large valley is observed between the electronic noise and the main feature of the pulse-height spectrum. The valley and pulse-height features change from *Box A* to *Box B*, but was still an obvious spectral feature. The change in valley width and depth from the pulse-height spectra obtained with *Box A* compared to *Box B* was due to the restricted reaction product ranges

in the P-10 gas. The adjacent Li foils were positioned 4.5 cm apart, a distance less than the triton reaction product range in P-10 gas (7.25 cm).

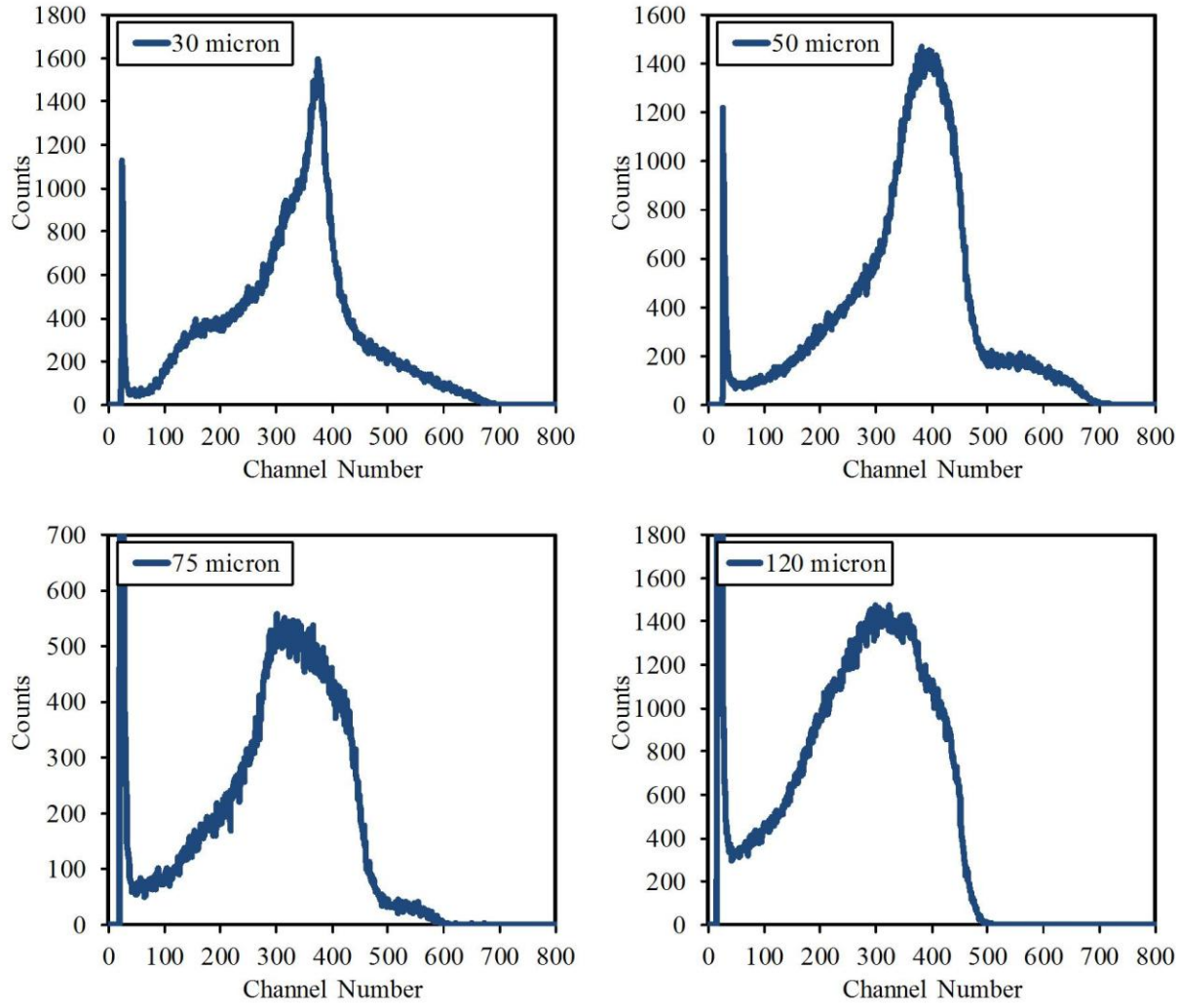

Figure 6.5: The neutron response pulse-height spectra of single layers of 30, 50, 75, and 120 µm thick Li foils obtained using Box A.

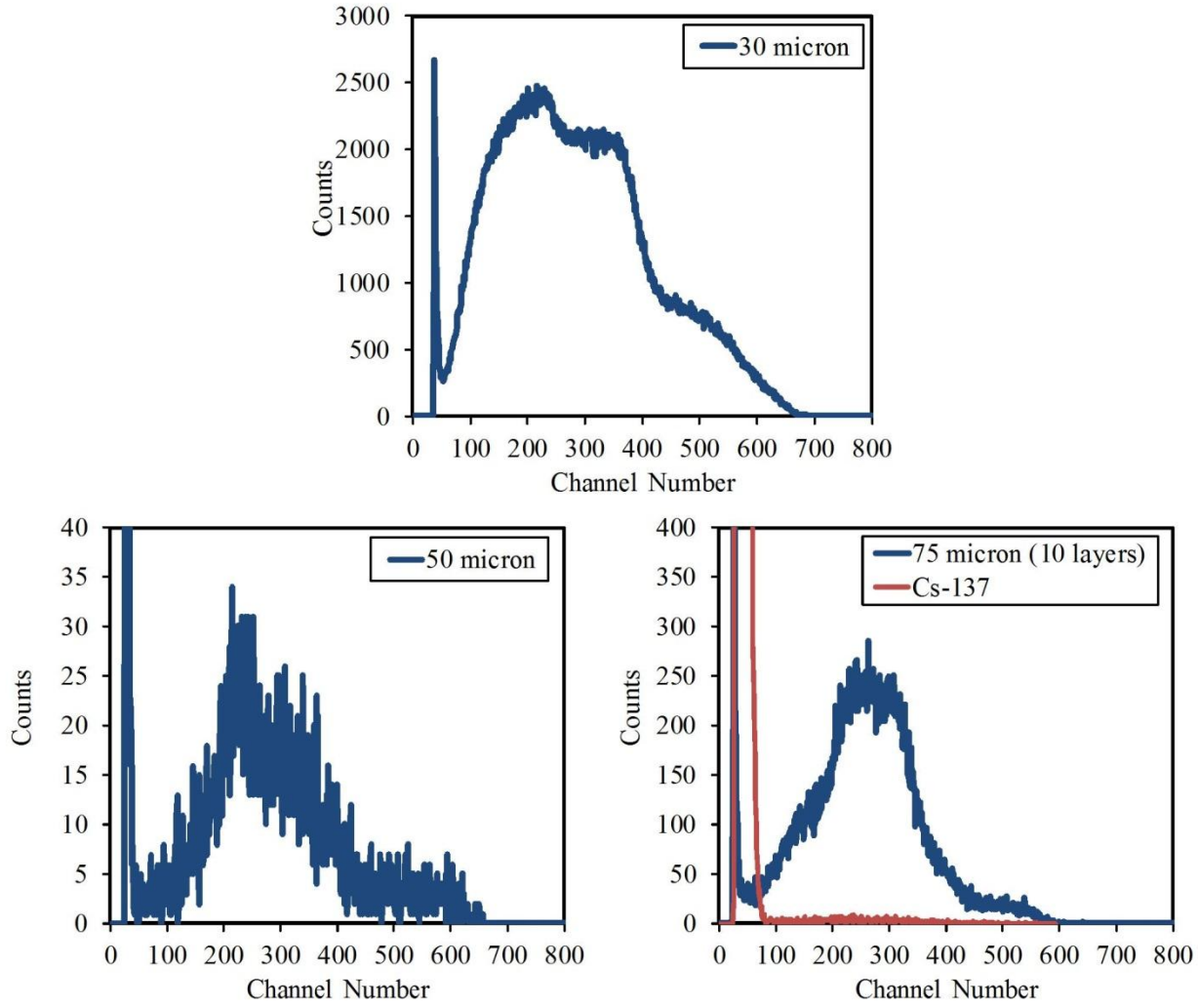

Figure 6.6: Neutron response pulse-height spectra obtained using 10 layers of 30, 50, and 75 µm thick natural Li foil in Box B.

The accuracy of the intrinsic thermal neutron detection efficiency measurements compared to the theoretical values was also a key component in the advancement of the detectors. The difference in efficiencies was less than 2.0%. Discrepancies in the measurements most likely resulted from short counting times, 300 sec, resulting in less than 10,000 total counts and, thus statistical error greater than 1.0%. Further, discrepancies could have arisen from inconsistency in Li foil thickness. The assumption was made that the Li foil thickness was uniform, but was never confirmed. However, because the experimental and theoretical neutron detection efficiency matched well, it was concluded that the predicted neutron detection efficiencies with the enriched ^{6}Li foil (Figure 3.2) should be possible.

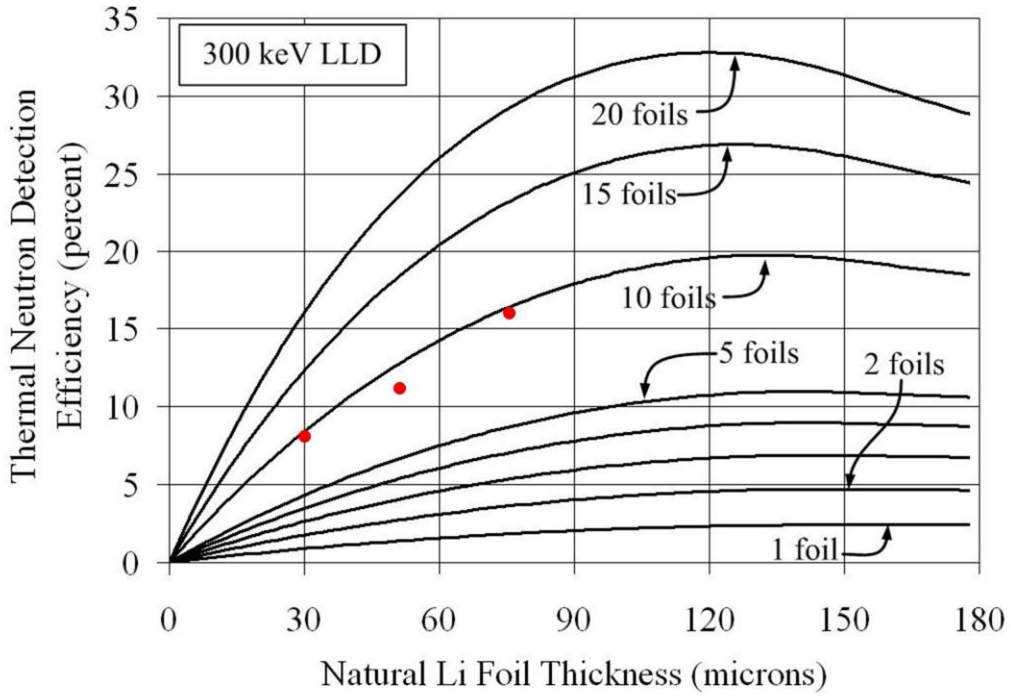

Figure 6.7: A plot of the intrinsic thermal neutron detection efficiency of the natural Li foil MWPC as a function of the foil thickness for various numbers of natural Li foil layers. The three red dots represent the experimentally calculated neutron detection efficiencies of the 30, 50, and 75 µm thick 10 layer devices.

Open-cell polyurethane foam impregnated with 10% LiF & B_2O_3 were fabricated by Future Foam, and single layers of foam approximately 3.0 mm thick, were positioned in the diffracted thermal neutron beam port using *Box A.* Pulse-height spectra obtained with the LiF and B_2O_3 impregnated foam using *Box A* are shown in Figure 6.8 and Figure 6.9, respectively. The streaming paths of reaction product trajectories and self-absorptions occurring in the LiF material and foam struts result in a broad continuum of reaction product energies entering the proportional gas. As described in the previous chapter, the goal is to measure both reaction products simultaneously on each side of the impregnated foam sheets. In order to ensure reaction products escape both sides of the absorber an energy calibration with the detector must be performed to demonstrate pulses greater than 2.73 MeV are measured. Any pulse larger than 2.73 MeV can occur only when both reaction products escape simultaneously and are measured concurrently in the gas volume. The probability of measuring both reaction products

simultaneously should increase as the foam thickness decreases. However, cutting the impregnated foam into sheets less than 2.0 mm thick because difficult due to the softness and cutting method required to create the impregnated foam sheets.

The strut density is approximate 1.2 g cm^{-3}, thus, the theoretical summed range of reaction products is approximately 63 μm. The average strut width, 50 μm, is less than the reaction products summed range. Thus, theoretically, reaction products should be able to escape the foam sheets simultaneously. However, the vertices where many struts join together has a thickness up to several hundred micrometers, and the reaction products will not be able to escape simultaneously. Conversely, the 50 μm thick reported average strut thickness is the strut diameter and, most likely, the reaction products will not traverse through the direct center of the strut. Most reaction products will travel through only a fraction of the total strut thickness.

The pulse-height spectrum obtained with the B_2O_3 impregnated foam sheet, has identifiable pulse-height features. The well-known wall effect is prevalent and a result of the boron oxide power granules being too large in diameter for both reaction products to escape simultaneously. Further, the strut thicknesses and density would not allow for both reaction products to escape the foam concurrently. As explained earlier, the stair-step pulse-height spectra is a result of a continuum of reaction product energies occurring from self-absorption of the alpha particle and Li ion reaction products in the material before entering the gas volume. One method that may reduce, or remove, the wall-effect in the ^{10}B impregnated foam pulse-height spectrum is to nano-size the B or use B nanotubes. The B granules would now be small enough that reaction products could escape simultaneously. However, the average foam strut diameter (50–60 μm) is too thick for reaction products to escape concurrently. If a material with smaller strut sizes, not necessarily foam, were to incorporate ^{10}B, then there would be an increased chance of both reaction products escaping simultaneously. An example of this material would be BN nanotubes woven together into a thin fabric.

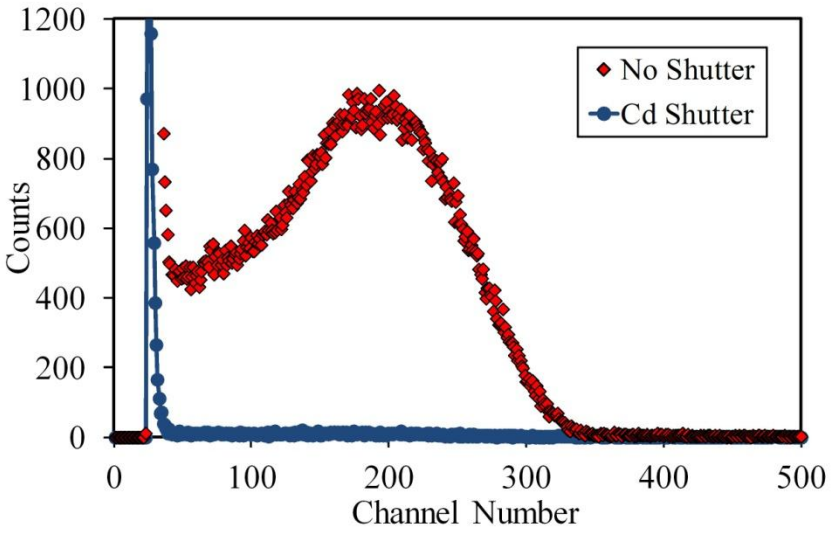

Figure 6.8: The neutron response pulse-height spectrum of a single layer of open-celled polyurethane foam impregnated with 10% natural LiF. An additional measurement was made with a Cd shutter to block all incident neutrons, thus, proving the pulse-height spectrum is truly a neutron response.

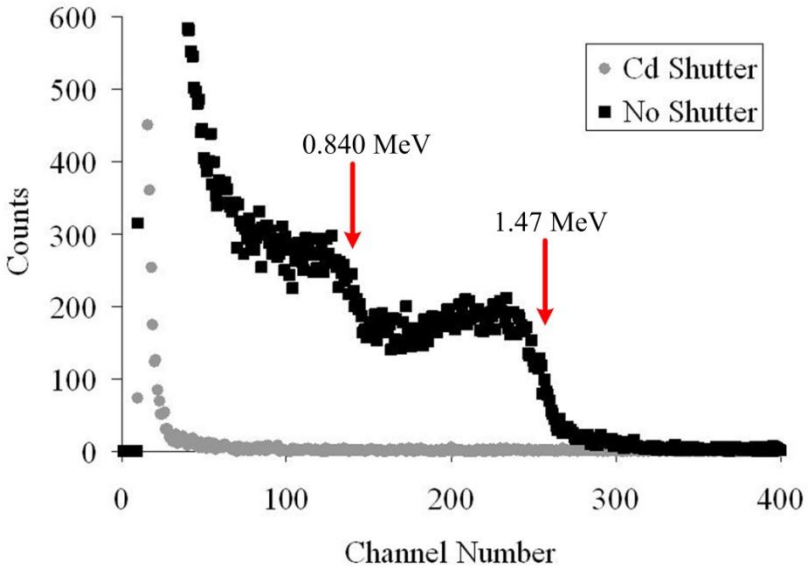

Figure 6.9: The neutron response pulse-height spectrum of a single layer of open-celled polyurethane foam impregnated with 10% natural B_2O_3. An additional measurement was made with a Cd shutter to block all incident neutrons, thus, proving the pulse-height spectrum is truly a neutron response.

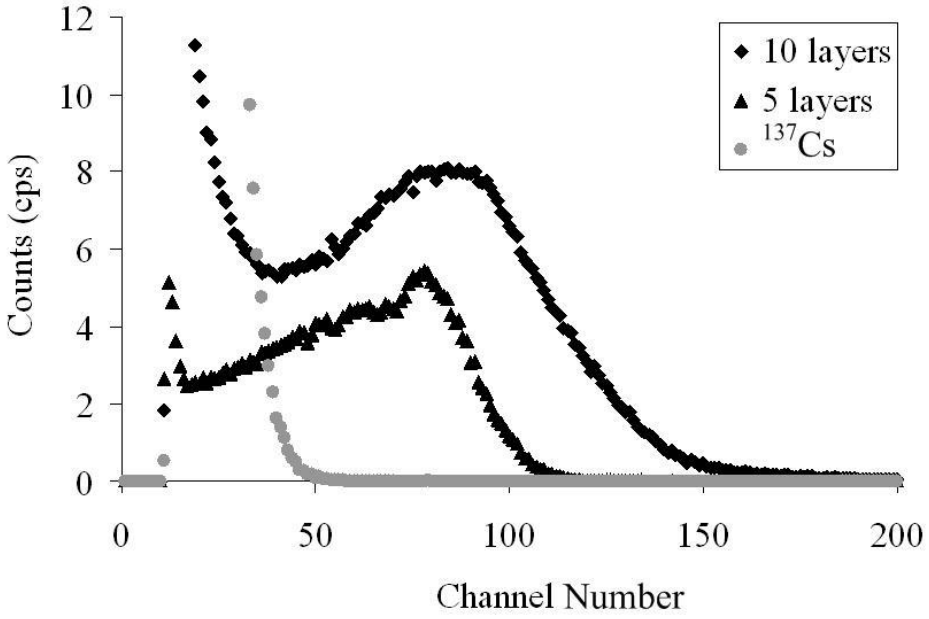

Figure 6.10: The neutron response pulse-height spectra of 5 & 10 layers of 4.5% ^{6}LiF impregnated open-celled polyurethane foam.

Boron impregnated foams were not investigated any further due to the wall-effect in the B_2O_3 impregnated foam pulse-height spectrum. However, the LiF impregnated foam pulse-height spectrum was encouraging because of the apparent valley between the electronic noise and the main feature of the pulse-height spectrum. Thus, enriched ^{6}LiF was used to impregnate foam to 4.5% and the sample was cut into 10 layers each approximately 2–3 mm thick. Foam sheets were positioned in *Box B*, and the intrinsic thermal neutron detection efficiency was determined experimentally, and was calculated to be 7.3%. In addition, five of the 10 foam layers were removed, which increased the distance between each foam layer to 9 cm. The valley depth in the pulse-height spectrum shown in Figure 6.10 increased when half of the foam sheets were removed. However, no easily identifiable pulse-height features were observed. A 70 mCi ^{137}Cs gamma ray source was used to test the gamma-ray sensitivity of the impregnated foam neutron detector. The signals from the gamma-ray exposure appear in the lower channels of the pulse-height spectrum and appear to occupy large portion of the neutron response pulse-height spectrum. However, the exposure rate was approximately 1000 mR hr^{-1} for the gamma-ray tests,

two orders of magnitude higher than typical gamma-ray sensitivity test requirements. These experiments were the most recent investigation of impregnated foam neutron detector, but nanoization of the LiF powder is currently being completed and saturation levels of the foam should be obtained soon.

6.3 Aerogel Neutron Sensitivity Results and Discussion

Borosilicate aerogel ($B_2O_{19}Si_{12}$) was the first known recorded use of an aerogel for neutron detection [67, 76]. The sample was a disc approximately 2.5 cm in diameter and 3.2 mm thick with a density of approximately 50 mg cm^{-3}. The borosilicate sample did not contain a high percentage of B, less than 0.1%, thus, the neutron detection efficiency was not measured. The disc was suspended in an Al frame allowing the aerogel sample to rest in the center of an Al cathode test chamber (Figure 5.9). Neutron sensitivity of the sample was tested at the KSU diffracted thermal neutron beam port. The resulting neutron response pulse-height spectra obtained with the borosilicate aerogel disc is shown in Figure 6.11, and resulted in two distinctive peaks occurring around channel numbers 50 and 63. The borosilicate aerogel sample was replaced with a silica sample (contained no ^{10}B) and had no spectral features in the pulse-height spectrum. Thus, the absence of peaks in the pulse-height spectrum with the silica aerogel sample proves that the peaks from the borosilicate aerogel were induced by neutron interactions. However, if pure ^{10}B was used in the sample, it would contain only 6% neutron sensitive material. This percentage is far too low to fabricate a valid ^{3}He replacement neutron detector.

Another factor affecting neutron detection efficiency with the aerogel samples is the reaction product escape probability. Determining reaction product ranges experimentally also proves to be difficult without knowing where the two peaks in the pulse-height spectrum originate. However, several samples were fabricated at thicknesses ranging from 3.0 mm up to 6.0 mm and neutron response pulse-height spectra were collected. A 6.0 mm thick borosilicate aerogel sample was used to collect a pulse-height spectrum, which the lower energy peak, seen in Figure 6.9, is significantly reduced, almost disappearing, as shown in Figure 6.12. Thus, the conclusion can be made that one of the reaction product ranges, may be less than 6.0 mm and greater than 3.0 mm.

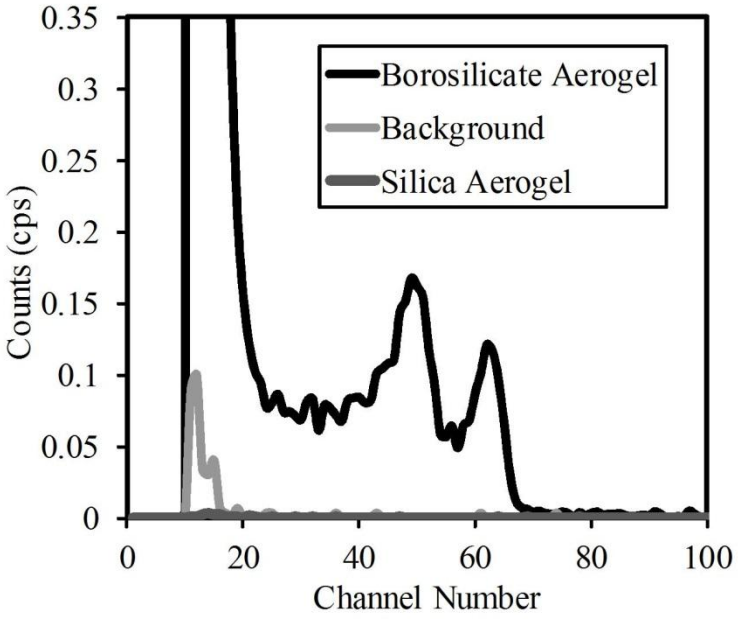

Figure 6.11: The thermal neutron response pulse-height spectra obtained from borosilicate and silica aerogel. This is the first known record of aerogel used as a neutron detector.

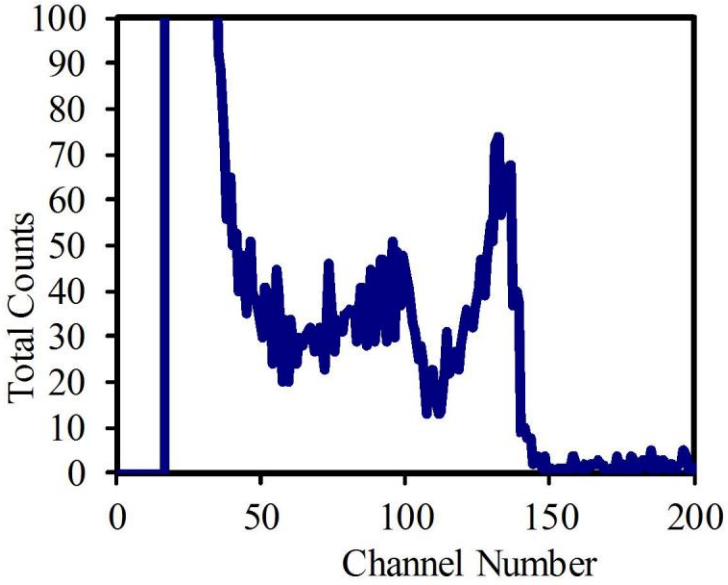

Figure 6.12: The thermal neutron response pulse-height spectrum obtained from a 6.0 mm thick borosilicate aerogel sample.

6.2 Li Foil MWPC Neutron Response: Large Area, Mid-Sized, and Form Fit

The mid-sized and large-area Li foil MWPC's containing 5 layers of 75 μm thick Li foil were investigated separately and positioned approximately 10 feet from a ^{252}Cf neutron source. The pulse-height and counting curves, shown in Figure 6.13, were obtained from the detectors while exposed to the ^{252}Cf neutron source to determine ideal operating voltage bias. The ideal bias was chosen to be 900V for both the mid-sized and large-area Li foil MWPC neutron detectors. The intrinsic thermal neutron detection efficiency was measured for each detector using the experimental methods described in Section 6.1 and calculated to be 53.8 ± 0.20% and 53.7 ± 0.24% for the mid-sized and large-area Li foils MWPCs, respectively. (The theoretical maximum is 55% for five layers of 95% enriched ^{6}Li foil.) Further, the mid-sized MWPC was angled such that the thermal neutron beam passed through all five Li foil layers. Angling the detector allowed the neutron beam passed through approximately 110 μm of Li foil in each layer because of the incident neutron angle. The measured intrinsic thermal neutron detection efficiency for the angled setup was calculated to be 58.6 ± 0.21%. The intrinsic thermal neutron detection efficiency increased when the detector was angled because the increased Li foil thickness absorbed more neutrons, but the reaction product escape probability remained constant.

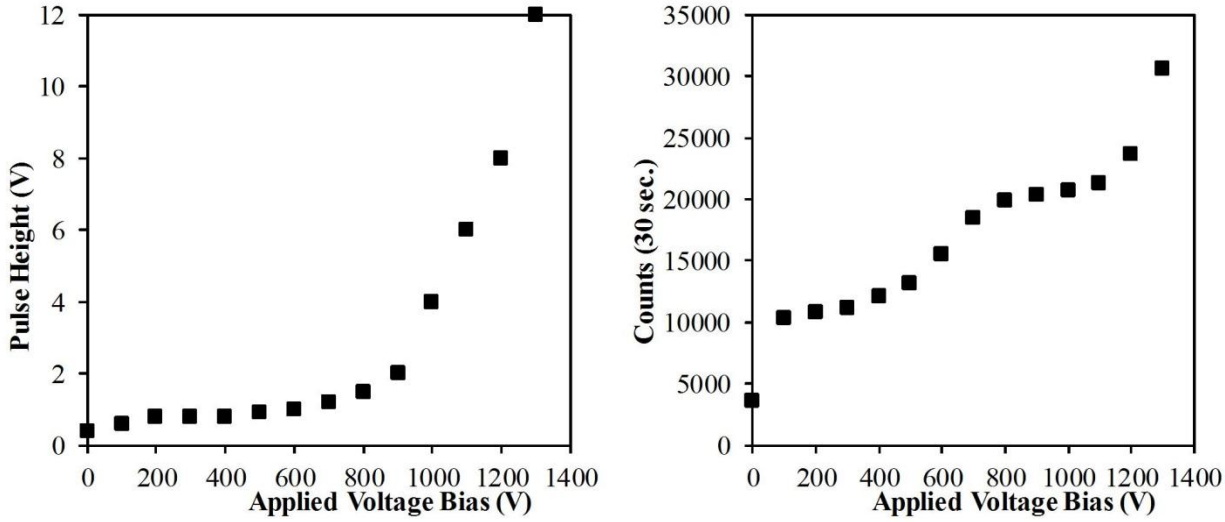

Figure 6.13: The pulse height curve (left) and counting curve (right) of the Li foil MWPC neutron detectors when positioned in front of the ^{252}Cf neutron source.

The thermal neutron response pulse-height spectra obtained with the mid-sized Li foil MWPC, shown in Figure 6.14, were obtained at P-10 gas pressures of 1.0, 1.5, 2.0, and 2.8 atm. The simulated pulse-height spectra obtained using MCNP6 are also included at each P-10 gas pressure. Examination of Figure 6.14 indicates that the MCNP6 predicted pulse-height spectra match well to the experimental results. The accuracy of the simulations yields confidence that such simulations are useful predictors for responses of additional detector geometries. The sharp structures in the simulated results are from the supposition that all energy deposited in the gas contributes to the pulse height spectrum with equal contribution, in other words, no charge collection differences from electric field variations or detector geometry were included in the simulation. These other influences smear the experimental results from the simulated results. Also, electronic noise adds to uncertainty and spectral 'smearing' in the experimental data. Even so, the salient features from the simulations are present in the experimental pulse-height spectra.

At 1.1 atm of P-10 gas pressure, the experimental pulse-height spectra are nearly a perfect match to the simulated data. The overlap between the simulated and measured pulse-height spectra is greatest for the 1.1 atm P-10 gas pressure, and the amount of overlap between the two spectra decreases as the P-10 gas pressure is increased. Raising the gas pressure reduces charge carrier mobility, which consequently reduces charge carrier velocity. Because all measurements were conducted at 900V, the velocity, and consequent charge collection, reduced as gas pressure increased.

The applied voltage was kept constant at all P-10 gas pressures investigated, thus, when the pulse-height spectra are not normalized to the same energy scale, the largest pulses occur for the lowest gas pressure, as shown in Figure 6.15. This difference in pulse height at different pressures is most likely a result of decreased mobility and increased recombination rate of electron-ion pairs with increasing pressure. However, changing the device pressure does not change the intrinsic thermal neutron detection efficiency, unlike typical gas-filled neutron detectors such as ^{3}He and $^{10}BF_3$. The measured intrinsic thermal neutron detection efficiency of the mid-sized Li foil MWPC at P-10 gas pressures of 1.5, 2.0 and 2.8 atm were 53.3%, 53.0%, and 52.9%, respectively. Obtaining ideal voltage biases of the Li foil MWPC at higher pressures would mostly likely increase the precision of the simulations and experimental pulse-height spectra at higher P-10 gas pressures. Because the pulse heights decrease with increasing gas pressure, the neutron detection efficiency decrease slightly due to pulses falling below the LLD

setting. The mid-sized Li foil MWPC was exposed to ^{252}Cf and AmBe neutron sources and ^{60}Co and ^{137}Cs gamma ray sources. The exposure rates of the ^{60}Co and ^{137}Cs gamma ray sources were 10 mR hr^{-1} and 70 mR hr^{-1}, respectively. The resulting pulse-height spectra obtained from the mid-sized Li foil MWPC at P-10 gas pressures of 1.0, 1.5, 2.0, and 2.8 atm with exposure to the two neutron and gamma ray sources are shown in Figure 6.16.

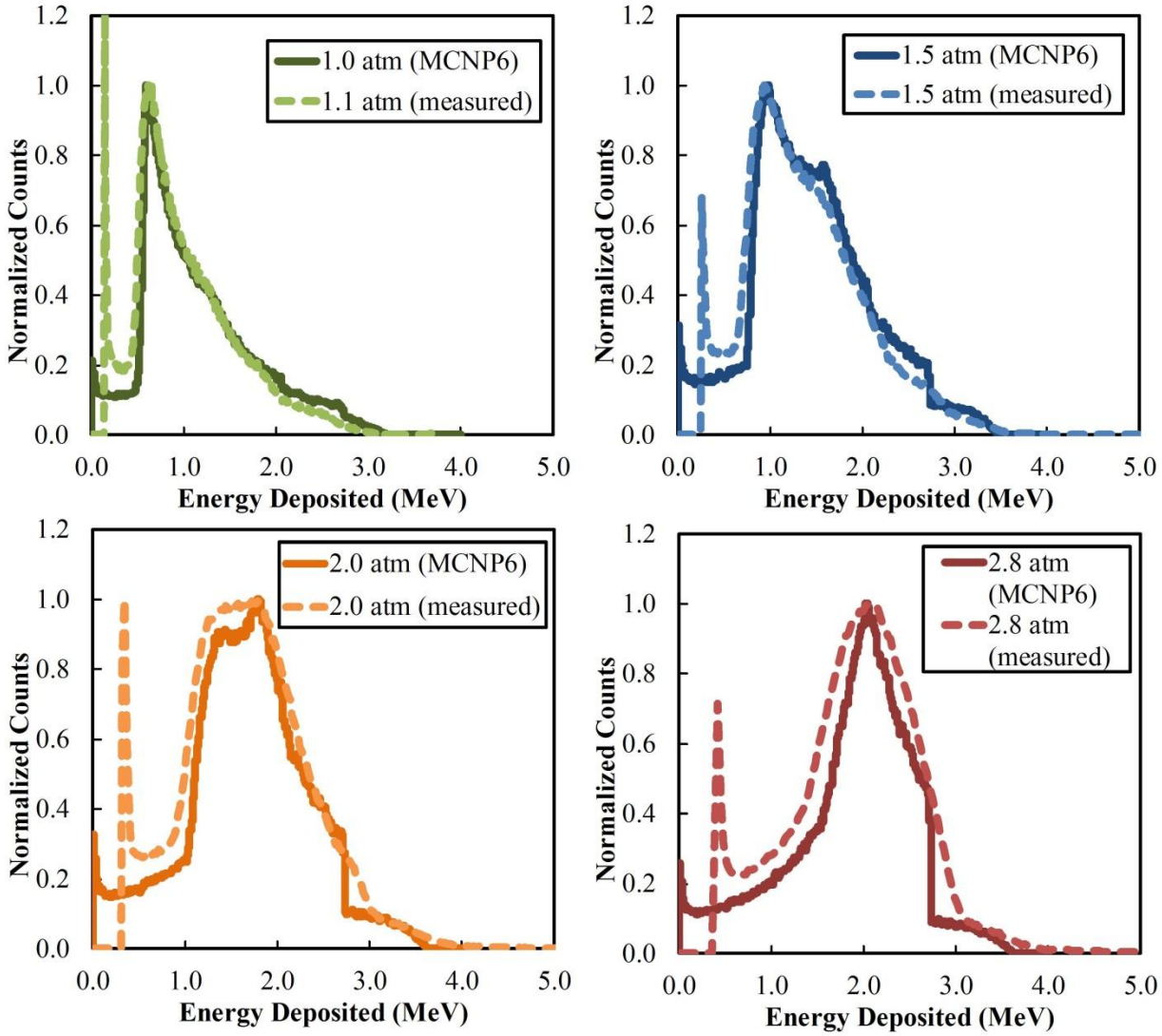

Figure 6.14: The thermal neutron response pulse-height spectra of the mid-sized Li foil MWPC obtained at P-10 gas pressures of 1.0, 1.5, 2.0, and 2.8 atm are shown in the lighter dashed lines. The simulated thermal neutron response pulse-height spectra obtained using MCNP6 are represented by solid lines.

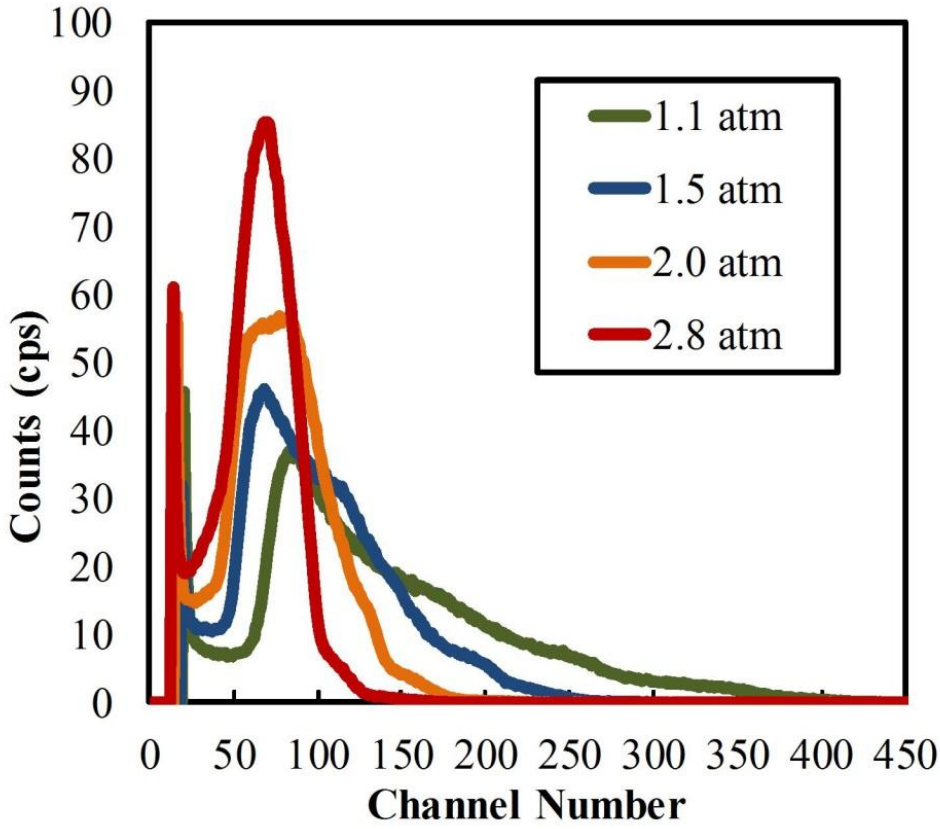

Figure 6.15: The thermal neutron response pulse-height spectra obtained with mid-sized Li foil MPWC at different P-10 gas pressures of 1.1, 1.5, 2.0, and 2.8 atm. The pulse-height spectra are not energy calibrated and larger pulses occur at lower gas pressures.

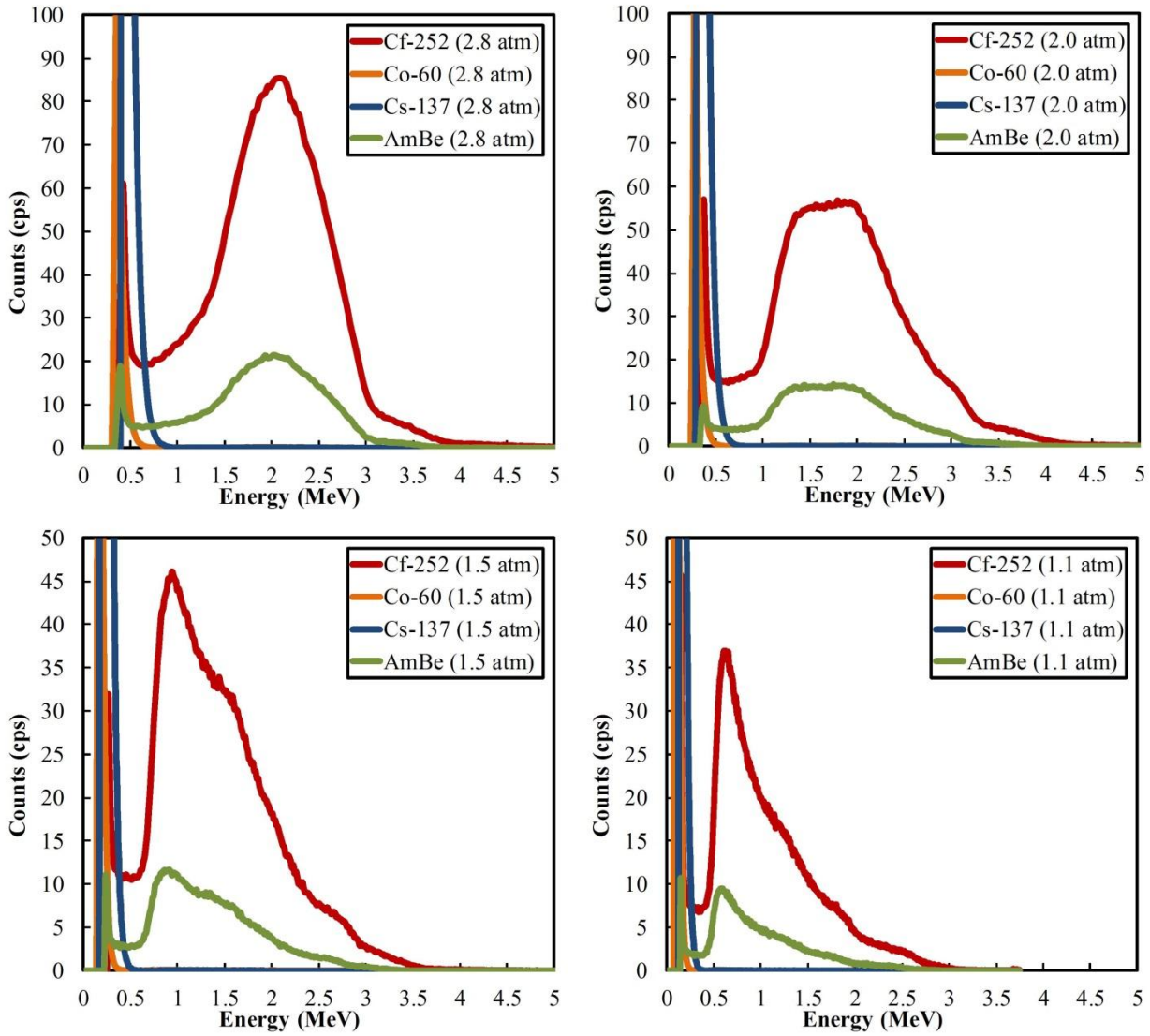

Figure 6.16: The neutron and gamma-ray response pulse-height spectra obtained with the mid-sized Li Foil MWPC from two different neutron and gamma ray sources. The detector was pressurized with P-10 gas to pressures of 1.1, 1.5, 2.0, and 2.8 atm.

The mid-sized Li foil MWPC was sent to the company Saint-Gobain Crystals (SGC) for PNNL RPM testing. The mid-sized Li foil MWPC, referred to as *Build 2*, was set up approximately 1.5 m above a concrete floor and positioned 2.0 m from the ^{252}Cf neutron source. The detector had 5.0 cm of HDPE moderator positioned on the front and 10.0 cm on the back. The ^{252}Cf source also had an optional moderator that consisted of 5.0 mm of Pb followed by 25.0 mm of HDPE. Measurements to calculate the absolute neutron detection efficiency (ε_{abs}), GRR, and GARRn were all collected with a ^{252}Cf source both moderated and unmoderated. Additionally, pulse-height spectra were collected for each measurement, which allowed the values to be plotted as a function of the LLD setting. The absolute neutron detection efficiency and GARRn are plotted as a function of the LLD energy in Figure 6.17, while the GRR is plotted in Figure 6.16. (The MCNP6 simulations allowed the LLD to be energy calibrated.) At a typical LLD setting (~500keV), the absolute neutron detection efficiency and GARRn were 0.75 cps ng^{-1} and 0.99, respectively. The GRR of the MWPC became negative around 400 keV as shown in Figure 6.18, a result of the background measurement having more counts than the GRR data set. However, the exposure rate of the ^{60}Co gamma ray source was increased to 40 mR hr^{-1} and the new calculated GRR and GARRn were 7.67 x 10^{-9} and 1.07. The GRR and GARRn meet the required values of the PNNL RPM replacement detector, but the absolute detection efficiency is lacking. The typical RPM allows for larger detectors than the mid-sized Li foil MWPC under investigation, and increasing the size of the detector will increase the absolute detection efficiency. Current RPMs are assembled in National Electrical Manufacturers Association (NEMA) boxes that contain all required RPM neutron detection equipment in dimensions of 30.5 cm x 215 cm x 12.7 cm.

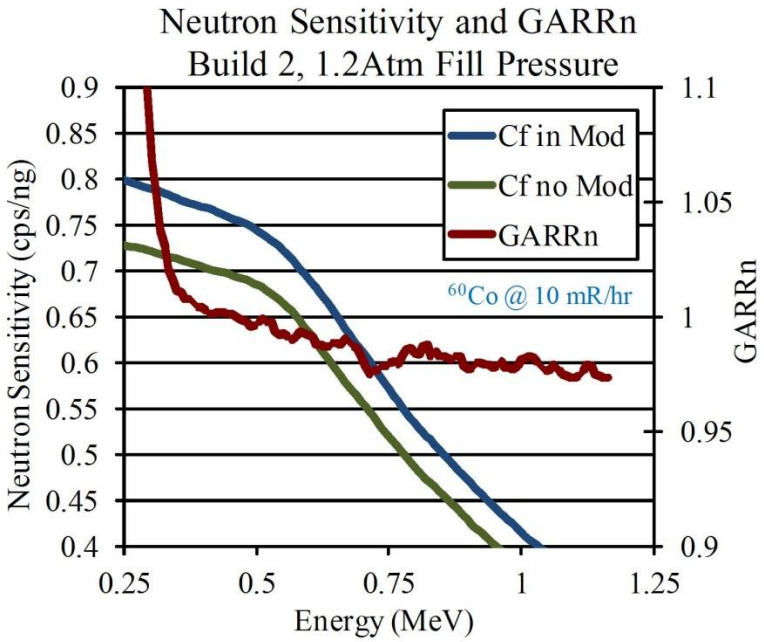

Figure 6.17: The GRR and GARRn of Build 2 (mid-sized Li foil MWPC) as a function of LLD energy. These values are within compliance of the PNNL RPM standard.

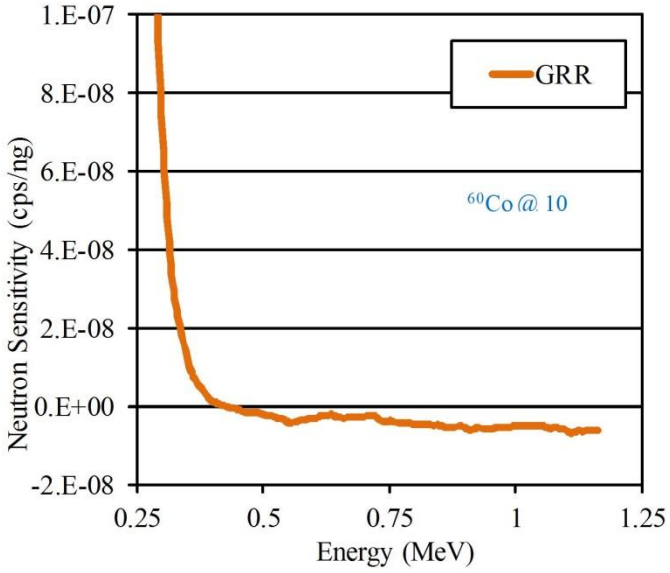

Figure 6.18: The GRR of Build 2 (mid-sized Li foil MWPC) as a function of the LLD energy. The values become negative because more counts were present in the background measurement.

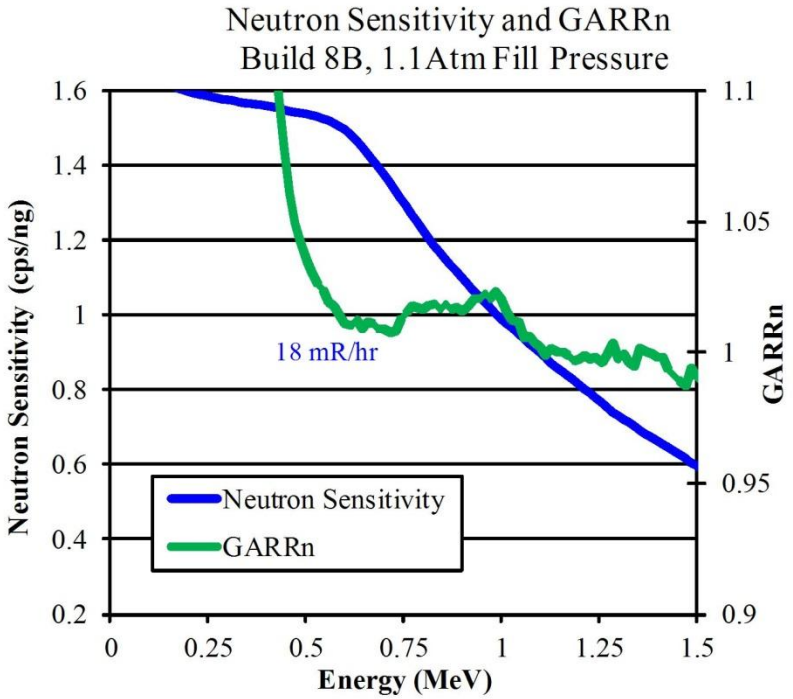

Figure 6.19: The absolute neutron detection efficiency and GARRn plotted as function of LLD energy for the large-area Li foil MWPC.

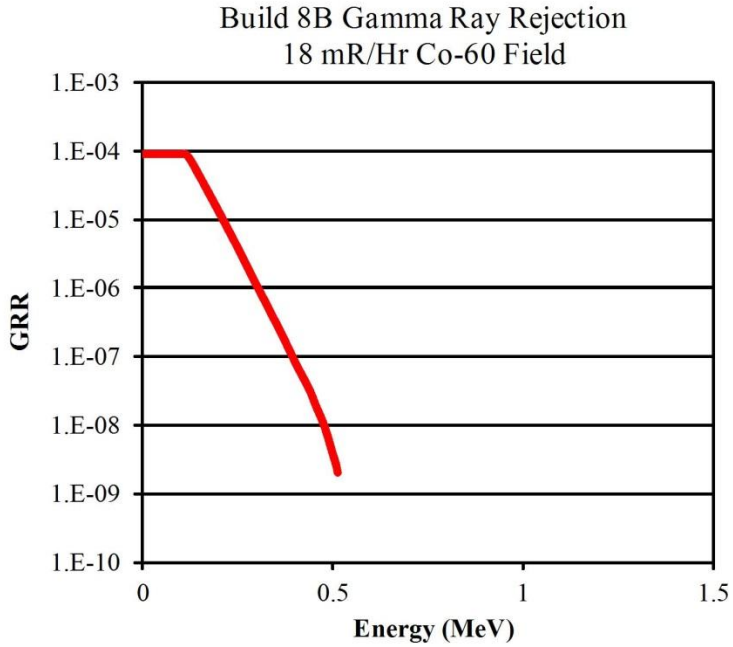

Figure 6.20: The GRR plotted as a function of LLD energy for the large-area Li foil MWPC. The values become negative after 500 keV.

The large-area Li foil MWPC was also sent to Saint Gobain Crystals for RPM measurements. The only difference in the tests was that the exposure rate from the ^{60}Co gamma ray source on the detector face was approximately 18 mR hr^{-1}, instead of 10 mR hr^{-1}. The absolute neutron detection efficiency and GARRn of the large-area Li foil MWPC, with a 650 keV LLD, were 1.5 cps ng^{-1} and 1.01. The absolute detection efficiency and GARRn were plotted as a function of the LLD energy in Figure 6.19. The GRR became negative again for this experiment at an LLD setting of 500 keV, as shown in Figure 6.20. The GRR and GARRn meet the requirements of PNNL RPM replacement neutron detectors. Even though the absolute detection efficiency doubled from 0.75 cps ng^{-1} to 1.5 cps ng^{-1} from the mid-sized to the large-area detector, the efficiency is still 1.0 cps ng^{-1} below the minimum requirement for RPMs. The RPM allows for three large-area devices to be stacked on top of one another. If the absolute neutron detection efficiency scales linearly with area, then the efficiency would result in ~4.5 cps ng^{-1}. However, the detector must become thinner (≤5 inch) in order to have moderator incorporated into the NEMA dimensional restrictions. Currently, the total detector thickness, including the HDPE, is approximately 30.0 cm, almost three times the allowed thickness.

6.2.1 Li Foil Corrugated Detector

The corrugated Li foil MWPC detector described in Section 5.7 was tested as a backpack neutron detector and compared to the mid-sized Li foil MWPC. Motivation for the corrugated Li foil MWPC design was the reduction in neutron streaming when neutrons traveled 90° to the front detector face. The corrugated Li foil MWPC was moderated with ¼″ thick HDPE on the sides, top, and bottom, and ¾″ of HDPE on the back. The corrugated MWPC with moderator was of the detector was positioned 15.5 feet from a ^{252}Cf source. Pulse-height spectra were collected with the corrugated MWPC at P-10 gas pressures of 1.0 and 1.5 atm and the results are shown in Figure 6.21. In the pulse-height spectra there is a valley between the electronic noise and the main feature of the pulse-height spectrum, similar to the results with the planar pattern Li foil MWPC. However, the valley is more narrow and shallow with the corrugated Li foil design than the planar configuration. The Li foil dimensions and geometry inside the corrugated MWPC detector restricted reaction product ranges. A triton reaction product escaping from the center of

a Li foil strip traveling at a 45° angle into an adjacent Li foil will not have sufficient energy to traverse the foil. Thus, reaction product ranges are more restricted in the corrugated MWPC than the planar pattern detector. Consequently, less energy is deposited in the gas with the corrugated design, thus, forming the more shallow and narrow valley in the pulse-height spectrum.

A planar pattern Li foil MWPC, with the same configuration and dimensions as *Build 2*, was also used as a backpack neutron detector and compared to the corrugated design. The planar pattern MWPC was tested first to determine optimal HDPE dimensions on the detectors. The weight limit for backpack neutron detectors is 25 lbs. The detector with no HDPE moderator weighed 17 lbs, thus, allowing for 7-8 lbs of HDPE moderator to be added to the detector. The three sets of HDPE thickness tested on the side and back of the detector were 1/8″ and 7/8″, 1/4″ and 3/4″, and 1/2″ and 1/2″, respectively. The highest neutron count rate from a ^{252}Cf source resulted when 1/4″ of HDPE was on the sides, top, and bottom in addition to 3/4″ on the back of the detector. The resulting pulse-height spectrum of the planar pattern detector with the HDPE is shown in Figure 6.22. Additionally, the detector gamma-ray sensitivity was tested with using a ^{137}Cs gamma ray source at exposure rates of 10 mR hr^{-1}, 100 mR hr^{-1}, and 400 mR hr^{-1} and the pulse-height spectra are also included in Figure 6.22. The same HDPE moderator thicknesses were positioned on the corrugated Li foil MWPC and neutron sensitivity measurements were collected. The count rates from the planar and corrugated Li foil MWPCs with HDPE moderator were 380 ± 1.1 cps and 279 ± 0.96 cps, respectively.

MCNP6 simulations were completed for the same detector and moderator geometries described previously for the planar and corrugated desigs. Angular sensitivity of each detector design was completed in the simulation by rotation a ^{252}Cf source around each detector from 0–180° in 10° increments. (Results are shown in Figure 6.23.) Even though the simulation predicted a higher angular neutron sensitivity with the corrugated MWPC, when tested experimentally, the planar pattern MWPC had a higher count rates.

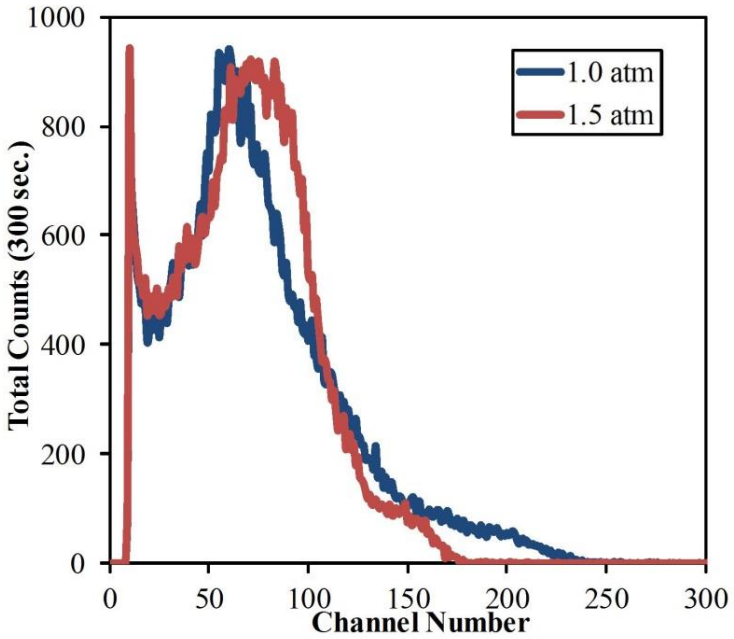

Figure 6.21: The neutron response pulse-height spectra collected from the corrugated pattern Li foil MWPC at P-10 gas pressures of 1.0 and 1.5 atm.

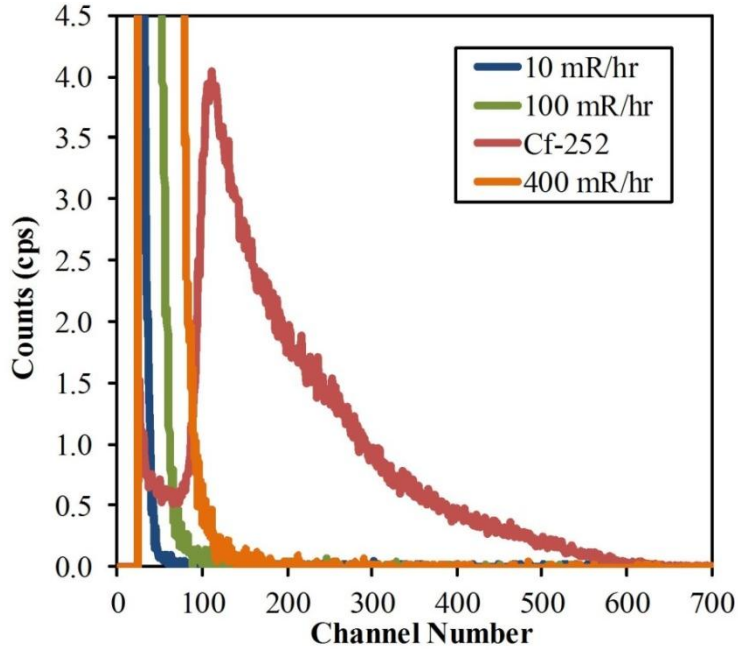

Figure 6.22: The pulse-height spectra obtained from the planar pattern backpack neutron detector. The detector gamma-ray sensitivity was tested at exposure rates of 10, 100, and 400 mR hr^{-1} using a ^{137}Cs source.

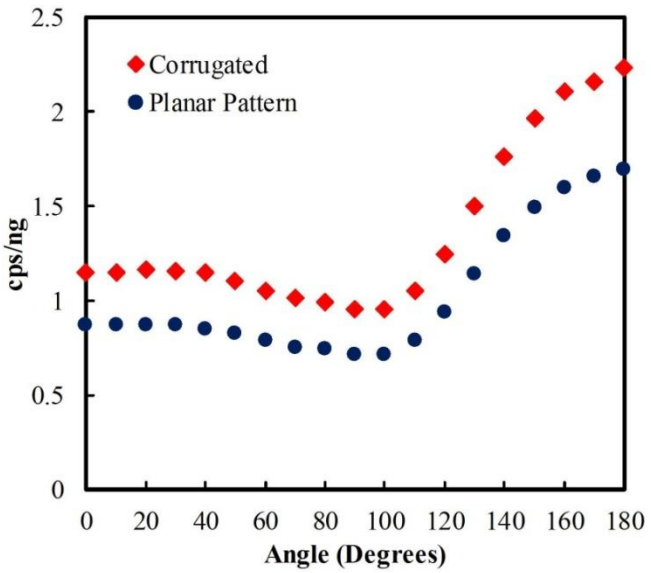

Figure 6.23: The absolute neutron detection efficiency of the small planar Li foil MWPC and the corrugated design as a function of the incident neutron angle. The phantom was positioned between the detector and the source at 0° (i.e. User facing away from the source).

Conceptually, neutrons are scattering in the HDPE moderator and traveling through the foils in non-normal incident angles. Because of the foil geometry in the corrugated design, there is a higher probability of absorbing these random incident angle neutrons than in the planar design. However, the count rates previously reported demonstrate otherwise because the percentage of open area in the planar pattern MWPC compared to the corrugated MWPC were not the same in the experiments and simulations. In the simulations, no Al foil support frames were included, thus, 100% open area was assumed for both the planar and corrugated patterns. However, the percentage of open area of the corrugated design was only 68%, while the planar pattern open area was 78%. Further, the planar pattern MWPC and contained 6% more ^{6}Li foil than the corrugated MWPC. The difference in open-area percentages is most likely the cause of the discrepancies between the experimental count rates and the simulation results.

6.2.2 Li Proportional Counter (LPC) Detector: Monster Truck Rally

Two large-area Li foil MWPC detectors were positioned back-to-back with 5 cm of HDPE positioned between the detectors and on the front and back of the assembly, referred to as the

Lithium Proportional Counter (LPC). Additionally, 1.0″ thick sheets of HDPE were included on the bottom, sides, and top of the detector system, which is shown in Figure 6.24. The detector weighed approximately 250 lbs, but the LPC could be easily disassembled and allowed the detector to be transported by two average sized men. The arrayed system was delivered to Oak Ridge National Laboratory (ORNL) for neutron and gamma-ray sensitivity testing.

Figure 6.24: The LPC detector delivered to ORNL for neutron and gamma-ray sensitivity testing.

Due to weight restrictions, the detector size was limited by the moderator weight. However, had there been no weight restriction, then the LPC could have been built on a much larger scale covering more area. The weight restrictions limited the LPC to two detectors and 15 cm of total HDPE moderator thickness. Shown in Figure 6.25 is a plot of the LPC HDPE moderator optimization. The LPC was modeled in MCNP6 by positioning a bare ^{252}Cf source 2 m from the front face of the detector and recording the intrinsic neutron detection efficiency of the LPC. Moderator optimization was completed by setting middle moderator thickness t_{middle} to constant values while varying ratios of front to back moderator thicknesses. For example, if the t_{middle} was 5 cm, that left a total of 10 cm of HDPE to split between the front and back moderators. If the

ratio of t_f to t_b (t_f/t_b) was 1.0, then the thicknesses of the front and back moderator were both 5 cm. If t_f/t_b was ~0.4, then the front and back moderator thicknesses were approximately 3 cm and 7 cm, respectively. A MCNP6 simulation was completed for each data point shown in Figure 6.25 and revealed the highest intrinsic thermal neutron detection efficiency occurred with t_f = 3.9 cm, t_{middle} = 6.0 cm, and t_b = 5.1 cm. However, HDPE thicknesses are not readily available at these thicknesses, but 5 cm (2″) thicknesses are available, thus, 5 cm of HDPE was used in all three sections. The 5 cm thickness in each section was assumed to be acceptable because from Figure 6.25 the intrinsic thermal neutron detection efficiency with 5 cm of HDPE in each section is almost the same as the efficiency with the optimized thicknesses. Also from Figure 6.25, the intrinsic neutron detection efficiency is dependent mostly on the middle moderator thickness. There is a larger change in the detection efficiency when the middle moderator thickness is varied than when the front and back moderator thicknesses are changed. Additional moderator optimization plots for one and three detector configurations are included in Appendix C.3.

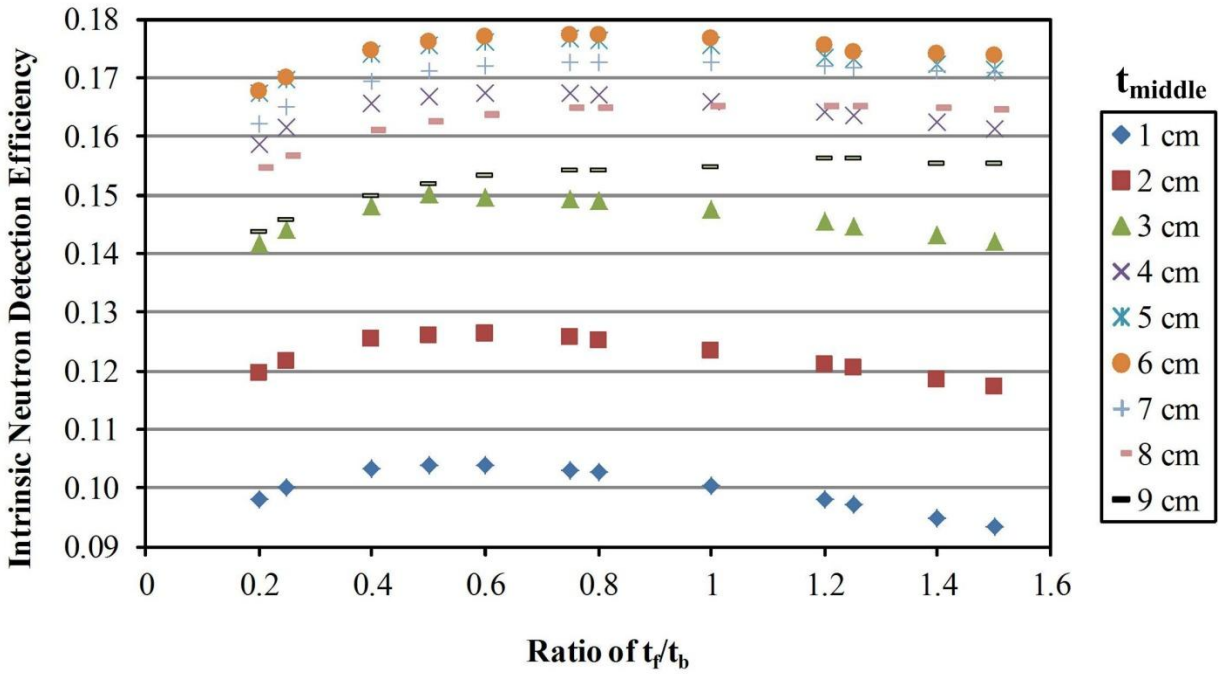

Figure 6.25: The HDPE moderator optimization was completed using MCNP6 by varying the ratio of the front (t_f) and back (t_b) moderator for different constant middle (t_{middle}) moderator thicknesses.

The weight restriction provided for the test was general: liftable by two graduate students. It was chosen that the moderator should weight approximately 200 lbs, which is a significant amount of HDPE moderator. One method to get around transporting the heavy moderator would be to use an empty water tank with positions for the MWPC detectors to reside. In other words, replace the HDPE with water by transporting a light weight empty water tank and filling it up with water once the detector is setup. The intrinsic thermal neutron detection efficiency with water moderator instead of 5 cm of HDPE in each section reduced the intrinsic neutron detection efficiency slightly from 17.6% to 16.2%. However, the lower transportation weight would allow more detector be included in the LPC, consequently, increasing the overall detection efficiency.

For the first neutron measurement, a 73 μCi (117 ng) ^{252}Cf neutron source was positioned at 1, 2, 4, 6, 8, and 10 meters from the front of the detector. The absolute neutron detection efficiencies (cps ng^{-1}) measured with the LPC at the aforementioned distances is shown in Figure 6.26 for three different source moderator configurations. A bare ^{252}Cf source with no HDPE moderator was tested first, followed by two spherical moderator thicknesses of 2.0 cm and 8.0 cm.[6] Three one-minute measurements were recorded for each test procedure. This three measurement collection method was repeated for all experiments described for the LPC detector. However, only a portion of the results are presented in this thesis, but all results were similar. As shown in Figure 6.26, the highest absolute efficiency resulted when the ^{252}Cf source was not moderated. Increasing moderator thickness decreased the absolute neutron detection efficiency. This response was expected because the detector was optimized to for a bare ^{252}Cf source using MCNP6 simulations.

The stationary distance measurements were repeated in the Ward Hall basement hallway. The sides and back of the ^{252}Cf source at KSU was shielded to reduce the amount of neutrons scattering off the cinderblock walls. A picture of the experimental setup in Ward Hall is shown in Figure 6.27. In the stationary LPC tests completed at KSU, count rates were recorded at source to detector distances of 1, 2, 4, 6, 8, and 10 meters for lengths of time in which at least 10,000 total counts were recorded. The absolute neutron detection efficiency was calculated and compared to ORNL results, shown in Figure 6.28, which were slightly lower due to the openness

[6] The three source configurations were tested in all LPC detector experiments described, but only a portion of the data is presented in this manuscript.

of the ORNL test facility. However, at the closest setting, 1.0 meters, results from KSU and ORNL were comparable due to reduction of wall scatter by source shielding; this experiment validated the ORNL tests. Additionally, the LPC detector was modeled in MCNP6 and a full description with simulated results is included in Appendix C.4.

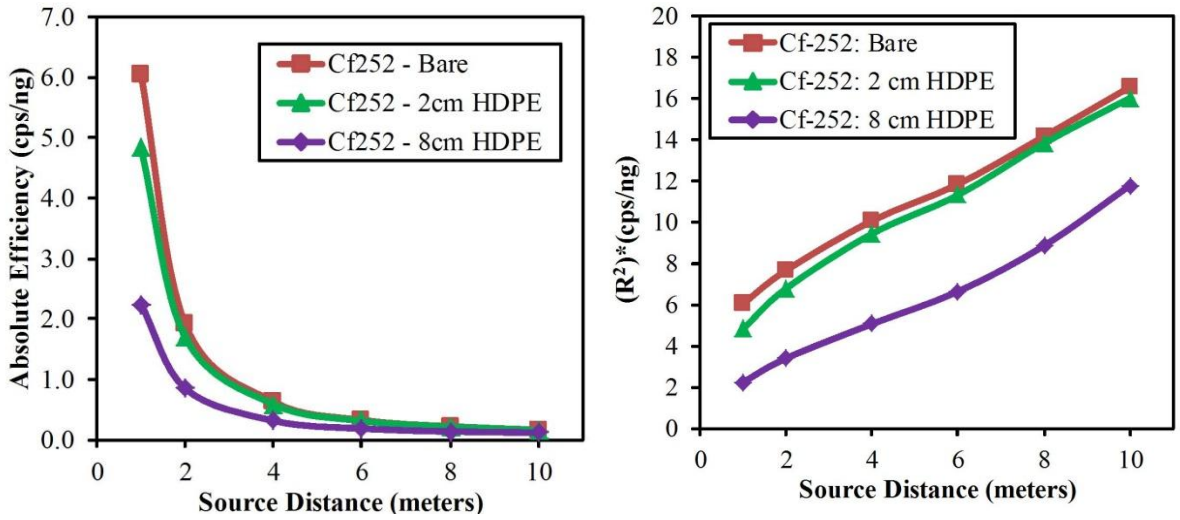

Figure 6.26: Stationary test results from ORNL. A ^{252}Cf neutron source was positioned at various distances from the front face of the detector and absolute neutron detection efficiency is plotted as function of source distance. The plot on the right is the same data set multiplied by R^2, which in an idealized environment would shape the data into a horizontal line.

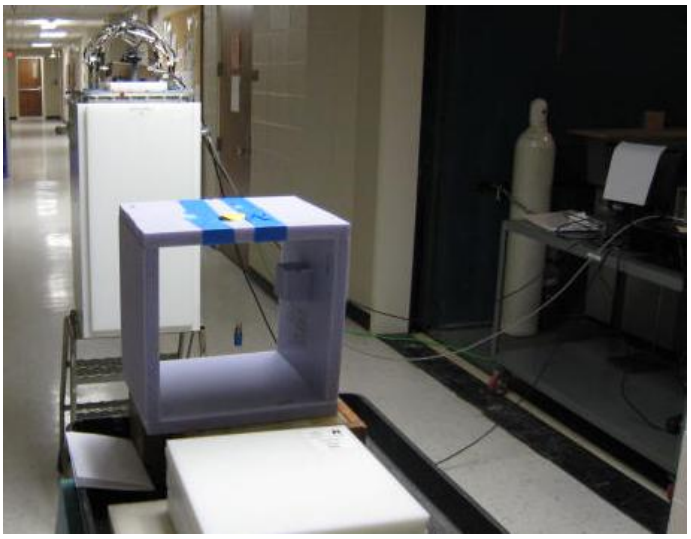

Figure 6.27: The stationary neutron response test setup at KSU. The ^{252}Cf is suspended in the center of the purple borated HDPE and centered in front of the LPC detector.

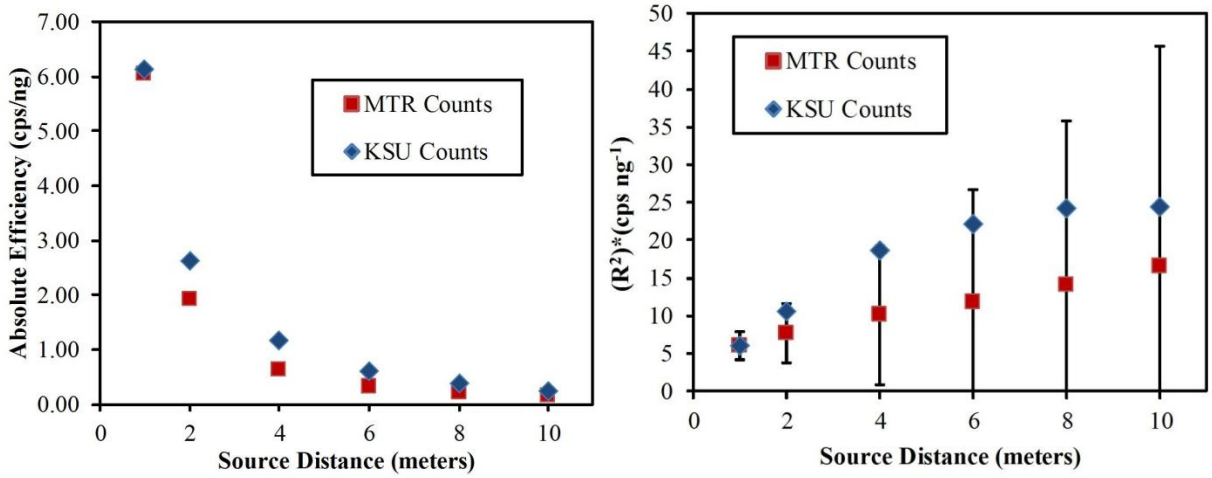

Figure 6.28: The ORNL bare ^{252}Cf static results (red) compared to the same test completed at KSU (blue). KSU results are less accurate due to neutrons scattering off of the cinderblock walls of the Ward basement hallway. The plot on the right is the same data set multiplied by R^2, which in an idealized environment would shape the data into a horizontal line.

In the stationary source tests results, shown in Figure 6.27 and Figure 6.28, should follow a $1/R^2$ trend where R is the distance from the source to the detector. The source intensity and distance relationship can be described by

$$I = \frac{S}{4\pi R^2}, \tag{6.29}$$

where S is the source activity and I is the relative measured intensity. In an idealized case where source and detector are in a vacuum, the trend described by Eq. 6.29 would be followed exactly. However, in the laboratory setting, air attenuation and neutrons scattering off of the surrounding building structure and ground/floor deviate the detector response from the idealized case. In Figure 6.27 and Figure 6.28 there are additional plots where the absolute efficiency is multiplied by R^2. In an ideal case, multiplying the count rate by R^2 would create a horizontal line on the plot, but the neutron scattering in the surround materials causes this data to be skewed to higher count rates. Error is included for both data sets in Figure 6.28, which was less than 1% for the

KSU data set[7], but three 1-minute measurements were completed by the ORNL team. This short counting time resulted in low count rates and poor statistics. The error is not included in Figure 6.27 to keep the error bars from cluttering the data sets, but had similar error to that shown in Figure 6.28.

A transient test was completed with the LPC detector by passing a ^{252}Cf neutron source in front of the detector at a constant rate. Two data sets were collected at different source to detector distances. The first data set was collected with the source 2.0 meters away at the closest distance, and the second data set with a 4.0 meter source distance. The LPC detector was operated in multi-channel-scaler (MCS) mode, thus the plot in Figure 6.29 shows the recorded cps plotted each second as the ^{252}Cf source passed in front of the detector. The transient tests were repeated 10 times for each distance setting, and four of those tests are shown in Figure 6.29 and Figure 6.30 for the 2.0 and 4.0 meter distances, respectively. The detector response at both distances was repeatable and consistent with each pass. In both distance settings, as the source approaches the detector the count rates increases and peaks at the closest distance. As the source moves away from the detector, the count rate decreases and returns to the background count rate. Furthermore, as expected, the count rate was approximately four times higher at the 2.0 meter distance than the 4.0 meter test.

[7] The error was small enough that the error bars on the plot are covered by the data point.

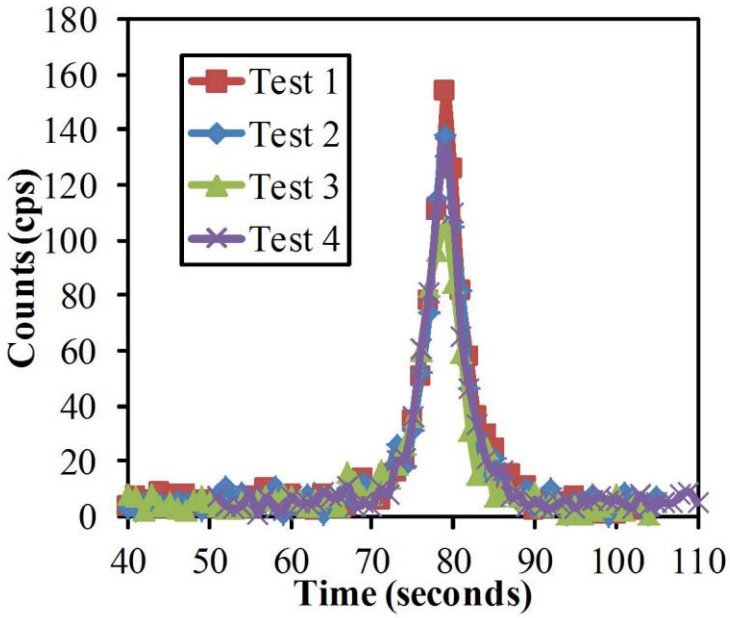

Figure 6.29: The transient response of the detector for four of the ten repeated measurements. The closest distance from the source to the detector face was 2.0 meters.

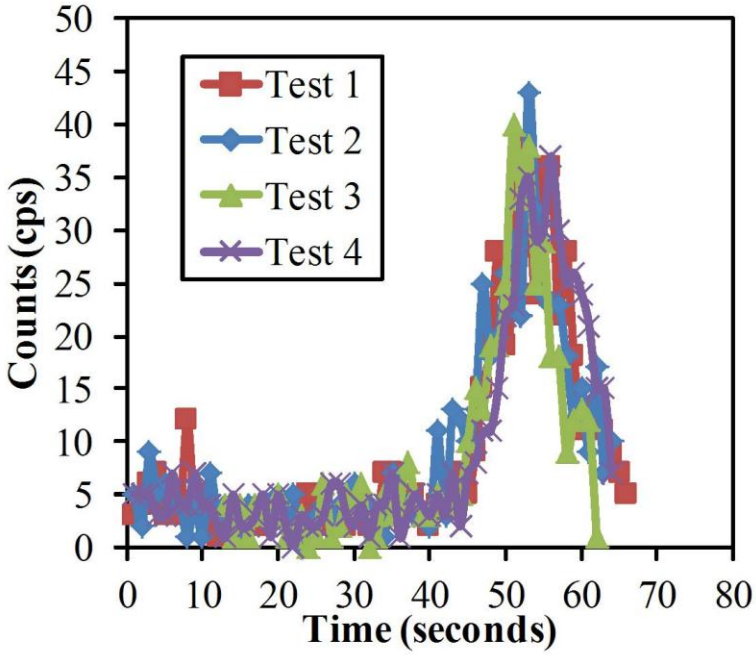

Figure 6.30: The transient response of the detector for four of the ten repeated measurements. The closest distance from the source to the detector face was 4.0 meters.

The third test investigated the lateral response of the LPC detector, referred to as the Field of View (FOV). The source was positioned at different lateral distances in 1.0 m increments up to 5.0 m away from centerline of the detector in both directions, as illustrated in Figure 6.31. Count rates were recorded over the entire lateral range when the source to detector distance was 25.5, 125.5, and 225.5 cm at the closest distance (0.0 m). The count rates recorded with the un-moderated ^{252}Cf neutron source are reported in Figure 6.32. The tests were repeated with source moderator thicknesses of 2.0 and 8.0 cm. The results with the ^{252}Cf source moderated are not included here, but had similar responses as the bare neutron source count rates. The count rate curves in Figure 6.32 appear to be symmetric about the 0.0 m centerline, as expected. Additionally, the background count rate was approximately 7.5 cps and count rates at -5.0 and 5.0 meters from the detector were approximately eight times greater than background.

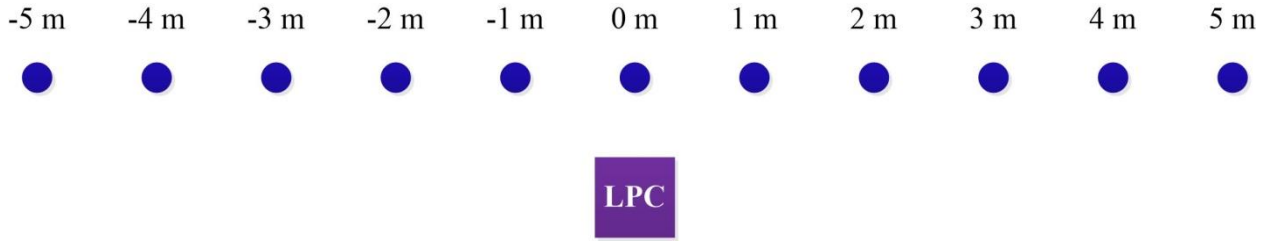

Figure 6.31: An illustration of the FOV experiment set up for the LPC tests. The ^{252}Cf neutron source (blue dot) was positioned at different lateral distances over a range of 10.0 meters. The closest distance at 0.0 m varied between 25.5, 125.5, and 225.5 cm.

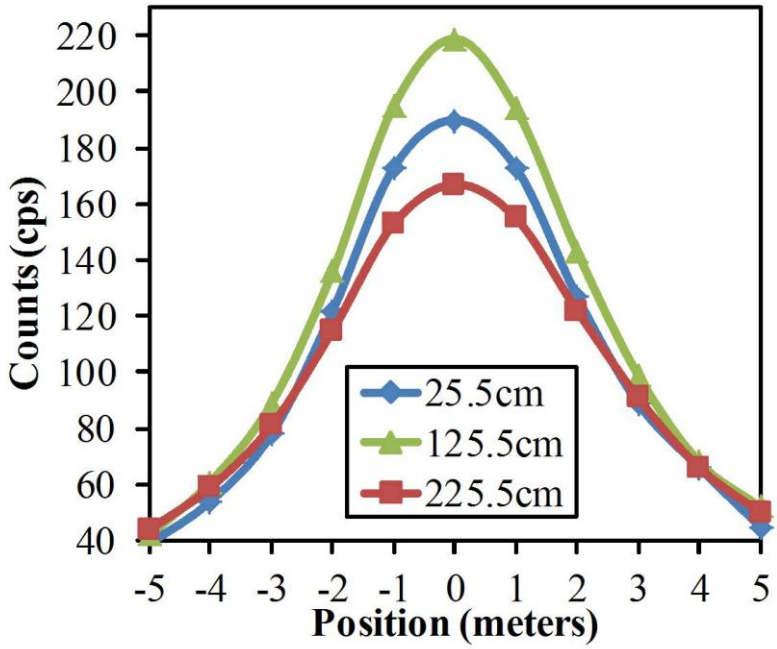

Figure 6.32: The LPC detector response to the FOV experiments. The background was approximately 7.5 cps, thus, the count rate was approximately eight times greater than the background count rate with the source 5.0 meters away.[8]

The data obtained by for the FOV tests are mislabeled, the labels presented are the titles given to the data sets by ORNL. More than likely more than one data set at the 0 m distance is mislabeled. This was determined by calculating the $1/R^2$ values at the 0 m distance using the following relations taken from Eq. 6.29,

$$I_a(A_2) = I_b(B_2) \tag{6.30}$$

where I_a and I_b are the count rates, or intensity, at source to detector distances of A and B. None of the data sets presented in Figure 6.32 follow this trend, thus more than likely two data sets are mislabeled. Further, as the source moves away latterly in each direction in the FOV test one would expect the data to follow a $1/R^2$ trend. However, due to the rectangular dimensions of the detector, as the source moves from 0 m to further distances, the solid angle also changes, which

[8] The data collected at ORNL may have been mislabeled as it would seem more probable to have a higher count rate at a closer distance. It may be assumed that the 25.5 cm and 125.5 cm data sets should be reversed.

ultimately affects the count rate of the detector. If the solid angles were included in the data set, the $1/R^2$ trend may be followed.

The last neutron test performed at ORNL investigated the angular response of the LPC. The angular neutron response was obtained by recording the count rate recorded by the LPC with an unmoderated ^{252}Cf source positioned 2.0 m from the center of the detector and rotating the source from 0°–360° in 30° increments. The angular response is plotted in Figure 6.33(polar) and Figure 6.34(Cartesian). The lowest count rates occur at 0°, 90°, 180°, 270°, all oriented 90° to each other. These angles are also the normal incident source angles to the detector faces. The highest count rates occur at 45°, 135°, 225°, and 315°, also all 90° of one another. The most probable reason for the higher count rates occurring at 45° from normal is the increased solid angle. At 0° the source is positioned directly in front of the LPC and the effective area of the LPC detector is defined by the HDPE detector moderator. The front face of the LPC detector has an effective area of 2620 cm^2 (Ω_f = 0.0051) at normal incidence, while at 45° from normal the effective area is 3705 cm^2 (Ω_f = 0.0072). There is a 40% increase in effective area from 0° to 45° incident angles. The 45° angle incidence causes more neutrons to scatter into the detectors, thus, the higher count rate. Due to symmetry of the LPC detector, the minimum and maximum count rate repeats at every 45° and 90° interval. The difference between minimum and maximum count rates was approximately 15%. Additionally, the detector response at 0° and 180° were similar to count rates at 90° and 270°. The primary difference between these source positions is the incident neutrons emitted from the ^{252}Cf source at 0° and 180° are perpendicular to the Li foils, and parallel to the Li foils at 90° and 270°. The similar count rates from the LPC detector at perpendicular and parallel incident neutron angles demonstrates that the HDPE configuration and symmetry of the detector assisted with angular uniformity of the detector.

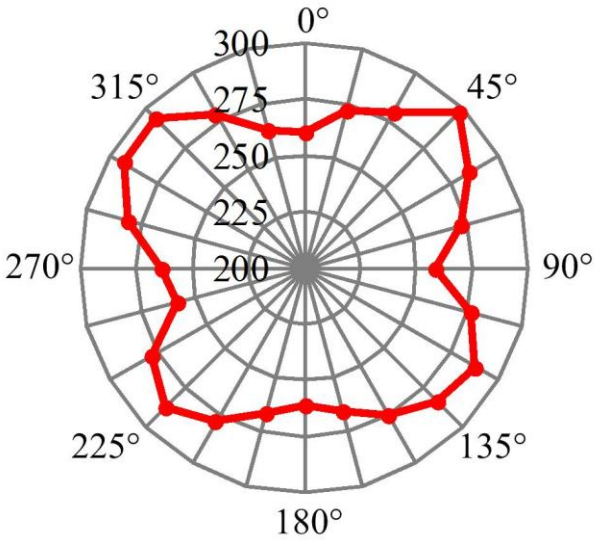

Figure 6.33: A polar plot of the LPC detector angular response. The source was positioned 2.0 meters from the center of the detector and rotated around the detector in 30° increments.

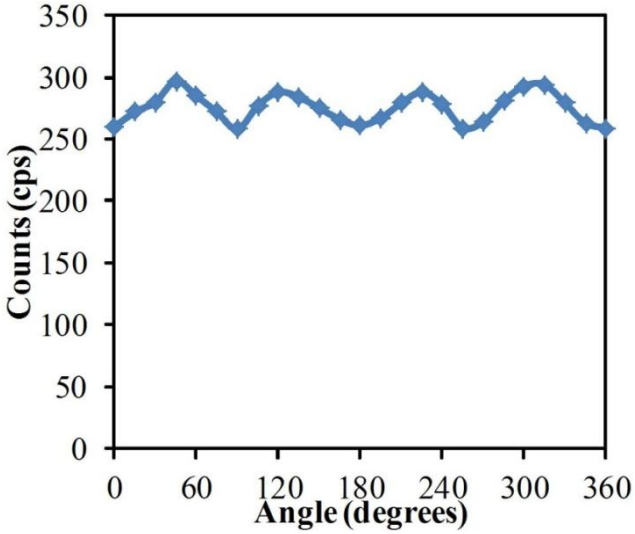

Figure 6.34: A Cartesian plot of the LPC detector angular response. The source was positioned 2.0 meters from the center of the detector and rotated around the detector in 30° increments. There was a 15% variance between minimum and maximum count rates.

Gamma-ray sensitivity tests were the final experiments conducted with the LPC detector. These tests used custom electronics provided by the Electronics Design Laboratory (EDL). The experiments consisted of exposing the detector to a ^{137}Cs source at various distances such that the front detector face received exposure rates of 1.0 µR/hr, 1 mR hr^{-1}, 10, mR hr^{-1}, 100 mR hr^{-1}, 1.0 R/hr, and 5 R/hr. The custom electronics provided by EDL had a TTL signal output and were

connected to a 2-channel counter/timer, thus, allowing count rates from the front and back detector to be recorded separately. Having two separate electronics systems designated for each detector reduced the dead time of the LPC to individual detectors rather than the two large-area MWPCs operating together. However, the gamma-ray sensitivity data was not shared with the KSU group, thus, the tests were repeated as best as possible using Ward Hall facilities. The exposure rates completed at KSU were 10, 50, 100, and 1000 mR hr^{-1} and pulse-height spectra were recorded using an Ortec MCA and Maestro program. This data collection method is not the same as the test methodology completed at ORNL and would result in a longer dead time, which may increase the gamma-ray sensitivity. However, the collected data can be compared to the neutron response as shown in Figure 6.35, something not possible with the ORNL tests. The solid angle for all gamma-ray exposure rates were different due to collimation of the ^{137}Cs source, thus calculating the GRR would correct for the differences. However, at an LLD of 1.0 MeV, all of the exposure rates resulted in a maximum GRR of 5.0×10^{-6}. This energy corresponds to approximately channel 130 in Figure 6.35 and would reduce the neutron detection efficiency by approximately 45%.

Additional gamma-ray sensitivity tests were completed with the LPC detector, but one EDL electronics unit was used to collect all data instead of a MCA. Investigated exposure rates with a ^{137}Cs source were 1, 2, 10, 50, 100, 500, and 1000 mR hr^{-1}. The custom electronics were switched back and forth between the front and back detectors while the source remained at a specific distance for each exposure rate. Using a single custom electronics system for the tests ensured identical LLD settings were used for both front and back Li foil MWPC detectors. The exposure rate, source distance, and count rates from the front and back MWPC detectors are shown in Table 4. The ^{137}Cs source used at ORNL had a higher activity and no solid angle effects needed to be considered. The KSU ^{137}Cs source has an approximate emission angle of 25° from normal. Thus, both detectors were completely irradiated when the source was at least 27 inches from the front detector face. At distances closer than 27 inches, solid angles of the front and back detectors were different. However, the clearest observation from Table 4 is the front MWPC detector consistently had a count rate 10–15 times greater than the back detector. The difference in count rates between the front and back Li foil MWPC detectors is most likely due to the gamma rays being attenuated by the front detector before reaching the back detector. Additionally, the gamma rays Compton scattered in the front detector, and still on a trajectory to

intersect the back detector, may be too low in energy to create a signal larger than the LLD. Furthermore, gamma rays attenuated by the front detector may be scattered at angles where they are no longer on paths to intersect with the back detector. Additional investigation is needed in order to determine the exact cause of the difference in count rates.

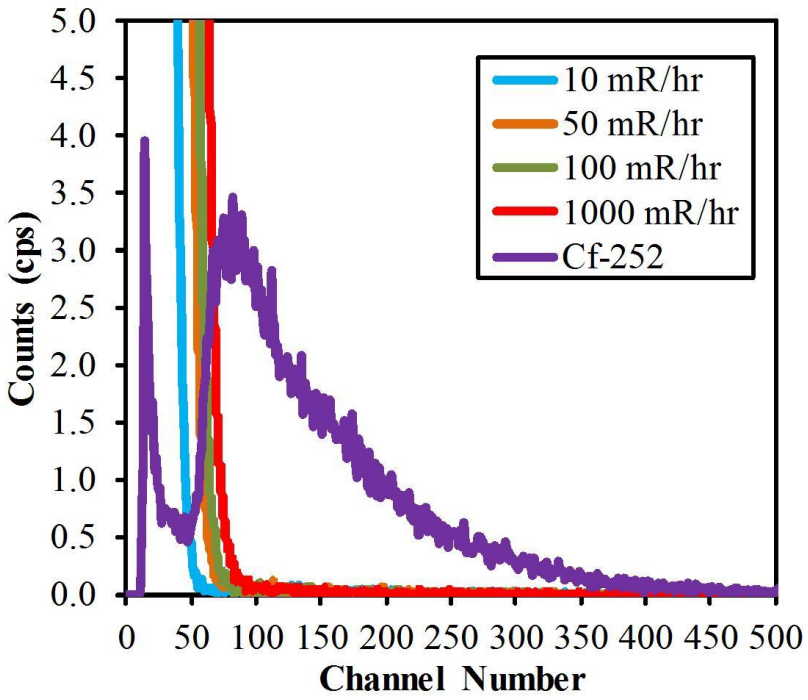

Figure 6.35: The LPC neutron response (purple) compared to exposure rates from a ^{137}Cs gamma ray source of 10, 50, 100, and 1000 mR hr^{-1}.

Table 4: The exposure rate, source distance, and count rates from the front, back, and total of the LPC detector collected using the EDL custom electronics and the KSU ^{137}Cs gamma ray source.

^{137}Cs Exposure Rate (mR/hr)	Source Distance (Inches)	Counts Front (cps)	Counts Back (cps)	Counts Total (cps)
1	463.6	17.7	4.4	22.1
2	304.8	51.2	6.2	57.5
10	146.3	304.0	13.8	317.8
50	65.5	1619.5	94.2	1713.6
100	46.3	2640.6	177.4	2818.0
500	20.7	4110.5	388.2	4498.8
1000	14.6	4462.4	426.2	4888.6

6.2.3 Form-Fit Detectors

The form-fit detectors were designed to be used in smaller neutron sensor applications such as handheld, backpack, or briefcase monitoring systems. Some designs were constructed such that they could be direct replacements for ^{3}He neutron detectors. Two form factors were investigated and include a cylindrical design (aerogel cruciform, Dual, Quad, and Wagon Wheel) and a square design (5-layer mini), which are shown in Figure 6.36. These detectors appear to have bulky connectors and gas-fill lines, but these devices are considered test chambers and are used only for feasibility studies. If they should fail, these devices are repairable and various proportional gases can be explored using the gas-fill line.

The five form-fit detector types discussed in the previous chapter (aerogel cruciform, Dual, Quad, Wagon Wheel, and 5-layer mini) were compared to the ^{3}He neutron detector described in Chapter 2. The detector comparison was completed by placing each detector approximately 1.0 meter from an unmoderated ^{252}Cf source while suspended at half the height of the detector moderator. The moderator used in the experiment for the cylindrical designs was 6″ x 9″ with a 2.5″ cutout in the center of the HDPE. The square 5-layer mini also had a moderator 6″ x 9″ with a 2″ x 2″ cutout in the center. Schematics of both moderators are shown in top-view perspective in Figure 6.37. The cylindrical moderator was used to test the aerogel cruciform, Dual, Quad, Wagon Wheel, and ^{3}He neutron detector. The gamma-ray sensitivity of each detector was also tested by exposing each detector (with moderator) to 10 and 50 mR hr^{-1} exposure rates using a ^{137}Cs source.

Figure 6.36: The two investigated form-fit configurations shown with and without the HDPE moderator. The cylindrical design (left two) was used for the aerogel cruciform, Dual, and Quad designs, while the square design (right two) was used for the 5-layer mini.

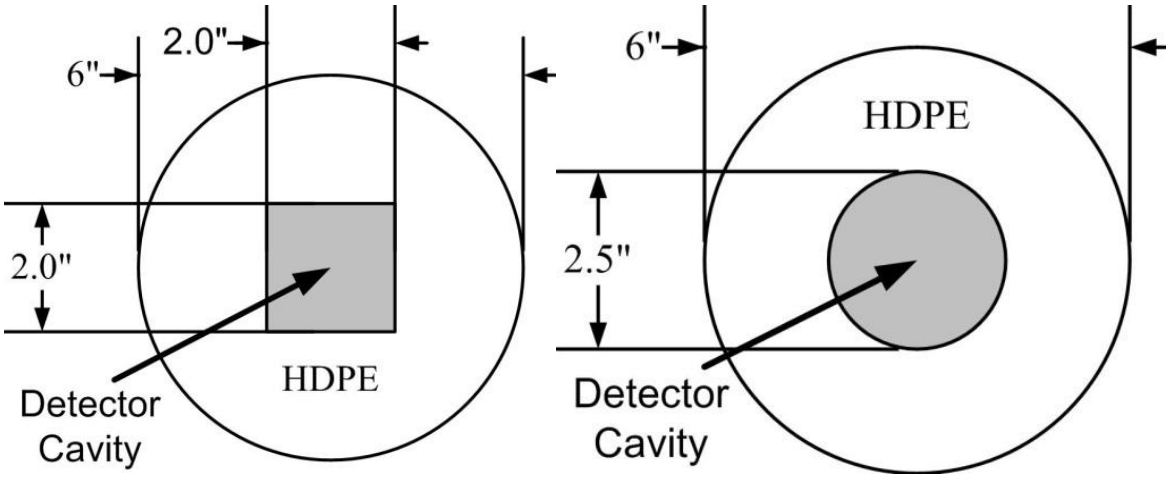

Figure 6.37: The HDPE used in ^{3}He neutron detector comparison tests was 6.0″ in diameter and 9.0″ in height. Top-view schematics of the HDPE with cutouts shaded in grey are shown.

The neutron response pulse-height spectra for the aerogel cruciform, Dual, Quad, and 5-layer mini are shown in Figure 6.38, Figure ***6.39***, Figure ***6.40***, and Figure ***6.41***, respectively. In each pulse-height spectra, the neutron response is plotted with the background measurement, thus, demonstrating that the detectors were sensitive to neutrons. The aerogel cruciform detector has no obvious spectral features except for a shoulder occurring around channel number 100, and counts that extend to higher channel numbers. Previously tested aerogel samples resulted in the appearance of at least one, sometimes two, peaks in the pulse-height spectra. However, these samples were slightly thicker than previous samples tested, so the assumption is made that the aerogel thickness is greater than the summed reaction product range, thus, possibly causing the peakless pulse-height spectra. Additionally, these aerogel samples included higher Li and B content, which would increase the aerogel density and reduce the reaction product ranges in the aerogel. Furthermore, the electric field was not uniform in the detector because the only grounded electrode in the quadrants defined by the aerogel was the 90° arc of the Al test chamber. Thus, it is unknown if reaction products emitted in the region between the anode wire and the center of the chamber would be in an electric field strong enough to migrate charge through the gas to the anode wire. Also, the reaction product range of the triton in P-10 gas is 7.25 cm, further than the possible path lengths in the test chamber. Thus, a small fraction of reaction product energy may be deposited in the gas, resulting in significantly smaller signals than capable with the previous test chambers. Consequently, these smaller pulses may be lower than the LLD setting and reduce the neutron detection efficiency.

The Dual and Quad designs have small peaks occurring relatively close to the electronic noise in the lower channels. These detectors have Li foil configurations which allow for both reaction products to enter the gas volume, and a perimeter Li foil coating in which only one reaction product can be measured per neutron absorption. Simulations may decipher which portions of the pulse-height spectra are contributed from *Case 1*, *Case 2*, and *Case 3* for these detector designs. (*Cases 1*, *2*, and *3*, are described in Chapter 3.) Gamma-ray responses are also shown for these devices and appear in the lower channel numbers close to the electronic noise, well below an ideal LLD setting.

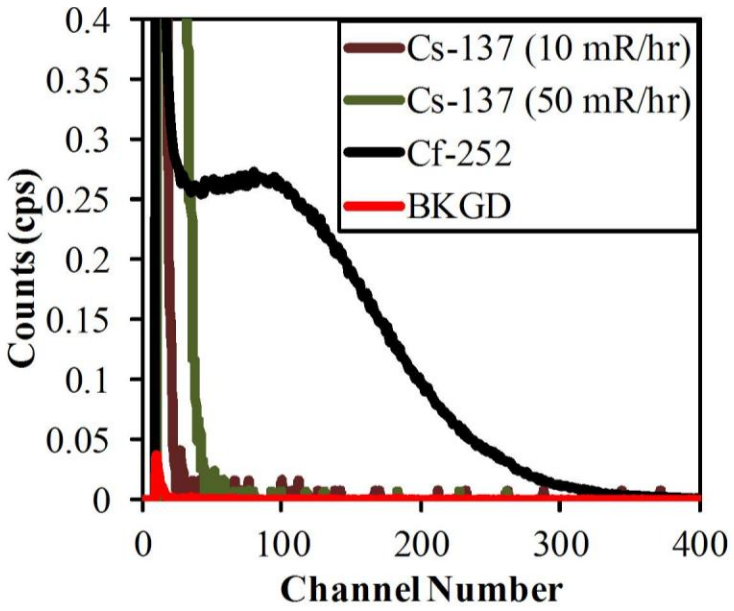

Figure 6.38: The neutron and gamma-ray response pulse-height spectra of the aerogel cruciform form-fit detector. The gamma-ray exposure rates investigated were 10 and 50 mR hr^{-1} using a ^{137}Cs source.

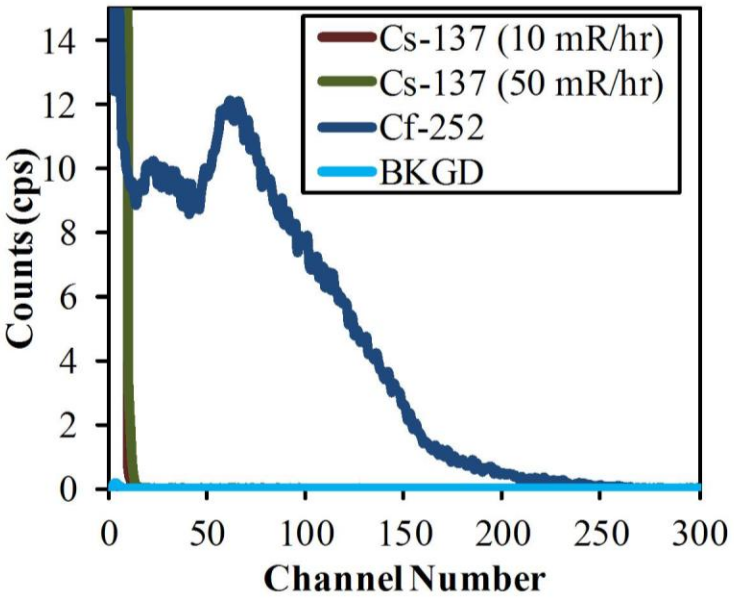

Figure 6.39: The neutron and gamma-ray response pulse-height spectra of the Dual form-fit detector. The gamma-ray exposure rates investigated were 10 and 50 mR hr^{-1} using a ^{137}Cs source.

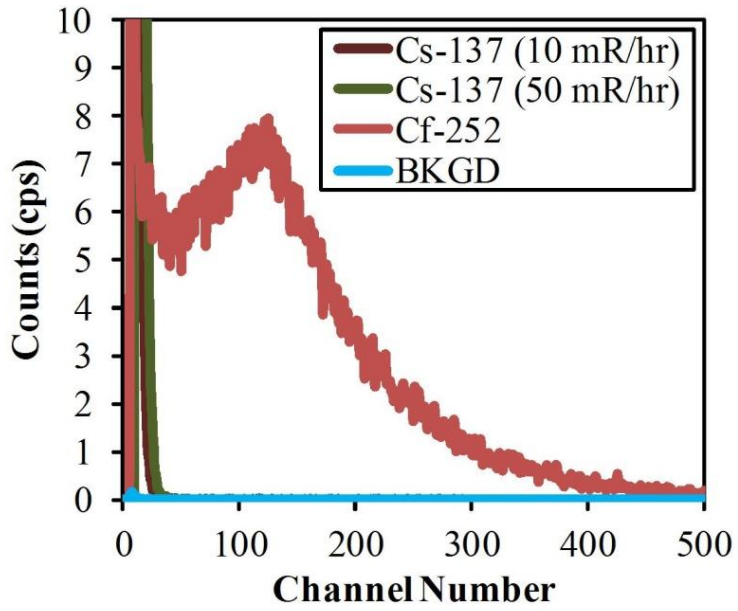

Figure 6.40: The neutron and gamma-ray response pulse-height spectra of the Quad form-fit detector. The gamma-ray exposure rates investigated were 10 and 50 mR hr^{-1} using a ^{137}Cs source.

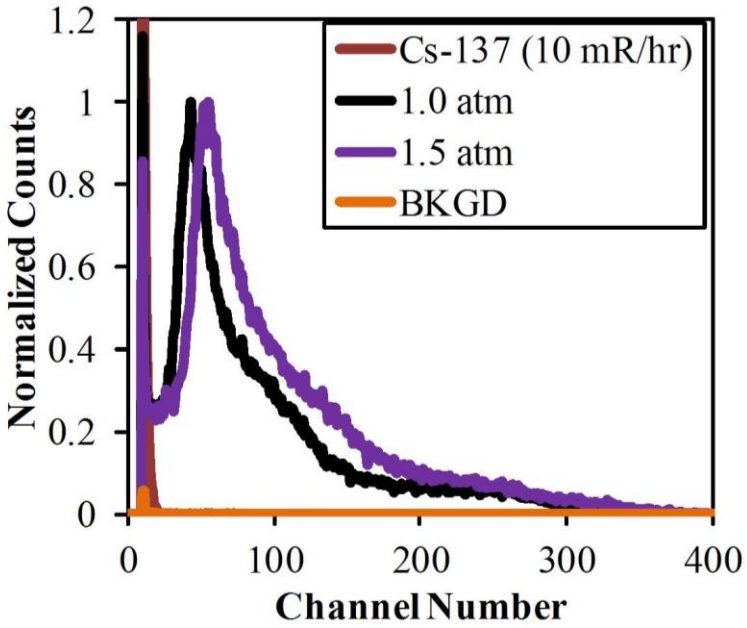

Figure 6.41: The neutron and gamma-ray response pulse-height spectra of the 5-layer mini form-fit detector. The gamma-ray exposure rates investigated were 10 and 50 mR hr^{-1} using a ^{137}Cs source.

The 5-layer mini detector has a different shaped pulse-height spectrum compared to the other three detectors discussed previously. A large valley exists in the pulse-height spectrum between the electronic noise and the main pulse-height feature, peaking at channel 60. Pulses caused by gamma-ray interactions also appear close to the electronic noise, well below a typical LLD setting. The valley assists with gamma-ray discrimination while maintaining relatively high intrinsic neutron detection efficiency. The 5-layer mini was also tested at a higher P-10 gas pressure of 1.5 atm. The collected pulse-height spectra of both 1.0 atm and 1.5 atm gas pressures are shown in Figure 6.41. However, there were no major improvements with the gas pressure increased by 0.5 atm. The only change with the increased gas pressure was the main feature increases eight channel numbers, most likely as a result of higher energy deposition of the reaction products from the increased gas pressure.

The ^{3}He neutron detector was positioned in the 6″ x 9″ HDPE moderator cylinder and the same neutron and gamma ray measurements completed with the Li foil and aerogel form-fit detectors was repeated, the resulting pulse-height spectra obtained with the ^{3}He neutron detector are shown in Figure 6.42. The two gamma-ray exposure rates indicate that a majority of gamma-ray interactions result in small signals that fell below the main neutron induced features of the pulse-height spectrum. The LLD was set to channel 100, and the total counts above this channel number were used to calculate the ^{3}He detector count rate. (Channel 100 was chosen because pulses from gamma-ray interactions were eliminated at the gamma-ray exposure rates investigated.)

The total count rates of the aerogel cruciform, Dual, Quad, 5-layer mini, Wagon Wheel – A, Wagon Wheel – B, and ^{3}He neutron detector are presented in Table 5. The total absorption length of the ^{3}He neutron detector was 13.0 cm and the total counting region was 6.5 cm. Therefore, approximately 50 percent of the neutrons absorbed in the ^{3}He neutron detector were recorded. The aerogel cruciform, Dual, and Quad, and Wagon Wheel devices were all designed to have a 13.0 cm absorption length, while the 5-layer mini was designed with a 6.5 cm long counting region. Columns were added to Table 5 to show detector normalization to 13.0 cm lengths. The normalization to 13.0 cm doubles the count rate of the 5-layer mini, making the count rate 137% of the 4.0 atm ^{3}He neutron detector. When the detectors are normalized to 6.5 cm, however, the 5-layer mini shows the most comparable results to the ^{3}He neutron detector.

However, as the length of the ^{3}He tube increases, the ratio of the total counting length to total absorption length increases.

Table 5: The total count rates of the six detectors tested against the ^{3}He neutron detector. Count rates were normalized to total absorption length, 13 cm, and total counting length, 6.5 cm, of the ^{3}He counter.

	Total Counts (cps)	13 cm normalization	6.5 cm normalization	GRR
Helium-3	**27±0.17**	27±0.17	**27±0.17**	-
5 layer mini	17±0.16	**34**	17±0.16	1 x 10^{-7}
Quad	24±0.23	24±0.23	12	3 x 10^{-7}
Dual	20±0.20	20±0.20	10	6 x 10^{-7}
Wheel – A	12.3±0.06	12.3±0.06	6	-
Wheel – B	13.7±0.09	13.7±0.09	6.5	-
Aerogel	3.5±0.04	3.5±0.04	1.75	4 x 10^{-7}

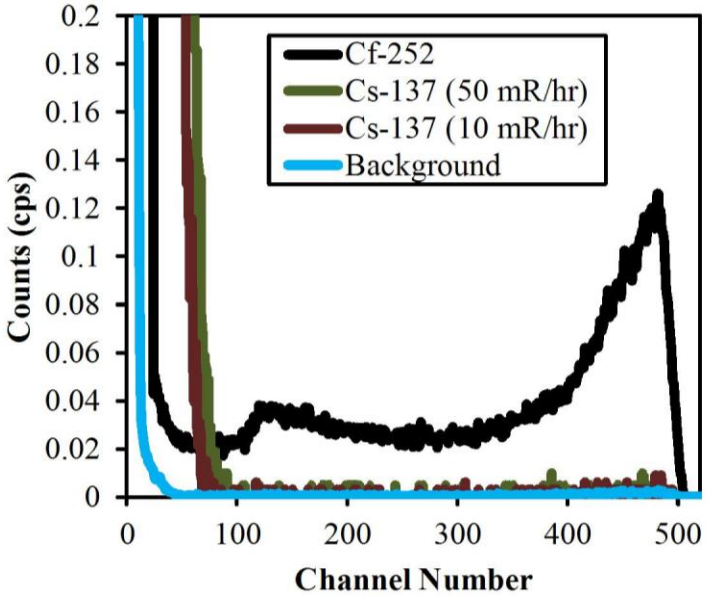

Figure 6.42: The neutron and gamma-ray response pulse-height spectra of the 3He neutron detector. The gamma-ray exposure rates investigated were 10 and 50 mR hr^{-1} using a ^{137}Cs source.

Two additional detectors were assembled and contain eight longitudinal Li foil fins emanating radially from the perimeter towards the central anode wire. As mentioned, it is unclear if electrically grounding the Li foil fins and the perimeter Li foil coating causes the electric field strength between the fins to be too low to extract free charges from the channel. Thus, two designs of the Wagon Wheel were constructed, one with grounded Li foil fins and one with electrically neutral, or floating fins. The first constructed Wagon Wheel used a 1/32″ thick sheet of perforated HDPE to separate the finned insert from the grounded Li foil perimeter coating, referred to as Wagon Wheel – A. The other detector was constructed in exactly the same manner except the HDPE sheet was not included, thus grounding the perimeter Li foil coating and longitudinal fins, referred to as Wagon Wheel – B. The same neutron sensitivity tests completed with the other form-fit detectors were repeated with both Wagon Wheel designs and the pulse-height spectra are shown in Figure 6.43 and Figure 6.44 for Wagon Wheel – A and Wagon Wheel – B, respectively.

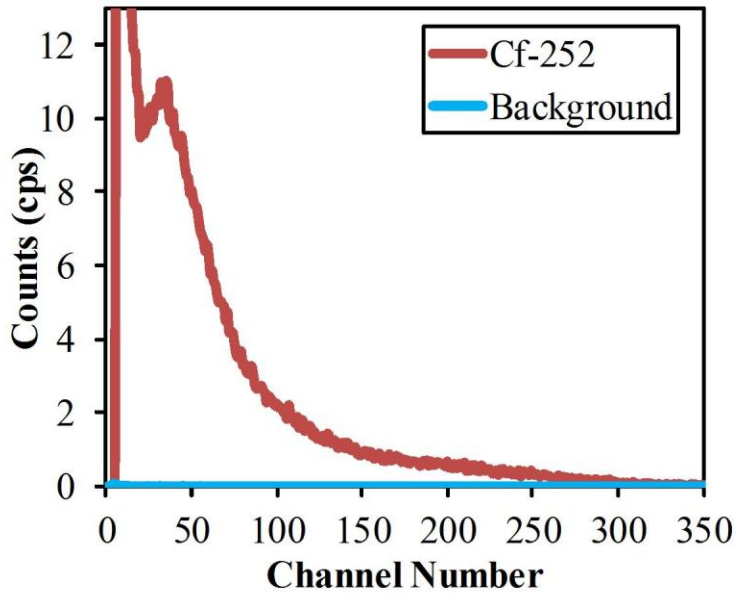

Figure 6.43: The neutron response pulse-height spectrum of the longitudinal finned detector with floating Li foil fins and grounded perimeter Li foil coating, referred to as Wagon Wheel – A.

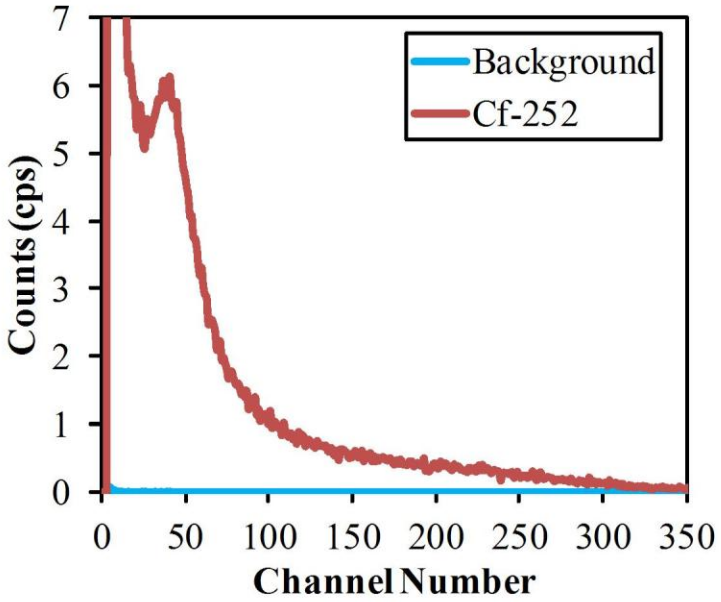

Figure 6.44: The neutron response pulse-height spectrum of the longitudinal finned detector with the Li foil fins and perimeter Li foil coating grounded, referred to as Wagon Wheel – B.

The two pulse-height spectra from Wagon Wheel – A and Wagon Wheel – B initially appear similar in shape, but the detector with grounded fins required half the electronic amplification, which was reduced from 24x to 11x. The reason for the difference in amplifier settings is unclear, but most likely is a consequence of electric field differences. Typically, as the distance between two electrodes decreases, the electric field strength increases. In the case of the grounded fin design, the edges of the foils closest to the anode wire are grounded. Thus, the distance between the ground electrode and anode is approximately 1.5 cm shorter than the floating fin design. Consequently, the electric field strength will be higher with the closer electrodes. Furthermore, the count rate was slightly higher for the grounded fin design versus the floating fin design, 13.7±0.09 cps and 12.3±0.06 cps, respectively. However, differences in the count rates may result from the thin perforated HDPE sheet blocking a portion of the reaction products from escaping the perimeter Li foil coating. Additional research needs to be conducted to make a strong conclusion on the influence of the electric field strength on the count rates. However, the conclusion can be made that no drastic difference exists between the two detector designs. Overall, the detectors had lower neutron sensitivity than the ^{3}He neutron detector, Dual, and Quad designs. An additional permutation of this design would be to use eight anode wires

and eight Li foil fins extending all the way to the center of the tube. This may also be interpreted as an improvement to the Quad design by doubling the number of gas compartments. However, as the Li foil fins come closer together, the amount of ionization in the gas also decreases due to the restricted reaction product ranges. Consequently, the electronic pulse heights are also smaller and may blend with the electronic noise, or fall below the LLD setting.

CHAPTER 7

CONCLUSIONS & FUTURE WORK

"If I have seen further than others, it is by standing on the shoulders of giants."

-Isaac Newton

The following chapter summarizes research achievements and compares experimental and simulated neutron and gamma-ray sensitivity results to current ^{3}He neutron detector replacement requirements. This chapter also briefly describes future work for Li foil, foam, and aerogel detectors. Lastly, final remarks about the technology are included.

7.1 Achievements and Comparisons

The Li foil MWPC neutron detector meets ^{3}He neutron detector replacement requirements based on neutron detection efficiency, effective area, gamma-ray insensitivity (or GRR), and cost. Large ^{3}He neutron detectors cover an area of 5 cm x 200 cm (1000 cm^{2}) and are typically filled with 1–4 atm of ^{3}He gas, resulting in approximate intrinsic thermal neutron detection efficiencies ranging from 40–80%. Typical RPMs use two ^{3}He tubes and cover approximately 32% of the total area available (2000 cm^{2} of 6100 cm^{2} available). The large-area ^{6}Li foil MWPC neutron detectors cover more area (1250 cm^{2}) and have a measured intrinsic thermal neutron detection efficiency of 53.8 ± 0.2%. In addition, stacking three large-area Li foil MWPCs would fit within the height restriction of current NEMA RPM housing and cover 85% of the available area. Further, three Li foil MWPC detectors stacked on top of each other would exceed the PNNL RPM absolute neutron detection efficiency requirement of 2.5 cps ng^{-1}. Simulations predict the absolute neutron detection efficiency with three stacked Li foil MWPCs would be

approximately 4.2 cps ng^{-1}. The gamma-ray rejection ratio (GRR) requirement of 1 x 10^{-6} with an exposure rate of 10 mR hr^{-1} from ^{60}Co was exceeded by almost three orders of magnitude (GRR = 7.67 x 10^{-9}). Furthermore, the ^{6}Li foil MWPC detectors will cost less than current ^{3}He neutron detectors. (KSU is not a manufacturer, thus detailed cost analysis is not discussed as it would be inappropriate.) As mentioned previously, stacking three large-area Li foil MWPC wil meet the height requirement of RPMs. However, the Li foil MWPC thickness was greater than the NEMA RPM restrictions, and with the added HDPE moderator the total thickness of the Li foil MWPC was three times greater than the available space. However, a 2″ x 2″ 5-layer mini was designed, assembled, and tested, thus meeting thickness requirements while allowing for 3.0″ of additional neutron moderator. Once scaled to the larger sizes, 1.0″ of HDPE moderator can be added to the front of the detector while 2.0″ may be applied to the back of the detector.

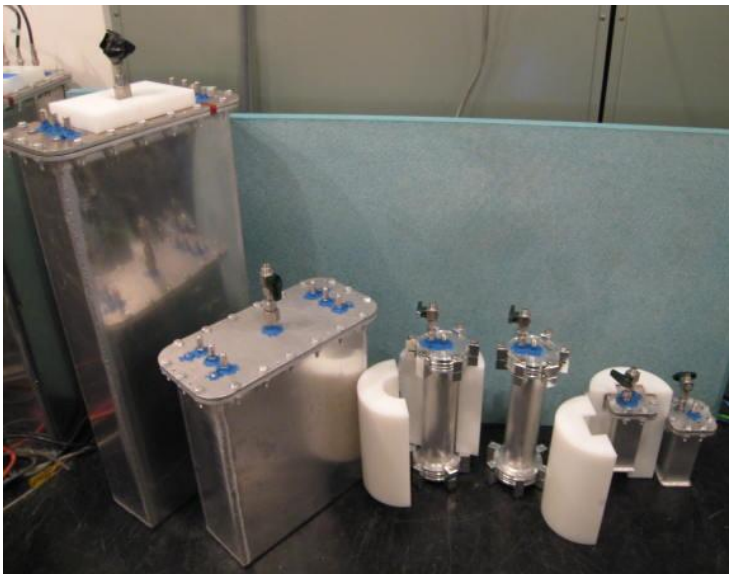

Figure 7.1: A picture of the large-area, mid-sized, and form-fit detectors side-by-side. HDPE moderators for form-fit devices are also included and open to expose the detector inside. This picture shows a relative scale in various sizes of detectors.

Both mid-sized and form-fit Li foil MWPCs were designed, assembled, and tested. The mid-sized detectors have a measured intrinsic thermal neutron detection efficiency of approximately 54% and have gamma-ray rejection ratios as low as 3 x 10^{-9}. The mid-sized Li foil MWPC (550 cm^2) are appropriate for backpacks or briefcases, while the form-fit smaller area devices (< 100 cm^2) are suitable for handheld detectors and smaller neutron monitoring systems. Recently, at a

DNDO backpack neutron detector test campaign, the mid-sized backpack neutron detector performed better than the standard ^{3}He backpack neutron detectors currently used by the military, thus, being accepted as a viable backpack neutron detector replacement. Furthermore, there is significant room for improvement in the backpack detectors, making the ^{6}Li foil backpack an even better option as a replacement. The smaller devices, however, require additional feasibility studies, but preliminary results indicate these devices will meet other ^{3}He replacement detector requirements such as ruggedness and cost. The four different sized detectors assembled at KSU are shown in Figure 7.1.

7.2 Novel Contributions

Two patents were filed on the detector technology, one awarded and one still pending, and are both based on the general concept of suspending thin neutron absorber materials in gas-filled devices. The suspended neutron absorber sheet allows for more than one reaction product to be measured simultaneously in the gas region from a single neutron absorption, a capability not accomplished or considered with gas-filled devices before the research presented in this thesis. Li foil has been used in detectors before, but this research, for the first time, suspends ^{6}Li foils to allow for the triton and/or alpha particle to be measured on both sides of a single foil sheet. The simulated neutron response pulse-height spectra were all original work. Although research still needs to be completed to optimize the aerogel and foam materials, this is the first time a neutron detector has been assembled with these materials. The success of the devices is demonstrated in the licensing of the patents and collaborative efforts with Saint-Gobain Crystals, who is in the process of commercializing these neutron detectors. Lastly, other original work includes the detectors discussed in chapter 4.

7.3 Future Work

Development of the large-area Li foil MWPCs has led to other research areas these detectors could be applied besides RPM replacements. Large-area high-efficiency detectors are also needed at neutron monitoring and measurement facilities worldwide. These detectors could also be adapted to 2-D neutron imaging devices, which are also used at neutron research facilities and

laboratories. Other areas these device could be applied include neutron multiplicity counters, neutron spallation facilities, and essentially anywhere current large-area ^{3}He neutron detectors are employed. Further, the intrinsic thermal neutron detection efficiency of the Li foil MWPCs can be increased by increasing the number of Li foils included in the detector. Currently, 55 μm thick ^{6}Li foils can be included immediately, which would increase the number of Li foils that maximizes the neutron detection efficiency from 5 to 10 (ε_{int} = 72%). The additional Li foils would increase the thickness of the detectors if foil spacing were kept at the current dimensions. However, some applications are more concerned with neutron detection efficiency rather than detector dimensions.

In order for the large-area Li foil MWPCs to be considered viable RPM replacements, the detector thickness must be reduced to fit the restricted dimensions of current RPMs. However, the 5-layer mini proves that the thinner detector profile is achievable. Once the thinner profile is incorporated in the large-area devices, a full-scale RPM should be built, tested, and compared to theoretical values. Additionally, HDPE optimization would be required for the thinner profiles, something solvable using MCNP6 simulations. However, neutron detectors should not be optimized for unmoderated ^{252}Cf sources. In mission scenarios of smuggled neutron emitting radioactive materials, the source is never bare, but hidden. Thus, optimization should occur for moderated, or shielded, neutron sources with possible neutron energies ranging from 1–100 keV.

The ratio of neutron absorbing area to moderator area of a mid-sized MWPC, or backpack, must approach 1.0 in order to optimize the neutron sensitive region. The backpack neutron detector had an absorber to moderator ratio of 0.43. In other words, less than half of the moderator area overlaps with the ^{6}Li foil area. Increasing this ratio will also increase the total count rate while maintaining detector weight. Furthermore, most of the detector weight lies in the lid, gas-line, and flange, all of which can be reduced to allow for additional HDPE moderator.

The results of the form-fit devices demonstrate the detectors meet some neutron detection efficiency requirements for smaller area ^{3}He replacement technology. There are additional cylindrical insert designs that should be explored including stacked ^{6}Li washers and stacked ^{6}Li foil cones or angled washers, a design with no neutron streaming paths. In addition, the device lengths should be increased to similar dimensions to that of backpack sensors (10″–12″). After length and other modifications are accomplished, a full backpack detector should be assembled with several of these form-fit devices and tested against current neutron detector alternatives.

Even though the LiF impregnated foam devices have lower neutron detection efficiency than the ^{6}Li foil detectors, they should not be abandoned. The impregnated foam MWPCs have the largest manufacturing capabilities. Thin sheets (2.5 mm thick) could be mass produced as large as 1.0 m x 2.0 m and stacked as long as 100 meters. The biggest research obstacle for this material is the saturation level of polyurethane foam. Nano-sized LiF may prevent clusters from forming in the foam synthesis process, thus, allowing both reaction products to escape the LiF granule simultaneously. Next, the foam saturation level should be determined and will most likely be higher than 30%. The same MWPCs assembled with the ^{6}Li foil should be made with the saturated foam and the same neutron and gamma-ray sensitivity tests repeated and compared to the ^{6}Li foil MWPC.

The aerogel neutron detectors require the greatest amount of research yet to be completed, but they have the greatest potential for making a high efficiency neutron detector compared to the foam and foil devices. Future research, however, is not necessarily dependent upon KSU, but Aerogel Technologies. The overall goal of the aerogel material should be to fabricate an aerogel with as high of neutron absorbing isotope content as possible while maintaining low density and high porosity. The aerogel material should also be thin enough that reaction products can escape both sides of an aerogel absorber slab simultaneously, but still maintain structural rigidity. Designs constructed with ^{6}Li foil should be repeated with the aerogel materials and the neutron and gamma-ray sensitivity results compared.

7.4 Final Remarks

The ^{6}Li foil MWPC is an acceptable ^{3}He neutron detector replacement for several different neutron monitoring system applications. Other technologies offer similar neutron and gamma-ray sensitivity, thus, optimization of the ^{6}Li foil detectors is still needed in order to maintain competitiveness. The foam and aerogel neutron absorber materials should not be abandoned, but investigated further and optimized. Furthermore, current collaborative work between SGC and KSU should continue. Lastly, this work was supported by the U.S. Defense Threat Reduction Agency (DTRA), under contract HDTRA1-12-c-0002.

REFERENCES

[1] J. Chadwick, "The Existence of a Neutron," pp. 692-708, 1932.

[2] E. Rutherford, "Bakerian Lecture: Nuclear Constitution of Atoms," *Proceedings of the royal Society of London,* vol. 97, pp. 374-400, 1920.

[3] *The History of the Discovery of Radiation and Radioactivity*. Available: http://mightylib.mit.edu

[4] E. Rutherford and T. Royds, "Spectrum of the radium emanation," *Philosophical Magazine,* vol. 16, pp. 313-317, 1908.

[5] E. Rutherford, "The scattering of alpha and beta particles by matter and the structure of the atom," ed: Taylor & Francis, 1911.

[6] E. Rutherford and H. Geiger, "An Electrical Method of Coungting the Number of alpha Particles from Radio-active Substances," *Proceedings of the Royal Society of London Series A,* vol. 81, pp. 141-161, 1908.

[7] B. B. Rossi and H. H. Staub, *Ionization Chambers and Counters: Experimental Techniques*. New York: McGraw-Hill Book Company, Inc., 1949.

[8] E. Segrè and C. Wiegand, "Boron Trifluoride Neutron Detector for Low Neutron Intensities," *Review of Scientific Instruments,* vol. 18, p. 86, 1947.

[9] N. Veall, "Small Boron Chambers for Slow Neutron Measurements," *Journal of Science Instruments,* vol. 24, 1947.

[10] I. L. Fowler, "Very Large Boron Trifluoride Proportional Counters," *Review of Scientific Instruments,* vol. 34, p. 731, 1963.

[11] S. A. Korff and W. E. Danforth, "Neutron Measurements with Boron-Trifluoride Counters," *Physical Review,* vol. 55, pp. 980-980, 05/15/ 1939.

[12] R. Batchelor, "Neutron Energy Measurements with Helium 3 Filled Proportional Counter," *Proceedings of the Physical Society A,* vol. 65, pp. 674-675, 1952.

[13] R. Batchelor, R. Aves, and T. H. R. Skyrme, "Helium-3 Filled Proportional Counter for Neutron Spectroscopy," *Review of Scientific Instruments,* vol. 26, p. 1037, 1955.

[14] A. Sayres, K. Jones, and C. Wu, "Interaction of Neutrons with He3," *Physical Review,* vol. 122, pp. 1853-1863, 1961.

[15] W. R. Mills, R. L. Caldwell, and I. L. Morgan, "Low Voltage He3-Filled Proportional Counter for Efficient Detection of Thermal and Epithermal Neutrons," *Review of Scientific Instruments,* vol. 33, p. 866, 1962.

[16] R. V. Babcock, R. E. Davis, and S. L. Ruby, "Coated Semiconductor Is Tiny Neutron Detector," *Nucleonics*, vol. 17, pp. 116-122, 1959.

[17] N. Tsoulfanidis, *Measurement and Detection of Radiation*, 2nd ed. Washington, DC: Taylor & Francis, 1995.

[18] G. F. Knoll, *Radiation detection and measurement*, 3rd ed.: John Wiley & Sons, 2000.

[19] P. E. Vanier, L. Forman, I. Dioszegi, C. Salwen, and V. J. Ghosh, "Calibration and testing of a large-area fast-neutron directional detector," in *Nuclear Science Symposium Conference Record, 2007. NSS '07. IEEE*, 2007, pp. 179-184.

[20] N. E. Holden, "Helium Isotopic Abundance Variation in Nature," in *IUPAC General Assmebly*, Lisbon, Portugal, 1993.

[21] D. A. Shea and D. Morgan, "The Helium-3 Shortage: Supply, Demand, and Options for Congress," *Congressional Reserach Services*, December 22 2010.

[22] R. T. Kouzes, "The End of Helium-3 As We Know It," in *Basic Energy Sciences*, 2010.

[23] (2010, June 20) DOE begins rationing helium-3. *Physics Today*.

[24] "NeuPort Monitor," S. G. Crystals, Ed., ed, 2010.

[25] D. Frank, "Backpack Radiation and Neutron Detection," I. A. Technologies, Ed., ed, 2010.

[26] R. T. Kouzes and J. H. Ely, "Status Summary of 3He and Neutron Detection Alternatives for Homeland Security," Pacific Northwest National Laboratory2010.

[27] J. L. Lacy, "Boron coated straw neutron detector," 2005.

[28] J. L. Lacy, A. Athanasiades, L. Sun, C. S. Martin, T. D. Lyons, M. A. Foss, *et al.*, "Boron-coated straws as a replacement for 3He-based neutron detectors," *Nuclear Instruments and Methods in Physics Research Section A: Accelerators, Spectrometers, Detectors and Associated Equipment,* vol. 652, pp. 359-363, 2011.

[29] S. L. Bellinger, "Advanced Microstructured Semiconductor Neutron Detectors: Design, Fabrication, and Performance," Doctorate, Mechanical and Nuclear Engineering, Kansas State University, 2011.

[30] S. L. Bellinger, R. G. Fronk, and W. J. McNeil, "Characteristics of the Stacked Microstructured Solid-State Neutron Detector," in *SPIE*, 2010.

[31] S. L. Bellinger, R. G. Fronk, and W. J. McNeil, "High Efficiency Dual-Integrated Stacked Microstructured Solid-State Neutron Detectors," presented at the IEEE Nuclear Science Symposium, 2010.

[32] W. J. McNeil, S. L. Bellinger, T. C. Unruh, E. L. Patterson, J. K. Shultis, and D. S. McGregor, "Perforated Diode Fabrication for Neutron Detection," *IEEE Nuclear Science Symposium*, vol. R08-2, 2006.

[33] G. Charpak, D. Rahm, and H. Steiner, "Some developments in the operation of multiwire proportional chambers," *Nuclear Instruments and Methods*, vol. 80, pp. 13-34, 4/1/ 1970.

[34] G. Charpak, R. Bouclier, T. Bressani, J. Favier, and Č. Zupančič, "Some read-out systems for proportional multiwire chambers," *Nuclear Instruments and Methods*, vol. 65, pp. 217-220, 11/1/ 1968.

[35] G. Charpak, R. Bouclier, T. Bressani, J. Favier, and Č. Zupančič, "The use of multiwire proportional counters to select and localize charged particles," *Nuclear Instruments and Methods*, vol. 62, pp. 262-268, 7/1/ 1968.

[36] D. S. McGregor, S. L. Bellinger, W. J. McNeil, M. F. Ohmes, and K. A. Nelson, "Gas-filled neutron detectors having improved detection efficiency," 8,519,350, August 27, 2013.

[37] S. L. Bellinger, D. S. McGregor, and K. A. Nelson, "Gas-filled Neutron Detectors and Imaging System and Array of Such," 2013.

[38] J. R. Taylor, C. D. Zafiratos, and M. A. Dubson, *Modern Physics for Scientists and Engineers*, 2nd ed.: Pearson Prentice Hall, 2004.

[39] W. N. Cottingham and D. A. Greenwood, *An Introduction to Nuclear Physics*, 2nd ed.: Cambridge University Press, 2001.

[40] S. K. and M. W., "The lifetime of the free neutron," *Journal of Physics G Nuclear Physics Supplement*, vol. 18, 1992.

[41] G. F. Knoll, *Radioisotope Neutron Sources*. New York: Pergamon Press, 1983.

[42] J. K. Shultis and R. E. Faw, *Fundamentals of Nuclear Science and Engineering*, 2nd ed. Boca Raton, FL: Taylor & Francis Group, 2008.

[43] (2011). *Evaluated Nuclear Data File (ENDF)*. Available: www.nndc.bnl.gov/exfor/endf00.jsp

[44] D. S. McGregor and J. K. Shultis, "Reporting detection efficiency for semiconductor neutron detectors: A need for a standard," *Nuclear Instruments and Methods in Physical Research Section A*, vol. 632, pp. 167-174, 2011.

[45] J. Libby, "Title," unpublished|.

[46] J. R. Lamarsh, *Introduction to nuclear reactor theory*. LaGrange Park, IL: American Nuclear Society, 1965.

[47] I. A. E. Agency, "Thermal neutron cross sections, resonance integrals, and Westcott factors," ed. www.iaea.org: IAEA.

[48] D. S. McGregor, M. D. Hammig, Y.-H. Yang, H. K. Gersch, and R. T. Klann, "Design considerations for thin film coated semiconductor thermal neutron detectors - I: basics regarding alpha particle emitting neutron reactive films," *Nuclear Instruments and Methods in Physical Research Section A,* vol. 500, pp. 272-308, 2003.

[49] E. M. Baum, H. D. Knox, and T. R. Miller, *Nuclides and Isotopes*, 16th ed., 2002.

[50] S. F. Mughabghab and D. I. Garber, "Neutron Cross Sections," 1976.

[51] D. S. McGregor, J. T. Lindsay, and R. W. Olsen, "Thermal neutron detection with CdZnTe semiconductor detectors," *Nuclear Instruments and Methods in Physical Research Section A,* vol. 381, pp. 498-501, 1996.

[52] G. Leinweber, D. P. Barry, M. J. Trbovich, J. A. Burke, N. J. Drindak, H. D. Knox, *et al.*, "Neutron Capture and Total Cross-Section Measurements and Resonance Parameters of Gadolinium," *Nuclear Science Engineering,* vol. 154, pp. 261-279, 2006.

[53] S. Alimov, S. Buzzetti, B. Bebauer, C. Petrillo, F. Sacchetti, C. Schulz, *et al.*, "Scientific Reviews: Microstrip Detectors with Gd-157 Converters," *Neutron News,* vol. 16, pp. 22-24, 2007.

[54] Y. Y. Berzin, P. T. Prokof'ev, and G. L. Rezvaya, "Conversion electroctrum emitted at thermal neutron capture by Gd-155 nuclei," *Latvijas PSR Zinatnu Akademijas Vestis, Fizikas un Tehnisko Zinatnu,* vol. 6, pp. 3-8, 1968.

[55] Y. Y. Berzin, A. E. Kruminya, and L. A. Neiburg, "Conversion electron and gamma-ray spectra from thermal neutron capture in Gd-157," *Latvijas PSR Zinatnu Akademijas Vestis, Fizikas un Tehnisko Zinatnu Serija,* vol. 5, pp. 3-7, 1972.

[56] P. Kandlakunta, L. R. Cao, and P. Mulligan, "Measurement of internal conversion electrons from Gd neutron capture," *Nuclear Instruments and Methods in Physical Research Section A,* vol. 705, pp. 36-41, 2013.

[57] L. V. Groshev, A. M. Demidov, and V. A. Ivanov, "Gamma-rays and conversion electrons from the (n,gamma) reaction on gadolinium isotopes," *Izvestiya Akademii Nauk SSSR,* vol. 26, pp. 1119-1133, 1962.

[58] J. K. Shultis and R. E. Faw, *Radiation Shielding*, 2000.

[59] E. E. Lewis, *Fundamentals of Nuclear Reactor Physics*. London: Elsevier, 2008.

[60] E. E. Lewis, *Fundamentals of Nuclear Reactor Theory*. Burlington, MA: Academic Press, 2008.

[61] T. W. Crane and M. P. Baker, "Neutron Detectors," in *Passive Nondestructive Assay of Nuclear Materials*, ed, 1991.

[62] D. S. McGregor, R. T. Klann, H. K. Gersch, and J. D. Sanders, "Designs for Thin-Film-Coated Semiconductor Thermal Neutron Detectors," *IEEE Transactions on Nuclear Science*, 2002.

[63] J. K. Shultis and D. S. McGregor, "Efficiencies of coated and Perforated Semiconductor Neutron Detectors," *IEEE Transactions on Nuclear Science*, vol. 53, 2006.

[64] W. J. McNeil, "Perforated Diode Neutron Sensors," Doctorate, Mechanical and Nuclear Engineering, Kansas State University, 2010.

[65] J. Ziegler and J. Biersack, "Stopping Ranges of Ions in Matter (SRIM)," 2008.

[66] K. A. Nelson, S. L. Bellinger, B. W. Montag, J. L. Neihart, T. A. Riedel, A. J. Schmidt, *et al.*, "Investigation of a lithium foil multi-wire proportional counter for potential 3He replacement," *Nuclear Instruments and Methods in Physics Research Section A: Accelerators, Spectrometers, Detectors and Associated Equipment*, vol. 669, pp. 79-84, 3/21/ 2012.

[67] K. A. Nelson, S. L. Bellinger, B. W. Montag, J. L. Neihart, T. A. Riedel, A. J. Schmidt, *et al.*, "Investigation of aerogel, saturated foam, and foil for thermal neutron detection," in *Nuclear Science Symposium and Medical Imaging Conference (NSS/MIC), 2011 IEEE*, 2011, pp. 1026-1029.

[68] S. Steiner. (2005). *Aerogel.org*.

[69] P. M. Dighe, D. N. Prasad, K. R. Prasad, S. K. Kataria, S. N. Athavale, A. L. Pappachan, *et al.*, "Boron-lined proportional counters with improved neutron sensitivity," *Nuclear Instruments and Methods in Physics Research Section A: Accelerators, Spectrometers, Detectors and Associated Equipment*, vol. 496, pp. 154-161, 1/1/ 2003.

[70] P. M. Dighe, "New cathode design boron lined proportional counters for neutron area monitoring application," *Nuclear Instruments and Methods in Physics Research Section A: Accelerators, Spectrometers, Detectors and Associated Equipment*, vol. 575, pp. 461-465, 6/1/ 2007.

[71] C. M. Lavelle, R. M. Deacon, D. S. Hussey, M. Coplan, and C. W. Clark, "Characterization of boron coated vitreous carbon foam for neutron detection," *Nuclear Instruments and Methods in Physics Research Section A: Accelerators, Spectrometers, Detectors and Associated Equipment*, vol. 729, pp. 346-355, 11/21/ 2013.

[72] C. Joram, "Multiwire Proportional Chamber (MWPC)," CERN2002.

[73] J. J. Duderstadt and L. J. Hamilton, *Nuclear Reactor Anaysis*: John Wiley & Sons, Inc., 1976.

[74] D. A. Monti, "Development of a one-dimensional small angle neutron scattering instrument at the university of illinois TRIGA reactor laboratory," Masters, Nuclear Engineering Dept., University of Illinois, Urbana, Illinois, 1995.

[75] T. C. Unruh, "Development of a neutron diffraction system and neutron imaging system for beamport characterization," Masters, Mechanical and Nuclear Engineering, Kansas State University, 2009.

[76] K. A. Nelson, J. L. Neihart, T. A. Riedel, A. J. Schmidt, and D. S. McGregor, "A novel method for detecting neutrons using low density high porosity aerogel and saturated foam," *Nuclear Instruments and Methods in Physics Research Section A: Accelerators, Spectrometers, Detectors and Associated Equipment*, vol. 686, pp. 100-105, 9/11/ 2012.

[77] M. S. Gossman, A. J. Pahikkala, M. B. Rising, and P. H. McGinley, "Providing solid angle formalism for skyshine calculations," *Journal of applied clinical medical physics*, vol. 11, pp. 278-282, 2010.

[78] M. S. Gossman, A. J. Pahikkala, M. B. Rising, and P. H. McGinley, "Letter to the Editor," *Journal of applied clinical medical physics*, vol. 12, pp. 242-243, 2011.

[79] A. V. Oosterom and J. Strackee, "The Solid Anlge of a Plane Triangle," *IEEE Transactions on Biomedical Engineering*, vol. BME-30, pp. 125-126, 1983.

[80] R. Nave. (November 21, 2013). *Hyperphysics*. Available: hyperphysics.phy-astr.gsu.edu

[81] K. F. Riley, M. P. Hobson, and S. J. Bence, *Mathematical Methods for physics and engineering*, 2nd ed. United Kingdom: Cambridge University Press, 2002.

APPENDIX A

MATLAB DETECTOR EFFICIENCY CODE

The theoretical intrinsic thermal neutron detection efficiency of the ^{6}Li foil, ^{6}LiF impregnated foam, aerogel, boron foil, and LiF foil neutron detectors were calculated based upon the equations derived by McGregor, et al [48]. These equations have simply been modified for the neutron absorber material properties used in the experiments described in this thesis. The basis of the equations multiplies two integrated quantities. The first quantity is the neutron absorption probability in a particular material of a specific total thickness. If the detector has multiple layers of neutron absorber sheets, then the quantity used is the total thickness of all sheets summed together. The second quantity is the reaction product escape probability a particular thickness of neutron absorber material. If multiple neutron absorber sheets, all of the same thickness, are used in the detector, then the reaction product escape probability is that of a single neutron absorber sheet. These equations developed by McGregor, et alli, show that for a particular detector and neutron absorber configuration, there are optimized neutron absorber layer thicknesses that maximize the thermal neutron detection efficiency. The proceeding MatLab code was used to develop the thermal neutron detection efficiency plots as a function of absorber thickness for various absorber layers. The computer code follows the precedent of assuming a normally incident thermal neutron beam and a LLD energy setting of 300 keV. In other words, the reaction products whose angles of trajectory result in less than 300 keV of energy deposited in the sensor volume are not included in the detector efficiency. Additionally, this simulation below lets the user choose what type of material to run in the program, these materials include: Li, ^{6}Li, LiMg, LiF, ^{6}LiF, B, and ^{10}B. However, the computer program could be easily adapted to other materials.

```
function [Df S Snoq efficiencyplot] = efficiency2()

Material = input('What material would you like to use? (1->LiMg 2->6-Li 3-
>LiF 4->6-LiF 5->10-B 6->B) : ');
```

```
%Mylar = input('Would you like to use a Mylar coating? (1->Yes 2->No) : ');
Mylar=2;
%Gas = input('What gas would you like to use? (1->P-10 2->Ar 3->10-BF3) : ');
Layers = input('How many layers? : ');

Branches = 0;   %Number of reacttion branches
Ratios   = 0;   %Branching ratio. Ratio(i) correspondes to branching ratio of
branch i.
Llr      = 0;   %Average range of long-range particle (in cm). Llr(i)
corresponds to Llr of branch i.
Lsr      = 0;   %Average range of short-range particle (in cm). Lsr(i)
corresponds to Lsr of branch i.

Name = [' Li  '; '6-Li '; ' LiF '; '6-LiF'; '10-B '; '  B  '];
Name = Name(Material,:);


% Sets most of material properties
switch Material
    case 1 % 3/1LiMg Li original absorb=3.28
        Branches = 1;
        Ratios   = [ 1 ];
        Llr      = [123]*10^-4;      %[ 126.77 ]*10^-4;
        Lsr      = [21]*10^-4;      %[ 19.055 ]*10^-4;

    case 2 %6-Li
        Branches = 1;
        Ratios   = [ 1 ];
        Llr      = [ 128.3 ]*10^-4;
        Lsr      = [ 18.63 ]*10^-4;

    case 3 %LiF
        Branches = 1;
        Ratios   = [ 1 ];
        Llr      = [ 29.239 ]*10^-4;
        Lsr      = [ 4.6454 ]*10^-4;

    case 4 %6-LiF
        Branches = 1;
        Ratios   = [ 1 ];
        Llr      = [ 29.239 ]*10^-4;
        Lsr      = [ 4.6454 ]*10^-4;

    case 5 %10-B
        Branches = 2;
        Ratios   = [ 0.06 0.94 ];
        Llr      = [ 3.5233 2.6475 ]*10^-4;
        Lsr      = [ 1.0453 0.8102 ]*10^-4;

    case 6 %B
        Branches = 2;
        Ratios   = [ 0.06 0.94 ];
        Llr      = [ 3.5233 2.6475 ]*10^-4;
        Lsr      = [ 1.0453 0.8102 ]*10^-4;
```

```
    otherwise
        error('Nonvalid material selected')
end

if Mylar ~=1 && Mylar ~=2
    error('Please select Mylar or no Mylar')
end
% Changes for gas
    % cross sections for Ar and P-10 gas do not affect efficiency so they
    % are left out

% Set absorber cross section
absorbercrosssection = [   12.15  43.56   4.31  57.51 500.00  95.72 ];
SigmaF = absorbercrosssection(Material);

SpfLlr  = zeros(150,Branches);
SpfLsr  = zeros(150,Branches);
SpbLlr  = zeros(150,Branches);
SpbLsr  = zeros(150,Branches);
Qsrlr  = zeros(150,Branches);
Qlrsr  = zeros(150,Branches);

Df     = zeros(150,1);
layercrosssection = 0;
layerthickness    = 5;

if Mylar ==1
    layercrosssection=0.013866;
    layerthickness=0.0002;
end

U = size(layercrosssection);
R = 1;
S    = zeros(150,1);
Snoq = zeros(150,1);

for i=1:U
    R=R*exp(-layercrosssection(i)*layerthickness(i));
end

if Material == 5 || Material == 6
    for i=1:150
        Df(i)=i*0.000003;
    end
else
    for i=1:150
        Df(i)=i*0.0001;
    end
end

for i=1:Branches % i cycles through different branches
    for j=1:150 % j cycles through thicknesses (1-150 microns)
        % Calculates Q values
        [ Qsrlr(j,i) Qlrsr(j,i) ] = Qcalc(Ratios(i), R, SigmaF, Df(j),
Llr(i), Lsr(i));
```

```
        % Calculates Spf and Spb (two products per branch)
        [ SpfLlr(j,i) SpbLlr(j,i) ] = Scalc(Ratios(i), R, SigmaF, Df(j),
Llr(i), Mylar);
        [ SpfLsr(j,i) SpbLsr(j,i) ] = Scalc(Ratios(i), R, SigmaF, Df(j),
Lsr(i), Mylar);

    end
end
% Combine all branches
SpfLlr  = sum(SpfLlr,2);
SpfLsr  = sum(SpfLsr,2);
SpbLlr  = sum(SpbLlr,2);
SpbLsr  = sum(SpbLsr,2);

Qsrlr  = sum(Qsrlr,2);
Qlrsr  = sum(Qlrsr,2);

% Weighted average of long and short ranged reaction products
WLlr = 0;
WLsr = 0;

% Calculates WLlr and WLsr
for i=1:Branches
   WLlr = WLlr + (Llr(i) * Ratios(i));
   WLsr = WLsr + (Lsr(i) * Ratios(i));
end

if Layers < 20
    [efficiencyplot] = multiplelayers(SpfLlr, SpbLlr, SpfLsr, SpbLsr, Qsrlr,
Qlrsr, SigmaF, WLlr, WLsr, 20, Df, Mylar);
else
    [efficiencyplot] = multiplelayers(SpfLlr, SpbLlr, SpfLsr, SpbLsr, Qsrlr,
Qlrsr, SigmaF, WLlr, WLsr, Layers, Df, Mylar);
end

Snoq = SpfLlr + SpfLsr + SpbLlr + SpbLsr;
S    = SpfLlr + SpfLsr + SpbLlr + SpbLsr -(Qlrsr + Qsrlr);

Thickness = (Df+layerthickness/2*(Mylar-2))*20000; % Thickness of deposition
layer in microns.
outputstring = sprintf('Efficiency of multiple %s detectors', Name);

if Mylar == 1
    outputstring = sprintf('Efficiency of multiple %s detectors with a mylar
coating', Name);
end

figure
plot(Thickness,efficiencyplot(:,1),Thickness,efficiencyplot(:,2),Thickness,ef
ficiencyplot(:,3),...

Thickness,efficiencyplot(:,4),Thickness,efficiencyplot(:,5),Thickness,efficie
ncyplot(:,10),...
    Thickness,efficiencyplot(:,15),Thickness,efficiencyplot(:,20));
```

```
title(outputstring)
xlabel('Thickness (\mum)')
ylabel('Efficiency (%)')
legend('1','2','3','4','5','10','15','20');

outputstring = sprintf('Efficiency of %d layers of %s', Layers, Name);

if Mylar == 1
    outputstring = sprintf('Efficiency of %d layers of %s with a mylar
coating', Layers, Name);
end

figure
plot(Thickness,efficiencyplot(:,Layers));
title(outputstring)
xlabel('Thickess (\mum)')
ylabel('Efficiency (%)')
end
```

Subroutine to determine 'Scalc' which is the stoping power of the materials for reaction products in materials with set thicknesses:

```
function [ Spf Spb ] = Scalc( Fp, PImultiplyer, SigmaF, Df, L, Mylar )
%S Computes Spf and Spb for a given Df and reaction product

if 2*Df<L
        Spf=0.5*Fp*PImultiplyer*((1-(1/(SigmaF*L)))*...
            (1-exp(-2*SigmaF*Df))+(2*Df/L*exp(-2*...
            SigmaF*(Df))));

        Spb=0.5*Fp*PImultiplyer*((1+(1/(SigmaF*L)))*...
            (1-exp(-2*SigmaF*Df))-(2*Df/L));
    else
        Spf=0.5*Fp*PImultiplyer*((1-(1/(SigmaF*L)))*...
            (1-exp(-SigmaF*L))+exp(-SigmaF*L));

        Spb=0.5*exp(-SigmaF*(2*Df-L))*Fp*PImultiplyer*...
            ((1+(1/(SigmaF*L)))*(1-exp(-SigmaF*L))-1);
end

end
```

Subroutine to determine the amount of charge entering the sensor volume:

```
function [ Qsrlr Qlrsr ] = Qcalc( Fp, PImultiplyer, SigmaF, Df, Llr, Lsr )
%Q Finds Qsrls and Qlrsr for a given Fp, multiplyer, SigmaF, Df, Llr, and
%Lsr

Theta   =   2*Df*Lsr / (Llr + Lsr);
Gamma   =   2*Df*Llr / (Llr + Lsr);
```

```
if 2*Df<=Lsr
       Qsrlr=0.5*Fp*PImultiplyer*(exp(-SigmaF*Theta)*...
           ((2*SigmaF*Df-Llr*SigmaF-...
           SigmaF*Theta-1)/(Llr*SigmaF))-...
           ((2*SigmaF*Df-Llr*SigmaF...
           -1)/(Llr*SigmaF))+exp(-2*SigmaF*Df)...
           *((2*SigmaF*Df-Lsr*SigmaF+1)/...
           (Lsr*SigmaF))+exp(-SigmaF*Theta)...
           *((Lsr*SigmaF-Theta*SigmaF-1)/...
           (Lsr*SigmaF)));

       Qlrsr=0.5*Fp*PImultiplyer*(exp(-SigmaF*Gamma)*...
           ((2*SigmaF*Df-Lsr*SigmaF-...
           SigmaF*Gamma-1)/(Lsr*SigmaF))-...
           ((2*SigmaF*Df-Lsr*SigmaF...
           -1)/(Lsr*SigmaF))+exp(-2*SigmaF*Df)...
           *((2*SigmaF*Df-Llr*SigmaF+1)/...
           (Llr*SigmaF))+exp(-SigmaF*Gamma)...
           *((Llr*SigmaF-Gamma*SigmaF-1)/...
           (Llr*SigmaF)));

elseif Lsr<2*Df && 2*Df<=Llr
        Qsrlr=0.5*Fp*PImultiplyer*(exp(-SigmaF*Theta)*...
           ((2*SigmaF*Df-Llr*SigmaF-...
           SigmaF*Theta-1)/(Llr*SigmaF))-...
           ((2*SigmaF*Df-Llr*SigmaF...
           -1)/(Llr*SigmaF))+((exp(-SigmaF*Lsr))/...
           (SigmaF*Lsr))+exp(-SigmaF*Theta)...
           *((Lsr*SigmaF-Theta*SigmaF-1)/...
           (Lsr*SigmaF)));

         Qlrsr=0.5*Fp*PImultiplyer*(exp(-SigmaF*Gamma)*...
           ((2*SigmaF*Df-Lsr*SigmaF-...
           SigmaF*Gamma-1)/(Lsr*SigmaF))+...
           ((exp(-SigmaF*(2*Df-Lsr)))/(SigmaF*Lsr))...
           +(exp(-2*SigmaF*Df))*((2*SigmaF*Df-...
           SigmaF*Llr+1)/(SigmaF*Llr))...
           +exp(-SigmaF*Gamma)*((Llr*SigmaF-...
           Gamma*SigmaF-1)/(Llr*SigmaF)));

elseif Llr<2*Df && 2*Df<=Llr+Lsr
        Qsrlr=0.5*Fp*PImultiplyer*(exp(-SigmaF*Theta)*...
           ((2*SigmaF*Df-Llr*SigmaF-...
           SigmaF*Theta-1)/(Llr*SigmaF))+...
           ((exp(-SigmaF*(2*Df-Llr)))/(SigmaF*Llr))...
           +((exp(-SigmaF*Lsr))/(SigmaF*Lsr))...
           +exp(-SigmaF*Theta)*((Lsr*SigmaF-...
           Theta*SigmaF-1)/(Lsr*SigmaF)));

        Qlrsr=0.5*Fp*PImultiplyer*(exp(-SigmaF*Gamma)*...
           ((2*SigmaF*Df-Lsr*SigmaF-...
           SigmaF*Gamma-1)/(Lsr*SigmaF))+...
           ((exp(-(2*Df-Lsr)*SigmaF))/(SigmaF*Lsr))+...
           ((exp(-SigmaF*Llr))/(SigmaF*Llr))+...
           exp(-SigmaF*Gamma)*((Llr*SigmaF-...
           Gamma*SigmaF-1)/(Llr*SigmaF)));
```

```
elseif Lsr+Llr<2*Df
        Qsrlr=0;
        Qlrsr=0;
end

end
```

Subroutine that determines the final efficiency:

```
function [efficiencyplot] = multiplelayers
(SpfLlr,SpbLlr,SpfLsr,SpbLsr,Qsrlr,Qlrsr,SigmaF,Llr,Lsr,Layers, df, Mylar)

%at the current time the program behaves similarly to the original when
%P-10 gas is introduced however the values are much higher then to be
%expected

fttn=zeros(150,Layers);
ftta=zeros(150,Layers);
spftriton2=zeros(150,Layers);
spbtriton2=zeros(150,Layers);
spfalpha2=zeros(150,Layers);
spbalpha2=zeros(150,Layers);
qrs2=zeros(150,Layers);
qlr2=zeros(150,Layers);
efficiencyplot=zeros(150,Layers);

for i=1:150
    for j=1:Layers
        if df(i)<(Llr)/2
            fttn(i,j)=exp(-SigmaF*df(i)*j*2);
        else
            fttn(i,j)=exp(-SigmaF*df(i)*j*2)*exp(-SigmaF*(2*df(i)-Llr));
        end
        if df(i)<(Lsr)/2
            ftta(i,j)=exp(-SigmaF*df(i)*j*2);
        else
            ftta(i,j)=exp(-SigmaF*df(i)*j*2)*exp(-SigmaF*(2*df(i)-Lsr));
        end
        if j==1
            spftriton2(i,j)=(SpfLlr(i));
            spbtriton2(i,j)=SpbLlr(i);
            spfalpha2(i,j)=SpfLsr(i);
            spbalpha2(i,j)=SpbLsr(i);
            qrs2(i,j)=Qlrsr(i);
            qlr2(i,j)=Qsrlr(i);
        else
            spftriton2(i,j)=spftriton2(i,j-1)+fttn(i,j-1)*spftriton2(i,1);
            spbtriton2(i,j)=spbtriton2(i,j-1)+fttn(i,j-1)*spbtriton2(i,1);
            spfalpha2(i,j)=spfalpha2(i,j-1)+ftta(i,j-1)*spfalpha2(i,1);
            spbalpha2(i,j)=spbalpha2(i,j-1)+ftta(i,j-1)*spbalpha2(i,1);
            qrs2(i,j)=qrs2(i,j-1)+fttn(i,j-1)*qrs2(i,1);
            qlr2(i,j)=qlr2(i,j-1)+fttn(i,j-1)*qlr2(i,1);
```

```
        end

efficiencyplot(i,j)=spftriton2(i,j)+spbtriton2(i,j)+spfalpha2(i,j)+spbalpha2(
i,j)...
            -qrs2(i,j)-qlr2(i,j);
    end
end

efficiencyplot=efficiencyplot*100;
end
```

The probability that the four *Cases* occur per neutron absorption was determined using an adjustment to the above program. This plot was generated using the reaction product escape probability at each thickness.

```
% When adjusting the program for new materials the sections that will need
% to be changed will be the Llr and Lsr for the materials and the material
% cross section. LLr and Lsr are the long and short range of the reaction
% produces in the material.

function [Thickness,efficiencyplot]=percentages
Material = input('What material would you like to use? (1->LiMg 2->6-Li 3-
>LiF 4->6-LiF 5->10-B 6->B) : ');
Mylar = 2;
%Gas = input('What gas would you like to use? (1->P-10 2->Ar 3->10-BF3) : ');
Layers = 1;

Branches = 0;   %Number of reaction branches
Ratios   = 0;   %Branching ratio. Ratio(i) corresponds to branching ratio of
branch i.
Llr      = 0;   %Average range of long-range particle (in cm). Llr(i)
corresponds to Llr of branch i.
Lsr      = 0;   %Average range of short-range particle (in cm). Lsr(i)
corresponds to Lsr of branch i.

Name = [' Li  '; '6-Li '; ' LiF '; '6-LiF'; '10-B '; '  B  '];
Name = Name(Material,:);


% Sets most of material properties
switch Material
    case 1 % 3/1LiMg Li
        Branches = 1;
        Ratios   = [ 1 ];
        Llr      = [101]*10^-4;     % if adjusting material change these
        Lsr      = [17.2]*10^-4;

    case 2 %6-Li
        Branches = 1;
        Ratios   = [ 1 ];
        Llr      = [ 126.77 ]*10^-4;
        Lsr      = [ 19.055 ]*10^-4;
```

```
    case 3 %LiF
        Branches = 1;
        Ratios   = [ 1 ];
        Llr      = [ 29.239 ]*10^-4;
        Lsr      = [ 4.6454 ]*10^-4;

    case 4 %6-LiF
        Branches = 1;
        Ratios   = [ 1 ];
        Llr      = [ 29.239 ]*10^-4;
        Lsr      = [ 4.6454 ]*10^-4;

    case 5 %10-B
        Branches = 2;
        Ratios   = [ 0.06 0.94 ];
        Llr      = [ 3.5233 2.6475 ]*10^-4;
        Lsr      = [ 1.0453 0.8102 ]*10^-4;

    case 6 %B
        Branches = 2;
        Ratios   = [ 0.06 0.94 ];
        Llr      = [ 3.5233 2.6475 ]*10^-4;
        Lsr      = [ 1.0453 0.8102 ]*10^-4;

    otherwise
        error('Nonvalid material selected')
end

if Mylar ~=1 && Mylar ~=2
    error('Please select Mylar or no Mylar')
end
% Changes for gas
    % cross sections for Ar and P-10 gas do not affect efficiency so they
    % are left out

% Set absorber cross section adjust number according to case number
absorbercrosssection = [   15.61   43.56    4.31   57.51 500.00   95.72 ];
SigmaF = absorbercrosssection(Material);

SpfLlr  = zeros(150,Branches);
SpfLsr  = zeros(150,Branches);
SpbLlr  = zeros(150,Branches);
SpbLsr  = zeros(150,Branches);
Qsrlr  = zeros(150,Branches);
Qlrsr  = zeros(150,Branches);

Df     = zeros(150,1);
layercrosssection = 0;
layerthickness    = 5;

if Mylar ==1
    layercrosssection=0.013866;
    layerthickness=0.0002;
end
```

```
U = size(layercrosssection);
R = 1;
S    = zeros(150,1);
Snoq = zeros(150,1);

for i=1:U
    R=R*exp(-layercrosssection(i)*layerthickness(i));
end

if Material == 5 || Material == 6
    for i=1:150
        Df(i)=i*0.000003;
    end
else
    for i=1:150
        Df(i)=i*0.0001;
    end
end

for i=1:Branches % i cycles through different branches
    for j=1:150 % j cycles through thicknesses (1-150 microns)
        % Calculates Q values
        [ Qsrlr(j,i) Qlrsr(j,i) ] = Qcalc(Ratios(i), R, SigmaF, Df(j),
Llr(i), Lsr(i));

        % Calcultes Spf and Spb (two products per branch)
        [ SpfLlr(j,i) SpbLlr(j,i) ] = Scalc(Ratios(i), R, SigmaF, Df(j),
Llr(i));
        [ SpfLsr(j,i) SpbLsr(j,i) ] = Scalc(Ratios(i), R, SigmaF, Df(j),
Lsr(i));

    end
end
% Combine all branches
SpfLlr  = sum(SpfLlr,2);
SpfLsr  = sum(SpfLsr,2);
SpbLlr  = sum(SpbLlr,2);
SpbLsr  = sum(SpbLsr,2);

Qsrlr  = sum(Qsrlr,2);
Qlrsr  = sum(Qlrsr,2);

% Weighted average of long and short ranged reaction products
WLlr = 0;
WLsr = 0;

% Calculates WLlr and WLsr
for i=1:Branches
   WLlr = WLlr + (Llr(i) * Ratios(i));
   WLsr = WLsr + (Lsr(i) * Ratios(i));
end

[efficiencyplot] = multiplelayers2(SpfLlr, SpbLlr, SpfLsr, SpbLsr, Qsrlr,
Qlrsr, SigmaF, WLlr, WLsr, Layers, Df, Mylar);
```

```
for i=1:150
    efficiencyplot(i,9)=100*(1-exp(absorbercrosssection(Material)*-
2*Df(i,1))); %percent should be absorbed
    efficiencyplot(i,2)=efficiencyplot(i,9)-efficiencyplot(i,1); %neither
    efficiencyplot(i,8)=100*efficiencyplot(i,2)/efficiencyplot(i,9); %neither
percent

efficiencyplot(i,3)=efficiencyplot(i,1)*efficiencyplot(i,3)/efficiencyplot(i,
9); %both

efficiencyplot(i,4)=efficiencyplot(i,1)*efficiencyplot(i,4)/efficiencyplot(i,
9); %just triton

efficiencyplot(i,5)=efficiencyplot(i,1)*efficiencyplot(i,5)/efficiencyplot(i,
9);%just alpha

efficiencyplot(i,6)=efficiencyplot(i,3)+efficiencyplot(i,4)+efficiencyplot(i,
5)+efficiencyplot(i,8);
end

Snoq = SpfLlr + SpfLsr + SpbLlr + SpbLsr;
S    = SpfLlr + SpfLsr + SpbLlr + SpbLsr -(Qlrsr + Qsrlr);

Thickness = (Df+layerthickness/2*(Mylar-2))*20000; % Thickness of deposition
layer in microns.
%outputstring = sprintf('Efficiency of multiple %s detectors', Name);

if Mylar == 1
    outputstring = sprintf('Efficiency of multiple %s detectors with a mylar
coating', Name);
end

figure
plot(Thickness,efficiencyplot(:,8),Thickness,efficiencyplot(:,3),Thickness,ef
ficiencyplot(:,4),...
    Thickness,efficiencyplot(:,5),Thickness,efficiencyplot(:,6));
title('Percentages')
xlabel('Thickness (\mum)')
ylabel('Percent')
legend('neither','both','triton only','alpha only','totatl');

end
```

APPENDIX B

MATLAB ^{6}LI FOIL PULSE-HEIGHT SPECTRA CODE

The theoretical thermal neutron response pulse-height spectra were determined using a Monte-Carlo method in MatLab for various ^{6}Li foil, ^{10}B foil, and ^{6}LiF foil thicknesses ranging between 1–180 μm. The equations and methodology used in the MatLab simulation were first developed by Bellinger for silicon trenches backfilled with ^{6}LiF, and a more detail explanation of the simulation can be found here [29]. These equations were adjusted for material properties used in the research described in this thesis. Assumptions made for the simulation include the reaction products traveled in straight lines, the energy and range straggling are minimal and thus ignored, and charge collection efficiency of electron-ions pairs was 100 percent, thus, no electron avalanching effects were included. A weighted distribution determined by the neutron absorption position through the material used in the simulation, which was also where the triton and alpha particle are born. The alpha particle and triton had random trajectories in the simulation, but were oriented 180° to each other. After the path lengths of the reaction products were determined, if they retained a minimum of 300 keV before escaping the neutron absorber sheet, the remaining energy was tallied as the energy that deposited in the gas volume. A histogram plot was generated from the various energy tallies to determine the theoretical thermal neutron response pulse-height spectrum.

```
clear all; clc; close all; clear global; format long;
%%

%Variables
n = 100;         %Histories
aHex = 170000;       %width of gas region
Depth = 170000;    %Length of gas region
tHex = 55;       %Foil thickness (microns)
%tMylar = 3;     %Mylar thickness (microns)


%Totaln = 0;
%TotalECum = 0;
```

```
for i=1:10

tic
load TotalEnergySiHex1020 TotalECum Totaln
[TotalEnergyDep] = CBSFunc(n,aHex,tHex,Depth);
TotalECum = cat(2,TotalECum,TotalEnergyDep);
Totaln=Totaln+n;
save ('TotalEnergySiHex1020', 'TotalECum', 'Totaln','Depth','aHex','tHex')
i=i
toc

end
```

Subroutine:

```
clear all; clc; close all; clear global;format long;
%%

%Variables
n = 100;         %Histories
aHex = 170000;       %width of gas region
Depth = 170000;    %Length of gas region
tHex = 55;       %Foil thickness (microns)
%tMylar = 3;     %Mylar thickness (microns)


%Totaln = 0;
%TotalECum = 0;

for i=1:10

tic
load TotalEnergySiHex1020 TotalECum Totaln
[TotalEnergyDep] = CBSFunc(n,aHex,tHex,Depth);
TotalECum = cat(2,TotalECum,TotalEnergyDep);
Totaln=Totaln+n;
save ('TotalEnergySiHex1020', 'TotalECum', 'Totaln','Depth','aHex','tHex')
i=i
toc

end
```

Subroutine:

```
function [EnergyDep_Si] =
EnergyDepSi(ResEnergy,n,type,Dirx,Diry,Dirz,Posx,Posy,Posz)
global UnitCellW UnitCellL Depth WaferThick LLD tHex aHex
format long
%Allocate Arrays for testing
EnergyDep_Hex = 2.05*(ones(1,n));
EnergyDep_Hex2 = 2.73*(ones(1,n));
```

```
EnergyDep_Si = zeros(1,n);
ResEnergy2 = zeros(1,n);
tHex = 55;
aHex = 170000;
Depth = 170000;
WaferThick = 170000;
LLD = 0.001;
UnitCellW = 170000;
UnitCellL = 170000;
%tMylar=3;



%all changes work untill this point
for i=1:n
%  Alpha Ion 2.05 MeV
    if(type == 1)
        while
((ResEnergy(i)>LLD)&&(Posx(i)>=(0))&&(Posx(i)<=UnitCellW)&&(Posy(i)>=(0))&&(P
osy(i)<=UnitCellL))
        %Check if in LiF Trench
        %Determine Residual Energy after removed from LiF Trench use Hexline
        %equation to track displacement and current position within cell
       HexLine1 = (Depth/2);
       HexLine2 = (Depth/2)+tHex;
       HexLine3 = (Depth/2)+tHex+2;%Initialize
        if((ResEnergy(i)>LLD)&&(Posz(i)>=HexLine1)&&(Posz(i)<=HexLine2)...

&&(Posx(i)>=(0))&&(Posx(i)<=UnitCellW)&&(Posy(i)>=(0))&&(Posy(i)<=UnitCellL))

            Path = 0.1; %Path Length Stepping by unit

            %Find Extra Path-Length to compensate Residual Energy Equation
            %Parameters from Shultis's "Path-Length to Reach Residual
            %Energy in Li-6" Empirical Formula
            a= 23.133142; b= 12.293099; c= 232.32791; d= -2.1426748; e= -
118.87426; f= 0.19955347;
            Rx =
(a+c*(ResEnergy(i))+e*(ResEnergy(i))^2)/(1+b*(ResEnergy(i))+d*(ResEnergy(i))^
2+f*(ResEnergy(i))^3);
            Rx = (Rx>=0 && Rx<23.12)*Rx + (Rx>=23.12)*23.12;

            %Track Energy
            dx=0;

while((ResEnergy(i)>LLD)&&(Posz(i)>=HexLine1)&&(Posz(i)<=HexLine2)...

&&(Posx(i)>=(0))&&(Posx(i)<=UnitCellW)&&(Posy(i)>=(0))&&(Posy(i)<=UnitCellL))

                x=Posx(i);
                y=Posy(i);
                z=Posz(i);
                %Keep track of last position
                Posx(i) = (Path)*Dirx(i)+Posx(i);
                Posy(i) = (Path)*Diry(i)+Posy(i);
```

```
                Posz(i) = (Path)*Dirz(i)+Posz(i);
                dx=sqrt((x-Posx(i))^2+(y-Posy(i))^2+(z-Posz(i))^2)+dx;
%Measure Inc. Dist. Traveled
                %Parameters from Shultis's "Residual Energy in Li6" Empirical
Formula
                a= 2.053770570587908; b= -0.04742708921702337; c= -
0.1781659003375961; d= -0.0001923618180423; e= 0.003869282702940299; f=
3.827645928721483E-05;
                %Empirical Formula for Residual Energy after Trench

ResEnergy(i)=(a+c*(dx+Rx)+e*(dx+Rx)^2)/(1+b*(dx+Rx)+d*(dx+Rx)^2+f*(dx+Rx)^3);

ResEnergy2(i)=(a+c*(dx+Rx+0.1)+e*(dx+Rx+0.1)^2)/(1+b*(dx+Rx+0.1)+d*(dx+Rx+0.1
)^2+f*(dx+Rx+0.1)^3);
                ResEnergy(i) =((ResEnergy(i)-
abs(ResEnergy2(i)))>0)*ResEnergy(i);
                %Locate particle within boundaries
                HexLine1 = (Depth/2);
                HexLine2 = (Depth/2)+tHex;  %Initialize
                %if dx > 6.05
                %    ResEnergy(i)=LLD;
                %end

            end

                EnergyDep_Hex(i) = EnergyDep_Hex(i)-ResEnergy(i);
        end

        %Parameters from Shultis's "Path-Length to Reach Residual Energy in
P10" Empirical Formula
        if((ResEnergy(i)>LLD))
            a= 12561.04659982151; b= 6.812850585193042; c= 65625.76613658024;
d= -1.233082253065215; e= -35016.81045667153; f= 0.1334964834325714;
            Rx =
(a+c*(ResEnergy(i))+e*(ResEnergy(i))^2)/(1+b*(ResEnergy(i))+d*(ResEnergy(i))^
2+f*(ResEnergy(i))^3);
            Rx = (Rx>=0 && Rx<12570)*Rx + (Rx>=12570)*12570;
        end

        %Track Energy
            dx=0;   %Initialize
            Res_E_Si = ResEnergy(i);   %Energy before lost in Si

            %Parameters from Shultis's "Residual Energy in P10" Empirical
Formula
            a= 2.051064712123166; b= -8.338958617006012E-05; c= -
0.0003183148093880542; d= -1.116042204867124E-10; e= 1.23574262610724E-08; f=
2.081276339547351E-13;

        while
((Posy(i)>=0)&&(Posy(i)<=UnitCellL)&&(Posz(i)>=HexLine2)&&(Posz(i)<=WaferThic
k)&&...
                (Posx(i)<=UnitCellW)&&(Posx(i)>=0)&&(ResEnergy(i)>LLD))||...

((Posy(i)>=0)&&(Posy(i)<=UnitCellL)&&(Posz(i)>=0)&&(Posz(i)<=HexLine1)&&...
                (Posx(i)>=(0))&&(Posx(i)<=UnitCellW)&&(ResEnergy(i)>LLD))
```

```
            Path = 0.5; %Path Length Stepping by unit

                x=Posx(i);y=Posy(i);z=Posz(i);      %Keep track of last
position
                Posx(i) = (Path)*Dirx(i)+Posx(i);
                Posy(i) = (Path)*Diry(i)+Posy(i);
                Posz(i) = (Path)*Dirz(i)+Posz(i);
                dx = sqrt((x-Posx(i))^2+(y-Posy(i))^2+(z-Posz(i))^2) + dx;
%Measure Inc. Dist. Traveled
                %Shultis's "Residual Energy in Si" Empirical Formula

ResEnergy(i)=(a+c*(dx+Rx)+e*(dx+Rx)^2)/(1+b*(dx+Rx)+d*(dx+Rx)^2+f*(dx+Rx)^3);

ResEnergy2(i)=(a+c*(dx+Rx+0.1)+e*(dx+Rx+0.1)^2)/(1+b*(dx+Rx+0.1)+d*(dx+Rx+0.1
)^2+f*(dx+Rx+0.1)^3);
                ResEnergy(i) =((ResEnergy(i)-
abs(ResEnergy2(i)))>0)*ResEnergy(i);
                %Locate particle within boundaries
                HexLine1 = (Depth/2);
                HexLine2 = (Depth/2)+tHex;  %Initialize
        end

        %Mirror off UnitCell walls to account for cross-cell energy deposit
%         if((ResEnergy(i)>LLD)&&((Posz(i)<=0)||(Posz(i)>=WaferThick)))
%
%            Path = 0.5; %Path Length Stepping by unit
%
            %Mirror by Change Direction
%                Dirz(i)=-Dirz(i);
%                %Move everything back one unit, so as to still be in Unit
Cell
%                Posx(i) = (Path)*(-Dirx(i))+Posx(i);
%                Posy(i) = (Path)*(Diry(i))+Posy(i);
%                Posz(i) = (Path)*(-Dirz(i))+Posz(i);
%        end
        %Sum energy loss in Si
        EnergyDep_Si(i) = Res_E_Si - ResEnergy(i); %+ EnergyDep_Si(i);
        end
    end
%%  Triton Ion 2.73 MeV
    if(type == 2)

        while
((ResEnergy(i)>LLD)&&(Posx(i)>=(0))&&(Posx(i)<=UnitCellW)&&(Posy(i)>=(0))&&(P
osy(i)<=UnitCellL))
        %Check if in LiF Trench
        %Determine Residual Energy after removed from LiF Trench use Hexline
        %equation to track displacement and current position within cell
        HexLine1 = (aHex/2);
        HexLine2 = (aHex/2)+tHex;
        HexLine3 = (Depth/2)+tHex+2;%Initialize
        if((ResEnergy(i)>LLD)&&(Posz(i)>=HexLine1)&&(Posz(i)<=HexLine2)...

&&(Posx(i)>=(0))&&(Posx(i)<=UnitCellW)&&(Posy(i)>=(0))&&(Posy(i)<=UnitCellL))
```

```
            Path = 0.1; %Path Length Stepping by unit

            %Find Extra Path-Length to compensate Residual Energy Equation
            %Parameters from Shultis's "Path-Length to Reach Residual Energy
in Li6" Empirical Formula
            a= 131.70444; b= -0.12460972; c= -34.566672; d= 0.024763819; e= -
4.9930397;
            Rx =
(a+c*ResEnergy(i)+e*ResEnergy(i)^2)/(1+b*ResEnergy(i)+d*ResEnergy(i)^2);
            Rx = (Rx>=0 && Rx<132.5)*Rx + (Rx>=132.5)*132.5;

            %Track Energy
            dx=0;

while((ResEnergy(i)>LLD)&&(Posz(i)>=HexLine1)&&(Posz(i)<=HexLine2)...

&&(Posx(i)>=(0))&&(Posx(i)<=UnitCellW)&&(Posy(i)>=(0))&&(Posy(i)<=UnitCellL))

                x=Posx(i);y=Posy(i);z=Posz(i);      %Keep track of last
position
                Posx(i) = (Path)*Dirx(i)+Posx(i);
                Posy(i) = (Path)*Diry(i)+Posy(i);
                Posz(i) = (Path)*Dirz(i)+Posz(i);
                dx=sqrt((x-Posx(i))^2+(y-Posy(i))^2+(z-Posz(i))^2)+dx;
%Measure Inc. Dist. Traveled
                %Parameters from Shultis's "Residual Energy in Li6" Empirical
Formula
                a= 2.729999410631117; b= -0.02045962210273644; c= -
0.06916603365506982; d= 0.0001426106129194996; e=0.0006413472991775354; f=-
3.688496589103268E-07; g=-2.556580971007554E-06; h=2.121780293046381E-10;
j=3.64016674496414E-09;
                %Empirical Formula for Residual Energy after Trench

ResEnergy(i)=(a+c*(dx+Rx)+e*(dx+Rx)^2+g*(dx+Rx)^3+j*(dx+Rx)^4)/(1+b*(dx+Rx)+d
*(dx+Rx)^2+f*(dx+Rx)^3+h*(dx+Rx)^4);

ResEnergy2(i)=(a+c*(dx+Rx+0.1)+e*(dx+Rx+0.1)^2+g*(dx+Rx+0.1)^3+j*(dx+Rx+0.1)^
4)/(1+b*(dx+Rx+0.1)+d*(dx+Rx+0.1)^2+f*(dx+Rx+0.1)^3+h*(dx+Rx+0.1)^4);
                ResEnergy(i) =((ResEnergy(i)-
abs(ResEnergy2(i)))>0)*ResEnergy(i);
                %if dx > 33.7
                %    ResEnergy(i)=LLD;
                %end
                %Locate particle within boundaries
               HexLine1 = (aHex/2);
               HexLine2 = (aHex/2)+tHex;  %Initialize
            end
            %dx

                EnergyDep_Hex2(i) = EnergyDep_Hex2(i)-ResEnergy(i);
        end
        %Parameters from Shultis's "Path-Length to Reach Residual Energy in
P10" Empirical Formula
        if((ResEnergy(i)>LLD))
            a= 71528.05412251205; b= -0.4240798671338062; c= -
42618.79652192698; d= 0.05941780314601744; e= 6028.129737421319;
```

```
            Rx =
(a+c*ResEnergy(i)+e*ResEnergy(i)^2)/(1+b*ResEnergy(i)+d*ResEnergy(i)^2);
            Rx = (Rx>=0 && Rx<71990)*Rx + (Rx>=71990)*71990;
        end

        %Track Energy
            dx = 0;     %intialize
            Res_E_Si = ResEnergy(i);   %Energy before lost in Si

            %Parameters from Shultis's "Residual Energy in P10" Empirical
Formula
            a= 2.724548677455965; b= -1.846076360587411E-05; c= -
7.206362560254313E-05; d= 7.177598939687537E-11; e= 4.749500816029316E-10;

        while
((Posy(i)>=0)&&(Posy(i)<=UnitCellL)&&(Posz(i)>=HexLine2)&&(Posz(i)<=WaferThic
k)&&...
                (Posx(i)<=UnitCellW)&&(Posx(i)>=0)&&(ResEnergy(i)>LLD))||...

((Posy(i)>=0)&&(Posy(i)<=UnitCellL)&&(Posz(i)>=0)&&(Posz(i)<=HexLine1)&&...
                (Posx(i)>=(0))&&(Posx(i)<=UnitCellW)&&(ResEnergy(i)>LLD))

            Path = 0.5; %Path Length Stepping by unit

                x=Posx(i);y=Posy(i);z=Posz(i);      %Keep track of last
position
                Posx(i) = (Path)*Dirx(i)+Posx(i);
                Posy(i) = (Path)*Diry(i)+Posy(i);
                Posz(i) = (Path)*Dirz(i)+Posz(i);
                dx = sqrt((x-Posx(i))^2+(y-Posy(i))^2+(z-Posz(i))^2) + dx;
%Measure Inc. Dist. Traveled
                %Shultis's "Residual Energy in Si" Empirical Formula

ResEnergy(i)=(a+c*(dx+Rx)+e*(dx+Rx)^2)/(1+b*(dx+Rx)+d*(dx+Rx)^2);

ResEnergy2(i)=(a+c*(dx+Rx+0.1)+e*(dx+Rx+0.1)^2)/(1+b*(dx+Rx+0.1)+d*(dx+Rx+0.1
)^2);
                ResEnergy(i) =((ResEnergy(i)-
abs(ResEnergy2(i)))>0)*ResEnergy(i);
                %Locate particle within boundaries
               HexLine1 = (aHex/2);
               HexLine2 = (aHex/2)+tHex;  %Initialize
         end

            %Mirror off UnitCell walls to account for cross-cell energy
deposit
%         if((ResEnergy(i)>LLD)&&((Posz(i)<=0)||(Posz(i)>=WaferThick)))

%            Path = 0.5; %Path Length Stepping by unit

            %Mirror by Change Direction
%               Dirz(i)=-Dirz(i);
%               %Move everything back one unit, so as to still be in Unit
Cell
%               Posx(i) = (Path)*(-Dirx(i))+Posx(i);
```

```
%                Posy(i) = (Path)*(Diry(i))+Posy(i);
%                Posz(i) = (Path)*(-Dirz(i))+Posz(i);
%         end
        %Sum energy loss in Si
        EnergyDep_Si(i) = ((Res_E_Si - ResEnergy(i))>0)*(Res_E_Si -
ResEnergy(i));% + EnergyDep_Si(i);
        end
    end
%% End Loop
end
end
```

subroutine:

```
clc; clear all; close all;

load TotalEnergySiHex1020 TotalECum Totaln Depth aHex tHex


%% INITIAL CONDITIONS
E = 5;              %MeV, Energy Max
chn = 256;          %512 Bin Channels
sigma = 0.2;        %MeV
BinE = E/chn;       %MeV/chn center of bin
SigmaChn = E/sigma; %How many channels are evenly spaced for var. channels
VarBins = 5;
x = 0:(BinE):E;
x2 = 0.098:E;
VarHist2=histc(TotalECum,x2);
VarHist = histc(TotalECum,x);   %Split up into var. seperate bins
efficiency = sum(VarHist2)/(Totaln(1))*100


%% FIND SPREADING MATRIX, NORMAL CDF DISTRIBUTION
for i = 1:VarBins+1
    p = normcdf([-i*sigma*SigmaChn/chn i*sigma*SigmaChn/chn],0,sigma);
    SpreadMatI(i) = (p(2) - p(1));
end
    SpreadMat = SpreadMatI;
for i = 1:VarBins
    SpreadMat(i+1) = (SpreadMatI(i+1) - SpreadMatI(i))/2;
end
for i = 1:(VarBins)
    Spread(i) = SpreadMat((VarBins+1)-i);
    Spread((VarBins-1)+i) = SpreadMat(i);
end
%% ARRANGE HISTOGRAM MATRIX INTO CODED VAR BINS
HistSpread = zeros(((VarBins-1)+VarBins),chn+((VarBins-1)+VarBins));
for i = 1:((VarBins-1)+VarBins)
    for j = 1:chn
    HistSpread(i,j) = VarHist(j).*1;%Spread(i);
    end
end
```

```
% HistSpreadRow = reshape(HistSpread,1,((VarBins-1)+VarBins)*chn);   %Reshape
matrix to combine
%% ARRANGE HISTOGRAM MATRIX INTO CODED VAR BINS
HistSmooth = zeros(((VarBins-1)+VarBins),chn+((VarBins-1)+VarBins));
for i = 1:((VarBins-1)+VarBins)
    for j = 1:chn
        HistSmooth(i,j+(i-1)) = HistSpread(i,j);
    end
end
% Sum the Arranged Matrix and move to the right
HistSmooth = sum(HistSmooth);
Smoothed_Spectrum = circshift(HistSmooth, [0, -(VarBins-1)]);
SmoothedSpect = zeros(1,chn);
for i = 1:(chn+1)
    SmoothedSpect(i) = Smoothed_Spectrum(i);
end


figure(1)
plot(x,SmoothedSpect);
ylim([1,10^3]);
xlabel('ENERGY DEPOSITED IN P-10
(MeV)','FontWeight','bold','FontName','Calisto MT');
ylabel('NUMBER OF INTERACTIONS','FontWeight','bold','FontName','Calisto MT');
```

Appendix B.1 – Pulse-Height Spectra: 55 µm ^{6}Li Foil

The optimized intrinsic thermal neutron detection efficiency for a 10 layer ^{6}Li foil MWPC occurs with Li foil thicknesses of 55 µm. The pulse-height spectrum is different than the reported 75 µm thickness Li foil MWPC because there is a reduction in self-absorption of the reaction products occurring in the foil. The theoretical pulse-height spectrum was simulated along with *Case 1*, *2*, and *3* for 55 µm thick Li foil, as shown in Figure B.1. This Matlab simulation shows that *Case 3* barely contributes to the overall pulse-height spectrum as a result of the relatively short reaction product range compared to the triton range and the pulse-height spectrum is dominated by the triton reaction product.

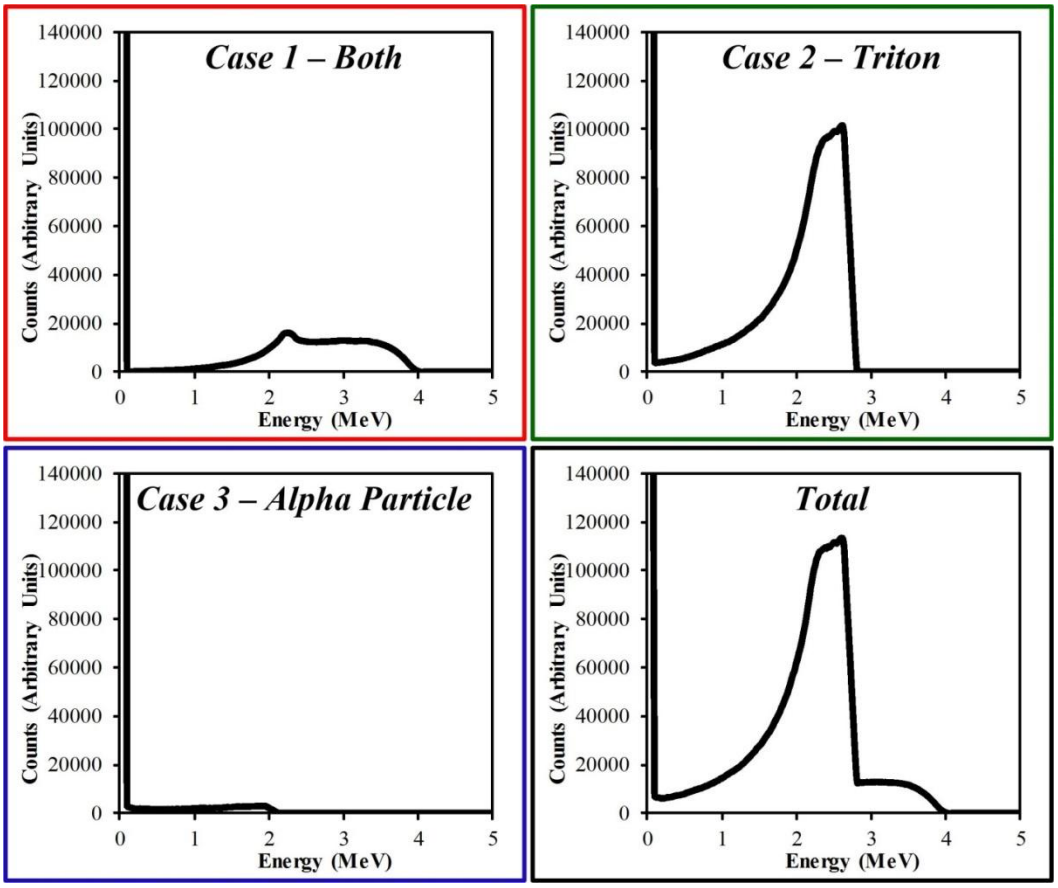

Figure B.1: The pulse-height spectrum contribution from the three cases where reaction product energy is deposited in the gas volume. The total of the three cases is summed into one pulse-height spectrum in the lower right. The plots are from 55 µm thick ^{6}Li foil.

Appendix B.2 – Pulse-Height Spectra: 35 µm ^{6}Li Foil

The optimized intrinsic thermal neutron detection efficiency for a 20 layer ^{6}Li foil MWPC occurs with foil thicknesses of 35 µm. The thinner Li foil changes the pulse-height spectrum from the reported 75 µm thickness Li foil MWPC because there is a reduction in self-absorption of the reaction products occurring in the foil. The theoretical pulse-height spectrum was simulated along with *Case 1*, *2*, and *3* for 55 µm thick Li foil, as shown in Figure B.2 and was created using MatLab. *Case 1* and *Case 2* almost completely dominate the overall pulse-height contribution due to the thickness of the foils and ranges of the reaction products.

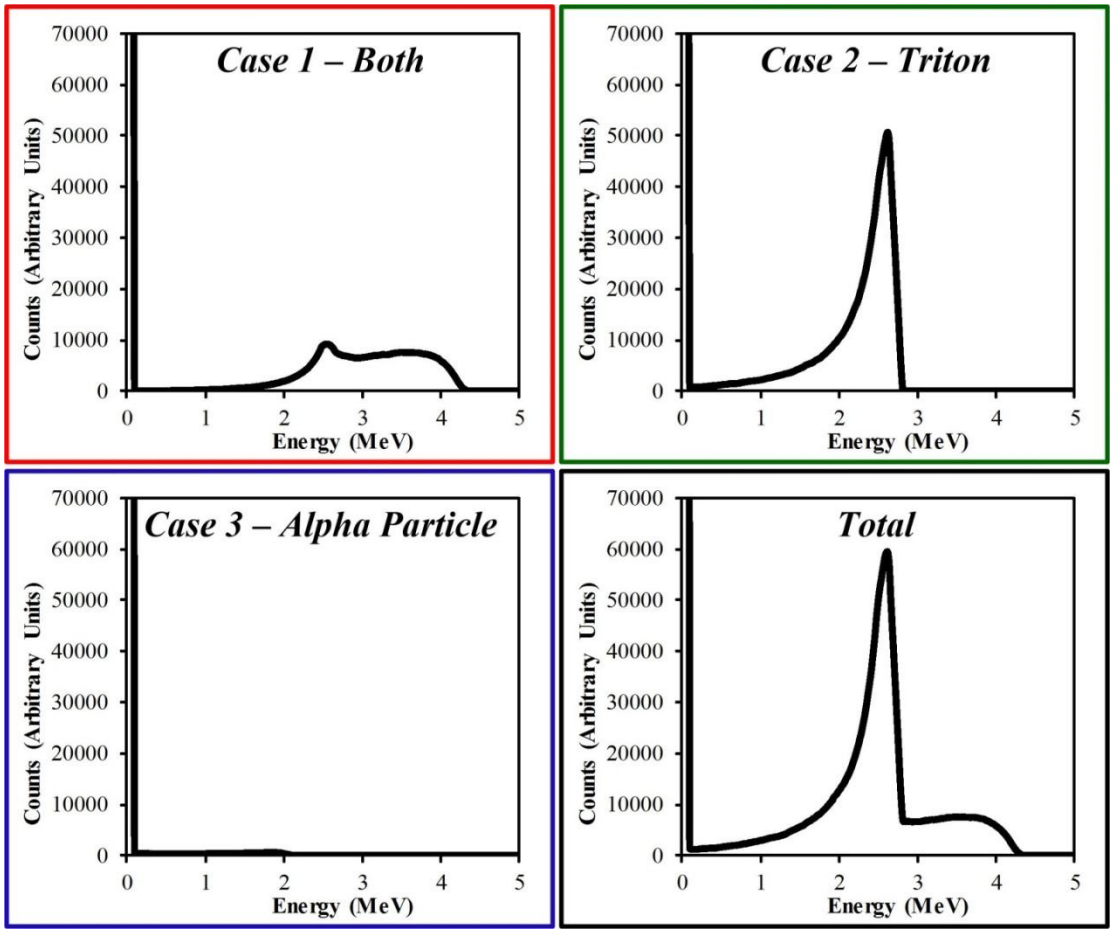

Figure B.2: The pulse-height spectrum contribution from the three cases where reaction products deposited energy in the gas volume. The total of the three cases is summed into one pulse-height spectrum in the lower right. The plots are for 35 µm thick ^{6}Li foil.

APPENDIX C

MCNP6 CODE

MCNP6 was used to obtain pulse-height spectra, evaluate absolute detection efficiency (cps ng^{-1}), and optimize detector moderator configurations the MWPCs. MCNP is a general purpose code used for a variety of applications including detectors, medical physics, shielding, and fission and fusion reactor design. MCNP6 has the ability to trace charged particles, neutrons, and heavy ions, which is critical for neutron detector designs.

MCNP6 was used to develop pulse-height spectra for Li foil MWPCs pressurized with P-10 gas, which gave the ability to energy calibrate experimentally obtained pulse-height spectra. The simulations assisted with setting LLD thresholds. Further, the ability to predict pulse-height spectra was especially valuable when designing new neutron detectors or new configurations, and also allowed for detector comparisons without construction. The MCNP6 program was also used to model the corrugated backpack neutron detector design and investigate and compare angular responses of both planar and corrugated backpacks. Further, the LPC for the MTR ORNL tests was modeled in MCNP6. The code was provided to a simulation team as a comparison to the experimental tests and was to be used to predict future experimental results.

Appendix C.1 – MCNP6 pulse-height spectra

The MCNP6 code used to develop the pulse-height spectra are shown below. The simplest method for investigating all detector materials and configurations was to include them all in one program, and comment out the portions of the code not to being investigated. The program below was used to obtain the single layer pulse-height spectra for different P-10 pressures, ^{6}LiF coated Mylar pulse-height spectra for different thicknesses of ^{6}LiF, pure ^{10}B foil pulse-height spectra, and estimate absolute and intrinsic detection efficiencies.

```
thermal neutrons incident on Li-6 foil neutron detector
c ================================ cell cards
==================================
101   1  -0.463     -20                  $ Li foil
110   3  -0.00156 -10 20 $ 21             $ P-10 gas
c 111   4  -1.4       -21
120   0  -99 10                          $ void around Al box
999   0   99                            $ problem graveyard

c ============================== surface cards
==================================
10 RPP  0.0 17       0.0 20.0075      0.0 17     $outer Al box
20 RPP  0.0 17       10.00028  10.00103      0.0 17     $ Li foil
21 RPP  0.0 17       10.00025 10.00028 0.0 17     $ mylar
99  so   500  $ graveyard boundary

c ================================ data cards
==================================
c --- problem specs ---
mode n t a
c
imp:n  1  2r  0
imp:t  1  2r  0
imp:a  1  2r  0
c
phys:n  6j  3  $ turn on NCIA algorithm
c
cut:n   2j  0
cut:t    j  0.001  0
cut:a    j  0.001  0
c
nps 5e6
prdmp j  1e8  1  1  1e8
dbcn 2j 1 10 24j 1
c print  100
c
c --- source: square monodirectional  ---
sdef  pos = 8.5  -200  8.5   rad=d1
      vec = 0 1 0  dir = 1
      erg = d3
si1   0  1
sp3  -5  2.53e-8
c sd4   125000
c
c --- tallies ---
f4:n  101
fm4  -1  1  105
c  sd4   1
c
f6:a     110
f16:t    110
c
f8:a,t   110
ft8  phl  2  6  1  16  1  0
```

```
e8   0  1e-5  254i  5
c The easiest way to run simple tests to include all materials into one
card and comment out the materials you do not want to include
c --- materials ---
m1   $ Li-6 metal  density 0.463 g/cm^3
      3006.66c  1
c m1 5010.66c  1 $ B-10, RHO = 2.158
c     9019.66c  0.5
c
c m2  $ Al metal;  density 2.6989 g/cm^3
c      13027.66c  1
c   $ P-10 gas; density at 2.8 atm = 0.004368 g/cm^3
m3   1001.66c   0.285714
     6000.66c   0.071429
     18000.66c  0.642857
m4  1001.24  0.3636 & $ Mylar, RHO = 1.4
     6000  0.4545 &
     8016.21  0.1818
```

Appendix C.2 – MCNP6 corrugated spectra and angular response

Discussed in chapters 6 and 7 are the construction details and neutron sensitivity measurements of the corrugated Li foil MWPC. The corrugated design results in 2.5 cm x 2.5 cm square channels of ^{6}Li foil containing a single anode wire. These designs were first developed in MCNP6 to obtain the theoretical pulse-height spectra, assisted in understanding the differences between the planar ^{6}Li foil pattern and corrugated MWPC designs. Additionally, the corrugated design was a candidate for the backpack neutron detector delivered to NNSS. It was assumed that angular response studies would be conducted at the NNSS testing, which is also critical information for missions that might deploy backpack neutron detectors. Thus, an MCNP6 simulation was conducted by rotating the neutron source around the corrugated and planar backpack MWPC designs, which is shown below. The results are discussed in Chapters 6 & 7 and the simulation code is shown below. Additionally, a phantom filled with water was included in the simulation as representation of a human torso.

```
thermal neutrons incident on Li-6 foil neutron detector
c ================================ cell cards
================================
100   2  -2.6989   11 -10               $ Al box
101   1  -0.65    -20                  $ Li foil
102   1  -0.65    -21                  $ Li foil
103   1  -0.65    -22                  $ Li foil
104   1  -0.65    -23                  $ Li foil
105   1  -0.65    -24                  $ Li foil
110   3  -0.004368 -11 20 21 22 23 24  $ P-10 Gas
63 6 -1.04 -16 5 -19                   $ human phantom
c 111   4  -0.98      -25                $ HDPE
112   4  -0.98     -26                  $ HDPE
113   4  -0.98     -27
114   4  -0.98     -28
120   0  -99 10 26 #63 27 28             $ void around Al box
999   0   99                            $ problem graveyard

c ============================== surface cards
================================
5 pz -17.45
16 sq 96.04 392.04 0 0 0 0 -37651.521 11 -10 0   $trunk
19 pz 52.35
10 RPP  -3.96 25.96       0.0 11.43      -3.81 28.46     $outer Al box
11 RPP -3.6425 25.6425   1.27 11.1125    -3.4925 28.1425 $inner Al box
20 RPP  0.0 22  3.1375 3.145  0  24.8 $ Li foil
21 RPP  0.0 22  4.7325 4.74  0  24.8 $ Li foil
22 RPP  0.0 22  6.3275 6.335  0  24.8 $ Li foil
23 RPP  0.0 22  7.9225 7.93  0  24.8 $ Li foil
24 RPP  0.0 22  9.5175 9.525  0  24.8 $ Li foil
25 RPP  -3.96 25.96      -5 0             -3.81  28.46       $ HDPE
26 RPP  -3.96 25.96     11.43 14.43              -3.81  28.46      $ HDPE
27 RPP  -6.96 -3.96      0.0 11.43       -3.81 28.46
28 RPP  25.96 28.96      0.0 11.43       -3.81 28.46
c 30 RPP  -19.48 41.48       -5 25.48         -21.59 -6.35     $ HDPE
99  so   500  $ graveyard boundary

c ================================ data cards
================================
c --- problem specs ---
mode n t a
c
imp:n   1 1 1 1 1 1 1 1 1 1 1 1 0
imp:t   1 1 1 1 1 1 1 1 1 1 1 1 0
imp:a   1 1 1 1 1 1 1 1 1 1 1 1 0
c
phys:n  6j  3  $ turn on NCIA algorithm
c
cut:n   2j  0
cut:t    j  0.001  0
cut:a    j  0.001  0
c
```

```
nps 2e6
prdmp j  1e8  1  1  1e8
dbcn 2j 1 10 24j 1
c print  100
c
c --- source: square monodirectional  ---
c sdef  pos = 1  -200  1 x=d1 y=0 z=d2 $ rad=d1
c       vec = 0 1 0  dir = 1
c       erg = d3
c si1   0  21
c sp1   0  1
c si2   0  21
c sp2   0  1
c sp3   -3  0.779 4.68927 $  -5  2.53e-8
c
C --- POINT ISO. 252CF SOURCE COLL. INTO A CONE ALONG THE X-AXIS.
SDEF  POS= 11 100 12.4 PAR= 1 ERG= D2 VEC= 0 -1 0  DIR= D1
SI1  -1  0.923880  1     $ -1 COS(CONE HALF-ANGLE) 1
SP1   0  0.961940 0.03806 $ 0 UO=(1+COS(CONE HALF-ANGLE))/2 (1-UO)
SB1   0. 0.       1.     $ SOURCE BIAS FOR EACH BIN
SP2  -3  0.779 4.68927  $ 252CF SRC, WATT SPECT.: 1.025 2.926
c --- tallies ---
f4:n  (101 102 103 104 105)
fm4  -1  1  105
c  sd4   1
c
f6:a     110
f16:t    110
c
f8:a,t   110
ft8  phl  2  6  1  16  1  0
e8   0  1e-5  254i  4
c
c --- materials ---
m1   $ Li-6 metal  density 0.463 g/cm^3
      3006.66c  1
c
m2  $ Al metal;  density 2.6989 g/cm^3
     13027.66c  1
c   $ P-10 gas; density at 2.8 atm = 0.004368 g/cm^3
m3   1001.66c   0.285714
     6000.66c   0.071429
     18000.66c  0.642857
m4  $  HDPE;  density 0.98 g/cm^3
     1001.66c   0.6666
     6000.66c   0.3334
c m5  1000 10.454E-02 6000 22.663E-02 7000 2.490E-02 8000 &
c     63.525E-02 11000 0.112E-02 12000 0.013E-02 14000 0.030E-02 &
c     15000 0.134E-02 16000 0.204E-02 17000 0.133E-02 19000 &
c     0.208E-02 20000 0.024E-02 26000 0.005E-02 30000 0.003E-02 &
c     37000 0.001E-02 40000 0.001E-02  $soft tissue
m6 $ water density 1
     1000.66  0.6667
       8000.66  0.3334
```

Appendix C.3 – HDPE Moderator Optimization

The five-layered Li foil MWPC neutron detectors were surrounded with HDPE neutron moderator. The ^{252}Cf source used in many of the experiments emits spontaneous fission neutrons at energies greater than 1.0 MeV. Thus, moderator was used to reduce the neutron energy to increase their absorption probability in the detector. Shown in Figure C.4 is the moderator optimization plot for a single Li foil MWPC obtained by positioning a bare ^{252}Cf source 2 m from the front face of the detector. Various ratios of front moderator thickness t_f to total moderator thickness t_{tot} were investigated with total thicknesses of 5, 7, 15, and 20 cm. The increase in intrinsic neutron detection efficiency was greater between 5 to 7 cm and 7 to 15 cm than the change from 15 to 20 cm. The increased neutron detection efficiency between 15 cm and 20 cm of total moderator thickness was not enough to justify 20 cm total thickness. Since the 15 cm total thickness was not significantly lower in detection efficiency, but was lighter weight than the 20 cm thickness, 15 cm was chosen as the total moderator thickness. The optimized HDPE configuration that gave the highest efficiency was 4.25 cm in front of the detector with 10.75 cm in back. However, these thicknesses of HDPE are not readily available, thus, 5 cm of moderator was used on the front of the detector and 10 cm was applied to the back. These moderator thicknesses do not change the intrinsic detection efficiency significantly from the optimized configuration.

Simulating a single large-area five Li foil layer MWPC with 5 cm of HDPE on the front and 10 cm on the back resulted in an intrinsic neutron detection efficiency of approximately 10% from a bare ^{252}Cf source. Adding a second detector to the configuration with 5 cm of HDPE positioned between the detectors and on the front and back resulted in a simulated intrinsic neutron detection efficiency of approximately 17.5%, increasing the efficiency 75% from just one detector. It would be a good assumption that adding a third detector to the configuration would increase the detection efficiency significantly more. However, the addition of the third detector with optimized moderator configuration resulted in an increase in detection efficiency of 12.5%. The three detector configuration had a maximum intrinsic neutron detection efficiency of 19.7% with t_f = 2.5 cm, $t_{middle1}$ = 5 cm, $t_{middle2}$ = 5 cm, and t_b = 2.5 cm. The plot in Figure C.2 showing the intrinsic neutron detection efficiency as a function of moderator optimization was completed using MCNP6 by keeping the middle thicknesses equal and constant and varying the

front t_f to back t_b moderator ratio. The plot shows that the middle moderator thicknesses impact the overall intrinsic neutron detection efficiency more than the front and back thicknesses. If the middle moderator thicknesses are less than 5 cm, then the neutron detection efficiency is lower than the maximum efficiency, most likely due to insufficient scattering of the neutrons. The reverse occurs when the middle moderator thicknesses are greater than 5 cm in which too much moderator causes neutrons to be scattered in the HDPE and not escape into an adjacent MWPC detector. A similar affect was observed with the middle moderator thickness of the two detector configuration shown in Chapter 6. Overall, it can be concluded that the intrinsic neutron detection efficiency of the two and three MWPC detector configurations was mostly dependent on the middle moderator thicknesses.

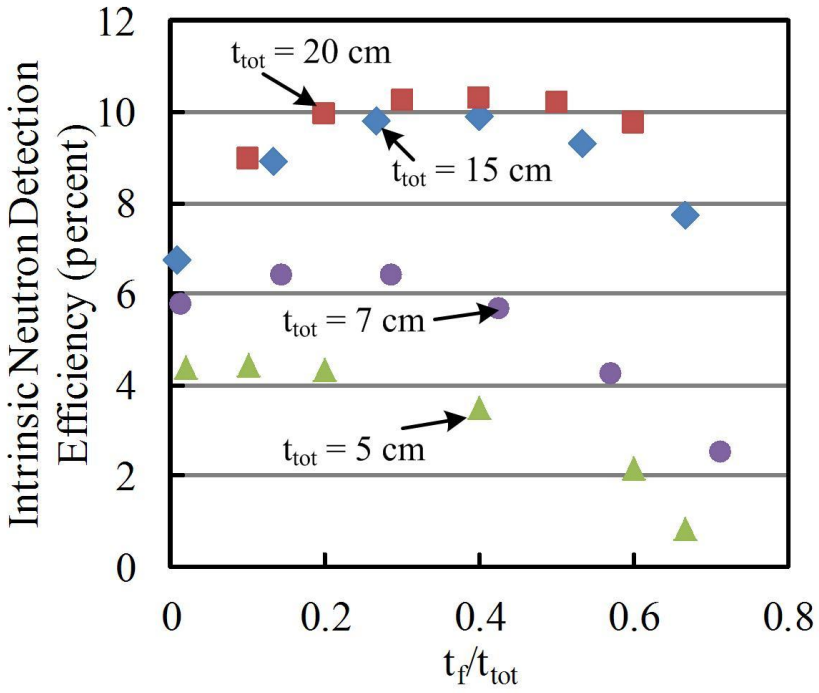

Figure C.1: The HDPE moderator optimization for a single detector was completed using MCNP6 by varying the ratio of front t_f to total t_{tot} moderator for 5, 7, 15, and 20 cm of total moderator.

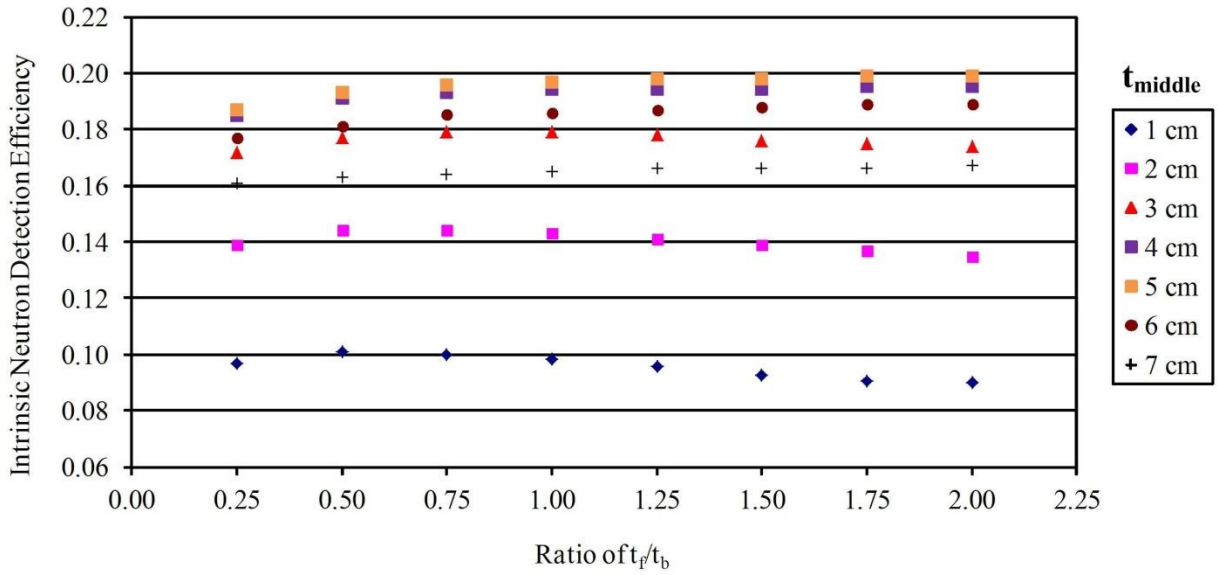

Figure C.2: The HDPE moderator optimization for three detectors all back-to-back was completed using MCNP6 by varying the ratio of the front (t_f) to back (t_b) moderators while the two middle layer thicknesses (t_{middle}) of HPDE remained constant for various middle thicknesses.

Appendix C.4 – LPC Modeling

The LPC modeling was completed using MCNP6 and the schematics of the detector dimensions and setup are shown in Figure C.3, Figure C.***4***, and Figure C.***5***. The LPC consisted of two large-area detectors positioned back-to-back with 5.0 cm of HDPE positioned between, front, and back of the detectors with 2.54 cm on the sides, top, and bottom. The detectors consisted of 5 layers of 75 µm thick ^{6}Li foil positioned 1.63 cm apart and each had an effective Li foil area of 1250 cm^{2}. In the simulation a bare ^{252}Cf source was positioned 2.0 meters from the front face of the detector. There was no ground or floor included in the simulation and neutron scattering through the air was considered negligible, thus, the rest of the simulation was considered void or vacuum. The simulation resulted in an absolute detector efficiency of 1.66 cps ng^{-1} with an intrinsic neutron detection efficiency of 13.7 percent. As expected, this is lower than the measured value at ORNL of 1.9 cps ng^{-1} for a bare source at 2.0 meters. The most likely reasons for the difference is the room, ground, and air scattering of the neutrons at ORNL, resulting in a higher count rate. The computer code used to generate these detector efficiencies are shown below.

```
thermal neutrons incident on Li-6 foil neutron detector
c ================================ cell cards
================================
c ------------------------------ Detector Setup -------------------------
------
100   2  -2.6989   -10  fill=1             $ Al box
101   1  -0.463    -20  u=1                $ Li foil
102   1  -0.463    -21  u=1                $ Li foil
103   1  -0.463    -22  u=1                $ Li foil
110   3  -0.004368 -11 20 21 22  u=1 $ P-10 gas
130   2  -2.6989   11   u=1                $ remaining space
141   like 100 but trcl=(31.19 0 32.3975)
142   like 100 but trcl=(31.19 0 0)
143   like 100 but trcl=(0 0 32.3975)
144   like 100 but trcl=(62.38 0 32.3975)
145   like 100 but trcl=(62.38 0 0)
c ---------------------------  Detector Moderator ----------------------
------
111   4  -0.98      -25 #100 #141 #142 #143 #144 #145             $ HDPE
c ------------------------------ Souce Moderator -------------------------
------
c 113   4  -0.98    -402 401              $ HDPE
c 114   5  -11.34   -401 400              $ lead
```

```
c ---------------------------------- Empty Space ----------------------------
------
120   0  -99 10 25           $ void around Al box
999   0   99                            $ problem graveyard

c ============================== surface cards
==================================
c ------------------------------ Detector Setup ----------------------------
------
10 RPP  -3.96 25.96       0.0 9.43      -3.81 27.3175          $ outer Al
box
11 RPP -3.6425 25.6425   1.27 9.1125    -3.4925 27      $ inner Al box
20 RPP  0.0 22  3.1375 3.145  0  25                          $ Li foil
21 RPP  0.0 22  4.7325 4.74  0  25                         $ Li foil
22 RPP  0.0 22  6.3275 6.335  0  25                          $ Li foil
23 RPP  0.0 22  7.9225 7.93  0  25                         $ Li foil
24 RPP  0.0 22  9.5175 9.525  0  25                          $ Li foil
c ----------------------------  Detector Moderator ----------------------
------
25 RPP  -5.23 89.61      -2.3333 14.0966             -6.35  64.795    $
HDPE
c ------------------------------ Souce Moderator -------------------------
------
400 RPP 10 12 -196 -194  11.4 13.4                              $ Lead inner
box
401 RPP 9.6 12.4 -196.4 -193.6 11 13.8                          $ Lead outer
box
402 RPP 7.1 14.9 -198.9 -191.1 8.5 16.3                         $ HDPE
c ---------------------------------- Empty Space ----------------------------
------
99  so   500  $ graveyard boundary

c ================================ data cards
==================================
c --- problem specs ---
mode n t a $ mode setting dictates what particles are tracked options are
n:neutrons t:tritons a:alpha h:gamma
c
c The following are the importance of particles each cell in descending
order if a cell is listed
c as zero importance the program will not keep track of the particle in
that cell.
imp:n  1 1 1 1 1 1 1 1 1 1 1 1 1  0
imp:t  1 1 1 1 1 1 1 1 1 1 1 1 1  0
imp:a  1 1 1 1 1 1 1 1 1 1 1 1 1  0
c
phys:n  6j  3  $ turn on NCIA algorithm
c
c The following are the energy cutoffs for tracking in ev
cut:n   2j  0
cut:t    j  0.001  0
cut:a    j  0.001  0
c
c nps is the number of particle histories ran e# = 10^#
```

```
nps 4e6
prdmp j  1e8  1  1  1e8
dbcn 2j 1 10 24j 1
c
c ------------------------------------- Souce Setup --------------------
----------------------
c Two sources are listed below. Monodirectional and cone source
c The cone source biases its counts to act like a isotropic source
c When specifying a position coordinates are in xyz
c --- source: square monodirectional  ---
c sdef  pos = 0  -200  0  rad=d1 $ x=d1 y=0 z=d2
c       vec = 0 1 0  dir = 1
c       erg = d3
c si1   0  1
c sp3   -3  0.779 4.68927      $ to use a monoenergetic source at thermal
energies input -5  2.53e-8
c
C --- POINT ISO. 252CF SOURCE COLL. INTO A CONE ALONG THE X-AXIS.
SDEF  POS= 31 -205 12.4 PAR= 1 ERG= D2 VEC= 0 1 0  DIR= D1 $ to adjust
direction change vec DO NOT ADJUST D1!
SI1  -1  0.923880  1                                          $ -1 COS(CONE
HALF-ANGLE) 1
SP1   0  0.961940 0.03806                                      $ 0
UO=(1+COS(CONE HALF-ANGLE))/2 (1-UO)
SB1   0. 0.       1.                                           $ SOURCE BIAS
FOR EACH BIN
SP2  -3  0.779 4.68927                                         $ 252CF SRC,
WATT SPECT.: 1.025 2.926
c
c ---------------------------------------- tallies ----------------------
------------------------
c
f4:n  (101 102 103) $ f4 tally keeps track of the flux through the listed
cells
fm4  -1  1  105            $ specific inputs used to adjust code do not
change
c
f6:a     110               $ f6 tally tracks the length estimate of
energy deposition for the listed particle type in the given cell
f16:t    110               $ f16 tally expansion for f6 to for a second
particle type
c
f8:a,t   110               $ f8 tally tracks energy disposition of pulses
in the detector
ft8  phl  2  6  1  16  1  0 $ specifications
e8   0  1e-5  254i  4      $ a list of starting energy, lowest energy
graphed, number of energy bins, largest energy graphed
c
c ---------------------------------------- materials ---------------------
----------------------
c
c for materials list the particle number then the specific isotope
followed by .66c  the second number is the atomic percentage
m1   $ Li-6 metal  density 0.463 g/cm^3
```

```
      3006.66c  1
c
m2  $ Al metal;  density 2.6989 g/cm^3
     13027.66c  1
c   $ P-10 gas; density at 1 atm = 0.00156 g/cm^3
m3   1001.66c   0.285714
     6000.66c   0.071429
     18000.66c  0.642857
m4  $  HDPE;  density 0.98 g/cm^3
     1001.66c   0.6667
     6000.66c   0.3334
m5  82000.66c 1 $ lead density 11.34 g/cm^3
```

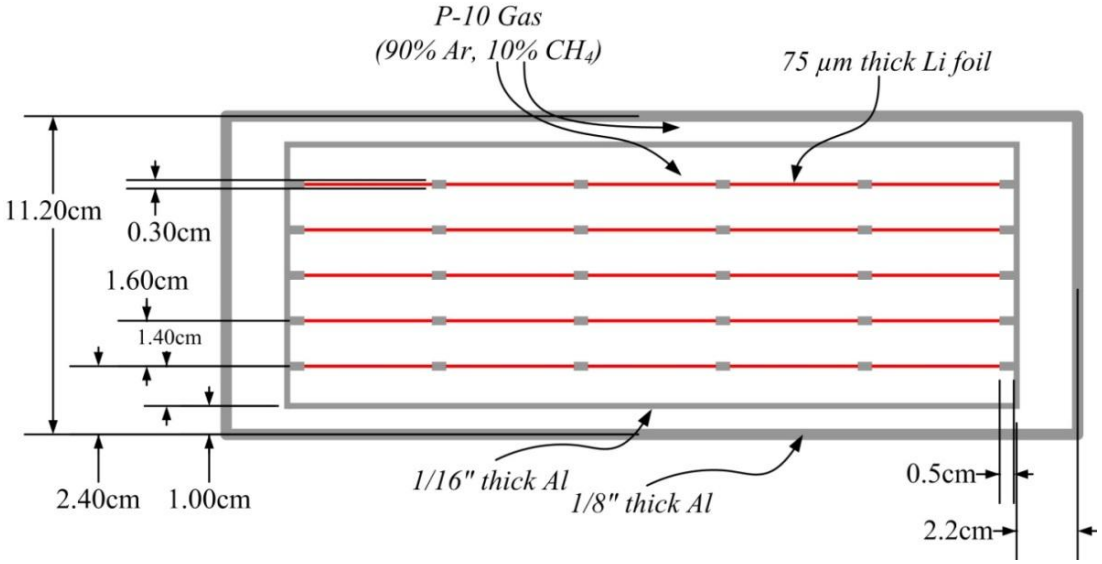

Figure C.3: A top cross-sectional schematic of the large area device used in the LPC for the MTR at ORNL. The device contains 5 parallel layers of 75 μm thick ^{6}Li foil spaced 1.6 cm apart. The schematic is proportional to scale except for the Li foil thickness.

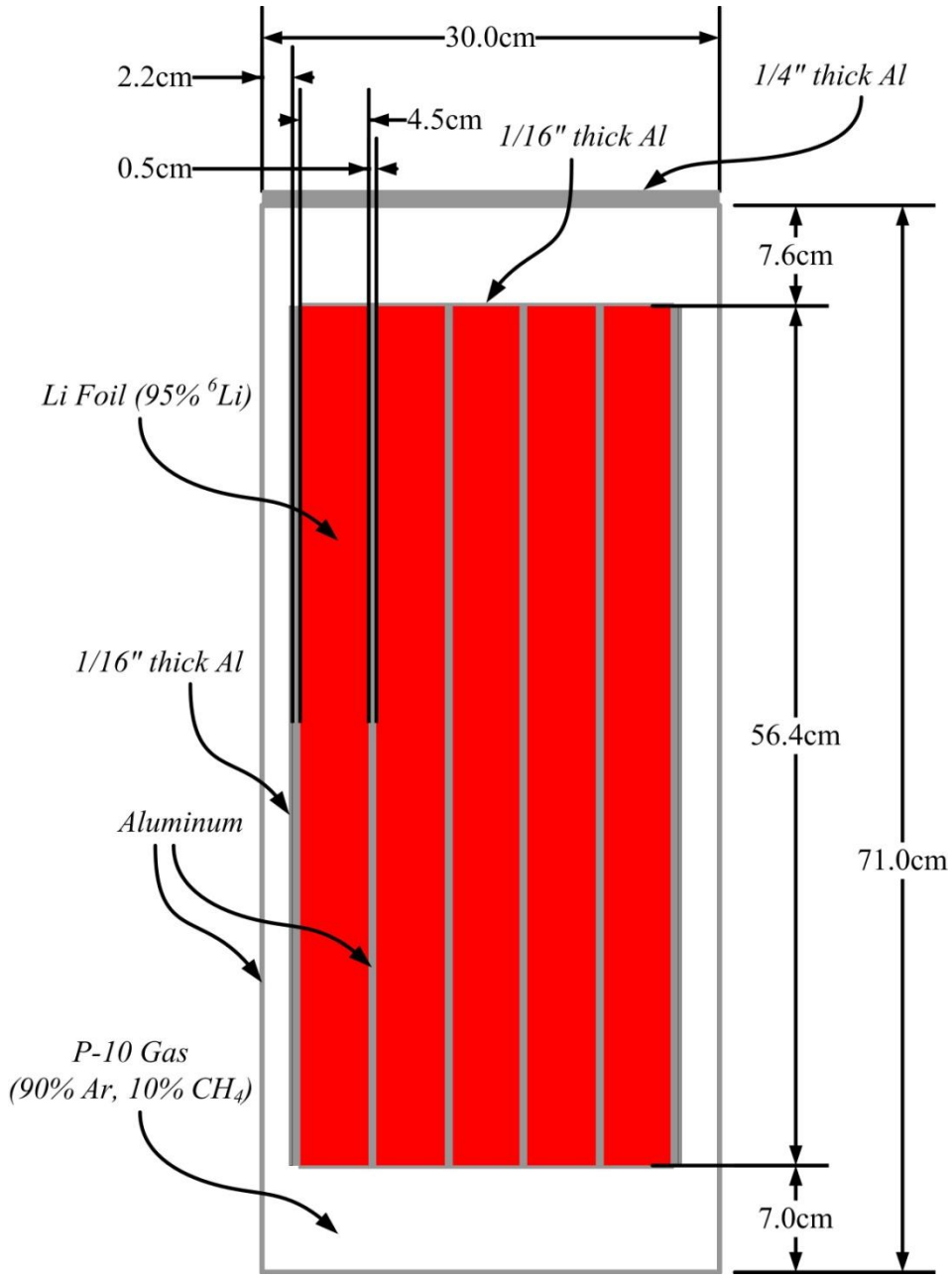

Figure C.4: A side cross-sectional schematic of the large area detector used in the LPC for the MTR at ORNL.

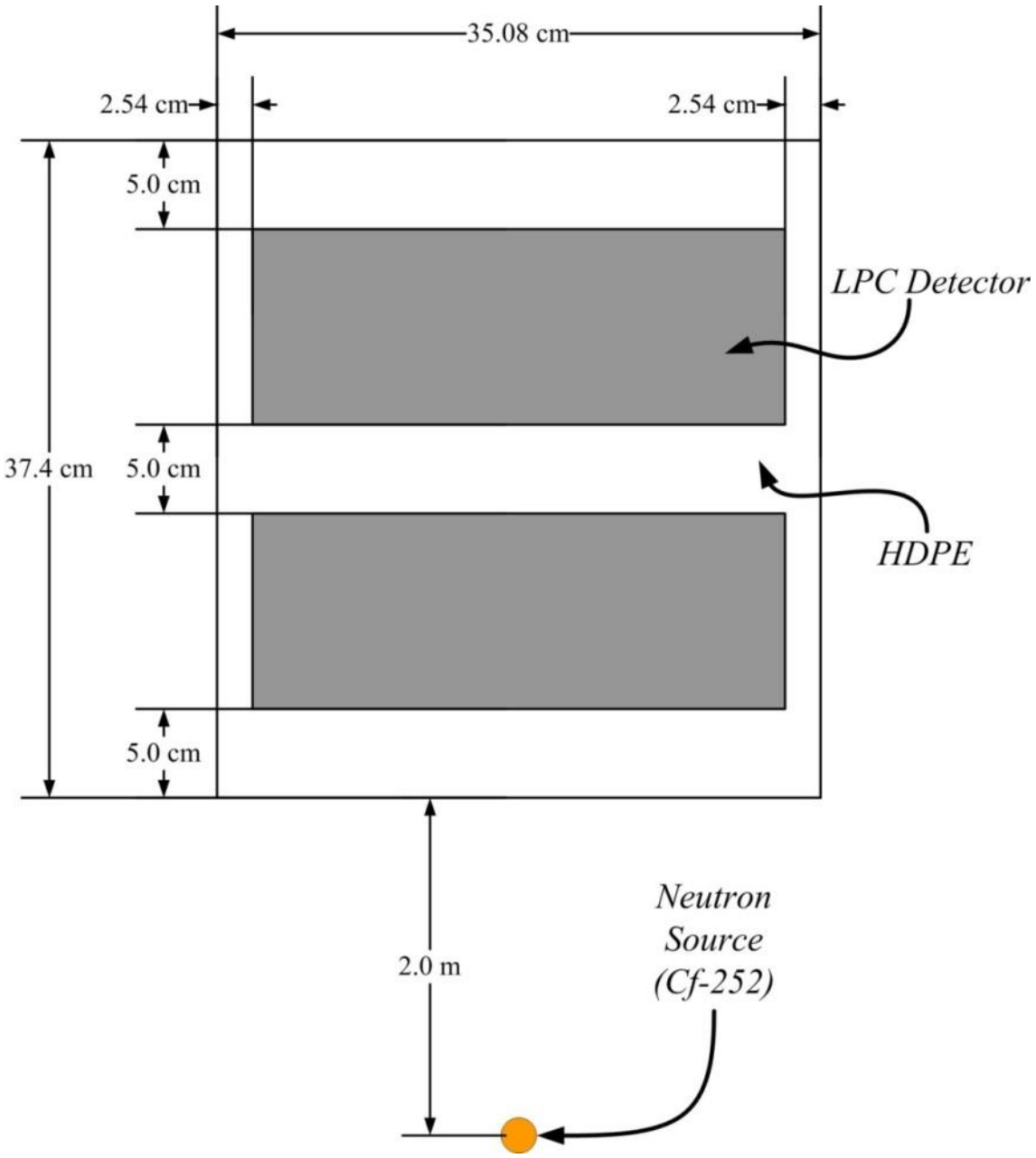

Figure C.5: A top view schematic of the LPC detector containing the two large area detectors.

APPENDIX D

SOLID ANGLE COMPARISON

The fractional solid angle formula ($\Omega_{f_{DNDO}}$) used in the RPM measurements was provided by DNDO and is [24]

$$\Omega_{f_{DNDO}} = \frac{1}{\pi}\arctan\left[\frac{W \times L}{4 \times D \times \sqrt{\frac{W^2}{4} + \frac{L^2}{4} + D^2}}\right], \tag{D.1}$$

where W is the detector width, L is the detector height, and D is the distance from the source to the detector. (For RPM testing D = 200 cm.) If a detector occupies the entire area available in RPMs, then W = 30.5 and L = 200 cm. Recently, a new solid angle formula ($\Omega_{f_{Gossman}}$) was developed by Gossman et alli [77-79] for a square aperture detector, which is expressed as

$$\Omega_{f_{Gossman}} = \frac{1}{\pi}\arcsin\left[\frac{W \times L}{\sqrt{(W^2 + D^2)(L^2 + D^2)}}\right]. \tag{D.2}$$

Applying the RPM dimensions to Eq. D.1 and Eq. D.2, the difference between $\Omega_{f_{DNDO}}$ and $\Omega_{f_{Gossman}}$ is 0.04%.

The fractional solid angle of a detector with a circular ($\Omega_{f_{Circle}}$) aperture is given by [17]

$$\Omega_{f_{Circlen}} = 0.5\left[1 - \frac{D}{\sqrt{(r^2 + D^2}}\right], \tag{D.3}$$

where r is the radius of the aperture and D is still the distance from the source to the detector. The area of a rectangular aperture can be set equal to the area of a circle to find the equivalent radius

$$r = \sqrt{\frac{W \times D}{\pi}} \,. \tag{D.3}$$

Substituting Eq. D.3 into Eq. D.4 gives an estimated fractional solid angle, but is not an accurate method to use in calculations. The three equations describing the fractional solid angle are plotted in Figure D.1 as a function of source to detector distance with the detector aperture equal to that of a RPM. In the figure $\Omega_{f_{DNDO}}$ and $\Omega_{f_{Gossman}}$ overlap, giving the appearance there are only two plots shown. The percent difference between $\Omega_{f_{Gossman}}$ and $\Omega_{f_{Circle}}$ is plotted in Figure D.2, which shows the percent difference at a distance of 200 cm for the RPM is 7.5%, large enough to skew calculated efficiency values.

The data plotted in Figure D.1 is only for RPM dimensions and shows the circular approximation is not a good method to use in detector evaluations. However, not all detectors have a rectangular aperture, such as backpack neutron detectors. As the rectangular aperture of a detector approaches a square geometry, the percent difference between $\Omega_{f_{Gossman}}$ and $\Omega_{f_{Circle}}$ is reduced. For example, if a 200 cm x 200 cm detector were positioned 200 cm from the source, the percent difference between $\Omega_{f_{Gossman}}$ and $\Omega_{f_{Circle}}$ is 0.62%. Further, for a 30.5 cm x 30.5 cm detector positioned at 200 cm the percent difference between $\Omega_{f_{Gossman}}$ and $\Omega_{f_{Circle}}$ is even less at 0.02%.

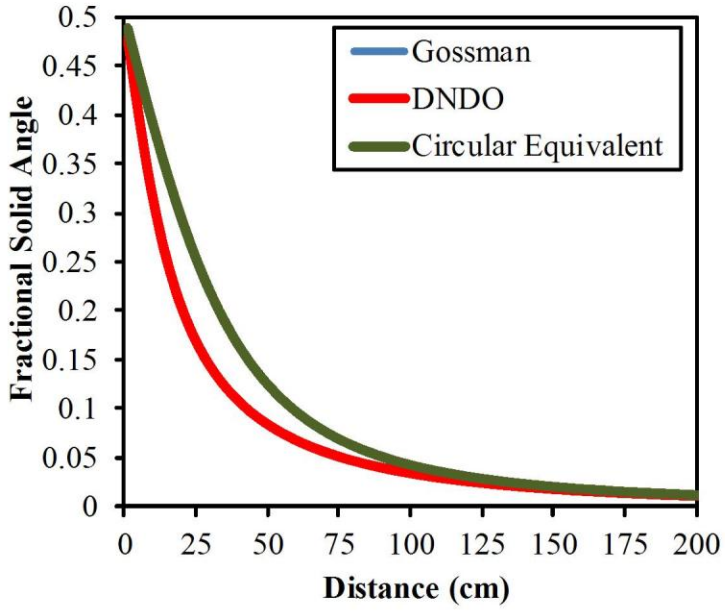

Figure D.1: The three fractional solid angle formulas plotted together as a function of the source to detector distance. (Gossman and DNDO overlap.)

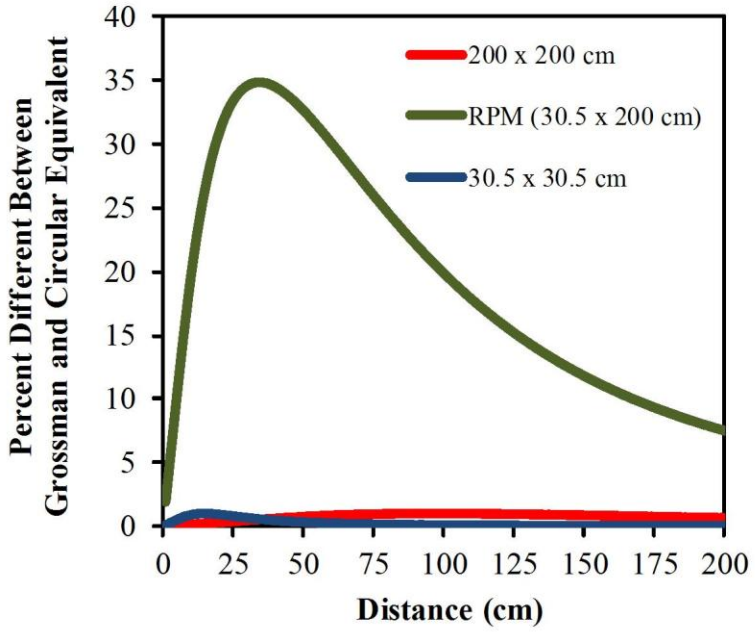

Figure D.2: The percent difference between the fractional solid angle presented by Gossman et alli and the circular equivalent for a rectangular aperture.

APPENDIX E

ADDITIONAL CALCULATIONS

Appendix E.1 – Electric Field Derivation from Gauss's law

Below is the derivation of the electric field in a coaxial gas-filled detector as a function of the axial position beginning with Gauss's law. Gauss's law relates the electric charge distribution to the electric field [80]

$$\Phi_E = \frac{Q}{\varepsilon_o}, \tag{E.1}$$

where Φ_E is the electric flux through a surface S enclosing any volume V, Q is the total charge enclosed by S, and ε_o is the electric constant. The electric flux can also be obtained by taking the surface integral of the electric field

$$\Phi_E = \oiint_S \overline{E} \bullet d\overline{A}, \tag{E.2}$$

where the dot product is obtained between the electric field $\overline{E}$ and the vector representing an infinitesimally area $d\overline{A}$. (Eq. E.2 is referred to as the integral form of Gauss's law.) Since we are dealing with coaxial devices, the surface area of a cylinder is defined as

$$\oiint_S dA = 2\pi r h, \tag{E.3}$$

where r is the radius of the cylinder and h is the cylinder height. Eq. E.3 can now be applied to Eq. E.2

$$\Phi_E = \oiint_S \overline{E} \bullet d\overline{A} = E \oiint_C dA = E 2\pi r h \tag{E.4}$$

Now that the height of the cylinder has been defined, the relationship to total charge density can be shown as

$$\Phi_E = \frac{Q}{\varepsilon_o} = \frac{\lambda h}{\varepsilon_o}, \tag{E.5}$$

Where λ is the charge per unit length, thus, the total charge density is the product of λ and h. Eq. E.4 and Eq. E.5 can now be set equal to each other to solve for the electric field

$$E(r) = \frac{\lambda}{2\pi\varepsilon_o}\frac{1}{r}. \tag{E.7}$$

The integral of Eq. E.7 with respect to r will result in the voltage V in the cylindrical space as a function of position between the anode and cathode

$$V = \int E(r)dr = \frac{\lambda}{2\pi\varepsilon_o}\int_a^b \frac{1}{r}dr = \frac{\lambda}{2\pi\varepsilon_o}\ln\left(\frac{b}{a}\right), \tag{E.8}$$

where b is the cathode radius and a is the anode wire radius. Eq. E.8 can be rearranged to show

$$\frac{\lambda}{2\pi\varepsilon_o} = \frac{V}{\ln\left(\frac{b}{a}\right)}, \tag{E.9}$$

which can be substituted in Eq. E.7 to show the electric field in a coaxial gas-filled detector as a function of the position in the device

$$E(r) = \frac{V}{r \ln\left(\frac{b}{a}\right)}. \tag{E.10}$$

Appendix E.2 – FWHM derivation from Gaussian function

The peaks observed in most pulse-height spectra can be approximated using the one dimensional Gaussian function, which is a probability density function of a normal distribution. A common evaluation of detectors is to compare peak resolutions, or full-width-half-maximums (FWHM), which can be derived starting with the Gaussian function [81]

$$f(x) = \frac{1}{\sigma\sqrt{2\pi}} \exp\left[\frac{-(x-\mu)^2}{2\sigma^2}\right]. \tag{E.11}$$

To find the FWHM, let x_o be half maximum points. Further, the first scaling term can be ignored in this case and *f(x)* is also divided by two to find half the maximum. Thus, we are left with

$$\frac{f(x)}{2} = \exp\left[\frac{-(x_o-\mu)^2}{2\sigma^2}\right]. \tag{E.12}$$

Also, $f(x_{max})$ occurs at $x_{max} = \mu$, so

$$\frac{f(\mu)}{2} = \exp\left[\frac{-(x_o-\mu)^2}{2\sigma^2}\right] = \frac{1}{2} \tag{E.13}$$

Solving for x_o,

$$\exp\left[\frac{-(x_o-\mu)^2}{2\sigma^2}\right] = 2^{-1} \tag{E.14}$$

$$-\frac{(x_o-\mu)^2}{2\sigma^2}=-\ln(2) \tag{E.15}$$

$$(x_o-\mu)^2=2\sigma^2\ln(2) \tag{E.16}$$

$$x_o=\pm\sigma\sqrt{2\ln(2)}+\mu\,. \tag{E.17}$$

The FWHM is therefore given by

$$FWHM\equiv x_+-x_-=2\sqrt{2\ln(2)}\approx 2.35\sigma \tag{E.18}$$